Ocean current variability in relation to offshore engineering.

A thesis submitted in partial fulfillment of the
requirements for the degree of

doktor ingeniør

by

Rune Yttervik

Trondheim, 2004

DEPARTMENT OF MARINE TECHNOLOGY
FACULTY OF ENGINEERING SCIENCE AND TECHNOLOGY
NORWEGIAN UNIVERSITY OF SCIENCE AND TECHNOLOGY

Acknowledgements

Abstract

This work adresses ocean current variability in relation to offshore engineering.

The offshore oil and gas activity has up until recently taken place mainly on the continental shelves around the world. During the last few years, however, the industry has moved past the continental shelf edge and down the continental slope towards increasingly deeper waters. In deep water locations, marine structures may span large spaces, marine operations may become more complicated and require longer time for completion and the effect of the surface waves is diminished. Therefore, the spatial and temporal variability of the current is expected to become more important in design and planning than before.

The flow of water in the oceans of the world takes place on a wide variety of spatial scales, from the main forms of the global ocean circulation ($\sim$km), to the microstructure ($\sim$mm) of boundary layer turbulence. Similarly, the temporal variability is also large. In one end of the scale we find variations that take place over several decades, and in the other end we find small-scale turbulence ($\sim$seconds). Different features of the flow are driven by different mechanisms. Several processes and properties (stratification[1], sloping boundary, Coriolis effect, friction, internal waves, etc.) interact on the continental slope to create a highly variable flow environment. Analysis of a set of observed data that were recorded close to the seabed on the continental slope west of Norway are presented. The data suggest that some strong and abrupt current events (changes in flow speed of $\sim$0.4 m/s in just a couple of hours) were caused by motions of the deep pycnocline[2], driven by variations in the surface wind field. This conjecture is partly supported by numerical simulations of an idealised continental slope and a two-layer ocean. The data also contains an event during which the flow direction at the sea bed changed

---

[1]Vertical distribution of density. In a stratified ocean or flow, the density of the water varies in the vertical direction.

[2]pycnocline=density surface between water masses. The pycnocline between two water masses of different density is defined by the maximum of the density gradient.

very rapidly (within a few minutes) from down-slope to up-slope flow. The change in speed during this event was as high as 0.5 m/s.

Another data set has been analyzed in order to illustrate the spatial variation in the current that can sometimes be found. It is shown that the flow in the upper layer is virtually decoupled from the flow in the lower layer at a location west of Norway. This is either caused by bottom topography, stratification or both.

High variability of the current presents new requirements to the way that the current should be modelled by the offshore engineer. For instance, it is necessary to consider which type of operation/structure that is to be carried out or installed before selecting design current conditions. Reliable methods for obtaining design current conditions for a given deep water location have yet to be developed, only a brief discussion of this topic is given herein.

It is shown, through calculations of VIV-response and simulations of typical marine operations, that the variability of the current will sometimes have a significant effect on the response/operation.

Contents

Nomenclature

General Rules

- Symbols are generally defined where they appear in the text for the first time.

- Symbols for vectors and matrices are written in bold face.

Roman symbols

u	water particle speed in x-direction
v	water particle speed in y-direction
w	water particle speed in z-direction
U	time averaged water particle speed in x-direction
V	time averaged water particle speed in y-direction
W	time averaged water particle speed in z-direction
u'	fluctuating water particle speed in x-direction
v'	fluctuating water particle speed in y-direction
w'	fluctuating water particle speed in z-direction
$\mathcal{T}$	water temperature
T	time averaged water temperature
T'	fluctuating water temperature
$\mathcal{S}$	water salinity
S	time averaged salinity
S'	fluctuating salinity
p	pressure
p_H	hydrostatic pressure
p'	non-hydrostatic pressure correction

R	Rossby radius of deformation
R_I	Internal deformation radius
N^2	buoyancy frequency, Brunt-Väisälä frequency
P_{atm}	atmospheric pressure
i	complex unit, $i = \sqrt{-1}$
$\overline{V_c}$	mean flow speed
$\overline{\mathbf{U}}_H$	mean horizontal velocity vector
$q_m(t)$	horizontal velocity vector in complex notation
$\mathbf{b}_m(\mathbf{x})$	the m'th empirical orthogonal function (EOF)
$\mathbf{w}_m(t)$	the m'th principal component
a_{nm}	complex representation of horizontal velocity vector
$\mathbf{B}$	matrix of EOFs
$\mathbf{W}$	matrix of principal components
$\mathbf{A}$	matrix of complex horizontal velocity vectors
$\mathbf{P}$	covariance matrix for principal components
$\mathbf{\Lambda}$	eigenvalue matrix
$\mathbf{C}$	covariance matrix for horizontal velocity vectors
$\hat{\mathbf{U}}_{P_{i,k}}$	velocity vector parallel with the sea floor at time instance i in HF time-trace no. k.
T_k	mean temperature in HF time-trace no. k.
V_{P_k}	mean flow speed parallel with the sea floor in HF time-trace no. k.
V_{MAX_k}	maximum flow speed parallel with the sea floor in HF time-trace no. k.
V_{RMS_k}	root mean square of the flow speed parallel with the sea floor in HF time-trace no. k.
f	Coriolis parameter
g	acceleration of gravity
C_v	heat capacity of seawater at constant volume
A_M	horizontal eddy viscosity
K_M	vertical eddy viscosity
A_H	horizontal eddy diffusivity
K_H	vertical eddy diffusivity
R_i	gradient Richardson number
f_{M_2}	semi-diurnal principal lunar frequency (M_2)
$\mathbf{V}_{P_k}$	mean velocity vector parallel with the sea floor for HF time-trace no. k.
f_v	vortex shedding frequency
S_t	Strouhal number
Re	Reynolds number
D	diameter of sphere or pipe

$\mathcal{F}_x$, $\mathcal{F}_y$, $\mathcal{F}_z$	parameterized friction forces in numerical ocean model
h_w	amplitude of wave-shaped perturbation of the pycnocline in numerical model
l_D	length of initial depression of pycnocline in numerical model
h_D	height of initial depression of pycnocline in numerical model
H	depth of undisturbed water column
c_0	linear speed of long internal waves in a two-layer fluid
S_m	independent scatter diagram
$S_{m|m_{pre}}$	conditional scatter diagram
$\mathbf{D}$	matrix of cell numbers
T_{VH}	measure of vertical variation of horizontal stiffness
$V_{H_{10}}$	10 minute mean horizontal speed
$p(v,\theta)$	2D probability density function for $V_{H_{10}}$ and $\theta_{H_{10}}$
$\hat{f}_{CF}$	non-dimensional frequency for cross-flow oscillations
$\hat{f}_{IL}$	non-dimensional frequency for in-line oscillations
$f_{osc,CF}$	cross-flow oscillation frequency
f_{sw}	eigenfrequency in still water
$\hat{f}_{sw}$	non-dimensional eigenfrequency in still water
$\hat{f}_{sw,IL}$	non-dimensional in-line eigenfrequency in still water
$E_{x,f_{osc}}$	excitation parameter for oscillation frequency f_{osc}
U_R	reduced veloctiy

Greek symbols

$\rho(\mathcal{T}, \mathcal{S}, p)$	density of seawater
$\sigma_t = \rho(\mathcal{T}, \mathcal{S}, 0)$	*in situ* density when the pressure effect is ignored
ρ'	density variation of seawater
ρ_0	reference density of seawater
κ_f	thermal conductivity of seawater
$\kappa_{\mathcal{T}}$	heat diffusivity of seawater
$\kappa_{\mathcal{S}}$	salt diffusivity of seawater
ϵ	dissipation rate per unit mass, $[m^2 s^{-3}]$
ρ_{ij}	complex correlation coefficient between velocity vectors
θ_{P_k}	mean direction of the flow that is parallel
	with the sea floor for HF time-trace no. k.
λ_w	length of wave-shaped perturbation
	of the pycnocline in numerical model
$\theta_{H_{10}}$	10 minute mean flow direction
γ	ratio between weight in water and drag force
$\vec{\tau}$	bottom stress
η	surface elevation
σ_n	standard deviation of noise in HF measurements
δ_{mk}	Kronecker delta
ω	internal wave frequency
ω	wave frequency
μ	dynamic molecular viscosity, $[\text{kgm}^{-1}\text{s}^{-1}]$
ν	kinematic molecular viscosity, $\nu = \mu/\rho$, $[\text{m}^2\text{s}^{-1}]$
ϕ	geographic latitude
Ω	angular speed of rotation of planet Earth about its axis
ϕ_M	prognostic value calculated by the numerical model
ϕ_F	prognostic value specified in the FRS-zone

Abbreviations

BBL	Benthic Boundary Layer (bottom boundary layer in the ocean)
VIV	Vortex Induced Vibrations
FRS	Flux Relaxation Scheme

Mathematical operators and other symbols

∇^2	Laplace operator
$\sum$	summation
$E[\cdot]$	expected value

CHAPTER 1

Introduction

1.1   The marine environment

Approximately 70% of the surface on Earth is covered by oceans. It is customary to consider the Southern Ocean (Antarctic Ocean), the Atlantic Ocean, the Pacific Ocean, the Indian Ocean and the Arctic Ocean to be the main oceans. Other bodies of water, or portions of oceans, are usually given the term 'sea'. Among these are the Mediterranean Sea, the Caribbean Sea, the Norwegian Sea, the Labrador Sea, the Weddell Sea, the China Seas and the Tasman Seas.

These oceans and seas, their dynamics, biology, physiology and chemistry, is what constitute the marine environment.

1.2   Humans and the marine environment

Humans have interacted with the marine environment for thousands of years. Activities such as fisheries, exploration, trade and war started early. Archaeological investigations have provided evidence that there was a well established trade-port in Lothal in India as early as 2400 B.C.

Early sea-farers, such as the Phoenicians, Egyptians, Arabs, Greek and Polynesians, started to collect information about the oceans around 1500 B.C. For a long time, navigation, trade and mapping the World was the main concern for these sailors. Since then, our knowledge of the oceans has increased gradually.

During the Ming dynasty the Chinese explored the China Seas and the Indian Ocean using their unique 'treasure fleet'[1] (Levathes 1997). They concluded, however, that nothing of significance was to be found outside of their borders, and, as a consequence, isolated themselves until well into the nineteenth century.

At the end of the 15th century, a series of important ocean voyages were initiated. The primary reasons for these voyages were, then, as they are now, economical and political. After a while it became clear that good knowledge of the ocean could be of good use in war and trade, and the desire to explore many aspects of the oceans lead to a mulititude of new discoveries. Sailing routes from Europe to China, India and the West-Indies were discovered by Vasco da Gama[2] and

---

[1]The Chinese treasure fleet, under the command of eunuch admiral Zheng He, sailed the seas between 1405 and 1433. This was a unique armada at the time. The largest ship in the fleet was four hundred feet long and had nine masts. In comparison, the Santa Maria, used by Colombus on his first journey to the New World in 1492, was only about 80 feet long.

[2]Vasco da Gama rounded the Cape of Good Hope in 1497, 10 years after Bartholomew Diaz of Portugal.

Christopher Colombus[3]. Much was contributed to the development of charts by the circumnavigations of Ferdinand Magellan (from 1519 to 1522) and Sir Francis Drake (from 1577 to 1580). Later, the voyages of Captain James Cook (between 1768 and 1779) provided more accurate charts than before, charts of new areas and also observations of winds, current and water temperatures.

In 1770 Benjamin Franklin published a chart of the Gulf Stream in order to enable shipmasters to select the fastest route between destinations in the North Atlantic. The first systematic collection of wind and current data, however, was made by Lieutenant Matthew F. Maury of the U.S. Navy, leading to the publication of his book `The Physical Geography of the Sea` in 1855. This book is by many scientists considered to be the first book on oceanography.

Tidal variations were observed early[4], but the physical mechanism responsible for these variations was not known. Johannes Kepler and Galileo Galilei did not succeed in presenting satisfactory explanations, and the physics of the tide was not fully understood until Sir Isaac Newton, some years later, formulated a correct, although somewhat simplistic, explanation of the phenomenon in his `Principia` of 1687.

Observations of marine organisms at several locations and depths were made by Alexander von Humbholdt, Charles Darwin and others, and in 1887, Victor Hensen discovered the plankton. In 1872 the first major scientific expedition, intended solely for the investigation of the ocean, set out. The Challenger expedition, lead by Sir Wyville Thomson, lasted for three and a half years (21/12-1872 until 24/5-1876). It took 23 years and almost 30000 pages to process and publish the findings made during this expedition, which is considered to be the starting point of oceanography as a modern science. This branch of science has continued to evolve rapidly until the present day.

Today, the marine environment still serves as an arena for fisheries, war and trade, but also for fish-farming, exploitation of fossil fuels like oil and gas and even as a construction site in which floating airports, submerged tunnels and other types of structures are being built. During the recent years the offshore oil and gas industry has looked towards increasingly deeper waters in its pursuit of profitable fossil fuel deposits. Fields at water depths exceeding 1000 meters are presently being developed, and several fields at water depths of 1500 to 2500 meters are being considered for development.

---

[3]Columbus arrived in the West Indies in 1492, some 500 years after the Vikings reached Vinland (Newfoundland).

[4]The Greek navigator Pytheas, around 300 B.C., related the tidal variations to those of the moon.

1.3   Motivation for the present work

Marine structures in the ocean are exposed to forces from hydrostatic pressure, temperature differences, waves and current flow. For certain spatial and temporal scales, these environmental loads vary in either time or space or both. Wave forces are important in the splash zone and on short time scales (minutes, seconds). Below the splash zone, however, the global response of slender structures such as risers, umbilicals and intervention lines is in some cases governed by the current flow. In other cases the response can be indirectly governed by the surface waves through the motions of one or more surface vessels attached to the slender structure. The spatial current variations in the ocean cover all scales from basin width to microscale, and temporal variations occur on periods from seconds to years. The variations containing sufficient energy such as to be important for marine structures/operations normally occur on scales larger than those of surface waves.

Traditionally, the offshore engineer assumes the current flow velocity to be constant in time when calculating dynamic response of marine structures or when planning and preparing for marine operations. As water depths increase, however, the current flow will be increasingly important in the analysis of global response of slender structures. Mooring lines, risers, umbilicals and intervention lines may span a large area when oil and gas fields are being developed at large water depths. If this area becomes large enough, using only a constant (in space) current profile, may not be enough to model the current with sufficient accuracy. Furthermore, complex marine operations at these large water depths may require such a large time window that flow speed and direction have time to change significantly during the operation. In the case that the current load on cables, intervention lines or hanging loads is of significance during critical moments of a marine operation, then variations of the current velocity could result in unforeseen and, possibly, unwanted events. Indeed, such events have already caused increased cost and added complexity to marine operations.

It is the increased importance of the spatial- and temporal variations in the current flow as the offshore engineering activity moves towards larger water depths that is the motivation for the present work.

1.4   Purpose of the work

When one is involved in the design of marine structures, or the planning of marine operations, for a certain offshore location one must find satisfactory answers to the following questions :

- What is the current flow like in the area?

- How is the structure/operation affected by this current?

There are, of course, several other issues that require attention and may be much more important than those mentioned above. The purpose of this work, however, is to shed some light on the issues raised by these two questions.

The circulation of water in the World's oceans vary from one location to the next. Previously, most of the offshore activity was taking place on the continental shelf. Now, however, more and more of this activity take place on the slope from the shelf edge to the deep water. Therefore, in an effort to address the issues stated above, the focus will be on the variability in time and space of the current flow near and above the continental slope and its effect on marine structures/operations in that area.

1.5 Outline of the thesis

An overview of the global circulation of water in the oceans, and the governing mechanisms, can be found in chapter 2. At several locations in the ocean (almost everywhere), local variations in the current flow exist on a variety of time- and length scales. An account of the properties of some of these variations, and of the mechanisms responsible for them, is given in section 2.3.1. Certain areas of the World's oceans have special and characteristic features to its current flow. The features of some of these areas, particularly those interesting for the offshore industry, are described in section 2.3.2. Finally, a detailed description of some processes taking place on the slope from the continental shelf to the deep ocean (the continental slope) is provided in section 2.4.

Chapter 3 contains a description of ocean current measurements, carried out at some locations on the continental slope outside Mid-Norway, and a discussion of the results. Measurements of flow velocity in the entire water coloumn at two locations are presented. These measurements were carried out using averaging periods of 10 and 30 minutes. In addition to these data, recordings of current velocity and water temperature at four locations near a small underwater hill, sampled at 1 Hz, are reported.

A numerical study on the velocities that occur when internal waves on a deep pycnocline[5] encounter an idealised continental slope is reported in chapter 4. An existing numerical ocean model is modified and used for this study. The results

---

[5]pycnocline=density surface between water masses. The pycnocline between two water masses of different density is defined by the maximum of the density gradient.

from the simulations are compared to model test results obtained by Grue (2002).

Ocean current variability applied in ocean engineering is reviewed and discussed in chapter 5. Some outlines and ideas of how to include this variability in design and planning are provided.

Some effects on marine structures and -operations which are exposed to variable current environments are shown in chapter 6.

Chapter 7 contains conclusions and recommendations for further work.

CHAPTER 2

Ocean dynamics

2.1   Introduction

The oceans are important to human life. They provide the home for large quantities of natural resources (food end energy), they are a key element in transporting these goods, other goods and people, and they are very important for the climate on Earth. Because of the importance of the oceans, it is in our interest to learn as much as possible about them. Oceanography is defined as the scientific study of the oceans. It is customary to consider this science to comprise the fields of physical oceanography, chemical oceanography, biological oceanography and geological oceanography. Researchers within theses fields study the water masses in the oceans. The water masses in the oceans contain many different ingredients, such as sediments, chemicals and living organisms. These ingredients are being transported by the ocean currents. The ingredients in the sea water determine the density of the water, which is important for the development of ocean currents. Living organisms in the ocean depend upon nutrients being transported by the ocean currents. For these reasons, along with several other reasons, researchers within one of the fields of oceanography often find it beneficial to cooperate with those working in one (or more) of the other fields. Thus, the various fields of oceanography cannot be viewed as entirely isolated from one-another, they are related.

The focus in this thesis is on the current flow in the ocean, a subject which belongs to the science of physical oceanography.

An overview of the global circulation, and the mechanisms governing this circulation, is given in this chapter. Current patterns in the major oceans are discussed. Local variations in the current flow exist on a variety of time- and length scales. Such variations can be instabilities, turbulence, eddies, etc. An account of the properties of theses variations and of the mechanisms responsible for them is given in section 2.3. Certain areas of the oceans of the world have special and characteristic features to its current flow. The features of some of these areas, particularly those interesting for the offshore industry, are described in section 2.3.2. Finally, a detailed description of some processes taking place on the slope from the continental shelf to the deep ocean (the continental slope) is presented.

2.2   Global ocean circulation

The major pathways of water in the world oceans are referred to as the global ocean circulation pattern. This circulation transports water, and therefore also matter and energy, from one part of the world to another. It is therefore an important factor in determining the climate in various parts of the world.

The mechanisms governing the large scale flow of water in the world oceans, together with the major features of the currents, will be introduced in the following. The scope of this thesis, namely the variability of the current flow near and above the continental slope and its effect on marine structures/operations in such areas, only allow for an overview on the subject of global ocean circulation. Such an overview is included because the variations at a specific location depend strongly upon the flow and the water properties on a larger scale in the surrounding area, and, thus, in the end on the global circulation.

More comprehensive treatments of the topic of descriptive physical oceanography and global ocean circulation can be found in e.g. Sverdrup et al. (1942), Pickard and Emery (1990), Cushman-Roisin (1994), Gill (1982) and Reddy (2001), which have all been used as sources for this chapter.

2.2.1 Sea water

Typical horizontal dimensions of the oceans are 5000-15000 kilometers. The maximum depth of the ocean is more than 11000 meters[1]. The ratio between vertical and horizontal scale in the ocean is thus $O(10^{-3})$, which is the same order of magnitude as the ratio between the radius of the Earth and the deepest place of the ocean. This ratio is very small, and the ocean can therefore be viewed as a very thin layer, or film, on the surface of the Earth. The oceans contain water masses of varying temperature and salinity. Although seawater posess other properties than just salinity and temperature, these two are the most important ones for the circulation, and they are therefore particularly interesting. Volumes of water with similar properties are referred to as *water masses*, and in many cases they tend to move as separate masses. The salinity and temperature of a water sample from an area can be entered into a T-S diagram, which gives the distribution of salinity and temperature over the depth, and these diagrams can be used to identify different water masses and, in some cases, their origin. Reddy (2001) classifies the water masses into the groups listed in Table 2.1.

water type group	typical depth
surface (near surface)	< 500 meters
intermediate	500-1200 meters
deep water	1200-4000 meters
bottom water	> 4000 meters

Table 2.1: *Water mass classification according to Reddy (2001).*

---

[1]The Mariana Trench east of the Phillipphines in the Pacific Ocean.

Observations of temperature and salinity of the water in the main three oceans (Atlantic, Pacific and Indian) suggest the existence of 19 different water masses in the upper 500 meters (Emery and Meincke 1986). Differences in temperature and salinity from one water mass to another occur for several reasons. Temperatures vary due to heating on the surface by the sun, heating through the sea bed, up-/down welling of water near a coast, transport of water by the major current systems and cooling of the water surface on high latitudes. Salinity varies due to evaporation, precipitation, river inflow, up-/down welling, ice formation/melting and mixing.

2.2.2 Mechanisms driving and governing the ocean circulation

The circulation of fluids in the atmosphere and in the ocean is ultimately driven by energy radiated by the sun. The water in the ocean, and its circulation, is subject to the laws of nature. Conservation laws for mass, heat and angular momentum apply along with Newton's laws of motion and gravitation. Pond and Pickard (1983) classifies the important forces as primary forces (causing motion) and secondary forces (resulting from motion). Forces on the water which cause motion (primary forces) are gravity (terrestrial, sun and moon), wind-stress, atmospheric pressure, heat exchange with the atmosphere and the solid earth and seismic forces. Gravity and wind-stress forces are the driving forces responsible for the thermohaline circulation and the wind driven circulation, respectively, as described in section 2.2.3. Once the water is moving, additional forces come into effect. The first of these is the Coriolis force (Corilois-effect), which is an apparent force on the moving fluid when the motion is observed relative to the rotating Earth. Another secondary force is the friction force, either within the fluid itself, or at its boundaries.

The large scale circulation in the oceans and the atmosphere is often referred to as *geophysical fluid flow*. The effects of stratification and rotation are crucial to this type of flows, and they are therefore also important for local flow features.

The combined effects of rotation and friction is the reason why, according to classical Ekman theory, the net wind-driven water transport in the upper layer of the ocean is 90 degrees to the right of the wind direction on the northern hemisphere[2]. This surface layer is known as the Ekman layer, and is described in several books on geophysical fluid dynamics, see e.g. Cushman-Roisin (1994) and Pond and Pickard (1983). The flow direction changes throughout the Ekman layer. At the surface, the wind driven current flows at an angle of 45° to the right of the wind direction (on the northern hemisphere). At the lower part of the surface Ekman layer, how-

---

[2]On the southern hemisphere the transport is 90 degrees to the left of the wind direction

ever, the relative direction between wind and current flow is approximately 180°. An Ekman layer is also formed at the sea bed when friction acts on the water flowing above the sea bed. The transport in the bottom Ekman layer is to the left of the direction of the undisturbed flow (on the northern hemisphere). Another feature of the combined effect of friction and rotation is the intensification of the current flow at the western boundaries of all oceans. There are strong currents with high shear in the west of the main oceans, but slower currents with much less shear in the eastern part of the same oceans. The explanation of this 'westward intensification' of the flow was provided by Stommel (1948) and is directly linked to the rotation of the Earth and friction between the flowing water and the coast. Ekman veering and westward intensification are features of the large scale circulation.

2.2.3 Main circulation types

Generally, the large scale circulation of water in the oceans is characterized as either thermohaline or wind driven. These two types of circulation cover the flow of water in the deep ocean and in the upper layers, respectively.

Thermohaline circulation

Gravitation is a primary force, acting on the water in the ocean. As we have already mentioned, the distribution of temperature and salinity (and thus density) in the oceans is not homogenous. For large parts of the ocean the vertical water coloumn can be divided into three parts according to the distribution of water temperature. In the upper zone (from the surface to a depth of 50-200 meters)[3] the water is well mixed and the temperature is fairly constant. Below this zone (200-1000 meters) the temperature decreases rapidly. In the deep zone (below 1000 meters) the temperature decreases slowly. See Figure 2.1 for an illustration. The thermocline is located in the zone where the temperature is decreasing rapidly (the thermocline zone), at the depth where the temperature gradient is at its maximum, see Figure 2.1. Observations indicate that the thermocline (zone) exist continously and at more or less the same depth at a given location in latitudes from about 0° to 40° North and South. In order for this to be possible, cold water must flow in from below to counteract the effect of heating from the sun on the surface. It is believed that this in-flow of cold water is provided by the thermohaline circulation.

Near the equator, and at mid-latitudes, the surface water is heated by the sun. Cooling of the water takes place at high latitudes in the Atlantic Ocean, increasing the density and causing it to sink. Deep water then flows towards the tropics, and

---

[3]The thickness of the upper layer (mixed layer) varies from one day to the next and also between the seasons. In winter the mixed layer tends to be deeper than in summer. Warming of the surface water during summer may sometimes cause a seasonal thermocline to appear.
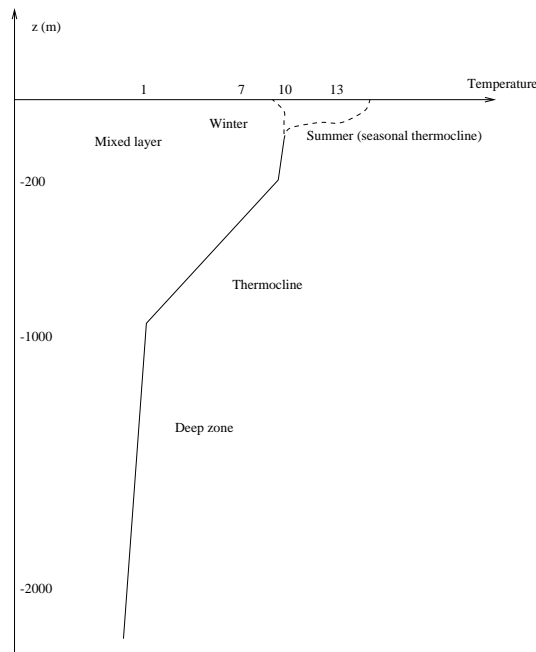
Figure 2.1: *Vertical temperature profile in the ocean (typical for mid-latitudes).*

the warmer waters in the upper layer flow from the tropics towards higher latitudes. This is the essence of the theory of the large scale thermohaline circulation as it was put forward by Stommel (1958). It is believed that there are two 'deep water factories' in the World. One is east of Greenland and the other one is in the Weddel Sea in the Antarctic. Deep water from these sources flow into the Atlantic Ocean, the Pacific Ocean and the Indian Ocean. The full details of the thermohaline circulation are not yet known, but it is believed that the mechanism is responsible for the relatively slow current flow in the deep zone (below 1000 meters).

Wind driven circulation

Whereas the thermohaline circulation transports water vertically and horizontally, the wind-driven circulation is considered to be mainly horizontal[4]. The winds in the atmosphere are driven by solar energy. Friction between the wind, blowing along the ocean surface, and the ocean surface itself, transfers energy into the surface layer of the ocean, and the water in this layer start to move. Friction forces between the moving water in the upper layer and the water immediately below, causes the water in the lower layer to also start moving, and so on. Thus, the effect of the wind stress on the surface causes the upper layer of the ocean to

---

[4]Some of the consequences of the wind driven circulation, such as Ekman pumping and up-/downwelling, however, involve vertical transport of water, see section 2.4.5

move. It is the wind stress that is the major cause of the circulation in the upper few hundred meters of the open ocean areas of the World.

2.2.4 Governing equations of the ocean circulation

Newton's second law for seawater on a rotating Earth

A mathematical formulation of Newton's second law (per unit volume) for water moving in a rotating framework (Earth seen from a fixed reference point) can be written,

$$\frac{Du}{Dt} + 2\Omega \cos \phi \cdot w - 2\Omega \sin \phi \cdot v = -\frac{1}{\rho}\frac{\partial p}{\partial x} + \frac{\mu}{\rho}\nabla^2 u \tag{2.1}$$

$$\frac{Dv}{Dt} + 2\Omega \sin \phi \cdot u = -\frac{1}{\rho}\frac{\partial p}{\partial y} + \frac{\mu}{\rho}\nabla^2 v \tag{2.2}$$

$$\frac{Dw}{Dt} - 2\Omega \cos \phi \cdot u = -\frac{1}{\rho}\frac{\partial p}{\partial z} - g + \frac{\mu}{\rho}\nabla^2 w \tag{2.3}$$

where u, v and w are the flow velocity components in a cartesian coordinate system with the x-axis pointing towards east, the y-axis pointing towards north and the z-axis pointing vertically upwards. Other parameters are latitude ϕ, angular velocity of Earth's rotation $\Omega(= 7.29 \cdot 10^{-5} \ rad \cdot s^{-1})$, density of sea water ρ, pressure p, dynamic viscosity μ, and acceleration of gravity g. The terms containing the Laplace operator

$$\nabla^2 = \frac{\partial^2}{\partial x^2} + \frac{\partial^2}{\partial y^2} + \frac{\partial^2}{\partial z^2}. \tag{2.4}$$

represent friction force per unit mass, assuming that the fluid is Newtonian. The time derivative is the material derivative,

$$\frac{D}{Dt} = \frac{\partial}{\partial t} + u\frac{\partial}{\partial x} + v\frac{\partial}{\partial y} + w\frac{\partial}{\partial z}$$

The use of a cartesian coordinate system is a simplification. Spherical coordinates can be used, but the equations become somewhat more complicated. Assuming that the length scale of the flow we study is much smaller than the radius of Earth, it is acceptable to use the cartesian coordinate system.

Conservation of mass, energy and salt

Conservation of mass requires that

$$\frac{\partial \rho}{\partial t} + \frac{\partial}{\partial x}(\rho u) + \frac{\partial}{\partial y}(\rho v) + \frac{\partial}{\partial z}(\rho w) = 0, \tag{2.5}$$

often referred to as the *continuity equation*, and the first law of thermodynamics yields the energy equation,

$$\rho C_v \frac{D\mathcal{T}}{Dt} + p\left(\frac{\partial u}{\partial x} + \frac{\partial v}{\partial y} + \frac{\partial w}{\partial z}\right) = \kappa_f \nabla^2 \mathcal{T} \tag{2.6}$$

where C_v is the heat capacity at constant volume, $\mathcal{T}$ is the absolute temperature and κ_f is the thermal conductivity of the fluid. Conservation of salt requires that

$$\frac{D\mathcal{S}}{Dt} = \kappa_{\mathcal{S}} \nabla^2 \mathcal{S} \tag{2.7}$$

where $\kappa_{\mathcal{S}}$ is the coefficient of salt diffusion.

Equation of state for seawater

The equation of state for seawater gives the relation between density, pressure, temperature and salinity, and is needed in order to close the set of equations. Generally, the equation of state is given as,

$$\rho = \rho(p, \mathcal{T}, \mathcal{S}) \tag{2.8}$$

The Boussinesq approximation

The governing equations can be simplified by using the assumption that

$$\rho(x, y, z, t) = \rho_0 + \rho'(x, y, z, t) \tag{2.9}$$

$$\rho' << \rho_0$$

where ρ' is the density variation. This is the Boussinesq approximation. Applying this, and introducing the kinematic molecular viscosity, $\nu = \mu/\rho$, the momentum equations (2.1)-(2.3) can be reduced to the following,

$$\frac{Du}{Dt} + 2\Omega \cos\phi \cdot w - 2\Omega \sin\phi \cdot v = -\frac{1}{\rho_0}\frac{\partial p}{\partial x} + \nu \nabla^2 u \tag{2.10}$$

$$\frac{Dv}{Dt} + 2\Omega \sin\phi \cdot u = -\frac{1}{\rho_0}\frac{\partial p}{\partial y} + \nu \nabla^2 v \tag{2.11}$$

$$\frac{Dw}{Dt} - 2\Omega \cos\phi \cdot u = -\frac{1}{\rho_0}\frac{\partial p}{\partial z} - \frac{\rho g}{\rho_0} + \nu \nabla^2 w \tag{2.12}$$

Incompressible fluid

It is customary to introduce the approximation that seawater is incompressible, i.e. that $\frac{1}{\rho}\frac{D\rho}{Dt} = 0$. The continuity equation (2.5) is then reduced to an equation for conservation of volume,

$$\frac{\partial u}{\partial x} + \frac{\partial v}{\partial y} + \frac{\partial w}{\partial z} = 0 \tag{2.13}$$

and the energy equation reduces to

$$\frac{DT}{Dt} = \kappa_T \nabla^2 T \tag{2.14}$$

where $\kappa_T = \frac{\kappa_f}{\rho_0 C_v}$ is the heat diffusivity. The equation for conservation of salt, however, remains the same as before.

The pressure term in the equation of state is removed when the approximation of incompressible fluid is made, and the equation of state becomes,

$$\rho = \rho(T, S) \tag{2.15}$$

Considerations about the scale of the flow and Reynolds averaging

Further simplifications can be made by considering the relative magnitude of the terms in the equations, and neglecting those that are significantly smaller than the others.

The horizontal scale, L, of the ocean is much larger than the vertical scale, H, i.e. $H << L$. From the continuity equation in its reduced form (equation 2.13) it is then possible to deduce that the horizontal flow velocities in the ocean are much larger than the vertical flow velocities (i.e. $u, v \gg w$) when large scale flows are considered. Temporal variations of the same magnitude as the time required for one rotation of the Earth (or larger) are of interest when we consider the global circulation in the oceans, i.e. $T_{LS} \geq \Omega^{-1}$ and $u/L \leq \Omega$. Here, T_{LS} is a large-scale temporal scale.

It is customary to split the velocity components, salt and temperature into mean and fluctuating parts,

$$\begin{aligned} u &= U + u' \\ v &= V + v' \\ w &= W + w' \\ T &= T + T' \\ S &= S + S' \end{aligned} \tag{2.16}$$

where U, V, W, S and T are mean components and u', v', w', S' and T' are fluctuating parts with zero mean.

Inserting (2.16) into the governing equations, and then taking the time average, we obtain a new set of equations. These can be further simplified by applying the large scale requirements ($u, v \gg w$, $T_{LS} \geq \Omega^{-1}$ and $u/L \leq \Omega$), and assuming that the acceleration terms on the left side in equation (2.12) are small next to

the acceleration due to gravity on the right hand side of the equation (hydrostatic approximation), the Reynolds-averaged momentum equations for the water in the oceans on a rotating Earth can be written,

$$\frac{DU}{Dt} - fV = -\frac{1}{\rho_0}\frac{\partial p}{\partial x} + \frac{\partial}{\partial x}\left(-\overline{u'u'}\right) + \frac{\partial}{\partial y}\left(-\overline{u'v'}\right) + \frac{\partial}{\partial z}\left(-\overline{u'w'}\right) + \nu\nabla^2 u \quad (2.17)$$

$$\frac{DV}{Dt} + fU = -\frac{1}{\rho_0}\frac{\partial p}{\partial y} + \frac{\partial}{\partial x}\left(-\overline{v'u'}\right) + \frac{\partial}{\partial y}\left(-\overline{v'v'}\right) + \frac{\partial}{\partial z}\left(-\overline{v'w'}\right) + \nu\nabla^2 v \quad (2.18)$$

$$0 = -\frac{1}{\rho_0}\frac{\partial p}{\partial z} + \frac{\partial}{\partial x}\left(-\overline{w'u'}\right) + \frac{\partial}{\partial y}\left(-\overline{w'v'}\right) + \frac{\partial}{\partial z}\left(-\overline{w'w'}\right) - \frac{\rho g}{\rho_0} + \nu\nabla^2 w \quad (2.19)$$

where the overbar denotes a time average, and $f = 2\Omega\sin\phi$ is introduced (the Coriolis parameter). The terms containing $-\overline{u'u'}$, $-\overline{v'u'}$ etc. originate from the non-linear terms in the momentum equations (equations 2.1-2.3), and can be viewed as stresses. These are the Reynolds stresses, and they are much larger than the stresses from molecular friction, so the last term in equations (2.17), (2.18) and (2.19) are normally neglected. The equations for conservation of mass, salt and temperature become

$$\frac{\partial U}{\partial x} + \frac{\partial V}{\partial y} + \frac{\partial W}{\partial z} = 0 \quad (2.20)$$

$$\frac{DS}{Dt} = \kappa_{\mathcal{S}}\nabla^2 S + \frac{\partial}{\partial x}\left(-\overline{S'u'}\right) + \frac{\partial}{\partial y}\left(-\overline{S'v'}\right) + \frac{\partial}{\partial z}\left(-\overline{S'w'}\right) \quad (2.21)$$

$$\frac{DT}{Dt} = \kappa_{\mathcal{T}}\nabla^2 T + \frac{\partial}{\partial x}\left(-\overline{T'u'}\right) + \frac{\partial}{\partial y}\left(-\overline{T'v'}\right) + \frac{\partial}{\partial z}\left(-\overline{T'w'}\right) \quad (2.22)$$

The terms containing $-\overline{S'u'}$, $-\overline{T'u'}$ etc. represent turbulent fluxes of salt and temperature in the respective directions, meaning that $-\overline{S'u'}$ is turbulent flux of salt in the x-direction. These fluxes, often referred to as *Reynolds fluxes*, are normally much larger than the diffusion terms $\kappa_{\mathcal{S},\mathcal{T}}\nabla^2(S,T)$.

Small scale parametererization and the closure problem

There are not enough equations to determine the Reynolds stresses, meaning that the system of equations is not closed. It is not possible to close the system unless the turbulence terms (Reynolds stresses) are parameterized in some way. Several methods have been proposed, see e.g. Mellor and Yamada(1974, 1982), Galperin et al. (1988) and Heidvogel and Beckman (2000) for furter details. A simple method for solving the closure problem is that of eddy viscosity and eddy diffusivity, using

$$A_M\frac{\partial U}{\partial x} = -\overline{u'u'} \quad A_M\frac{\partial U}{\partial y} = -\overline{u'v'} \quad K_M\frac{\partial U}{\partial z} = -\overline{u'w'}$$

$$A_H \frac{\partial S}{\partial x} = -\overline{S'u'} \quad A_H \frac{\partial S}{\partial y} = -\overline{S'v'} \quad K_H \frac{\partial S}{\partial z} = -\overline{S'w'} \tag{2.23}$$

$$A_H \frac{\partial T}{\partial x} = -\overline{T'u'} \quad A_H \frac{\partial T}{\partial y} = -\overline{T'v'} \quad K_H \frac{\partial T}{\partial z} = -\overline{T'w'}$$

where A_M and K_M are values of eddy viscosity and A_H and K_H are values of eddy diffusivity. Numerical values for these variables must be found based on observations of turbulence.

2.2.5 Major current systems in the Atlantic Ocean

The Atlantic Ocean is open towards the south, where it borders against the Southern Ocean. Towards the north, the Atlantic Ocean borders against the Arctic Ocean. At the Subtropical Convergence water from the Antarctic meets that of the South Atlantic and there is a distinct temperature difference.

The circulation of water in the upper layers of the Atlantic Ocean is characterized by two large gyres. The rotation is clockwise on the northern hemisphere and counter-clockwise on the southern hemisphere, see Figure 2.2. The major wind field over the Atlantic Ocean is dominated by the trade winds in the tropics and the westerlies at mid-latitude ($\sim 40^o$). The trade winds blow steadily in a northeasterly direction (towards soutwest)[5] on the northern hemisphere and in a southeasterly direction (towards nortwest) on the southern hemisphere. The westerlies (blowing towards east) are not as steady as the trade winds, but they are still distinct. Each of the trade wind systems drive their own ocean current gyre.

The different parts of the gyres have their own names, see Figure 2.2. At the southern border the *Antarctic Circumpolar Current* runs completely around the globe in an eastward direction. This flow is on the southern boundary of the Atlantic Ocean. Near the Equator, the south-easterly trade winds drive the *South Equatorial Current* westwards. Part of this current crosses the Equator and enters the North Atlantic. What is left of the South Equatorial Current turns south and becomes the *Brazil Current*, following the coastline. When the Brazil Current reaches $\sim 30^o S$ it meets the water of the *Malvinas Current* and separates from the coast and flows towards the south for a while before it starts flowing across the Atlantic as part of the Antarctic Circumpolar Current. When the water of the once warm Brazil Current eventually reaches South Africa it turns nortwards, now as the cold *Benguela Current*. Detailed descriptions of water masses and currents in the upper layers of the South Atlantic Ocean can be found in Peterson and

---

[5]It is customary to define wind direction as the direction from which the wind is blowing. This is in accordance with the tradition established in the days of the sailing ships. Current direction, however, is given as the direction towards which the current is flowing
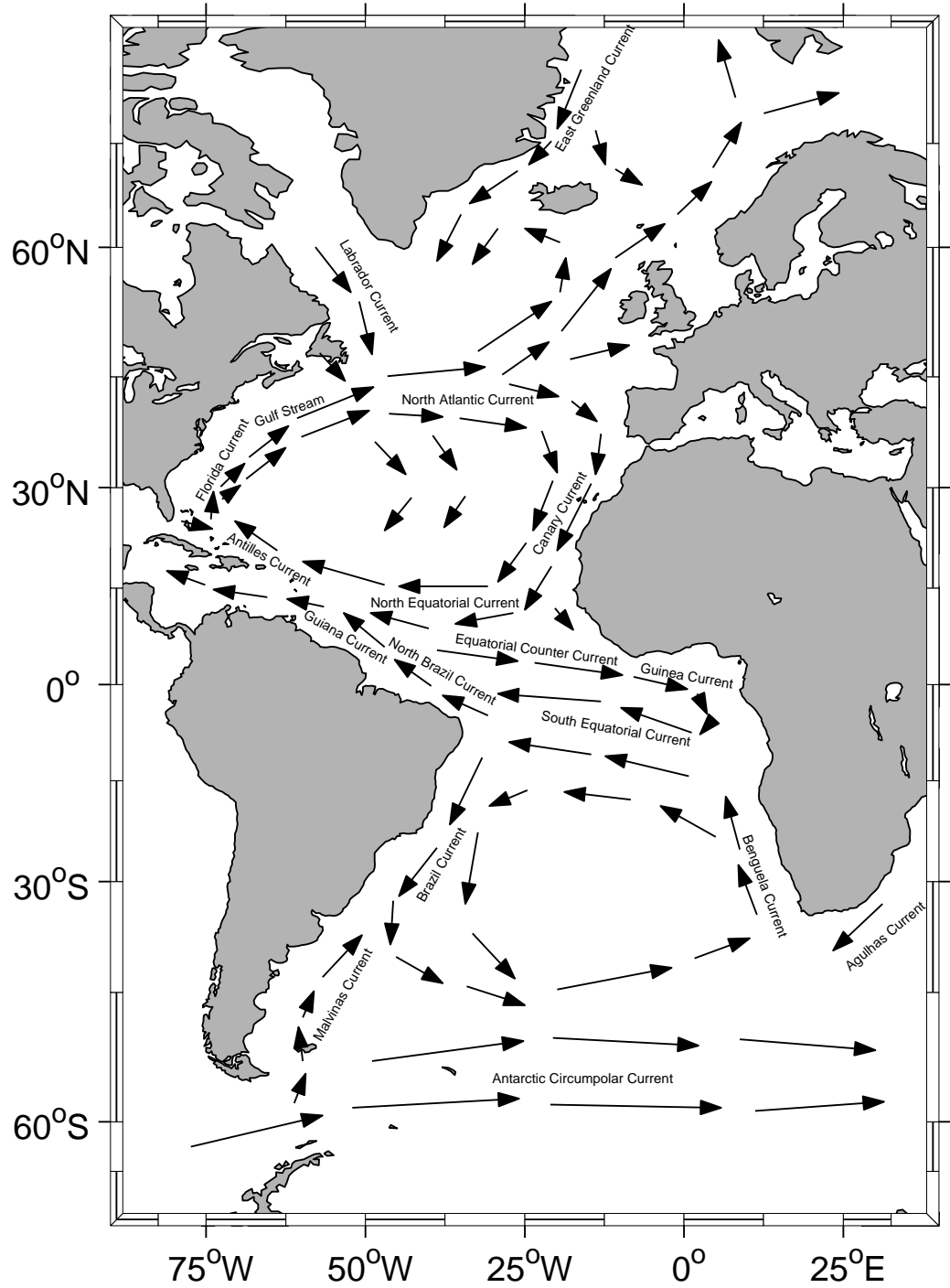
Figure 2.2: *Major surface currents in the Atlantic Ocean.*

Stramma (1990).

On the northern hemisphere the norteasterly trade winds drive the *North Equatorial Current* towards the west. This current is joined by the part of the South Equatorial Current which crosses the Equator, and the *Guiana Current* is formed. This current flows towards the north-west for a while before separating into one branch flowing in a more northerly direction (the *Antilles Current*) and another branch flowing into the Caribbean Sea and the Gulf of Mexico. The latter exits the Gulf of Mexico between Florida and Cuba as the *Florida Current* and flows into the North Atlantic where it meets the Antilles Current and flows in a northeasterly direction for a while. Then it separates from the coast of North America and forms the *Gulf Stream*. This flow is narrow and fast (westward intensification). Upon reaching the Grand Banks of Newfoundland the Gulf Stream meets the *Labrador Current*, which consist of water flowing out of the Arctic Ocean. One part of the Gulf Stream continue north-eastwards as the *North Atlantic Current*. When the North Atlantic Current reaches Europe, some water enters the Norwegian Sea between Scotland and Iceland. This water contribute to the circulation of the Arctic Ocean. The other part of the North Atlantic Current flows towards the south to close the North Atlantic circulation gyre. This southward flow is quite broad and slow.

2.2.6 Major current systems in the Pacific Ocean

The Pacific Ocean is the World's largest ocean. To the south, the Pacific Ocean has an open border towards the Southern Ocean, and to the north it is closed in by North America and North-East Asia with just a narrow passage from the North Pacific Ocean to the Arctic Ocean (the Bering Strait), see Figure 2.3.

Generally, the circulation in the upper layer of the Pacific Ocean is similar to that of the Atlantic Ocean with a clockwise rotating gyre on the northern hemisphere and a counter-clockwise rotating one on the southern hemisphere, as can be seen in Figure 2.3. The wind field in the Pacific Ocean is also similar to that of the Atlantic Ocean, with trade winds blowing towards southwest (northern hemisphere) and northwest (southern hemisphere) near the equator, and westerlies (blowing towards east) at higher latitudes. The two current gyres, seen in Figure 2.3, are driven by these trade wind systems, just as is the case for the circulation in the Atlantic Ocean.

The surface currents near the equator are zonal, and comprise the following currents, Reddy (2001)

- *North Equatorial Current.* This current flows from east to west, driven by the northeasterly trade winds on the northern hemisphere.

- *South Equatorial Current.* This current flows from east to west, driven by the southeasterly trade winds on the southern hemisphere.

- *North Equatorial Counter Current.* This current flows from west to east in the calm belt between the southeasterly and the northeasterly trade wind systems. The current is driven by the pressure gradient which occur from pile-up of water in the western Pacific due to the trade winds.

- *South Equatorial Counter Current.* This current flows from west to east. It is weak in comparison with the other equatorial currents.

On the northern hemisphere, the main part of the North Equatorial Current turns north and, soon afterwards, north-east to become the *Kurioshi Current*, see Figure 2.3. The Kuroshio Current is a western boundary current, and it can be viewed
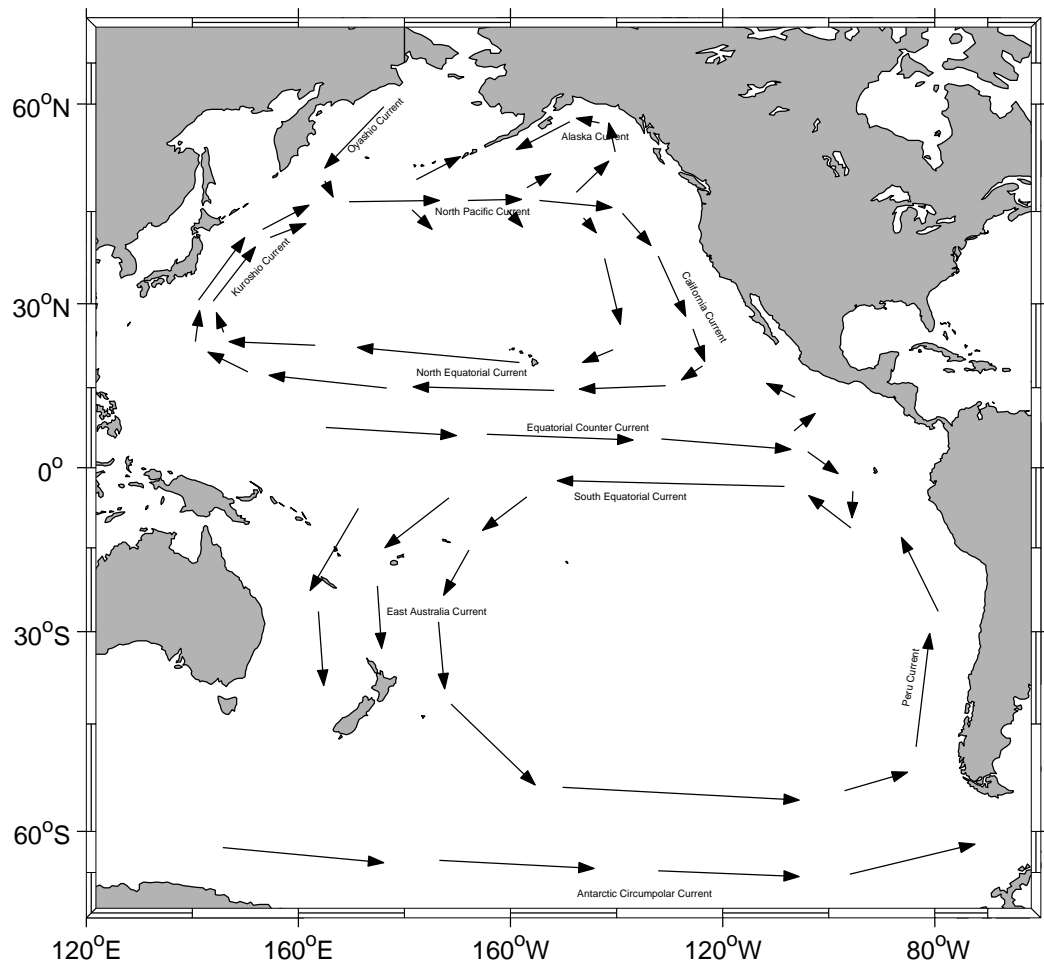
Figure 2.3: *Major surface currents in the Pacific Ocean.*

as the Pacific counterpart to the Florida Current (or vice versa). The Kuroshio Current flows northeastwards along the east coast of Japan, but eventually it leaves this coastline, in the same way as the Florida Current leaves the coast of North America to become the Gulf Stream. The Kuroshio Current, however, becomes the *Kuroshio Extension*, flowing mainly towards east. This current is then joined by the *Oyashio Current* from the Bering Sea, and the *North Pacific Current* is formed. The main part of this current flows east, towards North America, but some water separates from the main flow and enters the Bering Sea. Once the North Pacific Current encounters North America it splits into the *California Current*, flowing towards the southeast, and the northeastwards flowing *Alaska Current*. The California Current is slow and broad, and closes the North Pacific circulation gyre. Some of the water in the Alaska Current enters the Bering Sea. Some of the water that enters the Bering Sea from the North Pacific Current (and from the Alaskan Current) continues into the Arctic Ocean (approximately 16% of the inflow to the Arctic Ocean enters through the Bering Strait (Pickard and Emery 1990).

On the southern hemisphere the circulation gyre is counter clockwise. The South Equatorial Current turns southwards and splits into one part feeding the *East Australian Current* while the rest heads south where it joins the Antarctic Circumpolar Current, flowing towards the east. Upon encountering South America, the flow splits into one branch to the southeast into the South Atlantic, and one branch to the north along the west coast of South America. This northward flow is referred to as the *Peru Current*, and it flows along the coast of Chile and Peru up to the equator to close the South Pacific circulation gyre.

A special feature, unique to the Pacific Ocean, is the relation between the El-Niño and the Southern Oscillation (ENSO). The North Equatorial Counter Current, which is an eastward flowing current, sometimes send a branch of warm water southwards along the coast of Chile/Peru. The name of this current branch is El-Niño. Occasionally, this current extends further south than usual, and this has serious consequences for the climate of the region, causing large rainfalls, floods, cyclones and a significant reduction in catches from the important fisheries outside the west coast of South America. These consequences have been so serious that they have prompted a substantial research effort in order to understand the phenomenon well enough such as to be able to predict it. The literature on the subject is therefore considerable. The book by Philander (1990), and the references therein, can be used as a starting point for the interested reader. It was found that the difference between atmospheric low pressures in the western part of the Pacific Ocean and high pressures in the southern part of the Pacific Ocean may cause water to be piled up in the western part of the ocean. It is the release of these water masses (by an average reduction in the winds) that initiates what is

commonly known as the El-Niño phenomenon.

2.3 Local variability of the circulation

2.3.1 Waves, instabilities, jets, eddies, turbulence, tides.

Waves.

Wind-generated surface waves dominate the water particle kinematics, and is a source of extensive mixing, in the upper hundred meters or so in the ocean. These waves have short periods.

The effect of rotation support features such as Kelvin waves, planetary waves and topographic waves. Also, the rise and fall of the tide can be viewed as a wave. These waves occur locally in the ocean, on the surface or in its interior, wherever thay can be generated and supported. Details of the waveforms can be found in e.g. Gill (1982) and Cushman-Roisin (1994). A main characteristic of these waves, is that they exist on time scales on the order of $T_\Omega = \frac{2\pi}{\Omega} (\sim 24h)$, and on length scales on the order of the Rossby radius of deformation, defined by

$$R = \frac{\sqrt{gH}}{f} \tag{2.24}$$

where H is the water depth, f is the Coriolis parameter, defined in section 2.2.4, and g is the acceleration due to gravity.

Barotropic instability.

Small perturbations to a barotropic flow with a horizontal shear may grow and become large if the shear is sufficiently large. This phenomenon is known as barotropic instability, and causes low-frequency oscillations to the flow.

Kelvin-Helmholtz instability.

A two-layer horizontal flow, separated by a thin interface with one layer heavier than the other and flowing at different speeds, is always unstable, Kundu (1990). This is the original Kelvin-Helmholtz instability, and it is responsible for the generation of the wind-induced surface waves of the oceans. In the ocean interior we rarely find a thin interface between two fluid layers. Instead, a continous stratification is mostly seen. Instabilities in horizontal parallell flow with a continous stratification is also referred to as *Kelvin-Helmholtz instability*. Miles (1961) and Howard (1961) have shown that such a flow is unstable when

$$R_i = \frac{-\frac{g}{\rho_0}\frac{d\rho}{dz}}{(\frac{dU}{dz})^2} = \frac{N^2}{(\frac{dU}{dz})^2} < \frac{1}{4} \tag{2.25}$$

where U is the undisturbed shear flow and ρ is the undisturbed density field. The stratification is expressed by the Brunt-Väisälä frequency, N^2, also known as the buoyancy frequency. Strong stratification and/or weak current shear prevents instability. The ratio between the buoyancy frequency (i.e. the stratification) and current shear is given by the gradient Richardson number, R_i, and it can be viewed as a ratio between potential and kinetic energy.

Jets, Eddies and turbulence.

Density fronts exist at locations where two different water masses meet. The flow along such fronts is driven by the horizontal pressure gradient, which is large in such areas, and geostrophically adjusted to flow with high pressure to the right (on the northern hemisphere). In a steady state flow, with zero friction, the geostrophic flow appears as a balance between Coriolis force and the pressure gradient, see e.g. Cushman-Roisin (1994). The flow along such fronts can be quite strong and narrow, like a jet.

It is well known that rivers on land meander. Jet flows in the ocean also have this behaviour. Meanders in the ocean may grow and create eddies, or vortices, which move away from the core of the jet in some cases. In other cases the eddies are absorbed by the mean flow again. Examples of currents with distinct meandering are the Gulf Stream, the North Brazil Current and the Norwegian Coastal Current.

The behaviour of eddies in the ocean is governed by the centrifugal force, the Coriolis force and the pressure force. For the large-scale eddies the centrifugal force is small compared to the other two. For eddies with a radius of the same order of magnitude as the internal deformation radius, the centrifugal force is comparable to the Coriolis force. The internal deformation radius is given by

$$R_I = \sqrt{\frac{g\delta\rho}{\rho_0} \cdot H} \cdot \frac{1}{f} = R \cdot \sqrt{\frac{\delta\rho}{\rho_0}} \tag{2.26}$$

where $\delta\rho$ is a horizontal density difference, H is the thickness of the vortice and ρ_0 is the mean water density. For even smaller eddies, the Coriolis force becomes negligible and the balance is between the pressure force and the centrifugal force. A flow speed of approximately 0.5 m/s in the Gulf Stream eddies is typical, and the horizontal scale is O(10 km).

The eddies take their energy from the mean flow. The energy is then transferred from large eddies to smaller and smaller eddies, and is finally dissipated at microscale ($\sim$1mm). This process is known as the energy cascade, see e.g. Tennekes and Lumley (1972), and is central in the theory of turbulence. Turbulence is considered to be a stochastic process, and it is generally not possible to predict or

describe the turbulent velocity field without the aid of statistical methods, see e.g. Bradshaw (1975).

Tides.

The gravitational pull from the sun, the moon and of Earth itself on the water in the oceans, and the relative motion between the sun, the moon and Earth, causes a cyclic rise and fall of the sea surface. These are the tidal changes, and they vary with periods of approximately 12-13 hours (semi-diurnal) in some places and about 24-25 hours (diurnal) in other places. There are several tide-producing constituents, see e.g. Pond and Pickard (1983), and their relative phase and amplitude varies for different locations. Horizontal current flow speed associated with the tidal rise and fall are generally larger near the coast than in the open ocean. Large speeds (> 5 m/s) may occur when the tide enters or exits through narrow passages. In the open ocean, however, the flow due to the rise and fall of the tide is O(0.1 m/s).

When the tidal wave encounter the continental shelf or slope in a stratified ocean, internal waves may be generated. Internal waves are supported by the vertical stratification in the ocean. Chapter 4 of this thesis contains more on the subject of internal waves. When internal waves occur on the tidal period they are referred to as *internal tides.*

Time scales of the tidal wave and the internal tides are much larger than the time scales of resonant response for typical marine structures, but the interaction between the internal tides and a sloping bottom may cause flow effects on smaller time scales, as will be described in section 2.4. Also, complex marine operations in deep water may last long enough for the tide to change notably, as we have already mentioned, and will return to in section 6.3.

2.3.2   Current conditions at some interesting locations

Some regions of the ocean are of particular interest to man because of the natural resources in or under these regions.

The fishery industry operate near the coast and far away at sea at places where the fishing is good. Knowledge about the current conditions at these locations is of importance to the fishermen working in these fields.

The offshore oil and gas industry, still concentrated near land, is steadily moving further away from shore. Main features of the current flow conditions in some regions which are of particular interest to the offshore industry, such as the Gulf of Mexico, the Norwegian Sea, West of Shetland, Brazil and West of Africa, are

described in this section.

The internet site at `http://oceancurrents.rsmas.miami.edu/index.html` was frequently used during the work with this section.

Gulf of Mexico

The Caribbean Current is the main surface current in the Caribbean Sea. Water from the North Equatorial Current, the North Brazil Current and the Guiana Current (see Figure 2.2) enters through the passage between the Lesser Antilles in the southeast. At first, this water flows westwards into the Caribbean Sea. Later on, the current shifts towards northwest and flows into the Gulf of Mexico as the *Yucatan Current*, see Figure 2.4. A small part of this current flows westwards over the Campeche Bank, but the main part flows towards the nortwest and thus consitute the start of the *Loop Current*. This is a current which makes a characteristic loop into the Gulf of Mexico before it exits through the Florida Straits as part of the Florida Current, see Figure 2.4.

The Loop Current intrusion into the Gulf of Mexico varies in size. Sometimes it can reach as far north as 29 degrees, whereas the flow at other times is almost directly from the Yucatan Channel to the Florida Straits. Anticyclonic[6] eddies (warm rings), typically 250-450 km in diameter and up to 1200 meters deep, sometimes separate from the Loop Current and propagate westwards/southwestwards, see e.g. Elliott (1982) and Hamilton et al. (1999). Such warm rings prevail for months in the Gulf of Mexico, and are important for the heat and salt budget and the general circulation in the western part of the Gulf. The Loop Current intrusion into the Gulf is often reduced significantly after a warm ring has been separated, but this is not always the case. Elliott (1982) found a warm ring which separated from the Loop Current in the winter without causing a withdrawal of the Loop Current from the Gulf.

A significant amount of research has been carried out on the Loop Current, anticyclonic eddies and the resulting dynamics of the circulation in the Gulf of Mexico. Vukovich (1988) studied infrared images of the Gulf, taken over a 15-year period. He found that the frequency of separation of warm anticyclonic rings from the Loop Current is highly variable, but estimated an average period of 10.9 months between separations. ARGOS-tracked drifting buoys are used for studying the circulation in the Gulf in the summer when the water temperature in the upper layers is uniform and, thus, rendering infrared images from satellites of little use. Glenn and Ebbesmeyer (1993) studied the paths of such buoys. They found that

---

[6]Cyclonic circulation is the term used for the flow around a low pressure system, either in the ocean or in the atmosphere. On the northern hemisphere the cyclonic circulation is counterclockwise (seen from above). Anticyclonic circulation is the opposite (clockwise).
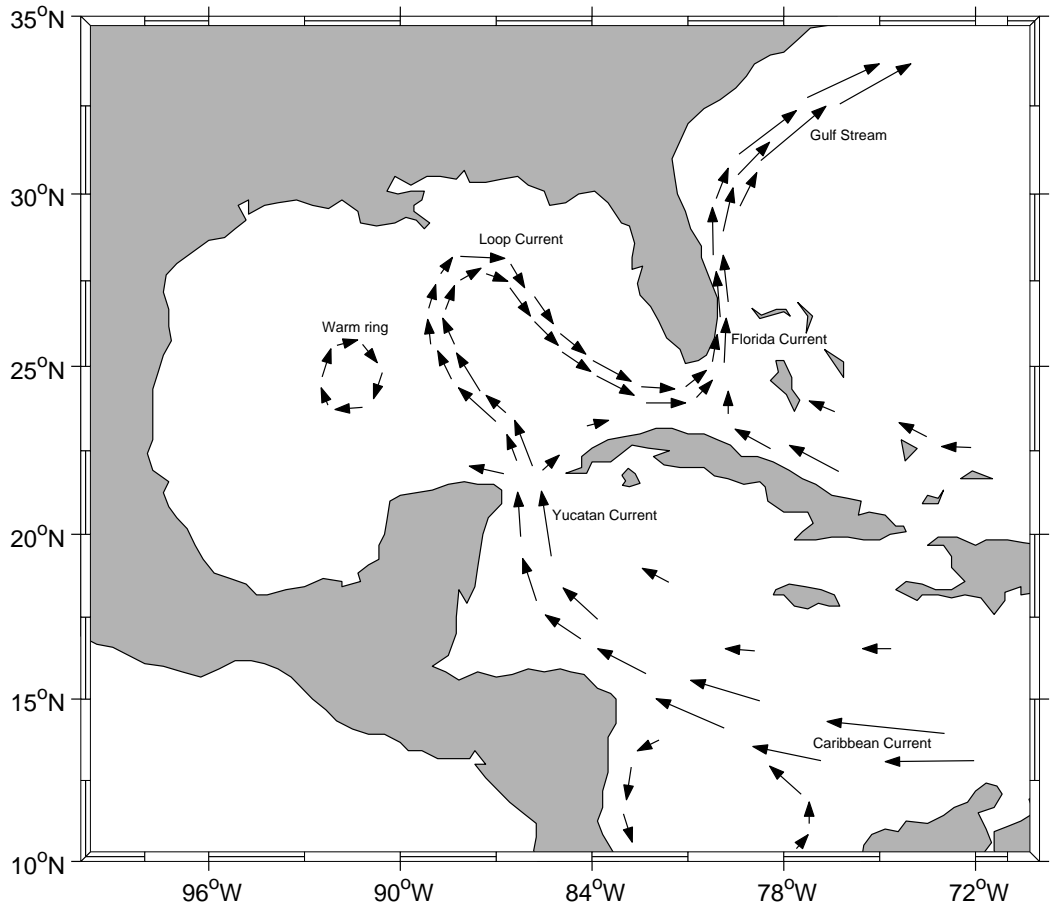
Figure 2.4: *Large-scale current patterns in and around the Gulf of Mexico.*

the eddies propagated in a series of short sprints separated by longer stalls. The speed of one of the eddies during one such sprint was as high as 19 cm/s. A similar study was conducted by Hamilton et al. (1999) who detected no apparent preferred paths of the eddies, neither in the main basin nor near the western slope, but the same stalling and sprinting behaviour as was seen by Glenn and Ebbesmeyer (1993) was found. Further, a clockwise rotation of the ellipse axis of the eddies was observed. This rotation, and also the swirl velocities, were found to decay with time.

Vukovich (1986) observed cyclonic cold perturbations (typically 100-250 km in diameter) to the south-southeastwards flowing Loop Current close to the West Florida Shelf. Associated with these cold perturbations were warm filaments of northwards flowing Loop Current water to the west of the cold perturbations. Flow speeds as high as 100 cm/s were estimated at certain places in these filaments. Cold perturbations are most pronounced on the northern and eastern boundaries of the

Loop Current.

The offshore structures in the Gulf of Mexico have been designed for the relatively large current flow speeds (>100 cm/s) that occur inside the anticyclonic eddies, and in relation with the high variability (smaller scale cyclones and anticyclones) that accompanies these eddies, or are generated by them. In the offshore industry, an anticyclonic eddy is termed *Eddy Current*. The anticyclonic eddies are only present in the upper 1000 - 1200 meters of the water column in the Gulf. Hamilton (1990) analyzed measurements of current velocity from below 1000 meters in the eastern, central and western parts of the Gulf and found evidence of topographic Rossby waves propagating towards the west. Fluctuations of the Loop Current were identified as the source of these waves, something which Sturges et al. (1993) also observed in their numerical simulations. In a later study, Hamilton and Lugo-Fernandez (2001) observed velocities greater than 85 cm/s close to the seabed at a depth of approximately 2000 meters close to the Sigsbee Enscarpment at the base of the continental slope in the northern Gulf of Mexico. Vigourous ($\sim$40 to 50 cm/s) near-bottom currents were seen to occur as part of nearly continous wave trains passing through the area. It was suggested that such deep energetic disturbances are generated by the passage of cyclonic eddies in layers higher up, and theat these disturbances travel westwards as topographic Rossby waves.

West of Shetland

The North Atlantic Current splits into two major branches at approximately 30°W (Orvik and Niiler 2002). One of these enter the Norwegian Sea over the Iceland-Faroe Ridge. It then flows eastwards as the *Iceland-Faroe frontal jet*, turns northwards and follows the bottom topography towards Jan Mayen and finally flows through the Fram Strait west of Spitsbergen. This flow constitute the western branch of the *Norwegian Atlantic Current* as described by Orvik and Niiler (2002). The other branch of the North Atlantic Current follows the continental slope nortwest of Ireland, through the Faeroe-Shetland Channel, where the flow is referred to as the *Continental Slope Current*, and into the Norwegian Sea. The larger part of the flow continues northeastwards along the Norwegian shelf edge as the eastern branch of the Norwegian Atlantic Current, see Figure 2.5, but some water sheds off into the North Sea and onwards into the Skagerak and the Baltic Sea. Most of the in-flow to the Norwegian Sea enters through the passage between Shetland and the Faeroes, and mainly along the eastern slope of the Faeroe-Shetland Channel (Continental Slope Current). This current runs through important areas for the oil and gas industry west of Shetland and Norway. Mean flow speed in this current is approximately 20 cm/s and peak values of more than 100 cm/s have been observed.

The slope currents along the Faeroe-Shetland Channel and along the shelf edge outside Norway can be viewed as jets, and they possess the features of jet flows in the ocean (eddies, meanders) discussed previously in this section. Also, the presence of the continental slope causes some significant variability to the flow in the deeper layers. This will be described in more detail in section 2.4.

Troll

Large current velocities (1.5 - 2.0 m/s) in the upper water layer ($\sim$100 meters) have been observed from time to time at the Troll offshore oil and gas field outside the western coast of Norway. Furnes et al. (2001) attribute these occurences of large flow speeds to extraordinarily large outflow from the Skagerak into the North Sea. Strong northwesterly wind in the North Sea, persisting over a longer period, will force water into the Skagerak. At the same time the outflow from the Skagerak to the North Sea will be reduced. Water will therefore pile up in the Skagerak and the Baltic Sea. The difference in sea level height between the Baltic Sea and the North Sea can be up to one meter during such conditions. A change in the wind direction, or a reduction in wind strength, will allow this excess water to flow back into the North Sea at greater speeds than are normally found in the outflow from the Skagerak. This outflow takes place near the coast of Norway (see Figure 2.5) in the form of a coastal jet, and a complex pattern of vortices is formed approximately at the southern tip of Norway and then proceeds northwards along the coast as indicated in the figure. Using a numerical model, Røed and Fossum (2004) found indication that these vortices are generated when the coastal flow, either caused by vortex squeezing or simply by separation due to coastline curvature, veers offshore just east of the southern tip of Norway and then becomes unstable. The propagation speed of the front containing the vortices is $\sim$0.3 m/s and typical size of the vortices is a diameter of $\sim$50 km and a depth of $\sim$100 m.

Based on direct measurements of the current in the Troll area, it has been estimated that such strong outflowing fronts occur 1-2 times per month on average (Furnes et al. 2001).

Brazil

The South Equatorial Current flows westwards in the Atlantic Ocean just south of the equator. When South America is encountered, the current splits into two branches. One of these flow towards the nortwest (North Brazil Current), into the Carribean Sea and eventually out into the North Atlantic, see Figure 2.2. The other branch of the South Equatorial Current breaks off southwestwards, feeding the Brazil Current close to the coast of Brazil, see Figure 2.6. The Brazil Current is a western boundary current, but it is not as strong as other currents of the same
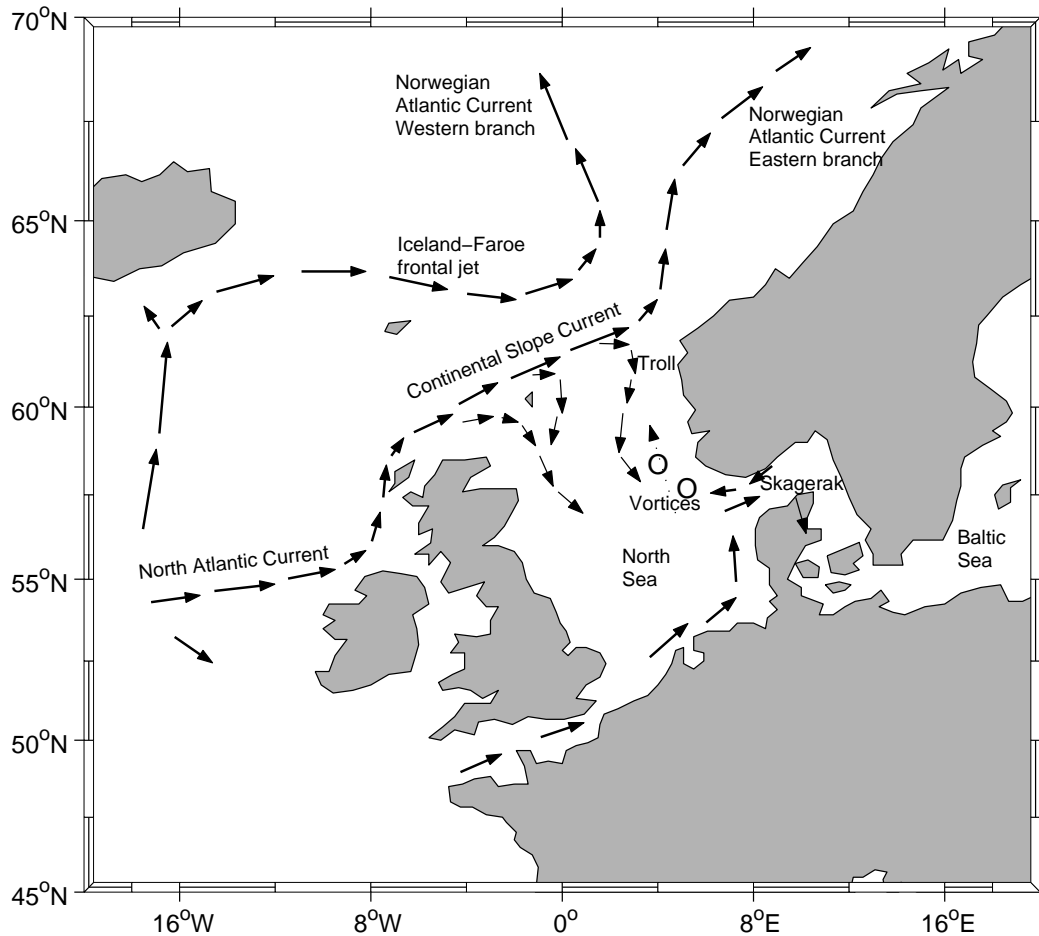
Figure 2.5: *Inflow of North Atlantic water to the Nordic Seas. The vortices outside the coast of Norway are also shown.*

kind (such as the Gulf Stream or the Kuroshio). The Brazil Current stays mainly on the continental margin on its way towards soutwest until it reaches approximately 35ºS. Here, the current meets with the northeastwards flowing Malvinas Current, leaves the east coast of South America and continues towards south together with the return flow of the Malvinas Current, see Figure 2.6.

The area in which the Brazil Current meets with the Malvinas Current lies between 35ºS and 40ºS, depending upon the time of year, and is referred to as the *Brazil-Malvinas Confluence* (Gordon and Greengrove 1986). The Malvinas Current is a strong (40-100 cm/s) flow of cold subantarctic water with low salinity, whereas the subtropic water in the Brazil Current is warmer and more saline. A sharp oceanic front exist between these water masses, resulting in the formation of cold and warm eddies from the Malvinas Current and the Brazil Current, respectively,
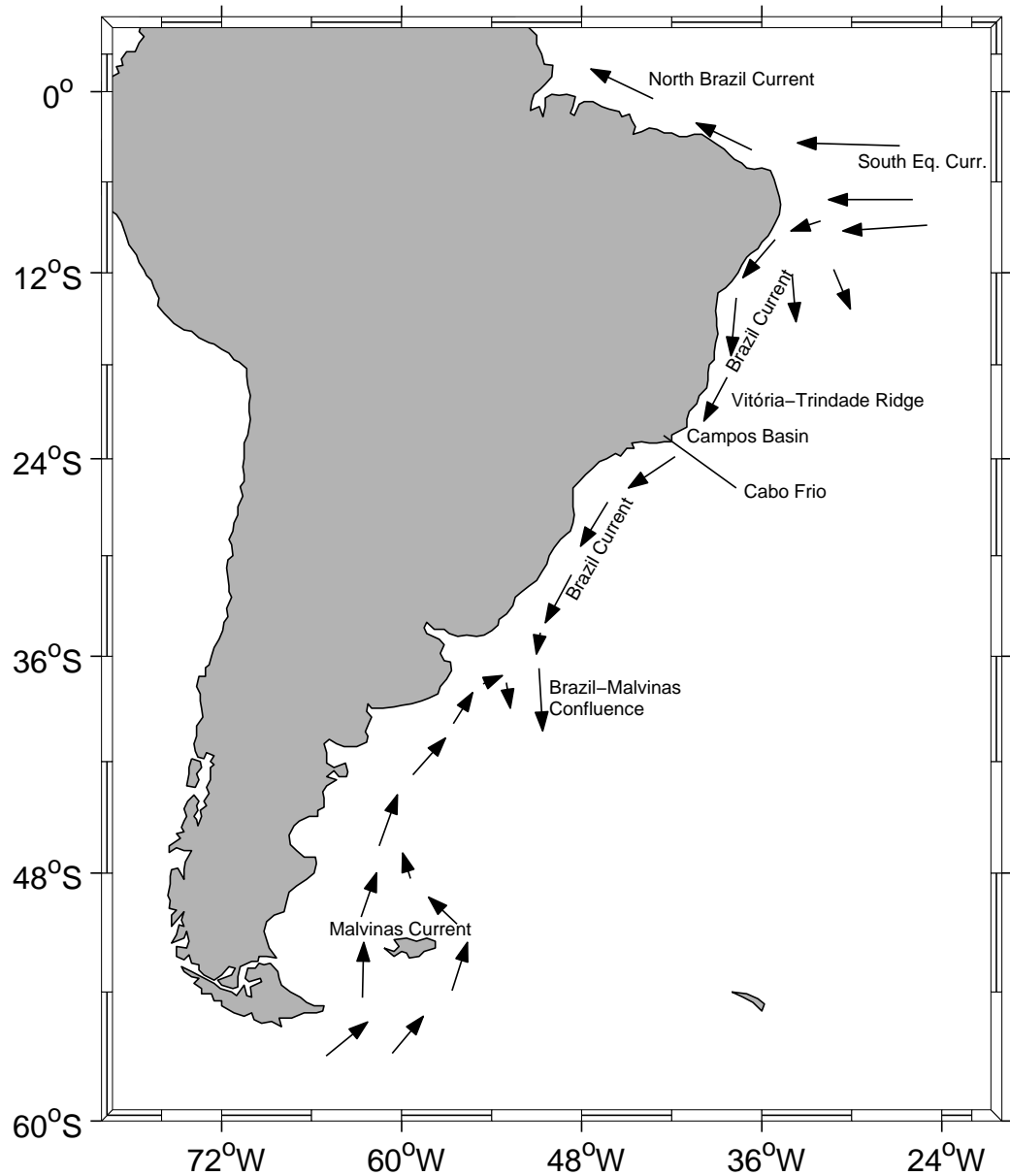
Figure 2.6: *Current patterns outside Brazil.*

see e.g. Garzoli and Garraffo (1989).

The Campos Basin, which is located in the area around 22°S and 40°W, see Figure 2.6, is the most important area for offshore oil production outside Brazil. This has resulted in high priority towards monitoring and predicting the circulation in the area (Vianna and de Menezes 2004). Garfield (1990) studied infrared images and found eddies and meanders in the Brazil Current in this area. A cyclonic

eddy was observed just south of the Vitória-Trindade Ridge in 1991 (the Vitória Eddy). Schmid et al. (1995) studied this eddy by means of hydrographic data, drifting buoys and satellite imagery. They found swirl velocities of 31-46 cm/s, eddy radiuses of 24-63 km and a clear tendency that the eddy interacted with local topography, the Brazil Current and a local upwelling regime just south of the Campos Basin (Cabo Frio). Vianna and de Menezes (2004) found that eddy perturbations to the Brazil Current cause unexpected mean currents near the shelf edge in the Campos Basin. They suggested a relation between the eddies and a large scale anticyclonic gyre east of Brazil.

West of Africa

Several offshore oil and gas fields outside West Africa (e.g. the Girassol, Bonga and Kizomba fields) have recently been developed or are presently being developed. In these parts we find the Benguela Current, the Angola Current and the Guinea Current.

The Benguela Current is the eastern part of the South Atlantic circulation gyre, described in section 2.2.5. Outside Cape Town the Benguela Current flows northwards, but it soon turns towards northeast, leaving the coastline, see Figure 2.7. Strong frontal jets, with current speeds as high as 120 cm/s were observed near Cape Town by Peterson and Stramma (1990). Typical flow speeds further north were smaller ($\sim$50 cm/s).

The dominating flow outside Angola is the Angola Current. This current contains warm saline waters, flowing southwards as part of a clockwise gyre in the Angola Basin, see Figure 2.7. Moroshkin et al. (1970) measured flow velocities of 50 cm/s and 70 cm/s at the surface and at 25 m depth, respectively. The Angola Current meets the Benguela Current and creates the Angola-Benguela Front.

Further north on the coast of West-Africa we find the Guinea Current, see Figure 2.7. This current is fed by the North Equatorial Countercurrent and the Canary Current as can be seen in Figure 2.2. Flow velocities near the Gulf of Guinea can be as high as 100 cm/s (Richardson and Reverdin 1987).
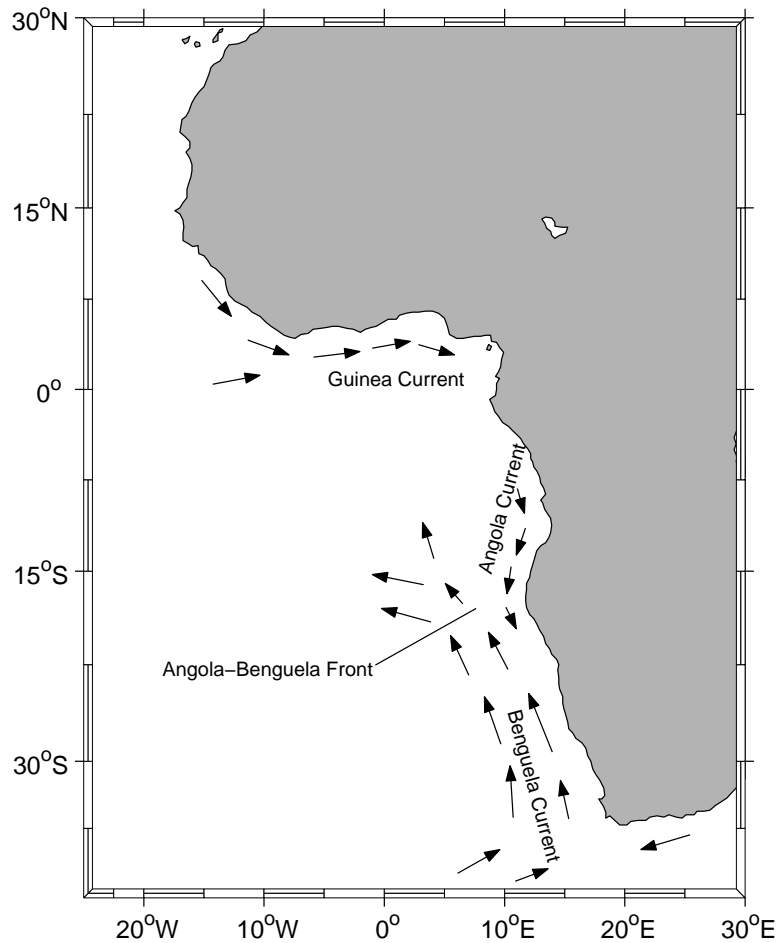
Figure 2.7: *Current patterns outside West Africa.*

2.4   Processes on the continental slope

2.4.1   Motivation for focusing on the continental slope

Most of the oil and gas extraction around the world today take place on continental shelf areas near shore. However, some of this activity has begun to move past the continental shelf edge. The continental shelf is the relatively flat plateau (average gradient is 1:500) near shore, see Figure 2.8. This plateau consists of sediments which have been eroded from the continent. Such sediments are constantly being transported from the shore towards the edge of the continental shelf (also referred to as the *shelf break*). Here the inclination of the bottom is increased many times. The continental slope is located between the shelf break and the deep ocean bottom and the average inclination angle is 3 degrees (Cacchione and Pratson 2004).

The dynamics of the fluid flow on a continental slope, or other sloping boundaries in the ocean, are complex and diverse. During the work that was carried out when establishing the metocean design basis for the development of the Foinhaven-field on the continental slope west of Shetland, Grant et al. (1995) found that the currents at the site were 'far more complex than those traditionally encountered by the oil industry in the shallower North Sea'.

Processes such as e.g. up/down-welling, breaking/overturning/reflection of internal waves and Ekman veering take place on the continental slope. These processes may interact, making such regions of the ocean a highly variable environment. A full account of these processes can be found in textbooks such as those by Phillips (1977) and Dewey et al. (1988), and only a short overview will be provided in this section.

The high variability seen near the continental slopes several places around the world is believed to be important for the global circulation in the world oceans (Eriksen 1985), but it is also of interest for the design and planning of marine structures to be placed or operated in such environments.

For a general review of physical processes at ocean margins, see Huthnance (1995).
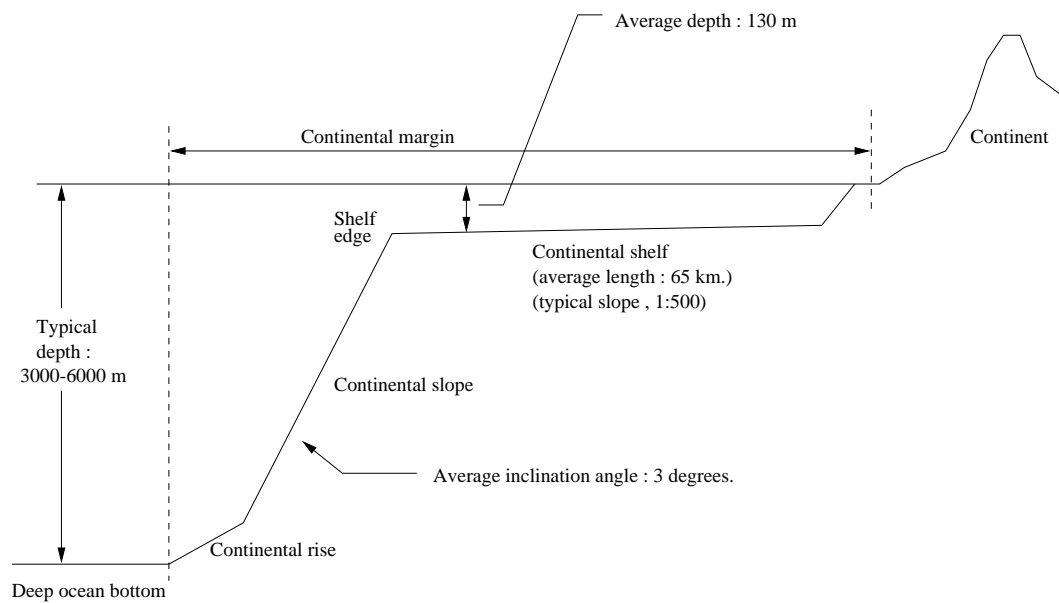
Figure 2.8: *Illustration showing the sea bed near the continental slope.*

2.4.2   Boundary layer dynamics

A boundary layer is developed between the interior of a flowing fluid and the physical boundary. Friction forces are important in this area. The literature on traditional laminar and turbulent boundary layers is extensive, see e.g. Schlichting et al. (2000) for a thorough treatment of the subject.

The boundary layer that exist between the sea bed and the waters of the ocean is often referred to as the *benthic boundary layer* (BBL). This boundary layer has not been subject to the same research effort as the atmospheric boundary layer, but important features of the BBL have nevertheless been revealed. Turbulent mixing near the sea bed in tidal currents have been studied by Bowden (1962). Later, Heathershaw (1979) studied the turbulent structure of such currents, defining length scales of motion contributing to the turbulence in the boundary layer on continental shelves. Wimbush and Munk (1970) provide a general description of both the atmospheric boundary layer and the BBL in which it is argued that these boundary layers are similar. This notion was confirmed by Soulsby (1977) when he demonstrated good agreement between turbulence spectra from the atmospheric boundary layer and the BBL, using similarity scaling (scaling the spectra by variance and measuring height).

In the BBL, the effect of rotation and friction, combined, is responsible for the development of the Ekman layer. The direction of the main flow over large-scale topography generally follows the isobaths (topographic steering). Near the sea bed the effect of friction and rotation diverts the flow to the left of the mean flow (on the northern hemisphere). The net transport in the bottom Ekman layer is diverted 90° to the left of the undisturbed free flow. Due to topographic steering of the undisturbed free flow over a continental slope, the Ekman transport will be either up-slope or down-slope. One particular feature of rotating stratified flow over a slope is the arrest of the Ekman layer by buoyancy forces, described by MacCready and Rhines (1993). Buoyancy forces arise due to the Ekman transport in the BBL, and finally grows large enough such as to counteract this transport. This results in a reduction of the boundary stress and, thus, a more slippery bottom boundary layer than that predicted by the traditional Ekman theory. This reduction in bottom drag is obviously of vital importance for the global circulation. Another property of the boundary layer on a slope is illustrated by Hosegood and van Haren (2003). They observed intermittent spike-like reductions in the current speed (duration less than 1 minute, magnitude ∼20-40 %) close to the continental slope of the Faeroe-Shetland Channel between depths of 470 and 1000 meters. The spikes had very short duration (less than 1 minute), and were only observed during downwelling favourable conditions (mean flow along the slope with shallow water to the right). Down-slope Ekman transport in the BBL of a stratified rotating fluid results in unstable stratification and, thus, turbulence, see e.g. Trowbridge

and Lentz (1991) and Lentz and Trowbridge (1991). Hosegood and van Haren (2003) propose that high-frequency current meter misalignment with the mean flow, caused by such turbulence, is the mechanism behind the spike-like observations, and that the intermittency of the spikes is due to the turbulent boundary layer bursting phenomenon described by Heathershaw (1974), Heathershaw and Thorne (1985) and Luchnik and Tiederman (1987).

Other contributions to the topic of Ekman layers on a sloping bottom can be found in e.g MacCready and Rhines (1991, 1993).

2.4.3   Internal waves interacting with the slope

Another mechanism, leading to variations in temperature and currents near the continental slope, is the interaction between the sloping boundary and internal waves. Internal waves are gravity waves in the interior of a fluid, supported by vertical stratification. In the atmosphere, such waves can be observed by watching cloud formations, and in the ocean thay can in some cases be observed from high above, e.g. satellite photos. Internal waves in the ocean are generally generated by conditions at the surface (moving pressure fields, travelling wind fields) or at the sea bed (flow over topography, earthquake). When internal waves are generated by the diurnal- or semi-diurnal tide they are often referred to as *internal tides.*

The buoyancy frequency, defined by

$$N^2 = -\frac{g}{\rho_0}\frac{d\rho}{dz} \tag{2.27}$$

is an important parameter in the study of internal waves. Analytical solutions for linear, inviscid internal waves can be found by solving a linearized version of equations (2.17)-(2.19) in which the Reynolds stresses are neglected and the term $\frac{\partial w}{\partial t}$ in equation (2.19) is reinstated. The dispersion relation is found by inserting solutions of the form $e^{i(lx+my+nz-\omega t)}$, where ω is the internal wave frequency, into the linearized set of equations. Gill (1982) gives the dispersion relation for internal waves propagating downwards with a characteristic angle, β, as seen in Figure 2.9, as

$$\omega^2 = N^2 \sin^2\beta + f^2 \cos^2\beta \tag{2.28}$$

Phase speed for internal gravity waves is defined in the same way as for surface gravity waves

$$c = \frac{\omega}{\sqrt{l^2 + m^2 + n^2}} \tag{2.29}$$

where the wave number vector is defined by $\boldsymbol{\kappa}=l\mathbf{i} + m\mathbf{j} + n\mathbf{k}$. The group velocity vector, defining the propagation direction of the internal wave energy, is given by

$$\mathbf{c}_g = \frac{d\omega}{d\boldsymbol{\kappa}} \tag{2.30}$$

The vertical component of $\mathbf{c}_g$ can be positive, zero or negative. If it is negative the internal wave energy propagates downwards towards the sea bed. Note that the group velocity vector is always perpendicular to the phase velocity vector, and that phase and energy always propagates in the same horizontal direction, but in opposite vertical direction. When such waves encounter the continental slope, as shown in Figure 2.9, they are reflected if the slope angle, α, is smaller than β. It is assumed that the azimuth of the wave is zero (i.e. the group velocity vector is perpendicular to the isobaths). Note that the internal wave reflection angle with the horizontal is β, regardless of the slope angle (as long as $\alpha < \beta$). If the internal
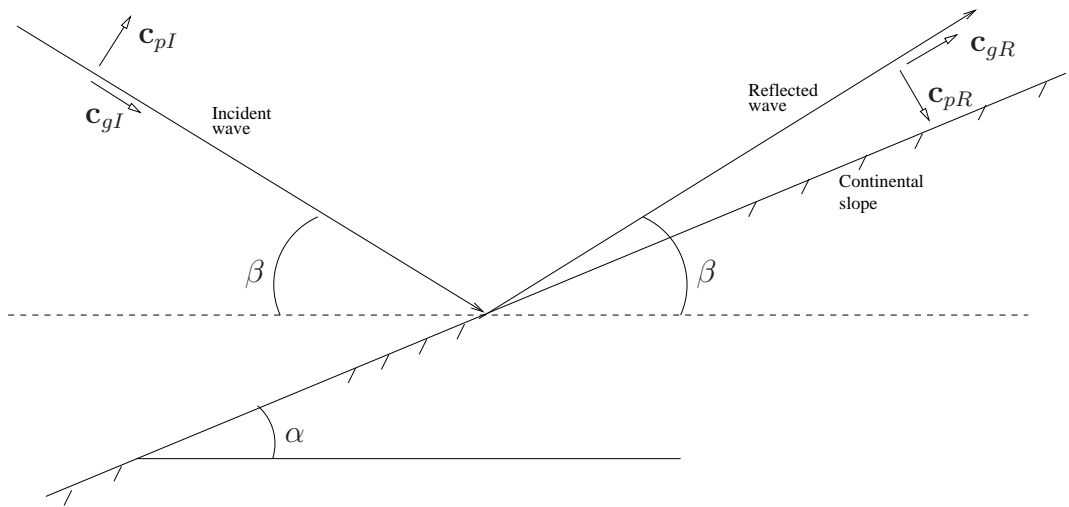
Figure 2.9: *Illustration of reflection of internal waves on the continental slope.*

wave frequency is such that $\beta \simeq \alpha$, the internal wave energy is trapped near the slope (according to linear theory) resulting in unstable conditions and, possibly, strong turbulence near the sea bed. Interaction between the incident wave and the reflected wave can also cause wave steepening, reduced stability and wave breaking near the slope (Thorpe 2001). If $\alpha > \beta$ the internal wave is reflected down-slope.

Cacchione and Pratson (2004) commented on the curious fact that, even though underwater piles of sediments can be stable with slopes of up to 15 degrees, the average inclination angle of the continental slope is only 3 degrees. They propose that internal tides, and their interaction with the continental slope, is the primary explanation of this. Their argument is that the density structure of the oceans is such that the characteristic angle of the internal tides is typically between 2 and 4 degrees, and that the strong currents which occur at the bottom when the characteristic angle is the same as the inclination angle of the slope actually prevents accumulation of sediments, not allowing the inclination angle to become larger than the characteristic angle.

Frequent occurrences of inversions close to the bottom on the continental slope southwest of Ireland were reported by Thorpe (1987a), who attributed them to instabilities of the boundary layer, possibly caused by internal wave breaking. The flow patterns that occur upon reflection of internal waves on a plane sloping bottom in a uniformly stratified ocean has been studied by many researchers. Reflection of internal gravity waves at a sloping seabed was nominated by Eriksen (1985) as a source of diapycnal[7] mixing, and, thus, a possible solution to the problem of the 'missing' vertical diffusivity needed to balance the thermocline and the mean vertical advection, Garrett (1979). The turbulence and mixing in the boundary layer due to interaction between internal waves and a sloping bottom has been investigated experimentally by Cacchione and Wunch (1974), Thorpe and Haines (1987), Ivey and Nokes (1989), Taylor (1993) and De Silva et al. (1997). Nonlinear features of the reflection of internal waves in a stratified fluid on a plane sloping bottom, such as rapid changes in density and conditions favourable for wave breaking, have been studied in detail by Thorpe (1987b, 1992b, 1997). Some results from numerical simulations, supporting theoretical and experimental findings, have been presented by Javam et al. (1999) and Slinn and Riley (1998).

Internal waves may be created at the shelf edge and travel down-slope towards deeper water. Gemmrich and van Haren (2001) observed rapid temperature reductions accompanied by brief down-slope current events above the continental slope in the Bay of Biscay, and they suggest that the stratification near the slope is made unstable by internal waves propagating down-slope. The collapse of this unstable stratification is then observed as moving thermal fronts. Changes in the alongslope flow speed from zero to approximately 0.5 m/s within 16 minutes were observed. This high variability can be of interest for the design and planning of marine structures to be placed or operated in such environments.

2.4.4 The effect of bottom topography

Large scale ocean circulation is governed by many factors, one of which is the bottom topography. Topographic steering of the mean flow is a well known phenomenon described in all textbooks on the subject of physical oceanography and geophysical fluid flow. One of the most striking features of the large-scale circulation in the North Atlantic Ocean is the focusing of currents above topographic gradients (topographic steering), such as along the continental slope regions (see e.g. Orvik and Niiler 2002). This is particularly pronounced along the shelf slope off Mid-Norway (Figure 3.2) where the currents outside the boundary layers (The Norwegian Atlantic Current) may exceed an average speed of 0.3 m/s with maximum values occasionally higher than 1 m/s. The currents along the isobaths appear as

---

[7]Diapycnal mixing is mixing across constant density surfaces.

a relatively distinct and well-defined jet. As it flows over a frictional bottom it generates a bottom boundary layer with cross-isobathic transport. When the flow is stratified it can generate horizontal density gradients within the boundary layer itself. The advection of buoyancy that hence takes place may impact the bottom stress and modify the overlying current profile.

Whereas topographic steering of the large scale circulation is a feature of large scale bottom topography, it is also clear that the small scale bottom topography has an effect on the large- and small-scale circulation. There are several areas all over the world where the bottom topography is considerably more irregular than other places. Such locations might be along continental margins or close to continental shelf edges. Depending on the length scales of the processes to be analyzed, the sea bed can not always be considered to be plane (whether it is flat or sloped). Berntsen and Furnes (2002) studied numerically how small-scale topography on an otherwise flat bottom extracts energy from the mean flow in a stratified fluid. Thorpe (1992a) investigated analytically the lee waves generated over rough topography on a slope, and found that the energy extracted from the mean flow upon generating lee waves around small scale topography ($\sim$0.1 - 10 km), under certain conditions, is comparable to that extracted by the bottom friction. MacCready and Pawlak (2001) extended Thorpe's wave solution to study horizontal flow seperation and pressure drag at an isolated, cross-slope oriented, ridge. Baines (1971, 1973) and Müller and Xu (1992) studied reflection and scattering of internal waves from sloping rough topography. Thorpe (2001) studied reflection and scattering of internal waves from a slope covered with sinusoidal ripples (representing rough topography) in a uniformly stratified ocean. He found that resonant interactions between incident, reflected and scattered waves occurred for certain combinations of slope angle, wave propagation direction relative to the slope and to the horizontal, wave amplitude and wavenumber (of both waves and topography).

2.4.5   The effect of wind.

Wind is an important factor in driving the large scale global ocean circulation (Sverdrup 1947; Veronis 1973), but it is also responsible for features on smaller scales on continental margins such as up- and downwelling (Yoshida 1955) and the generation of shelf waves (Adams and Buchwald 1969). A simple analytical model of wind-forced displacements of the thermocline at a continental shelf edge was established by Csanady (1973), but numerical models are generally needed close to the shelf break and near the sea bed due to the importance of nonlinearities such as e.g. bottom topography and large motions of the thermocline. A dynamic surface wind field at or near the continental margin may, depending upon latitude, wind field properties and shelf area geometry, set up shelf wave oscillations, near-inertial oscillations and long baroclinic wave modes (Gjevik 1991).

It has been proposed that strong current events on the continental slope in the area west of Norway might be related to atmospheric conditions on the sea surface, affecting the motion of a deep pycnocline. These events have been observed near the sea bed and are characterized by a slowly increasing water temperature and down-slope flow just prior to a swift drop in the temperature, followed by a strong up-slope burst of water. Some previous work (Vikebø et al. 2004) indicate that atmospheric conditions play an important role as an initiating mechanism for this type of events. Due to the close proximity of a deep pycnocline at these depths (∼600 m), it is believed that the events are linked to the interaction between this pycnocline, the sloping bottom and surface winds. This interaction is discussed more extensively in section 3.6.

2.4.6   Turbidity currents.

Sediments may settle and accumulate on the continental shelf and slope. A turbidity current is the term used for the gravity driven flow that occurs when such unstable deposits are disturbed and run down the continental slope like submarine avalanches. Other names for the phenomenon are 'density currents' and 'gravity currents'. The sediments in the flow gives the current a higher density than the ambient water, and quite large velocities can arise even though most turbidity currents are slow. A typical initiator of turbidity currents are earthquakes.

In 1929 there was an earthquake in the New England and Maritime Provinces of Canada. The center of this earthquake was off the edge of the Grand Banks outside Newfoundland (Grose 2002), and the resulting turbidity current travelled at more than 10 m/s, breaking several transatlantic telegraph cables on its way down the continental slope.

Turbidity currents may pick up sediments on their way, increasing their density and speed until they reach the deep ocean bottom (see Figure 2.8). The continental rise (see Figure 2.8) is created by sediments transported down the continental slope by turbidity currents.

A comprehensive overview of gravity currents can be found in the book by Simpson (1997).

CHAPTER 3

Current measurements west of Norway

3.1 Introduction

This chapter contains a short introduction to some methods and procedures for measuring ocean currents in general, and some recommendations of how to carry out such measurements in relation to offshore engineering in particular. Descriptions of, and results from, current measurements outside the coast of Mid-Norway are included. First, the measurement sites and the water masses in the area are described, then measuremens of current profiles at two different depths are reported. Finally, some measurements close to the sea bed in an area with a rough bottom topography are presented and discussed.

3.2 Measuring ocean currents

3.2.1 General

One of the goals of the physical oceanographer is the accurate and detailed description of the three-dimensional temporal flow field in the ocean, $\mathbf{U}(\mathbf{x}, t)$. Another important goal is to obtain knowledge and a clear understanding of the driving mechanisms behind the observed flow. Field observations are of vital importance in achieving these goals. Two different types of methods for obtaining information about the ocean circulation are available, the direct method and the indirect method.

3.2.2 Direct methods

Direct measurements of the ocean circulation provides information about the flow velocity at a finite number of fixed points in the ocean space (Eulerian flow field), or, alternatively, about the positions of individual water particles at all time (Lagrangian flow field). The current flow data, discussed in this chapter, are recorded by direct methods, using two different types of Eulerian current measurement devices.

Rotor current meters

Rotor current meters for direct measurements of the flow speed are based on counting the rotations of a propeller over a time span. The orientation of the instrument relative to the current is always such that the flow is parallel to the propeller axis. This is achieved by allowing the instrument to rotate around a vertical axis, governed by a guiding vane. Records of current direction was mechanical in early rotor current meters, like the Ekman current meters, but today the magnetic compass is used and the data are stored on digital data files.

The Aanderaa RCM-7 current meters, which were used for some of the measurements discussed herein, calculates the vector averaged current velocity based on the number of revolutions of a rotor and the compass direction of the instrument. The current data are stored digitally on file inside the instrument.

Acoustic current meters

Acoustic Doppler Current Profilers (ADCPs) can be mounted aboard ships or held in place by mooring lines. An example of such an instrument can be seen in Figure 3.1. One ADCP can record the current velocity at several depths below or over its position in the water column. Records of flow speeds are obtained by emitting a series of short sound wave pulses, and then measuring and analysing the reflected signal from particles which travel with the flow. The method is, thus, based upon the assumption that particles which are suspended in the water follow the flow.

Figure 3.1: *Acoustic Doppler Profiler from Aanderaa (RDCP600). The RDCP600 is approximately 60 cm high and 20 cm wide.*

Drifters

The Lagrangian flow field in an area can be studied by the use of instruments drifting along with the current. In the early days of ocean current mapping such drifters could simply be bottles with a message inside, asking the finder to send a return message, telling where and when the bottle was found. Today, however, drifters exist that are able to stay at certain depths, go to the surface at regular intervals (or pre-programmed time instances) and report time, position, temperature and salinity via satellite, and then submerge to a the pre-selected depth again.

3.2.3   Indirect methods

Measurements of water properties (temperature and salinity) over an area and knowledge about some physical principles, combined with some assumptions and simplifications, may provide valuable information about the 3D flow field in the area. Such methods, i.e. estimating a parameter by measuring other parameters, are termed indirect methods. It is easier to measure water properties such as temperature, salinity, oxygen contents etc. than it is to measure the flow speed directly. Furthermore, it would be very expensive and time-consuming to use direct methods to establish the flow field in the entire ocean. An inherent assumption, however, of indirect methods is that the flow field does not change noteworthy over the time period necessary for establishing the distribution of the water properties. It is, thus, assumed that a set of collected water properties represent a synoptic (simultanous) picture of distribution of water properties in the area. The large scale flow in the ocean generally fulfills this assumption, but the circulation near shore and on continental margins generally does not.

Geostrophic method

The geostrophic method is a much used indirect method for measuring flow velocity in the interior of the ocean. If the flow on a large temporal (> 10 days) and spatial (width$\sim$1000 km, depth$\sim$1000 m) scale is to be considered, one can use dimensional analysis in order to reduce equations (2.17), (2.18) and (2.19) from section 2.2.4 to the very simple geostrophic equations,

$$-fV \;\; = \;\; \frac{1}{\rho_0}\frac{\partial p}{\partial x} \tag{3.1}$$

$$fU \;\; = \;\; \frac{1}{\rho_0}\frac{\partial p}{\partial y} \tag{3.2}$$

$$p \;\; = \;\; -\rho g z + P_{atm} \tag{3.3}$$

The geostrophic equations express a balance between the Coriolis force and the horizontal pressure gradient for non-diffusive, inviscid and stationary flow. The

density distribution can be obtained by measurements of salinity and temperature for a number of locations, using equation (2.15). The horizontal pressure gradient, needed to estimate U and V, can then be found from the hydrostatic pressure equation.

The geostrophic method is described in detail in most introductory texts on physical oceanography, see e.g. Cushman-Roisin (1994), Reddy (2001) and Pickard and Emery (1990).

Distribution of water properties - description method

As we have mentioned earlier (section 2.2.1), it is possible to identify as many as 19 different water masses in the upper 500 meters of the ocean (Emery and Meincke 1986). An indirect way of obtaining the flow pattern in the ocean is to track the different water masses by mapping the distribution of water properties. Using this method, it is possible to arrive at a good qualitative description of the global circulation. The description is qualitative in the sense that only information about the flow pattern, and not about the flow speed, is found. In order to find flow velocity indirectly it is necessary to expand the analysis of the water property distribution by introducing some physical principles and assumptions. This leads to the geostrophic method.

3.2.4 Requirements to current measurements used in offshore engineering

The large scale circulation can be obtained by indirect methods, but direct methods are necessary for establishing a detailed picture of the flow. Offshore engineers involved in design and planning of marine structures and operations need information about the current flow at the sites where structures are to be installed. The long-term distribution of current speed and direction is of course important, but the variability on short scales in time and space should also be considered for deep-water fields (see section 1.3).

Up until now it has been common practice to use averaging periods of 10 minutes and longer when recording the current flow directly. This is sufficiently short for observations of planetary waves, large eddies, tidal components and other features of the flow which have return periods in the order of hours, but it is too long for resolving variations on time scales which correspond to dynamic response periods of marine structures. Such periods are in the order of seconds or minutes, and this should be considered when planning measurement programs aimed at establishing design current data for offshore engineering activity in any given deep-water field.

Mathiesen (1996) recommended that current flow data be recorded with a sampling frequency of 1 Hz close to the sea bed when looking for design criteria for free-spanning pipelines.

Records of salinity and (especially) temperature can also be very helpful in providing information about the driving mechanisms causing the current flow, and should be included in the measurement program if possible.

The number of current meters at a site or along a pipeline route must be finite, and there will always be some uncertainty about what the flow field is like between the current meters. One way of reducing this uncertainty would be to install an ADCP on an AUV[1] and have it navigate between the current meters at the site or along the pipeline route. Current data recorded by the AUV's ADCP could then be compared to those recorded by the fixed current meters, and transfer functions could be established such as to be able to determine the flow at any given location based on readings from the current meters at their fixed locations. AUV technology for use in the offshore industry is being developed, and a few vehicles are currently in use, mainly for seabed mapping and sub-bottom profiling. AUVs have proven significantly cheaper, faster and easier to use for these purposes than the conventionally used tow-fish, and these advantages might be equally applicable to tasks such as pipeline inspection and current profiling. Up until now, however, current measurements using AUVs have mainly been for purely scientific oceanocraphic studies, see e.g. Dhanak et al. (2001), Ludvigsen et al. (2003), Schmidt et al. (1996) and Stansfield et al. (2001).

3.3   Current measurement sites

OCEANOR[2] and SINTEF[3] have collected current flow data on and above the continental slope outside the coast of Mid-Norway, see Figure 3.2. The flow speed measurements were carried out in order to obtain design parameters for sub-sea structures such as pipelines and riser systems in the area. Due to a large underwater slide that took place some 8000 years ago, this is an area with a rough bottom topography, see Figure 3.3.

The data collected at the sites marked 'OL-I' and 'OL-II' in Figure 3.2 were recorded using averaging periods of 10 and 30 minutes, whereas the data from

---

[1]An autonomous underwater vehicle (AUV) is an unmanned submarine with its own energy supply and no cable connection to any support vessel. An AUV can be pre-programmed to follow a certain route or it can be controlled by acoustic signals.

[2]Oceanographic Company in Norway. Internet : `www.oceanor.com`

[3]The Foundation for Scientific and Industrial Research at the Norwegian Institute of Technology (NTH) (now: the Norwegian University of Science and Technology: NTNU). Internet : `www.sintef.no`
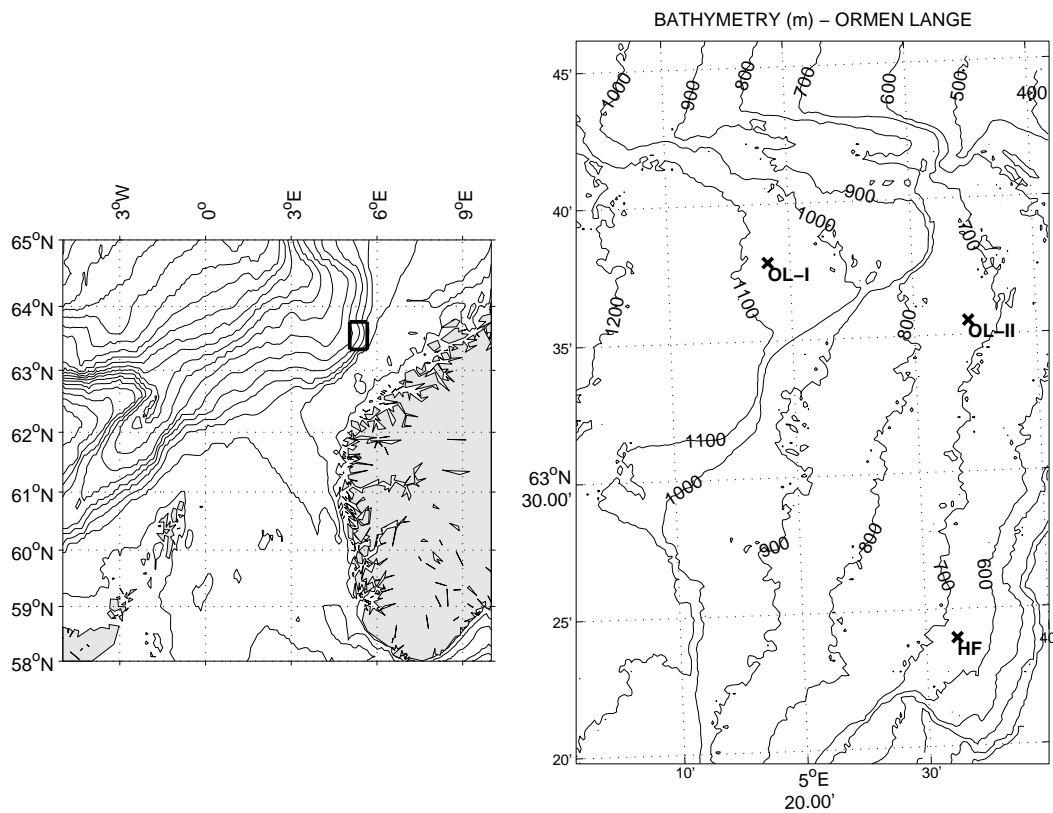
Figure 3.2: *Location of the current measurement sites. Current profiles were measured at OL-I and OL-II. Measurements near the sea bed were obtained at the spot denoted HF. The distance between OL-I and OL-II is approximately 14 kilometers.*

the site marked 'HF' were recorded using a sampling frequency of 1 Hz.

3.4 Water masses

The water masses in the area where the current measurements were carried out may be divided into different layers classified by their origin. The vertical stratification exhibits a three layer structure. Smoothed hydrographic profiles (salinity, temperature and density), recorded at a nearby section across the continental slope in February and April of year 2000, are shown in Figure 3.4. The seasonal pycnocline at 50 m depth and a deep pycnocline at about 500 m depth is clearly seen. A thin surface layer (∼50 m thick) of relatively fresh and cold water of coastal/shelf origin constitute the upper mixed layer. The thickness of this layer is strongly influenced by the winds and displays significant variation from one day to the next and also over the seasons. In the summer this surface layer is normally warmer
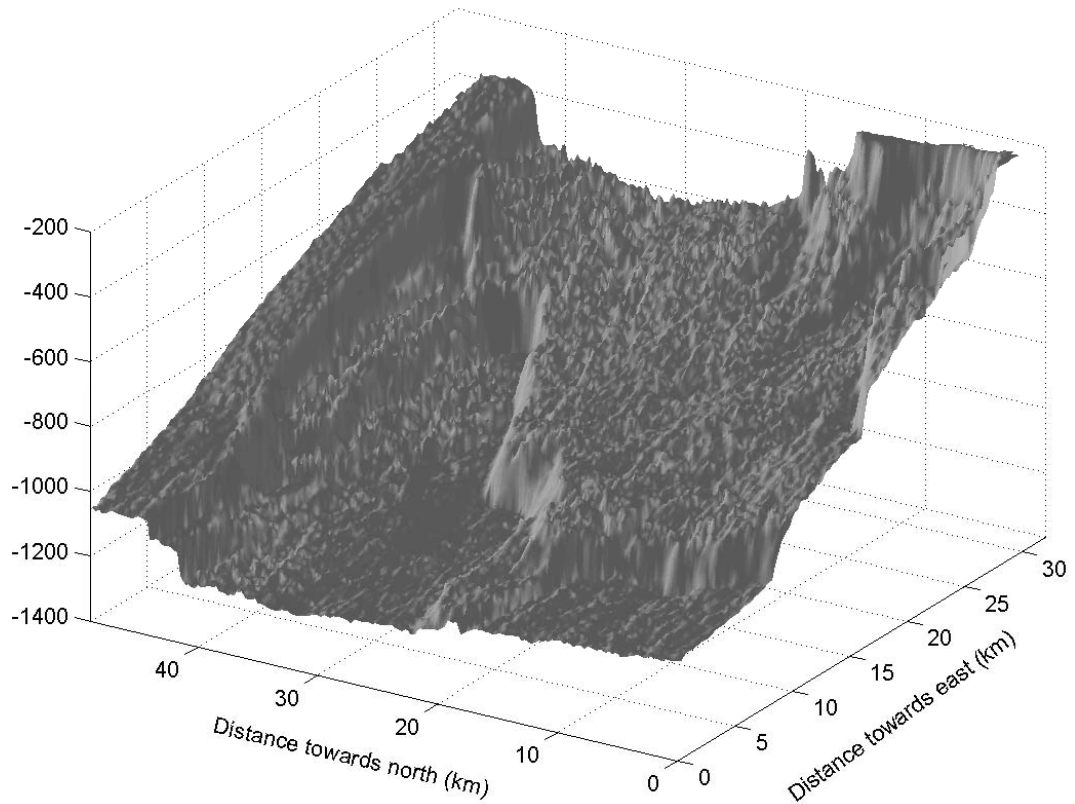
Figure 3.3: *Section of the Storegga slide area.*

than the water underneath. Below this water is the inflow of warm ($\sim 8^oC$) and saline (> 35 ppt) water to the Norwegian Sea, i.e. the North Atlantic Current (see section 2.2.5). The lower interface of the Atlantic inflow is located at a water depth between (roughly) 400 and 700 meters. The water in the layer below the Atlantic water is of Arctic origin and is often referred to as *Norwegian Sea Arctic Intermediate Water*. This water is very cold ($\div 0.5^oC - 0.5^oC$), but not as saline (~ 34.9 ppt) as the Atlantic water. At the interface between the Artic water and the Atlantic water we find the deep pychnocline. This is a pronounced density gradient caused by the differences in temperature and salinity between the two water masses. Detailed descriptions of water masses and currents in the Nordic Seas can be found in Hansen and Østerhus (2000) and Orvik and Niiler (2002).

3.5   Current profile measurements.

Measurements of current speed and direction for a number of depths at locations OL-I and OL-II (see Figure 3.2) were recorded. The instrumental set-up and some results are shown in the final report from the measurement campaign, Lønseth et al.
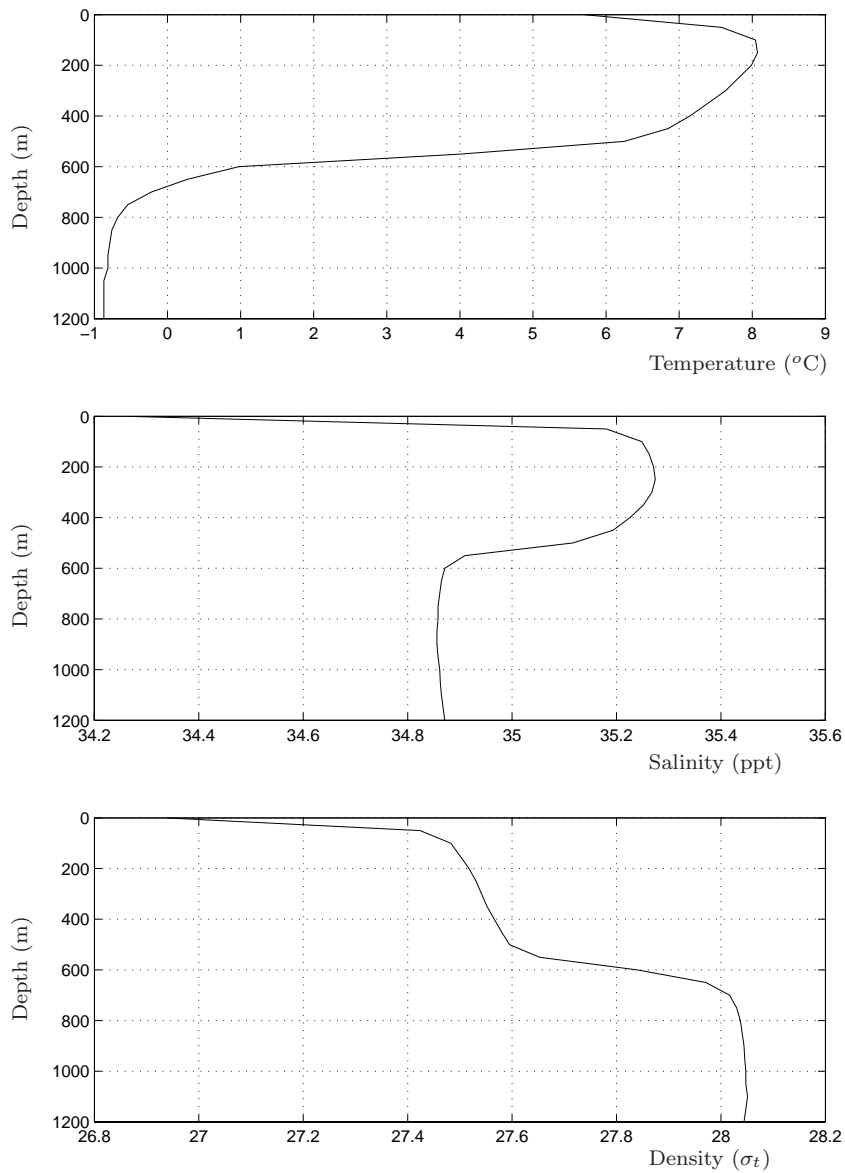
Figure 3.4: *Smoothed hydrography collected in February and April of year 2000.*

(2001). The results have been made available to this study, and a brief description
of the instrumental set-up and data recovery at OL-I and OL-II is presented in this
section. The main results (mean, max, direction of flow), an investigation into the
spatial correlation between the flow in different vertical layers and a closer look at
some interesting flow events are also provided. The description of the instrumental
set-up is largely based on the final report by Lønseth et al. (2001).

3.5.1   Description of current profile measurements

Locations and instrumental set-up

The locations of OL-I and OL-II can be seen in Figure 3.2. The current meters at OL-Ia, OL-IIa and OL-IIb were attached to a vertical mooring line from an anchor on the sea bed to submerged buoyancy elements. At OL-Ib, the current meter (Nortek ADP) was attached to a floating buoy. Exact positions of the various current meter moorings are shown in Tables 3.1 and 3.2.

Four different current meters were used.

- RDI Broadband ADCP (RD-BB-ADCP)
  This is a 75 kHz self-contained ADCP. Average velocity profile approximately 550 meters above the depth at which the instrument was installed was estimated every half hour.

- RDI Narrowband ADCP (RD-NB-ADCP)
  This is a 150 kHz self-contained ADCP. Average velocity profile approximately 200 meters above the depth at which the instrument was installed was estimated from the results of 300 pings emitted at 2 second intervals during the 10 minute averaging period.

- Nortek ADP
  This instrument is an acoustic doppler profiler (ADP), and it was mounted on a Seawatch buoy at OL-Ib. Average velocity profile from 4 meters depth to approximately 80 meters depth was estimated every hour over a 10 minute averaging period.

- RCM-7 rotor current meters
  This instrument measures the current at the position where it is installed. Current speed is measured by counting the number of rotations of a rotor, and the direction is obtained by a magnetic compass. Speed and direction (velocity) is recorded every 12 seconds, and the 10 minute vector averaged current velocity is recorded every 10 minutes. These current meters were also equipped with thermistors and a device for measuring the salinity of the water.

Tables 3.1 and 3.2 contain an overview of the depths where current flow data were recorded, and of which recording device was used at each specific depth. Two current meter moorings were used at OL-II and three moorings were used at OL-I, see Figures 3.5 and 3.6. The distances between the moorings at station OL-I is 704 meters between OL-Ia and OL-Ib, and 850 meters between OL-Ia and OL-Ir. Mooring OL-IIa is 515 meters away from mooring OL-IIb. We assume that the main features of the current flow measured at OL-Ia, OL-Ib and OL-Ir does not
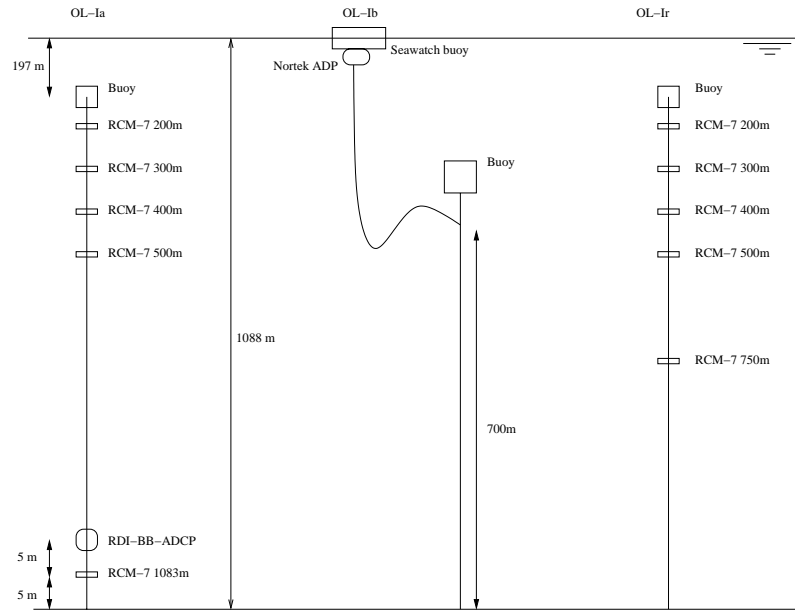
Figure 3.5: *Current meter moorings at OL-I (schematic).*
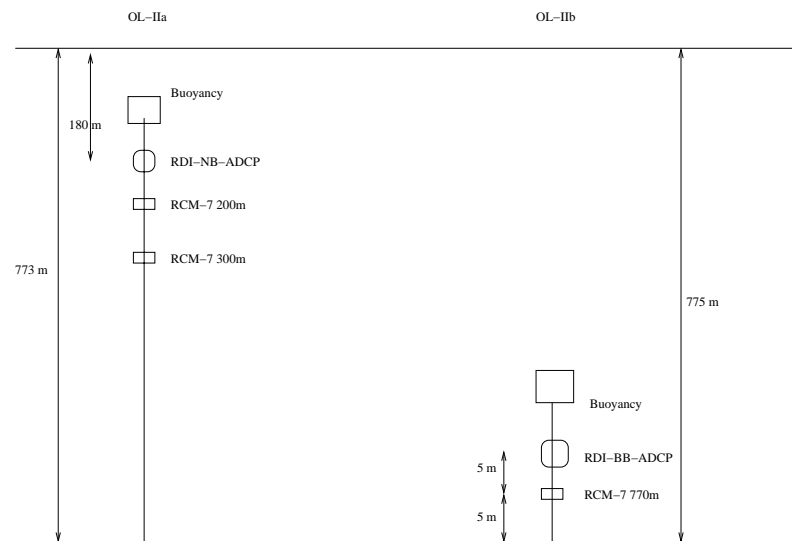
Figure 3.6: *Current meter moorings at OL-II (schematic).*

differ significantly. The same assumption is made for the current flow measured at OL-IIa and OL-IIb. Comparisons of the time traces of flow velocity logged at 300 meter water depth at OL-IIa (RCM-7) and at OL-IIb (RD-BB-ADCP) are shown in Figure 3.7. Even though it is clear from Figure 3.7 that the assumption that there is little variation of the flow in the horizontal plane within approximately
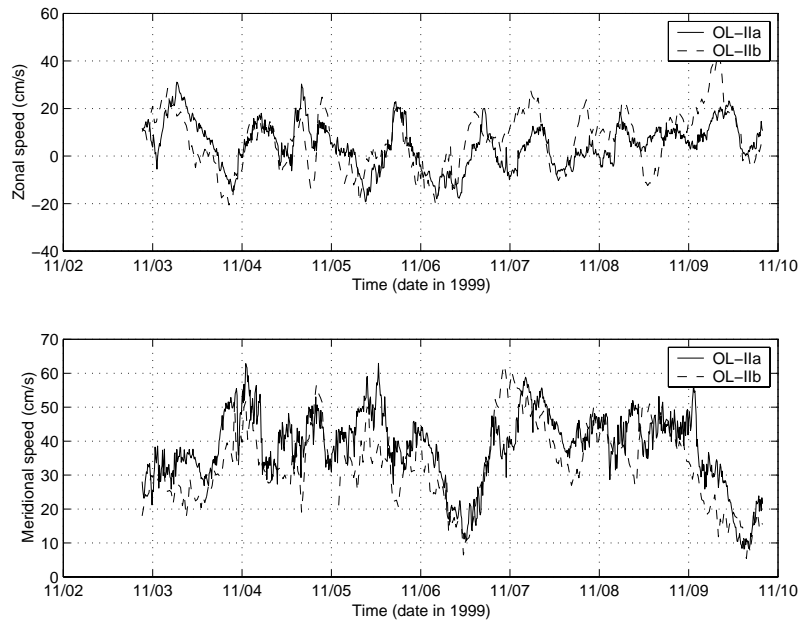
Figure 3.7: *Current measurements from 300 meters depth at OL-IIa and OL-IIb (515 meters apart from eachother).*

1000 meters is not always valid, it will still be upheld during the following studies of current profiles.

The data recorded at OL-Ir have been merged with the data from OL-Ia, and will from now on be referred to as data from OL-Ia.

As we have already mentioned (section 2.2.4), the horizontal flow velocities in the ocean are much larger than the vertical flow velocities when large scale flows are considered. When averaging periods of 10 and 30 minutes are used, the vertical velocity practically vanishes. The measured current profiles therefore consist of horizontal flow velocity measurements only.

Data recovery

The total measurement period at station OL-I ranges from 22/10-1999 until 20/10-2000. At station OL-II the total measurement period is from 23/10-1999 until 11/5-2001. All current meters listed in Tables 3.1 and 3.2 were not in place the whole time, and some of them failed to record flow data during some periods and/or time instances. Figures 3.8 and 3.9 contains an overview of the periods during which the respective current meters recorded useful data, and Tables 3.1 and 3.2 contains information about when current velocity was measured and how
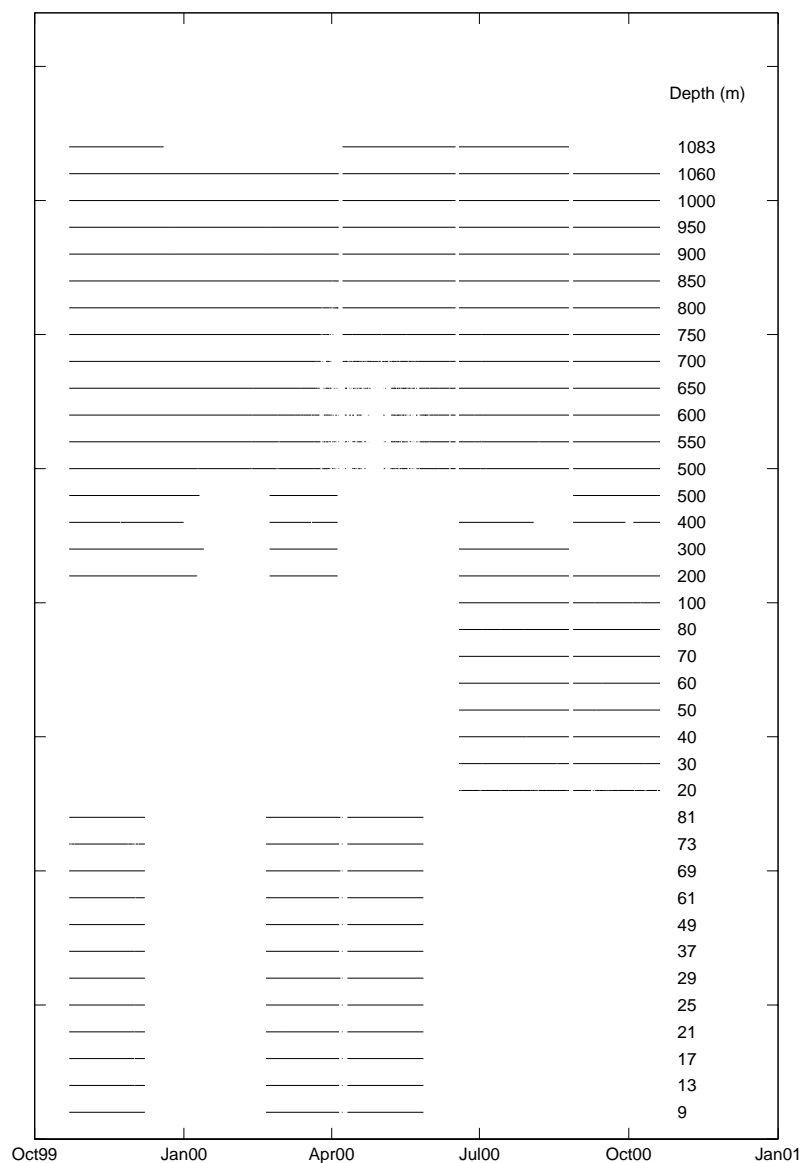
Figure 3.8: *Current data recovery at various depths at OL-I, starting in 1999.*

good the data recovery was at the respective depths. Data recovery for a current meter is defined as the ratio between the number of good data points during a period and the total number of data points for the same period.

Coordinate system

The current flow data were recorded according to the traditional convention of ocean current measurements that the x-axis is directed towards the East, the y-
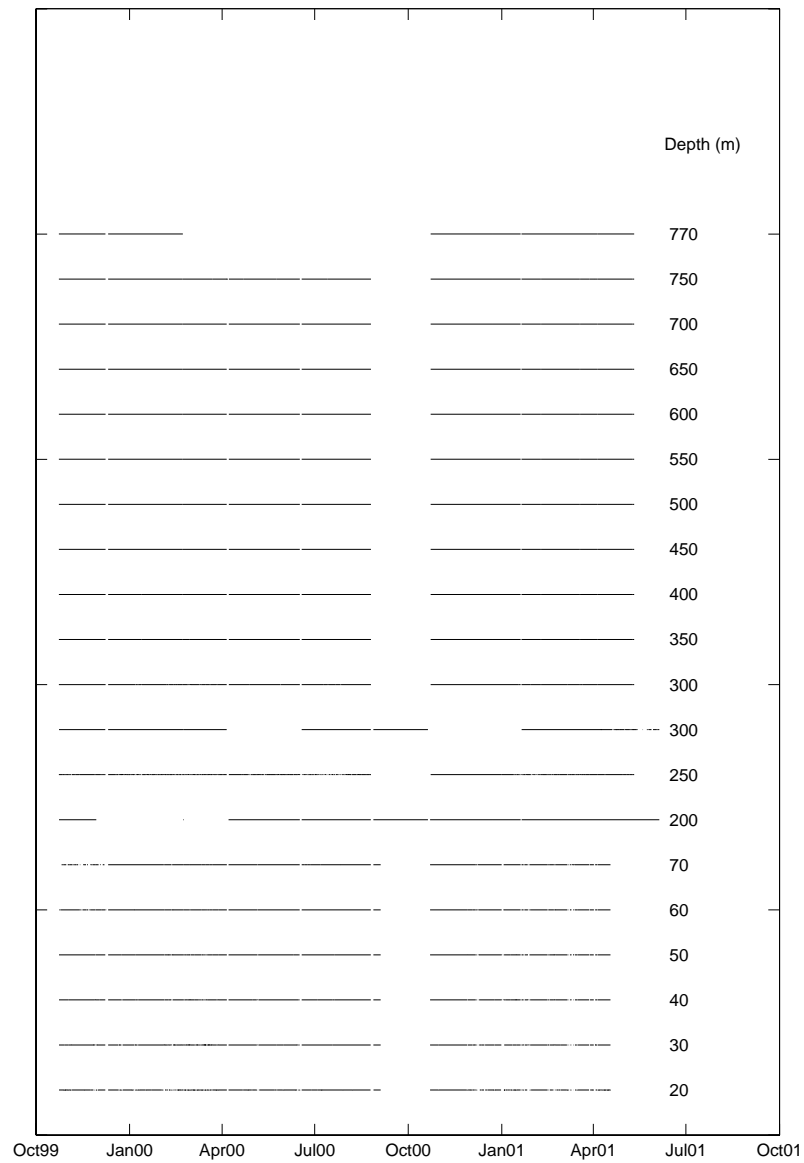
Figure 3.9: *Current data recovery at various depths at OL-II.*

axis is directed towards the North and the z-axis is directed vertically upwards. Flow along the positive x-axis (zonal flow) is eastwards with a compass direction of 90 degrees, whereas flow along the positive y-axis (meridional flow) is northwards with a compass direction of 0 degrees, see Figure 3.10.
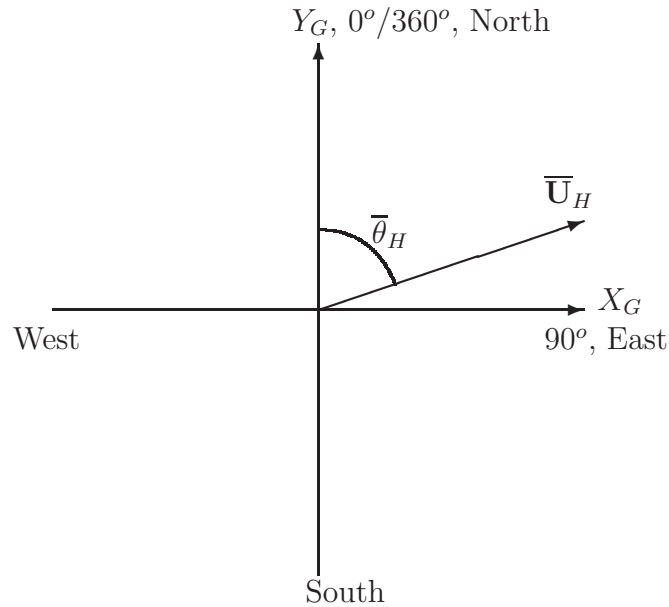
Figure 3.10: *Coordinate system.*

Postprocessing

Results from the current measurements were stored on digital data files. Some current meters failed to record good data during some periods and/or time instances. A value of -999.00 on a data file indicates that the current meter was not able to get a good reading at that time instance. All data points with flow speed values equal to -999.00 were consequently removed from the files prior to further processing.

As previously mentioned, the averaging period was 10 minutes for the RCM-7s and 30 minutes for the ADCPs. All data were resampled to discrete time instances separated by 10 minutes in the data processing that was performed after retrieving the data files.

3.5.2 Sources of error

During periods when the current was particularly strong, the drag on the mooring lines caused a significant horizontal offset of the current meters mounted on the mooring lines. As a consequence of this, the current meters were also pulled down. These vertical offsets were recorded by the pressure sensors on the RCM-7 current meters, and pressure increases as high as 20 bar, indicating a set-down of approximately 200 meters, were sometimes recorded during strong current events

Seawatch buoy OL-Ib

		Position 63° 37.518 N, 5° 18.558 E						Water depth 1088 m		
Current meter used	Logging depth	Start date	Stop date	Recovery %	Mean speed $\overline{V_c}$	Flow Stability $|\mathbf{U}_H|/\overline{V_c}$	Mean dir. $\overline{\theta_H}$	Speed	Max velocity dir.	Time of occurrence
	(m)				(cm/s)	(%)	(deg.)	(cm/s)	(deg.)	
NADP	9	22-Oct-99	27-May-00	38	37.7	54.9	60.3	103.5	91.8	03-Dec-99
NADP	13	22-Oct-99	27-May-00	38	36.3	49.6	60.7	98.5	81.9	01-Dec-99
NADP	17	22-Oct-99	27-May-00	38	35.8	48.6	60.8	95.0	88.6	01-Dec-99
NADP	21	22-Oct-99	27-May-00	38	35.7	48.2	60.8	94.0	74.4	01-Dec-99
NADP	25	22-Oct-99	27-May-00	38	35.6	47.8	60.6	88.9	91.9	21-Feb-00
NADP	29	22-Oct-99	27-May-00	38	35.4	47.7	60.1	122.7	79.0	01-Dec-99
NADP	37	22-Oct-99	27-May-00	38	35.2	47.4	59.4	86.1	83.2	03-Dec-99
NADP	49	22-Oct-99	27-May-00	38	35.0	47.1	58.2	86.0	53.7	01-Dec-99
NADP	61	22-Oct-99	27-May-00	38	34.5	47.5	56.4	85.5	51.7	01-Dec-99
NADP	69	22-Oct-99	27-May-00	38	33.9	48.1	54.3	82.8	82.2	03-Dec-99
NADP	73	22-Oct-99	27-May-00	37	33.5	48.7	53.5	81.7	82.8	03-Dec-99
NADP	81	22-Oct-99	27-May-00	38	32.4	50.9	49.5	83.2	54.8	01-Dec-99

Current meter mooring OL-Ia

		Position 63° 37.860 N, 5° 18.192 E						Water depth 1088 m		
Current meter used	Logging depth	Start date	Stop date	Recovery %	Mean speed $\overline{V_c}$	Flow Stability $|\mathbf{U}_H|/\overline{V_c}$	Mean dir. $\overline{\theta_H}$	Speed	Max velocity dir.	Time of occurrence
	(m)				(cm/s)	(%)	(deg.)	(cm/s)	(deg.)	
NB-ADCP	20	18-Jun-00	20-Oct-00	30	26.5	89.1	7.7	65.4	38.3	08-Sep-2000
NB-ADCP	30	18-Jun-00	20-Oct-00	33	30.2	90.4	8.5	64.3	355.2	18-Aug-2000
NB-ADCP	40	18-Jun-00	20-Oct-00	33	30.4	90.8	8.3	61.3	18.7	19-Sep-2000
NB-ADCP	50	18-Jun-00	20-Oct-00	33	30.5	90.8	8.3	58.5	322.9	19-Jun-2000
NB-ADCP	60	18-Jun-00	20-Oct-00	33	30.4	91.1	8.3	60.2	321.5	19-Jun-2000
NB-ADCP	70	18-Jun-00	20-Oct-00	33	30.3	90.8	8.1	59.3	9.2	08-Sep-2000
NB-ADCP	80	18-Jun-00	20-Oct-00	33	30.2	91.1	8.2	61.1	6.3	08-Sep-2000
NB-ADCP	100	18-Jun-00	20-Oct-00	33	29.5	90.9	8.2	64.0	37.3	16-Aug-2000
RCM-7	200	22-Oct-99	20-Oct-00	66	34.0	91.8	10.5	82.9	17.9	02-Nov-1999
RCM-7	300	22-Oct-99	25-Aug-00	52	34.1	90.6	8.6	87.7	13.8	25-Nov-1999
RCM-7	400	22-Oct-99	20-Oct-00	56	28.1	92.2	7.4	83.3	0.7	05-Nov-1999
RCM-7	500	22-Oct-99	20-Oct-00	48	18.9	88.9	10.4	65.5	13.2	04-Nov-1999
BB-ADCP	500	22-Oct-99	20-Oct-00	85	18.0	85.0	12.3	71.6	9.2	02-Feb-2000
BB-ADCP	550	22-Oct-99	20-Oct-00	86	14.0	77.1	10.8	64.8	2.0	07-Mar-2000
BB-ADCP	600	22-Oct-99	20-Oct-00	85	11.6	66.4	8.4	57.6	357.8	07-Mar-2000
BB-ADCP	650	22-Oct-99	20-Oct-00	85	10.3	59.2	4.2	52.6	357.4	07-Mar-2000
BB-ADCP	700	22-Oct-99	20-Oct-00	90	9.9	58.6	1.6	48.8	11.9	06-Mar-2000
BB-ADCP	750	22-Oct-99	20-Oct-00	95	9.9	60.6	359.8	56.3	18.7	06-Mar-2000
BB-ADCP	800	22-Oct-99	20-Oct-00	97	9.9	61.6	357.8	52.7	27.6	06-Mar-2000
BB-ADCP	850	22-Oct-99	20-Oct-00	97	9.9	62.6	357.5	40.5	24.8	06-Mar-2000
BB-ADCP	900	22-Oct-99	20-Oct-00	97	9.9	62.6	357.6	39.3	9.5	28-Feb-2000
BB-ADCP	950	22-Oct-99	20-Oct-00	97	9.9	63.6	357.9	39.4	355.3	06-Feb-2000
BB-ADCP	1000	22-Oct-99	20-Oct-00	97	9.9	62.6	358.2	38.2	3.8	24-Apr-2000
BB-ADCP	1060	22-Oct-99	20-Oct-00	97	10.1	61.4	354.6	41.2	353.1	24-Apr-2000
RCM-7	1083	22-Oct-99	25-Aug-00	53	8.6	65.1	339.3	32.6	333.1	24-Apr-2000

Table 3.1: *Mean and maximum values of current velocity at OL-I. (NADP = Nortek ADP).*

(see section 3.5.6).

3.5.3 Main results

Mean and maximum flow velocities

Mean and maximum values of current velocity at all current meters at OL-I and OL-II are listed in Tables 3.1 and 3.2. The flow velocity at a current meter is measured as flow speed, V_c, and direction, θ_c. Zonal and meridional components (U and V) are defined as

$$U = V_c \cdot \sin\theta_c \qquad (3.4)$$
$$V = V_c \cdot \cos\theta_c. \qquad (3.5)$$

OL-IIa

		Position 63° 35.538 N, 5° 34.458 E						Water depth 773 m		
Current meter used	Logging depth (m)	Start date	Stop date	Recovery %	Mean speed $\overline{V_c}$ (cm/s)	Flow Stability $|\mathbf{U}_H|/\overline{V_c}$ (%)	Mean dir. $\overline{\theta}_H$ (deg.)	Speed (cm/s)	Max velocity dir. (deg.)	Time of occurrence
NB-ADCP	20	23-Oct-99	17-Apr-01	66	28.2	79.1	14.3	106.8	347.5	25-Feb-00
NB-ADCP	30	23-Oct-99	17-Apr-01	74	31.2	82.7	13.4	108.2	353.9	25-Feb-00
NB-ADCP	40	23-Oct-99	17-Apr-01	77	32.0	84.1	12.6	103.6	349.5	25-Feb-00
NB-ADCP	50	23-Oct-99	17-Apr-01	78	31.8	84.6	12.1	98.1	356.9	25-Feb-00
NB-ADCP	60	23-Oct-99	17-Apr-01	78	31.7	84.9	11.9	98.3	28.5	12-Feb-00
NB-ADCP	70	26-Oct-99	17-Apr-01	75	31.7	85.2	11.6	99.7	1.9	11-Feb-00
RCM-7	200	23-Oct-99	04-Jun-01	76	26.4	85.6	11.6	93.8	2.1	29-Nov-99
RCM-7	300	23-Oct-99	04-Jun-01	68	27.7	88.1	11.5	90.0	9.5	28-Nov-99

OL-IIb

		Position 63° 35.328 N, 5° 34.044 E						Water depth 775 m		
Current meter used	Logging depth (m)	Start date	Stop date	Recovery %	Mean speed $\overline{V_c}$ (cm/s)	Flow Stability $|\mathbf{U}_H|/\overline{V_c}$ (%)	Mean dir. $\overline{\theta}_H$ (deg.)	Speed (cm/s)	Max velocity dir. (deg.)	Time of occurrence
BB-ADCP	250	23-Oct-99	11-May-01	68	27.1	77.1	17.2	107.4	22.8	28-Nov-99
BB-ADCP	300	23-Oct-99	11-May-01	83	26.4	75.8	17.3	100.3	25.9	28-Nov-99
BB-ADCP	350	23-Oct-99	11-May-01	84	25.6	74.2	16.2	91.7	17.5	28-Nov-99
BB-ADCP	400	23-Oct-99	11-May-01	84	24.3	71.6	14.7	86.3	3.2	10-Mar-01
BB-ADCP	450	23-Oct-99	11-May-01	84	22.5	68.0	12.8	89.2	7.1	10-Mar-01
BB-ADCP	500	23-Oct-99	11-May-01	84	20.0	63.0	9.6	80.5	42.3	29-Feb-00
BB-ADCP	550	23-Oct-99	11-May-01	84	16.4	59.2	5.9	72.0	5.5	02-Apr-01
BB-ADCP	600	23-Oct-99	11-May-01	84	12.8	53.1	6.7	67.8	7.2	08-Jan-00
BB-ADCP	650	23-Oct-99	11-May-01	84	10.4	47.1	17.8	49.5	49.8	11-Feb-00
BB-ADCP	700	23-Oct-99	11-May-01	84	8.9	38.2	31.4	46.0	31.3	08-Jan-00
BB-ADCP	750	23-Oct-99	11-May-01	84	8.7	23.0	58.2	55.3	47.3	19-Mar-00
RCM-7	770	23-Oct-99	11-May-01	54	7.9	25.3	53.1	49.4	36.6	26-Nov-99

Table 3.2: *Mean and maximum values of current velocity at OL-II.*

We can then write the horizontal velocity vector as

$$\mathbf{U} = U \cdot \mathbf{i} + V \cdot \mathbf{j} \qquad (3.6)$$

where $\mathbf{i}$ and $\mathbf{j}$ are unit length vectors along the X_G and Y_G axes (Figure 3.10), respectively. Mean flow speed, $\overline{V_c}$, is calculated according to

$$\overline{V}_c = \frac{1}{N} \sum_{n=1}^{N} V_{c_n} \qquad (3.7)$$

Mean horizontal velocity vector, $\overline{\mathbf{U}}_H$, is calculated according to

$$\overline{\mathbf{U}}_H = \frac{1}{N} \left(\mathbf{i} \cdot \sum_{n=1}^{N} U_n + \mathbf{j} \cdot \sum_{n=1}^{N} V_n \right) \qquad (3.8)$$

and the mean horizontal flow direction, $\overline{\theta}_H$, is the angle between this vector and the global y-axis as shown in Figure 3.10. Note that the mean direction is significantly different in the upper layer at OL-Ia than it is at OL-Ib. The results in the upper layer at OL-Ib and OL-Ia were not recorded at the same time of year, and this is indication that the mean flow direction at the site is seasonally adjusted. However, no further investigations into this are made and the data at OL-Ib are omitted from the following analyses.

Main profile direction

Generally, the intensity and direction of the flow at OL-I and OL-II varies with depth, and it is not always intuitive which direction is the 'main current profile direction'. A definition is proposed in this section. The definition is based on overall mass transport.

Current velocity is measured at M levels. At every level, m, a length, l_m, is defined as the depth interval for which the flow measured at current meter m applies. $V_{c_{mn}}$ and $\theta_{c_{mn}}$ are speed and direction, respectively, at level m at time t_n. We define the main transport at time t_n as the horizontal vector

$$\mathbf{M}_n = \mathbf{i} \cdot \sum_{m=1}^{M} l_m \cdot U_{mn} + \mathbf{j} \cdot \sum_{m=1}^{M} l_m \cdot V_{mn} \tag{3.9}$$

where the relationship in equations (3.4) and (3.5) are used. Total transport over the entire time period of the measurements is the sum of all $\mathbf{M}_n$ over the measurement period.

$$\mathbf{M}_T = \sum_{n=1}^{N} \mathbf{M}_n \tag{3.10}$$

and the main profile direction is then defined as the angle, θ_M, between the vector $\mathbf{M}_T$ and the global y-axis in Figure 3.10.

The main direction at OL-I, when considering the entire measurement period, was 8 degrees, which is almost due North, and at OL-II the main direction was found to be 13.4 degrees, i.e. not far from NNE. If we consider only the period 20/6-2000 until 2/8-2000, the mean profile direction is 4.4 degrees at OL-I, and 14.8 degrees at OL-II, suggesting that the mean profile direction is seasonally adjusted.

3.5.4   Correlation in the vertical

We can express the time series of the fluctuating (mean removed) horizontal current velocity at current meter m using complex notation

$$q_m(t) = u'_m(t) + i \cdot v'_m(t) \tag{3.11}$$

where i is the imaginary unit and u'_m and v'_m are fluctuating velocity components. In studying Ekman veering, Kundu (1976) introduced a complex correlation coefficient which he used as a measure of the average relative angular displacement between two vector time series. The complex correlation coefficient between velocity vectors at levels i and j, as defined by Kundu (1976), can be written,

$$\rho_{ij} = \frac{E\left[q_i^*(t) \cdot q_j(t)\right]}{\left(E\left[q_i^*(t) \cdot q_i(t)\right]\right)^{\frac{1}{2}} \cdot \left(E\left[q_j^*(t) \cdot q_j(t)\right]\right)^{\frac{1}{2}}} \tag{3.12}$$

where $q_i^*(t)$ is the complex conjugate of $q_i(t)$ and the $E[\cdot]$ operator is the ensemble average of the quantity in the brackets (Newland 1993), commonly known as the expectancy value of that quantity. The magnitude of the complex correlation coefficient can be viewed as a measure of the overall correlation between two vector series, and the phase angle can be seen as a measure of the average angle between the two vector series. The distribution in space of magnitudes of ρ_{ij} for some of the current meters at OL-I are shown in Figure 3.11. The phase angle of the complex correlation coefficient between the velocity vector at 100 m depth and other velocity vectors in the upper 400 meters are all close to zero, and the magnitude of the coefficients ranges from 0.6 to almost 1.0. This indicates good correlation in the upper layer. The correlation between the flow velocity at 100 m depth and the lower layer, however, is poor. It can also be seen that the velocity vector at mid-depth (500 m) is not particularly well correlated with neither the upper layer nor the lower layer. From Figure 3.2 it can be seen that there is a relatively steep rise from 1000 meters water depth to approximately 500 meter depth just north of OL-I. This abrupt change in the bottom topography may well be the cause of the poor correlation between the flow in the upper and lower layers. It should be noted, however, and we will return to this in the next section, that the interface between the North Atlantic water and the Arctic Intermediate water is located at approximately mid-depth, indicating that the stratification may also be important in decoupling the flow in the two water masses.

3.5.5 EOF analysis

Background

EOF is short for Empirical Orthogonal Functions. The EOF-analysis technique is used for representing a set of spatially distributed time series as a sum of orthogonal spatial functions (EOFs) multiplied with their temporal amplitudes (principal components). A current profile, defined at the locations in $\mathbf{x}$, can, thus, be expressed by

$$\mathbf{U}(\mathbf{x}, t) = \sum_{m=1}^{M} \mathbf{b}_m(\mathbf{x}) \cdot \mathbf{w}_m(t) \tag{3.13}$$

where $\mathbf{b}_m(\mathbf{x})$ is the m'th empirical orthogonal function, $\mathbf{w}_m(t)$ is the corresponding principal component and M is the number of data points (locations in $\mathbf{x}$). The principal components (PCs) and the empirical orthogonal functions (EOFs) are equally important in representing the data. In this section, the following terms will be used :

- Empirical orthogonal function (EOF) : spatial variation

- Principal component (PC) : time-varying amplitude of the corresponding orthogonal function
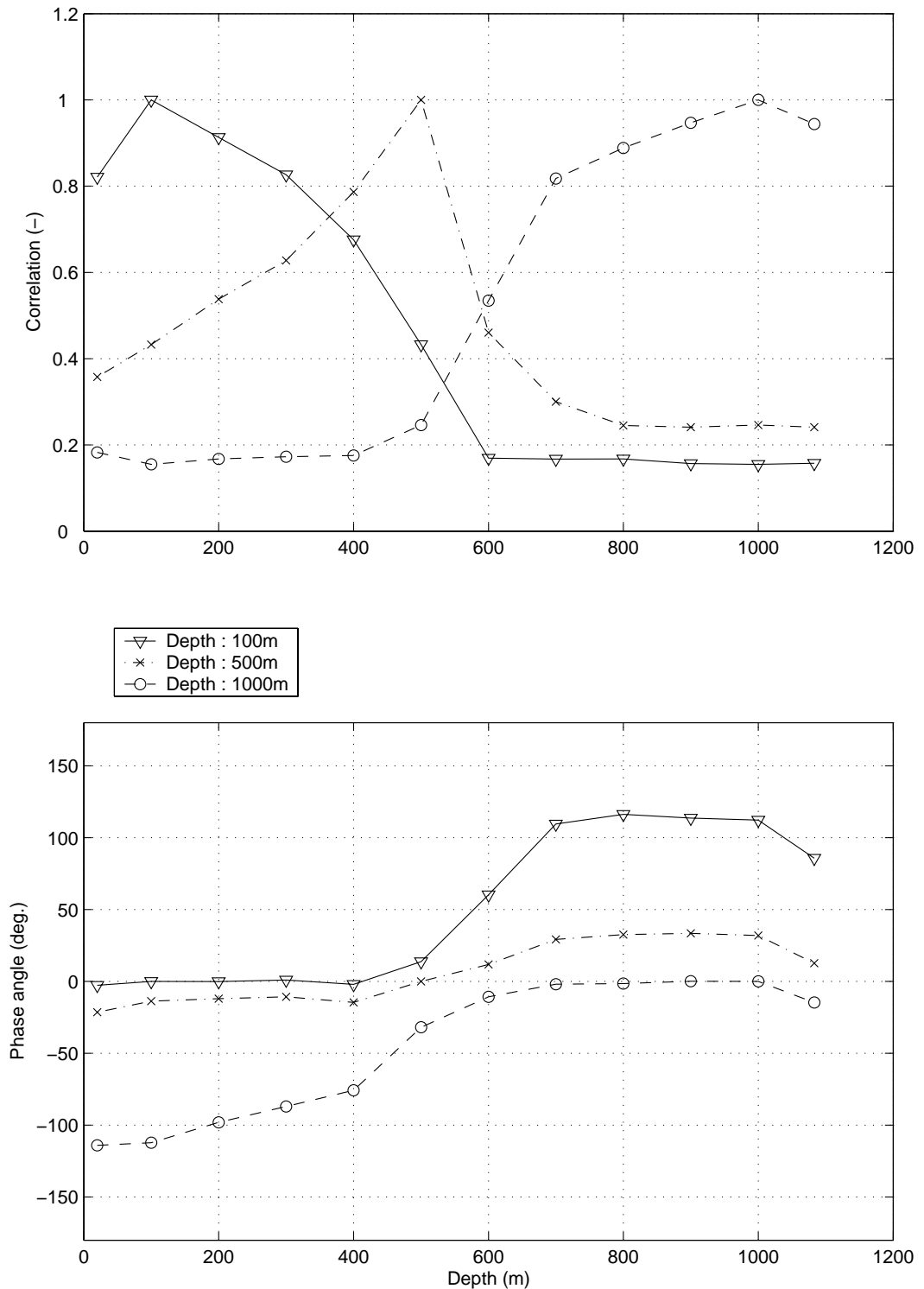
Figure 3.11: *Correlation magnitude and phase angle at OL-I. The time period analysed is from 20/6-2000 until 2/8-2000. Note that the phase angle has little or no meaning when the magnitude of the correlation coefficient is small. Current meters at the depths where the markers appear were included in the analysis.*

- EOF-mode : Empirical orthogonal function together with its principal component

The EOF-analysis technique for data processing is used frequently in oceanography, meteorology and climate research. Emery and Thompson (2001) mention Lorenz (1956) as the first researcher to apply the technique to geophysical fluid dynamics. As the offshore oil and gas industry is moving towards deeper and deeper waters, offshore engineers have also begun using the EOF-technique for various other purposes, see e.g. Meling et al. (2002), Jeans and Feld (2001), Jeans et al. (2002), Forristal and Cooper (1997) and Kleiven (2002).

Purpose

The purpose of applying the EOF analysis technique is to exploit the main advantage of the method:

- EOF-analysis is the most effective way of reducing the amount of data in a data set and still keeping most of the variance (energy). Most of the variance is usually contained in the first few (2-5) EOF-modes.

EOF-analysis is well suited for use on spatially distributed time series, such as those retrieved from the current meters at OL-I and OL-II.

Interpretation

EOF-modes are 'statistical' modes, representing the variance in the data set, and not generally linked with any physical processes responsible for creating that variance. Even though the shape of the EOF-modes and the frequency contents of the principal components can give valuable clues as to the driving mechanisms behind a data set or some general feature of the flow, one should in general be careful in drawing conclusions of this kind based solely on EOF-analysis.

Theory

Assume that we have a data set of time traces of horizontal current flow velocity from M current meters. Also assume that there are N data points in each time trace. The measurements can be described as in equation (3.13), but in the following outline we shall use matrix notation and organize the data in a complex $N \times M$ matrix, defined as,

$$\mathbf{A} = \begin{bmatrix} \mathbf{a}_1^T & \mathbf{a}_2^T & \dots & \mathbf{a}_m^T & \dots & \mathbf{a}_M^T \end{bmatrix} \tag{3.14}$$

$$\mathbf{a}_m = \begin{bmatrix} a_{1m} & a_{2m} & \dots & a_{nm} & \dots & a_{Nm} \end{bmatrix} \tag{3.15}$$

$$\mathbf{A} = \begin{bmatrix} a_{11} & a_{12} & \dots & a_{1M} \\ a_{21} & a_{22} & \dots & a_{2M} \\ a_{31} & a_{32} & \dots & a_{3M} \\ \vdots & \vdots & & \vdots \\ a_{N1} & a_{N2} & \dots & a_{NM} \end{bmatrix} \tag{3.16}$$

The elements of $\mathbf{A}$ are complex representations of the velocity vectors,

$$a_{nm} = U_{nm} + i \cdot V_{nm} \tag{3.17}$$

where U_{nm} and V_{nm} are zonal and meridional flow speeds, respectively, at current meter m at time instance n. The time record at current meter m is stored in the complex vector $\mathbf{a}_m$. The formulation of EOF-analysis using complex notation is based on the work by Kundu and Allen (1976). Note, however, that the EOF-analysis explained and used herein is not the truly complex EOF-analysis, described by Horel (1984), in which propagating features of the flow can be detected.

We wish to write $\mathbf{A}$ as a weighted sum of orthogonal functions in space. On matrix form this can be formulated

$$\mathbf{A} = \mathbf{W} \cdot \mathbf{B}^H \tag{3.18}$$

where

$$\mathbf{B} = \begin{bmatrix} \mathbf{b}_1^T & \mathbf{b}_2^T & \dots & \mathbf{b}_m^T & \dots & \mathbf{b}_M^T \end{bmatrix} \tag{3.19}$$

is an $M \times M$ matrix containing the complex orthogonal functions, and $\mathbf{B}^H$ is the complex conjugate transpose of $\mathbf{B}$. This means that we can get no more than M orthogonal modes from M current meters. Mode m is given by

$$\mathbf{b_m} = \begin{bmatrix} b_{1m} & b_{2m} & \dots & b_{km} & \dots & b_{Mm} \end{bmatrix} \tag{3.20}$$

where b_{km} can be viewed as mode 'size' at current meter k in mode m. The matrix of modal weights, $\mathbf{W}$, contains the complex amplitudes of each of the modes at all time instances. These are also referred to as *principal components*. A principal component is a time series of complex amplitudes for a mode, given as

$$\mathbf{W} = \begin{bmatrix} \mathbf{w}_1^T & \mathbf{w}_2^T & \dots & \mathbf{w}_m^T & \dots & \mathbf{w}_M^T \end{bmatrix} \tag{3.21}$$

$$\mathbf{w_m} = \begin{bmatrix} w_{1m} & w_{2m} & \dots & w_{nm} & \dots & w_{Nm} \end{bmatrix} \tag{3.22}$$

and is an $N \times M$ matrix in which every column is a time series of weights (amplitudes) for their respective modes. We can now write the entire matrix multiplication $\mathbf{W} \cdot \mathbf{B}^H$ as

$$
\begin{bmatrix}
w_{11} & \cdots & w_{1m} & \cdots & w_{1M} \\
\vdots & & \vdots & & \vdots \\
\vdots & & \vdots & & \vdots \\
w_{n1} & \cdots & w_{nm} & \cdots & w_{nM} \\
\vdots & & \vdots & & \vdots \\
\vdots & & \vdots & & \vdots \\
w_{N1} & \cdots & w_{Nm} & \cdots & w_{NM}
\end{bmatrix}
\cdot
\begin{bmatrix}
b_{11}^* & \cdots & b_{k1}^* & \cdots & b_{M1}^* \\
\vdots & & \vdots & & \vdots \\
b_{1m}^* & \cdots & b_{km}^* & \cdots & b_{Mm}^* \\
\vdots & & \vdots & & \vdots \\
b_{1M}^* & \cdots & b_{kM}^* & \cdots & b_{MM}^*
\end{bmatrix}
\tag{3.23}
$$

where b_{ij}^* is the complex conjugate of b_{ij}.

In order for the functions $\mathbf{b}_m$ to be orthogonal, we require that

$$
\mathbf{B} \cdot \mathbf{B}^H = \delta_{mk} = \mathbf{I} \tag{3.24}
$$

where δ_{mk} is the Kronecker delta, defined by

$$
\delta_{mk} = \begin{cases} 0 & \text{if } m \neq k \\ 1 & \text{if } m = k \end{cases} \tag{3.25}
$$

The covariance matrix for the principal components can be written

$$
\mathbf{P} = \frac{1}{N-1} \cdot \mathbf{W}^H \cdot \mathbf{W} =
\begin{bmatrix}
p_{11} & p_{12} & \cdots & \cdots & p_{1M} \\
p_{21} & p_{22} & p_{23} & \cdots & p_{2M} \\
p_{31} & p_{32} & \ddots & \ddots & \vdots \\
\vdots & \vdots & \ddots & \ddots & \vdots \\
p_{M1} & \cdots & \cdots & \cdots & p_{MM}
\end{bmatrix}
\tag{3.26}
$$

Now, we make sure that the principal components are uncorrelated by imposing the requirement that

$$
p_{ij} = \begin{cases} \lambda_{ij} & \text{for } i = j \\ 0 & \text{for } i \neq j \end{cases} \tag{3.27}
$$

The covariance matrix, $\mathbf{P}$, then reduces to

$$
\mathbf{P} = \frac{1}{N-1} \cdot \mathbf{W}^H \cdot \mathbf{W} = \mathbf{\Lambda} =
\begin{bmatrix}
\lambda_{11} & 0 & \cdots & \cdots & 0 \\
0 & \lambda_{22} & 0 & \cdots & 0 \\
0 & 0 & \ddots & \ddots & \vdots \\
\vdots & \vdots & \ddots & \ddots & 0 \\
0 & \cdots & \cdots & 0 & \lambda_{MM}
\end{bmatrix}
\tag{3.28}
$$

where λ_{ii} is the contribution from EOF-mode i to the total variance in the data.

If the mean values are removed from each of the measured time traces in $\mathbf{A}$, we can write the complex covariance matrix as

$$\mathbf{C} = \frac{1}{N-1} \cdot \mathbf{A}^H \cdot \mathbf{A} \tag{3.29}$$

Inserting equation (3.18) into equation (3.29), and using the relationship in equation (3.28) and the known relation from linear algebra that $(\mathbf{AB}^H)^H = \mathbf{BA}^H$, we get

$$\mathbf{C} = \frac{1}{N-1}(\mathbf{W} \cdot \mathbf{B}^H)^H \cdot (\mathbf{W} \cdot \mathbf{B}^H) = \frac{1}{N-1} \cdot \mathbf{B} \cdot \mathbf{W}^H \cdot \mathbf{W} \cdot \mathbf{B}^H = \mathbf{B} \cdot \mathbf{\Lambda} \cdot \mathbf{B}^H \tag{3.30}$$

The next step is to multiply by $\mathbf{B}$ on both sides in equation (3.30), and impose the orthogonality requirement, stated in equation (3.24).

$$\mathbf{C} \cdot \mathbf{B} = \mathbf{B} \cdot \mathbf{\Lambda} \tag{3.31}$$

Equation (3.31) expresses M complex eigenvalue problems. The solutions to these eigenvalue problems give us $\mathbf{B}$ and $\mathbf{\Lambda}$. The eigenvalues in $\mathbf{\Lambda}$ are real and we have required that the eigenvectors in $\mathbf{B}$ be orthogonal. Thus, matrix $\mathbf{C}$ is Hermitian ($\mathbf{C}{=}\mathbf{C}^H$), which is analogous to a real matrix being symmetric.

The principal components, $\mathbf{W}$, can now be found from,

$$\mathbf{W} = \mathbf{A} \cdot \mathbf{B} \tag{3.32}$$

The eigenvalues in $\mathbf{\Lambda}$ tell us how much the respective EOF-modes contribute to the variance (energy). This information is contained in the principal components, $\mathbf{w_m}$. All of the variance in the data is described by the variance in the principal components. The first eigenvalue is larger than the second eigenvalue and so on. Thus, the first EOF-mode contains more energy (variance) than the second one, which in turn contains more energy than the third one, and so on. This means that we only need the first few modes in order to generate a data set which contains a significant percentage of the energy in the original data set. A reconstructed data set, $\tilde{\mathbf{A}}$, of dimension $N \times M$ is found by multiplying the $N \times P$ sub-matrix of $\mathbf{W}$ with the $P \times M$ sub-matrix of $\mathbf{B}^H$. The elements of $\tilde{\mathbf{A}}$ can be written as,

$$\tilde{a}_{nm} = \sum_{j=1}^{P} w_{nj} \cdot b_{mj}^* \tag{3.33}$$

where P is the number of EOF-modes that are included in the reconstruction.

EOF analysis of current at OL-I

The data recorded at some of the current meters at OL-I in the time period from 20/6-2000 until 2/8-2000 have been processed according to the procedure described above. The same data set that was used in creating Figure 3.11 was also used for the EOF-analysis.

We saw in the correlation study (section 3.5.4) that there is a clear tendency that the flow in the layer above approximately 500 meters depth is decoupled from the flow in the layer below. This is also indicated by the shape of the complex empirical orthogonal functions, see Figure 3.12. The first EOF in Figure 3.12 is stronger in the upper layer than in the lower layer. Also, the orientation of the EOF (i.e. the phase between the real and complex components) is different in the two layers. The largest changes occur at a water depth of approximately 550 meters, and this is well within the depth range in which we would expect to find the deep pycnocline (see Figure 3.4). Knowing that the first mode contributes most to the total variance in the data, this indicates that there is more variability in the upper layer than in the lower. The second EOF in Figure 3.12, on the other hand, is weak above the deep pycnocline and strong below.

In the left part of Figure 3.13 we can see how the EOF-modes at the various current meters contribute to the total variance in the data. It is confirmed that the first EOF-mode contains most of the variance in the upper layer. The figure also tells us that most of the variance in the deep layer (below 500 meters) is represented by the second EOF-mode. In Figure 3.12 it is seen that the largest contribution from the third EOF is at the surface and at a depth of 400-500 meters. The energy contributed at the surface is most likely related to wind stress variations. At 400-500 meters depth, however, the variability in the data is probably due to the close vicinity of the pycnocline. The right part of Figure 3.13 shows how much each EOF-mode contributes to the variance at the different water depths. Again we see how modes one and two are dominant in the upper and lower layer, respectively. We also see that, at some depths, a large number of EOF-modes must be included in order to account for more than 95% of the variance at that level. This is particularly clear at the current meters below the pycnocline. One normally expects to find that most of the energy (more than 95%) in the data is contained in the first few (2-5) modes. When the directional variation is taken into account, however, as we do in our analysis, and the decoupling between the flow in the upper and lower water layers is as distinguished as it is here, it seems that more modes must be included in order to describe the variance in the data sufficiently well.

The power spectra of the principal components from an EOF-analysis of data from a somewhat shorter time period than what was used in the EOF-analysis shown
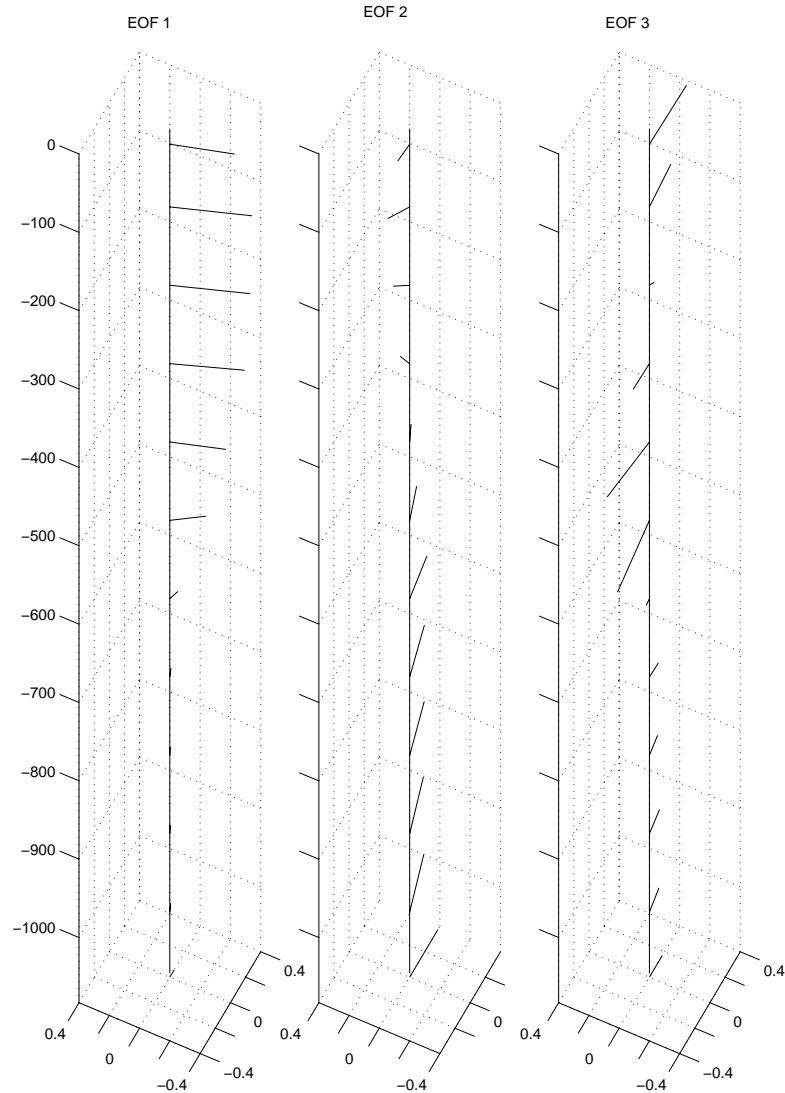
Figure 3.12: *The three first complex EOFs at OL-I, using data from the period from 20/6-2000 until 2/8-2000. Current meters at depths 20, 100, 200, 300, 400, 500, 600, 700, 800, 900, 1000 and 1083 meters were included in the analysis.*

earlier, and also for a reduced number of current meters, have been calculated. The results can be seen in Figure 3.14. The reason for omitting certain time periods and current meters is that the data from the omitted time periods and current meters contained gappy data. The power spectra for the velocity components at each depth have also been calculated. The power spectrum for zonal flow speed was added to the power spectrum of meridional flow speed and plotted in Figure 3.14. As one would expect, the major energy content is in the lower principal components. Spectral peaks at the diurnal and the semi-diurnal frequencies are
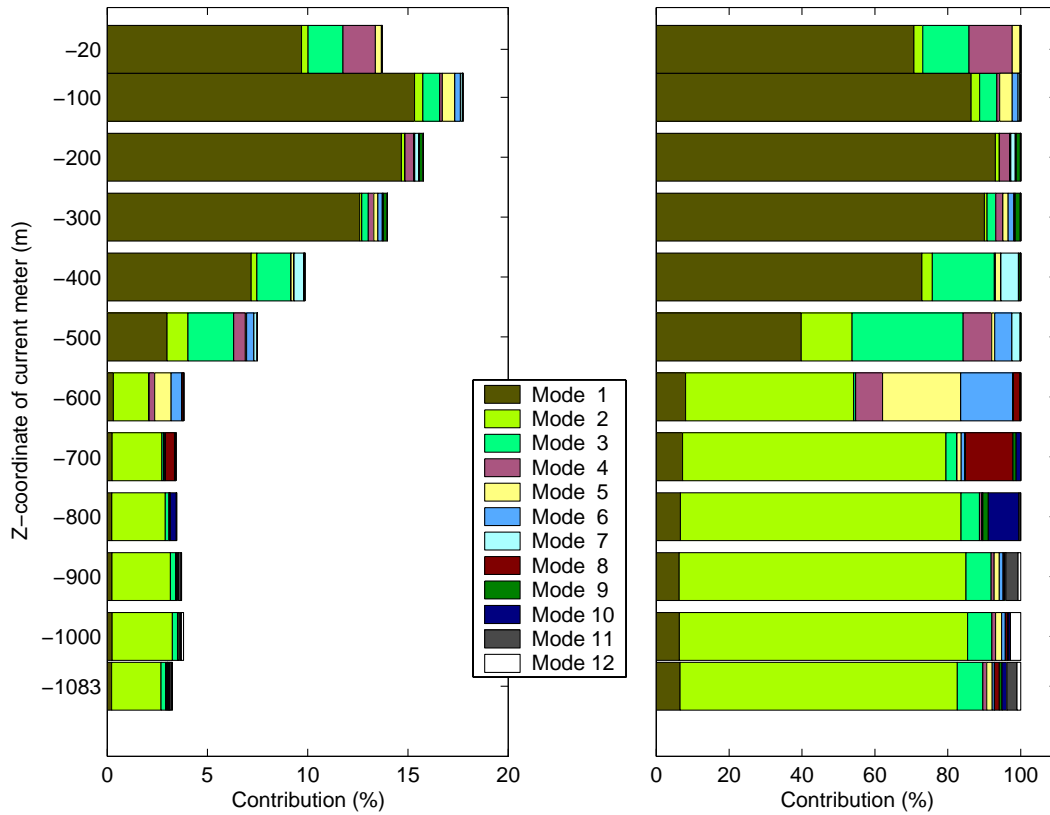
Figure 3.13: *Contribution to the total variance (left), and to the variance at each specific current meter (right), from the EOF-modes at different water depths at OL-I, using data from the period from 20/6-2000 until 2/8-2000.*

clearly seen, especially for the spectra of the lower principal components.

3.5.6 A closer look at some strong current events

Results from close inspection of the flow variations during two short time periods, containing some strong current events, are presented in this section.

Strong current events at mid-depth, OL-I

Records of temperature, pressure and flow speed from the period between 20/2-2000 and 28/3-2000 at station OL-I are shown in Figure 3.15. There are three shorter periods within this period during which the current is particularly strong. The first is from day 58 to day 60, the second is from day 66 to day 67 and the third is from day 84 to day 86. Note the increased pressure and reduced water temperature during all of these periods. This indicates that the current meters
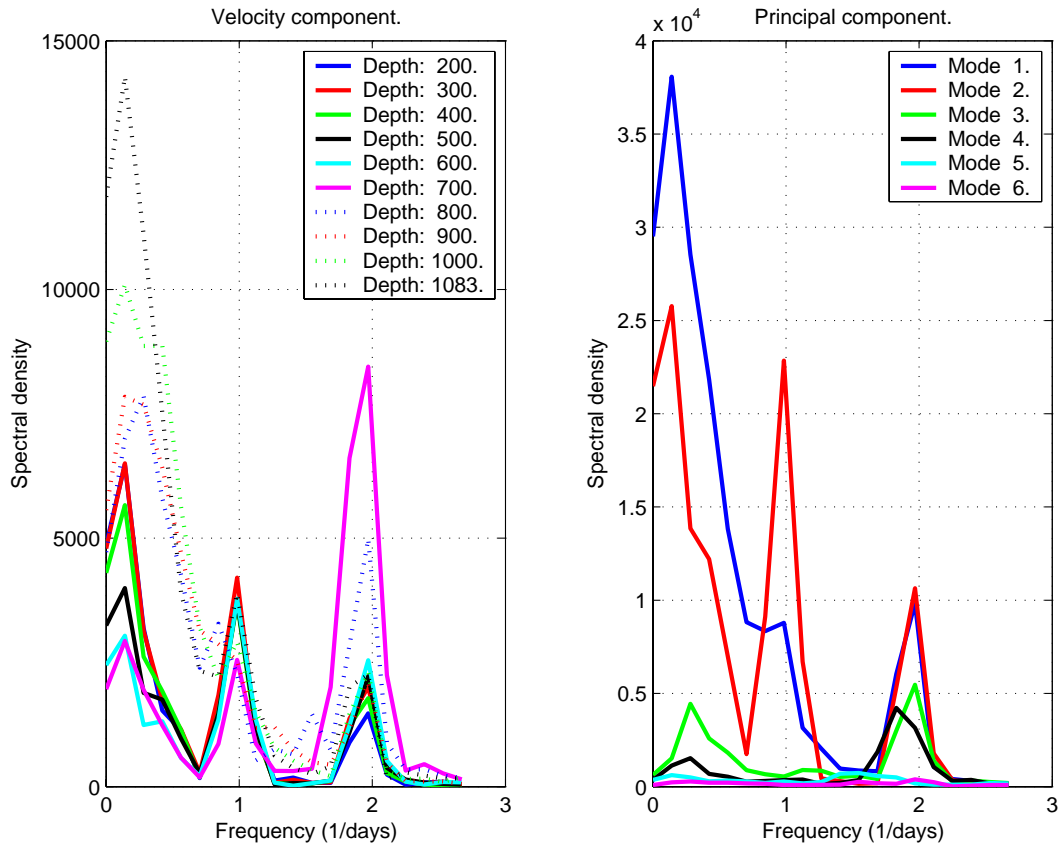
Figure 3.14: *Power spectra of the real and imaginary velocity components were added and are plotted on the left, and power spectra of the real and imaginary parts of the the first six principal components were added and are plotted on the right. Data from the period from 6/7-2000 until 2/8-2000 at OL-I were used.*

are pulled down by the drag on the mooring line. The pressure increase is around 20 bar at its largest, corresponding to a pull-down of as much as 200 meters.

Strong current events at mid-depth, OL-II

The RCM-7s at 200 and 300 meters water depth at OL-II recorded water temperature data as well as current velocity. Some strong current events were recorded at these current meters, see Figure 3.16. As can be seen in the figure, there is a quite strong (~ 0.5 m/s) flow towards south on the 24th of December 2000. This flow weakens and is slow for a few days before it grows strong again, only this time the flow is towards north. Lønseth et al. (2001) propose that this observation is related to variations in the surface winds and atmospheric pressure fields in the same period, possibly causing a meander of the near-by slope current to
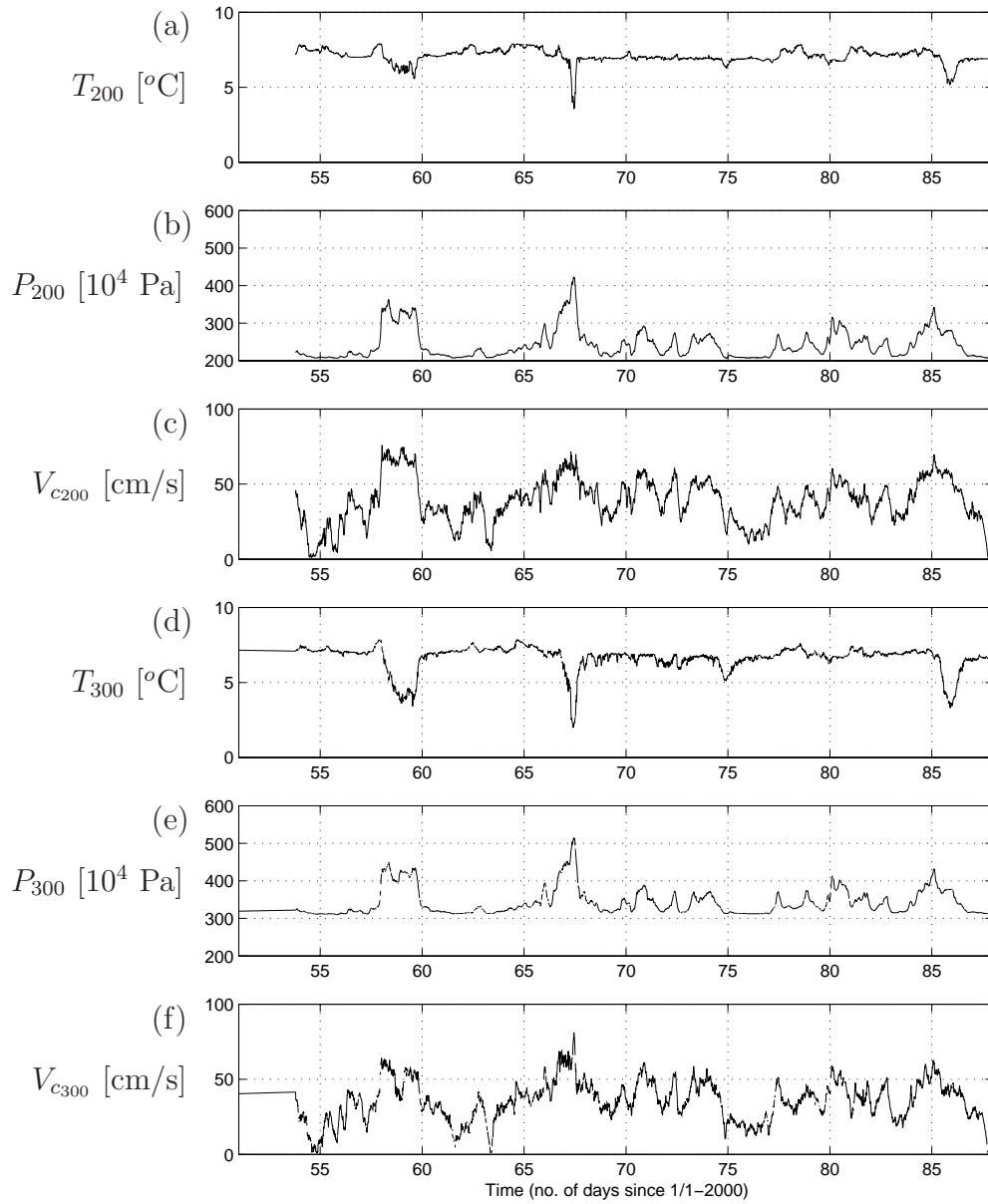
Figure 3.15: *Temperature, pressure and flow speed at 200 meter depth (a-c) and at 300 meter depth (d-f). The data were recorded at OL-I in the period from 20/2-2000 until 28/3-2000.*

develop into a closed clockwise rotating loop. If such a loop has passed to the west of OL-I it would cause strong southwards flow at the current meters there. The strong northwards flow a few days later is by Lønseth et al. (2001) attributed to meandering of the slope current. Large flow speeds were recorded at depths between 200 and 500 meters on January 1st, see Table 3.3 and Figure 3.16. The

Waterdepth (m)	Max. speed (cm/s)	Direction (deg.)	Time of occurrence (date)
20	47.9	-29.7	29-Dec-2000 05:30:00
50	78.7	9.2	31-Dec-2000 23:30:00
70	72.7	8.4	31-Dec-2000 23:00:00
200	62.0	-2.2	01-Jan-2001 14:40:00
250	89.9	-6.6	01-Jan-2001 16:20:00
300	83.3	5.6	01-Jan-2001 17:20:00
400	71.4	-9.2	01-Jan-2001 06:50:00
500	57.5	21.7	02-Jan-2001 17:50:00
600	36.1	20.9	01-Jan-2001 11:50:00
700	26.5	26.5	01-Jan-2001 10:50:00
770	17.9	6.7	01-Jan-2001 10:50:00

Table 3.3: *Maximum flow speeds, recorded at OL-II on Dec. 31st 2001.*

flow velocity vectors are quite similar at these depths, and the flow can therefore be said to be uniform during this period over this depth range (the flow is near barotropic). A close inspection of the velocity vectors in Figure 3.16, as the flow velocity starts to increase on January 1st, tells us that the flow is towards NNE. As the flow speed continues to increase, the flow direction changes towards NNW, and then it rotates in a clockwise direction. This happens at all depths between 200 and 500 meters of waterdepth. Below 500 meters depth (not shown) the flow is less uniform and also less directionally stable.

Strong near-bed current event at OL-II.

In the time period from November 26 until November 30 in 1999 the largest flow speeds for the entire measurement period at OL-II were recorded at depths 200m, 250m, 300m, 350m and 770 m, as can be seen in Table 3.2. The direction of the flow when maximum speed occurred is ranging from N to NNE. The temperature records from 300 and 770 meters depth, and the velocity vectors from 770 meters depth for this period are shown in Figure 3.17. The temperature 5 meters above the sea bed (770 meters depth) is constant at approximately -0.3^{o}C for some time, and on November 22 it starts increasing. This increase lasts for approximately 75 hours, after which the temperature reaches 3°C. Next, the temperature suddenly drops to 0°C in less than 3 hours. The flow speed increases significantly when the temperature drops, and the direction changes, from SW during the increase, to NE during the subsequent temperature drop.

Such near-bed features, or similar ones, of the flow have been observed at another location on the continental slope outside Mid-Norway (marked HF in Figure 3.2),
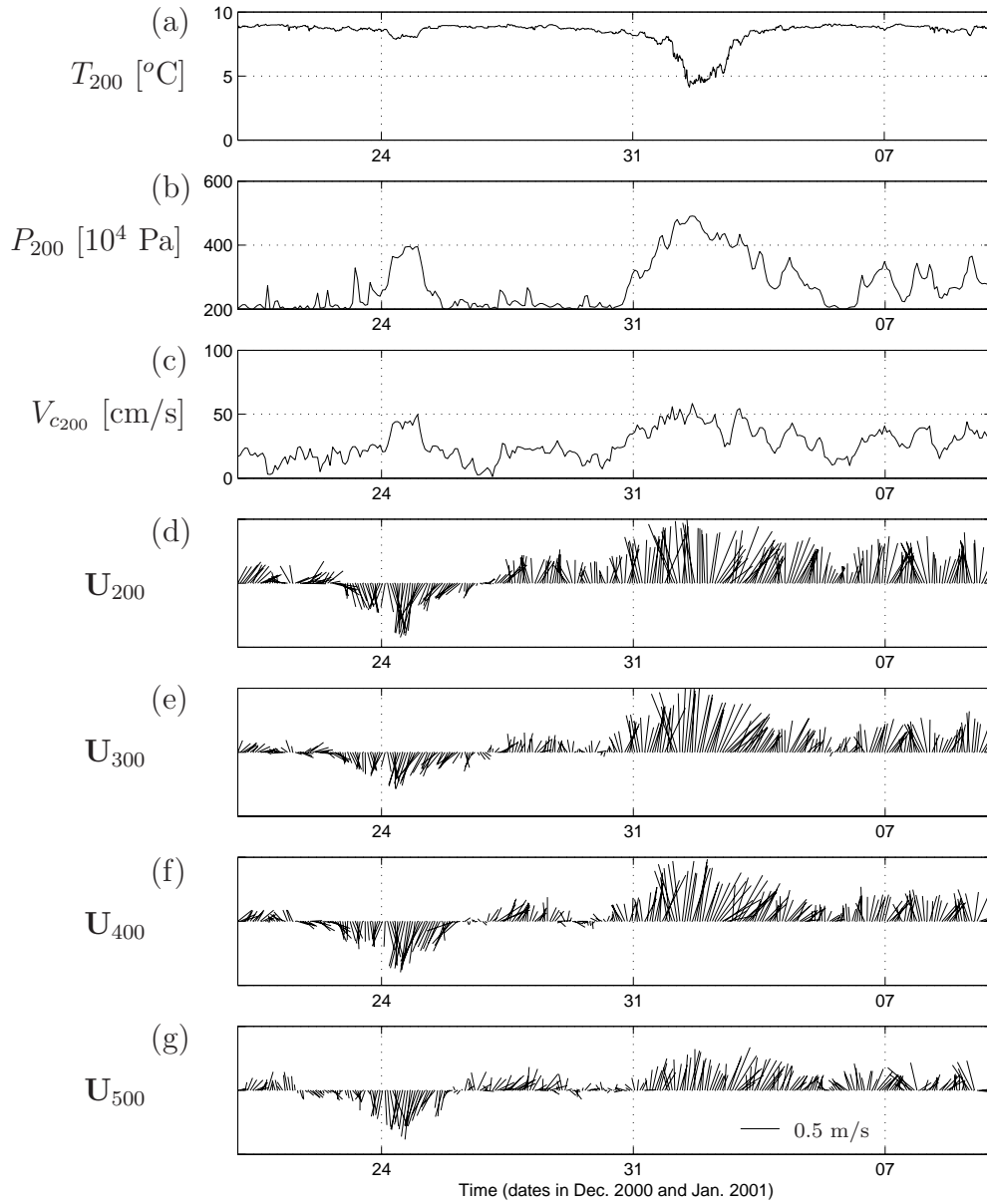
Figure 3.16: *Temperature, pressure and flow speed at 200 meter depth at OL-II during late December 2000 and early January 2001 are plotted in windows (a)-(c). Horizontal velocity vector* **U** *at 200, 300, 400 and 500 meter depth at the same location during the same time period are plotted in plots (d)-(g). The scale of the velocity vectors is shown in window (g).*

and is discussed in more detail in section 3.6.
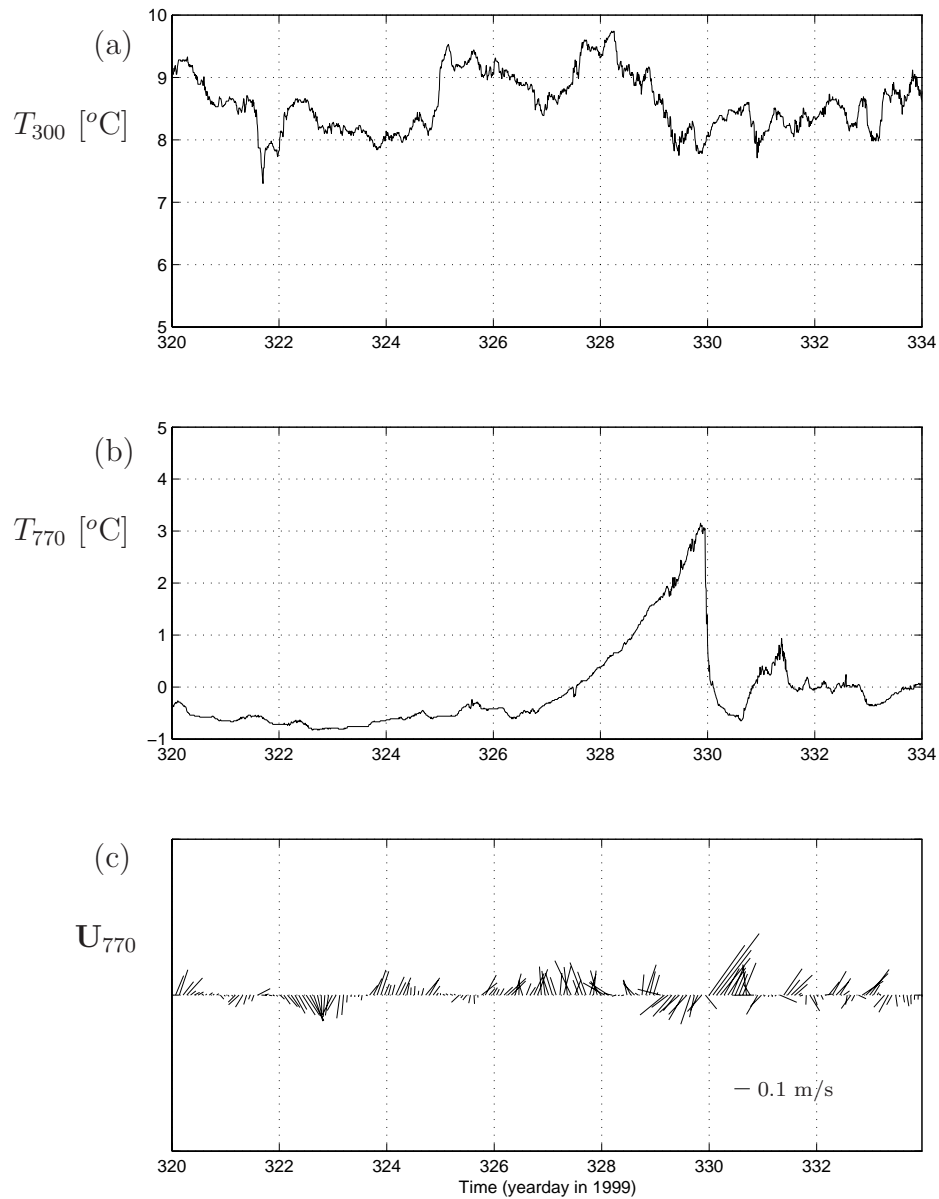
Figure 3.17: *Strong near-bed current event at OL-II. Temperature at 300 and 770 meters depth is plotted in (a) and (b), respectively. Velocity vectors at 770 meters depth is plotted in (c).*

3.6 Near-bed current measurements.

This section contains the main parts of another manuscript (Yttervik and Furnes 2005).

3.6.1 Abstract

Data from field measurements of current velocity and water temperature close to the sea bed on the continental slope west of Norway are presented and discussed. Several strong current flow events were found in the data. These were associated with gradually increasing water temperature and a down-slope flow, followed by a rapid temperature drop and then a strong up-slope flow. The current meters were located close to the interface between the Atlantic inflow to the Norwegian Sea and the Norwegian Sea Arctic Intermediate Water, and it is proposed that the strong current events are linked to the pycnocline between these water masses and its interaction with the continental slope. Downwelling favourable winds, causing steepening of the isopycnals at the slope, are a possible driving mechanism for the strong current events. Hindcast data of wind velocity on the sea surface in the area of the measurements provide some support for this theory.

The sampling frequency for the current meters was 1 Hz. A detailed study of the high frequency structure of the current flow, during an event which captured the transition from down-slope flow to up-slope flow, shows that the up-slope flow starts near the sea bed before it extends further up into the boundary layer. It was also found that the velocity shear can be very strong during this type of events.

Evidence of vortex-induced oscillations of the current meter moorings during strong current events was found in the data.

3.6.2 Introduction.

The current flow on continental slopes, or other sloping boundaries in the ocean, is often highly variable and dominated by strong turbulence. It is therefore important for the energy budget of the global circulation in the world oceans and of great interest for the design and planning of marine structures to be placed or operated in such environments. Huthnance (1995) gives a comprehensive review of physical processes on ocean margins.

Large scale ocean circulation is governed by many factors. Two such factors are wind and bottom topography. Whereas topographic steering of the large scale circulation is a feature of large scale bottom topography, it is also clear that the small scale bottom topography has an effect on the large- and small-scale circulation (Berntsen and Furnes 2002). Likewise, wind is one of the factors driving the large scale global ocean circulation (Sverdrup 1947; Veronis 1973), but it is also responsible for features on smaller scales such as up- and downwelling (Yoshida 1955) and the generation of shelf waves (Adams and Buchwald 1969). A simple analytical model of wind forced displacements of the thermocline at a continental shelf edge was established by Csanady (1973), but numerical models are generally

Station	Measurement position UTM Zone 31, ED-50		Current meter	Height above	Start time	Number of days
	East	North		seabed (m)		
A	626985.41	7032759.60	A1	5	2001-10-18 15:00	81.6
			A2	10	2001-10-18 15:00	75.0
			A3	20	2001-10-18 15:00	67.6
B	627015.02	7032752.04	B1	5	2001-10-18 13:00	79.3
			B2	20	2001-10-18 13:00	70.4
C	626998.35	7032784.94	C1	5	2001-10-18 21:00	81.9
			C2	10	2001-10-18 21:00	74.9
			C3	20	2001-10-18 21:00	21.3
D	626963.26	7032771.02	D1	5	2001-10-18 19:00	81.6
			D2	20	2001-10-18 19:00	81.6

Table 3.4: *Position of the logging stations, layout of the current meters, start time and total duration of data logging at each current meter. All flow velocity data at position C3 after November 9 contain large errors due to a malfunction in the measurement device, hence the short logging time at this position.*

needed close to the shelf break and near the sea bed due to the importance of non-linearities such as e.g. bottom topography and large motions of the thermocline. A dynamic surface wind field at or near the continental margin may, depending upon latitude, wind field properties and shelf area geometry, set up shelf wave oscillations, near-inertial oscillations and long baroclinic wave modes (Gjevik 1991). Numerical simulations by Vikebø, Berntsen, and Furnes (2004) indicate that the current flow near the sea bed on a continental slope is highly influenced by the surface winds.

In this paper we study the possible connection between strong current events near the sea-bed on a continental slope and the wind conditions at the surface. Measurements of current flow and water temperature close to the sea bed on the continental slope west of Norway (Figure 3.18), are presented and discussed.

3.6.3 Flow measurements.

Data were logged at four stations at a water depth of approximately 680 meters, see Figure 3.18. The logging stations were located on the slope from the continental shelf to the deep ocean in an area where the bottom topography is quite irregular as a result of the Storegga underwater slide which took place some 8000 years ago.

Exact positions for the logging stations, distribution of current meters with depth and details of measurement periods can be found in Table 3.4. The positioning of the current meter moorings was assisted by remote operated vehicles (ROVs), normally used for sub-sea operations related to the offshore oil and gas industry. Smoothed hydrographic profiles, recorded at a nearby section across the shelf slope in February and April of the year 2000, are shown in Figure 3.4. These profiles pro-
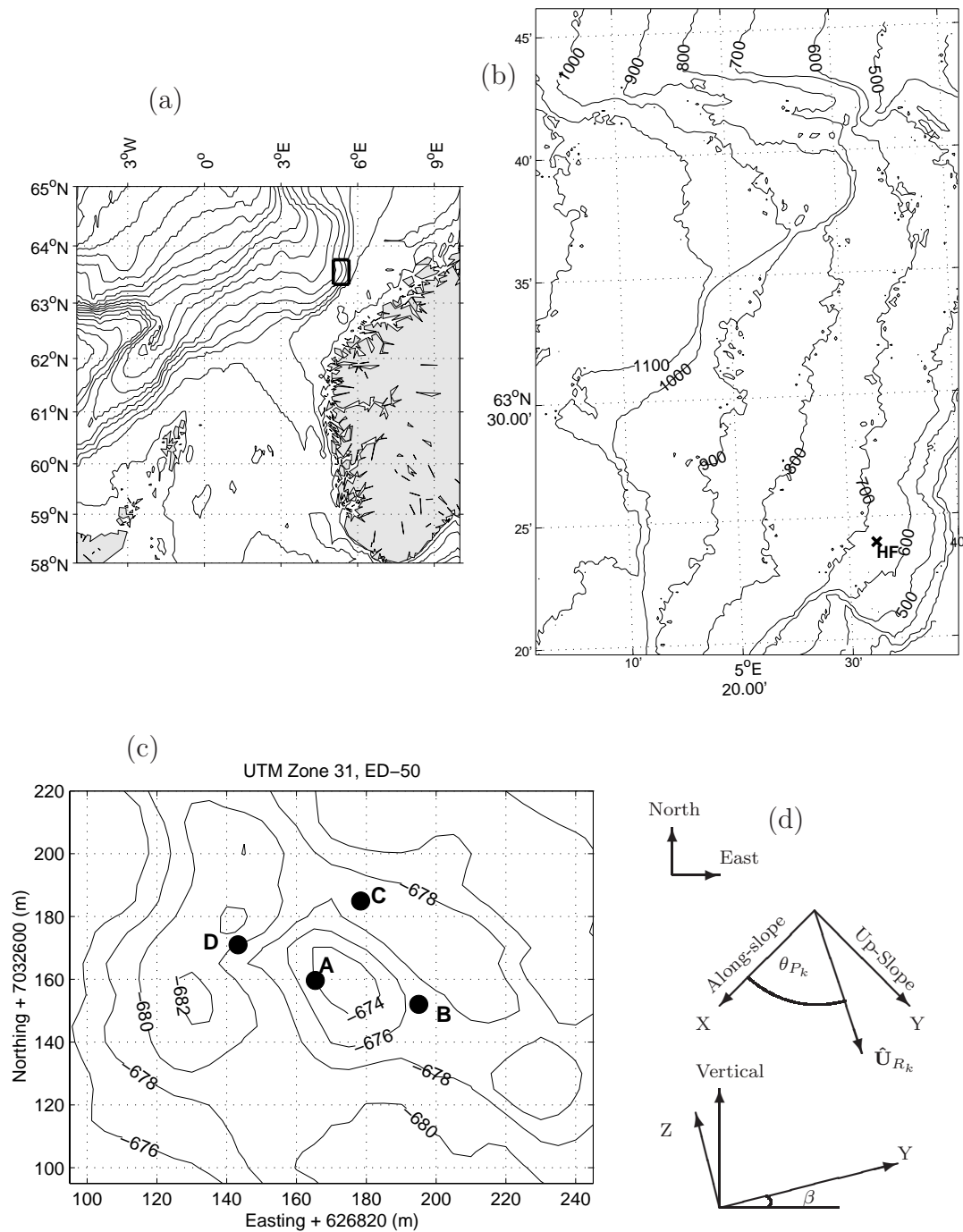
Figure 3.18: *Global location of the Storegga slide area on the continental slope west of Norway is shown in picture (a). The depth contours in (a) start at 100 meters depth and continue to 3700 meters depth in intervals of 200. More detailed bottom topography near the current measurement site is shown in picture (b), local topography and distribution of current meter moorings at the site are seen in picture (c) and the coordinate system used for reporting current data is drawn in picture (d). The measurement site is located at the location labeled 'HF' in picture (b).*

vide a conceptual view of the stratification in the area. The vertical stratification below 200 meters exhibits a two-layer structure with a deep pycnocline at a depth of about 500 meters. The thin surface layer is water of coastal/shelf origin. Below this is the Atlantic inflow to the Norwegian Sea (the Norwegian Atlantic Current). Its lower interface is located at a depth of between (roughly) 400 and 700 meters. The water mass in the layer below the Atlantic water is the Norwegian Sea Arctic Intermediate Water. See Hansen and Østerhus (2000) and Orvik and Niiler (2002), and references therein, for a review of water masses and currents in the Nordic Seas.

A set of Nortek Aquadopp current meters were used for logging time, flow velocity components, pressure and temperature. These current meters use Doppler technology in order to determine the current velocity in three orthogonal directions (zonal, meridional and vertical). The current meters were mounted on moorings as shown in Figure 3.19. The motions of the moorings are small (1.5 m maximum horizontal displacement of upper buoyancy element and a downdraught of 0.05 m), but there is evidence that the mooring systems sometimes oscillate as a result of vortex shedding from the buoyancy elements. Eigenvalue and spectral analysis indicate that the mooring systems oscillate at a frequency of 0.06 Hz. A more detailed exposition of current meter mooring motions can be found in section 3.6.8.

The sampling rate of the current meters was 1 Hz. The accuracy of the current measurements is given as 1% of measured value ± 0.5 cm/s. There is an inherent (white) noise associated with the Doppler measurement technique (Lohrmann 2003). The standard deviation of the noise, σ_n, is about 1.5 cm/s for each beam component. The compasses were not rotated before use, so there is a relatively large (± 10 degrees) uncertainty in measured flow direction. However, this error is not so large as to be a problem when up-slope flow is to be distinguished from down-slope flow. Compass readings were sampled at 1 Hz. The response time of the compass, however, is much shorter than one second, and the compass heading can be logged at a frequency of 32 Hz (Nylund 2003). The response time of the temperature sensors is 10 minutes.

The length of each time-trace is 34.17 minutes (2050 seconds), and the time-traces were recorded once every two hours. Hourly means of the flow velocity components and the temperature were also recorded.

3.6.4   Postprocessing and data analysis.

After retrieving the measurement devices, unphysical data were removed from the data channels by linear interpolation. All values larger than 10 times the RMS value of the time trace were deemed unphysical. For some time instances, data were logged more than once. These double recordings were eliminated by keeping the first occurrence of data logged for a specific time instance in a data channel
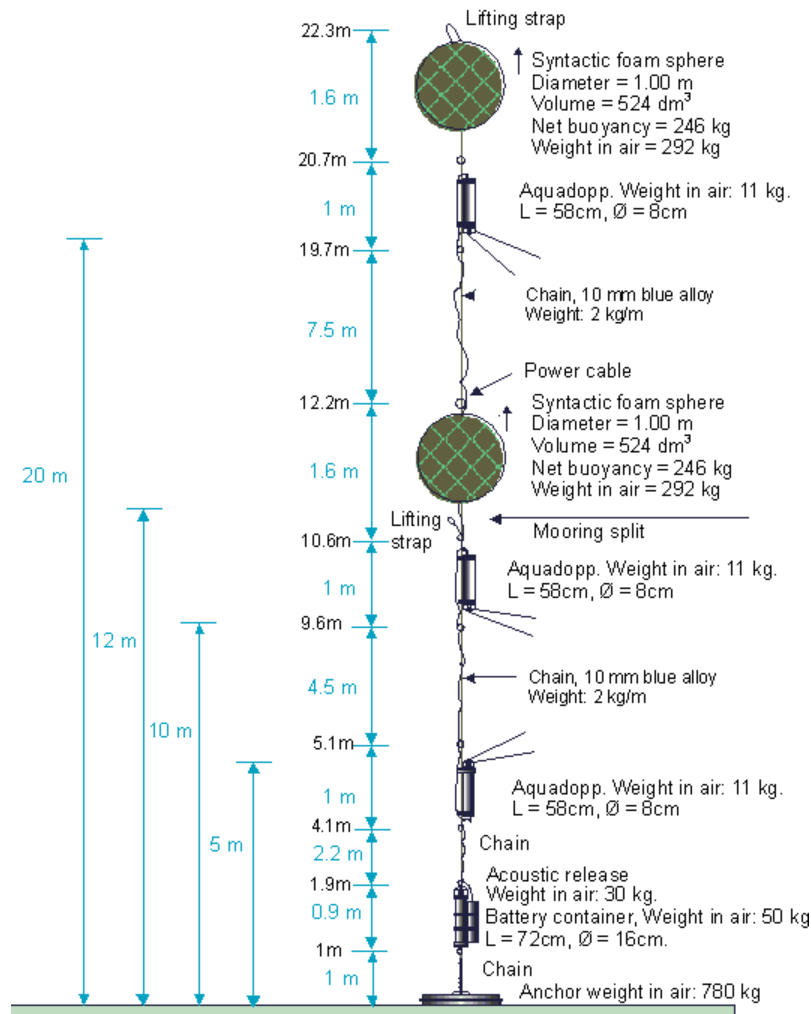
Figure 3.19: *Current meter mooring type I (stations A and C). The moorings at stations B and D (mooring type II) are similar, but they are only equipped with two ADCPs each.*

and removing all the other occurrences. This reduced the length of the time-traces somewhat. In order to be able to work with time-traces of equal length (for processing purposes), we have used only the first 1900 seconds of each time-trace. The data set has been synchronized in time. However, the data from A2 was excluded because it was not possible to synchronize it with the data from the other current meters for more than about 25 minutes. After these procedures we obtained 800 syncronized time traces for the measurement period from October 18 until December 25. In the following, these time-traces are referred to as *the HF time-traces*, and the time period containing the 800 HF time-traces will be referred to as *the entire measurement period*. Each of the HF time-traces contain data logged at a

sampling frequency of 1 Hz over a period of 1900 seconds.

Current flow data have been transformed into a coordinate system (XYZ) which is oriented relative to the large-scale features of the slope on which the measurement devices were moored. We define the up- and down-slope directions on a relatively large scale (~ 10000 meters, Figure 3.18 a) at the measurement site as shown in Figure 3.18 d. The up-slope direction is at an azimuth angle of approximately 120°. The average slope angle, β, in the vicinity of the measurement site is estimated to be 3°.

The velocity vector which is parallel with the sea floor at time instance i, in HF time-trace no. k, can be seen as a vector,

$$\hat{\mathbf{U}}_{P_{i,k}} = \left[\hat{U}_{i,k}, \hat{V}_{i,k}\right] \quad , \quad i = 1, \cdots, N \quad , \quad k = 1, \cdots, 800 \tag{3.34}$$

where $\hat{U}$ and $\hat{V}$ are the velocity components in the X- and Y-direction, respectively, and $N = 1900$. Mean temperature and mean- and maximum flow speed parallel with the sea floor on HF time-trace no. k are calculated according to

$$T_k = \frac{1}{N} \sum_{i=1}^{N} \hat{T}_{i,k} \quad , \quad k = 1, \cdots, 800 \tag{3.35}$$

$$V_{P_k} = \frac{1}{N} \sum_{i=1}^{N} \sqrt{\hat{U}_{i,k}^2 + \hat{V}_{i,k}^2} \quad , \quad k = 1, \cdots, 800 \tag{3.36}$$

$$V_{MAX_k} = \max_{i=1,\cdots,N} \left(\sqrt{\hat{U}_{i,k}^2 + \hat{V}_{i,k}^2} \right) \quad , \quad k = 1, \cdots, 800 \tag{3.37}$$

where $\hat{T}_{i,k}$ is temperature at time instance i in HF time-trace no. k. Mean direction of the flow that is parallel with the sea floor, θ_{P_k}, is calculated by constructing a resulting velocity vector

$$\hat{\mathbf{U}}_{R_k} = \sum_{i=1}^{N} \hat{\mathbf{U}}_{P_{i,k}} \quad , \quad k = 1, \cdots, 800 \tag{3.38}$$

and then calculating the angle between this vector and the x-axis (see Figure 3.18 d). A mean parallel velocity vector, $\mathbf{V}_{P_k}$, is defined by this angle and the magnitude of V_{P_k}.

Root-mean square (RMS) of the fluctuating velocity is calculated as

$$V_{RMS_k} = \sqrt{\sigma_{u_k}^2 + \sigma_{v_k}^2 + \sigma_{w_k}^2 - 3\sigma_n^2} \quad , \quad k = 1, \cdots, 800 \tag{3.39}$$

where σ_{u_k}, σ_{v_k} and σ_{w_k} are the standard deviations of the X-, Y- and Z-components of the flow velocity, respectively.

3.6.5 Global properties of the flow.

After synchronizing the data, time-traces of statistical parameters for each station were constructed. By calculating V_{P_k} for all the 800 HF time-traces available for one position ($k = 1, \cdots, 800$) we obtain a time-trace of V_P for that position. This procedure was also carried out for V_{RMS}, θ_P, T and V_{MAX}. 'Global' time-traces of these parameters were thus obtained.

Hindcast data of wind and atmospheric pressure at the sea surface for position 63.1N, 5.4E, for the entire measurement period, have been provided by the Norwegian Meteorological Institute.

Mean flow, maximum flow speed and water temperature fluctuations at current meter B2, together with hindcast wind vectors at the sea surface, are plotted in Figure 3.20. From the record of mean water temperature at B2 it is clearly seen that the temperature fluctuations are larger during some periods than they are during other periods. For instance, the mean temperature is nearly constant from approximately day 350 until the end of the measurement period whereas large oscillations can be seen between day 327 and day 342. Notice the gentle rise, followed by a sudden drop, in water temperature at some of the temperature peaks in Figure 3.20. This has also been seen in earlier measurements in this area (Vikebø, Berntsen, and Furnes 2004).

Spectra of the hourly mean flow components for station B are shown in Figure 3.21. The inertial period, which is 13.4 hours at this location, is very close to the M_2 tidal period. It seems, though, that the peaks in the spectra are at the M_2-frequency. The spectra also suggest that the cross-slope component is more energetic than the along-slope component for the current meters farthest from the bottom, indicating that the major axis of the tidal ellipse is oriented in an upslope/downslope direction higher up in the boundary layer. Deeper inside the boundary layer, however, the current is equally energetic in the along-slope and cross-slope directions, thus indicating a circular motion. This is in good agreement with results reported by Davies and Furnes (1980).

3.6.6 Current flow events.

Some peaks in the time-traces of V_P, V_{MAX} and T are particularly large (Figure 3.20). We define an 'event' to be represented by such a peak and the corresponding HF time-trace.

We have selected four events for closer study in this paper. The time of occurrence, and the values of θ_P, V_P, V_{RMS}, V_{MAX} and T, for the events are listed in Table 3.5.
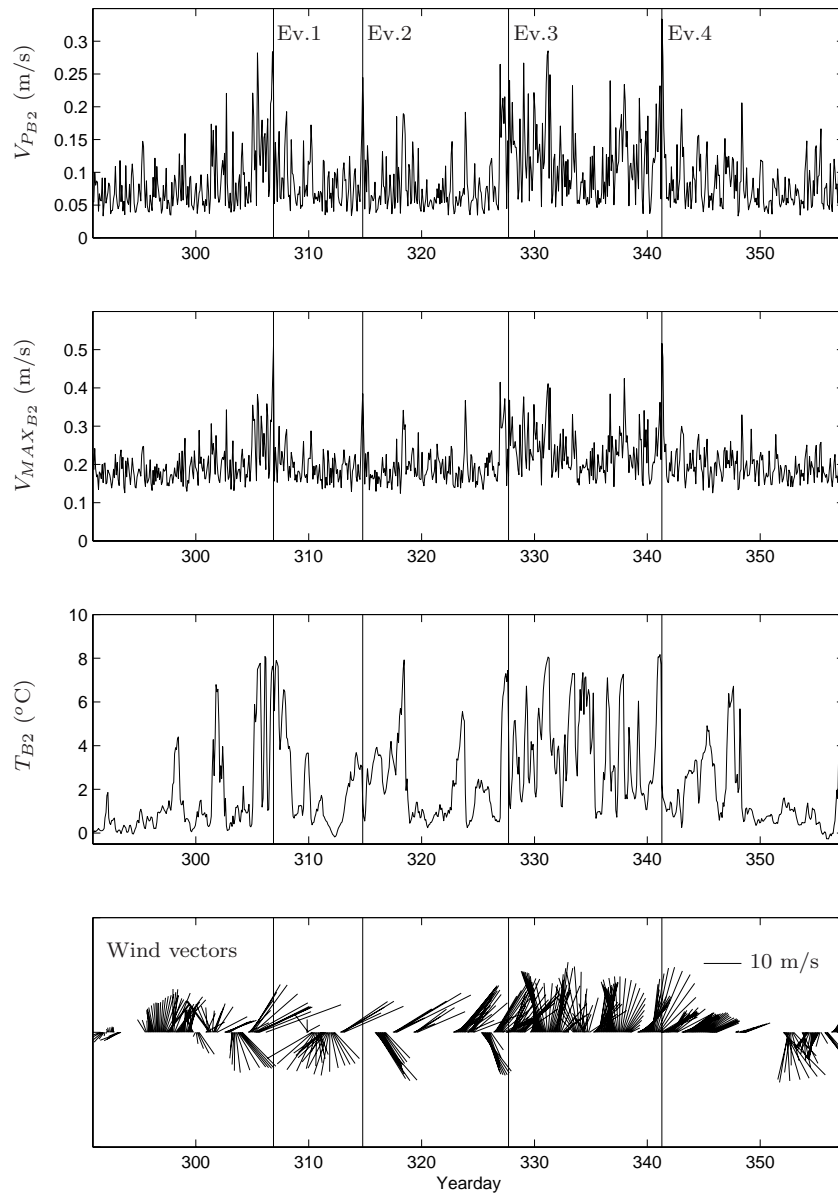
Figure 3.20: *Plots of V_P, V_{MAX} and T at position B2 for the entire measurement period. The data at the other current meters are similar. Four current 'events' are marked with vertical lines. Hindcast wind vectors at the sea surface are also shown. Wind vectors pointing upwards represent wind towards North. For clarity, only up- and downwelling favourable wind directions have been plotted.*

Wind-induced deep currents.

Strong temperature oscillations near the sea bed at approximately 680 meters depth are shown in Figure 3.20. This is close to where we would expect to find the
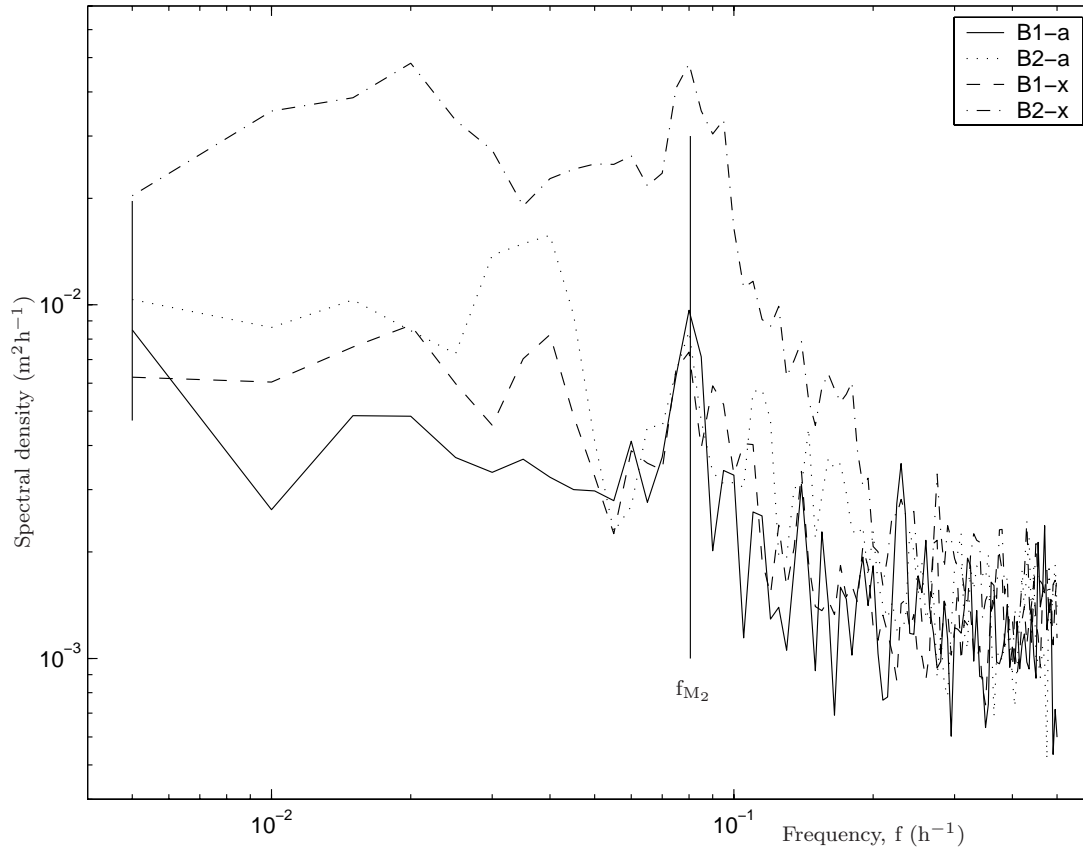
Figure 3.21: *Power spectra of cross-slope ('x') and along-slope ('a') components of the hourly mean current velocity at the current meters at station B. Positions B1 and B2 are located 5 and 20 meters above the sea bed, respectively. The 95% confidence interval is given by a vertical bar on the left. The M_2-frequency, f_{M_2}, is indicated by a vertical line.*

deep pycnocline (see Figure 3.4). Csanady et al. (1988) found that the near-bed currents were much more energetic than those farther away from the bottom in the area where the pycnocline and the continental slope outside the east coast of North America intersect, thus indicating enhanced internal wave activity at that location. It seems plausible that the temperature variations and current events in our data are also directly related to up- and down-slope motion of the pycnocline. All selected events take place in connection with such pycnocline motions.

The physical mechanisms causing one particular event need not be the same as those causing other events. Due to the large variability during some periods, it is difficult to identify the exact mechanism(s) which cause the events within these periods, but there is some indication that some of them can be linked to the wind

Event no. and Time of occurrence			A1	A3	B1	B2	C1	C2	C3	D1	D2
1											
03-Nov-2001 21:00	θ_P	(deg.)	190	221	139	222	204	206	215	188	207
	V_P	(m/s)	0.22	0.25	0.17	0.23	0.17	0.18	0.24	0.15	0.17
	V_{RMS}	(m/s)	0.20	0.16	0.14	0.19	0.17	0.16	0.17	0.15	0.18
	V_{MAX}	(m/s)	0.47	0.49	0.40	0.51	0.41	0.40	0.49	0.38	0.42
	T	(°C)	6.9	8.5	6.9	7.4	7.4	7.1	8.1	7.3	8.0
2											
11-Nov-2001 19:00	θ_P	(deg.)	100	120	145	107	110	131	n.a	169	109
	V_P	(m/s)	0.24	0.21	0.09	0.24	0.17	0.16	n.a	0.15	0.07
	V_{RMS}	(m/s)	0.06	0.05	0.09	0.07	0.08	0.08	n.a	0.07	0.07
	V_{MAX}	(m/s)	0.38	0.31	0.28	0.39	0.36	0.31	n.a	0.34	0.33
	T	(°C)	1.0	2.5	1.0	1.4	1.6	1.2	n.a	1.7	2.1
3											
24-Nov-2001 21:00	θ_P	(deg.)	66	257	46	184	75	100	n.a	87	96
	V_P	(m/s)	0.15	0.15	0.17	0.07	0.17	0.18	n.a	0.12	0.06
	V_{RMS}	(m/s)	0.06	0.05	0.06	0.05	0.05	0.05	n.a	0.08	0.06
	V_{MAX}	(m/s)	0.26	0.25	0.30	0.17	0.29	0.27	n.a	0.29	0.16
	T	(°C)	2.9	8.6	2.3	4.7	2.7	2.4	n.a	2.9	5.1
4											
08-Dec-2001 07:00	θ_P	(deg.)	75	94	69	82	78	84	n.a	60	81
	V_P	(m/s)	0.38	0.35	0.10	0.33	0.32	0.31	n.a	0.12	0.37
	V_{RMS}	(m/s)	0.11	0.11	0.09	0.12	0.09	0.11	n.a	0.12	0.11
	V_{MAX}	(m/s)	0.54	0.51	0.30	0.52	0.50	0.51	n.a	0.35	0.56
	T	(°C)	1.5	4.2	1.3	2.2	1.8	1.5	3.1	1.9	2.9

Table 3.5: *Global parameters of the flow for the selected events.*

conditions on the surface. Wind vectors with azimuth angles in a sector from approximately −45º to 70º are downwelling favourable in the area where the current measurements are carried out. Such winds have a significant component which is parallel with the isobaths, with shallow water to the right, in the area surrounding the current meters when a length scale in the order of magnitude of tens of kilometers (see Figure 3.18 a) is considered. The direction of the isobaths in this area changes from SW-NE to SE-NW, and the sector in which winds are downwelling favourable therefore gets quite large. Consequently, wind vectors with azimuth angles in the sector from approximately 135º to 250º are upwelling favourable in the area. The boundary constraint necessary for such winds to be down- and upwelling favourable, respectively, is provided by the continental shelf edge. Hindcast wind vectors at the sea surface are plotted in Figure 3.20.

The link between surface winds and up- and down-slope motion of the deep pycnocline is illustrated in Figure 3.22. Downwelling favourable winds set up an on-shore Ekman transport near the surface, causing a surface elevation near the coast/shelf edge and, thus, a cross-slope pressure gradient. This pressure gradient sets up a geostrophic current in the interior of the ocean which adds to the Norwegian Atlantic Current, causing an increase in the along slope current in the interior just outside the shelf edge. The combined effect of down slope Ekman transport near the sea bed, caused by this strengthened current, and the downwelling, caused by

the on-shore transport of water near the surface, advects warm water down-slope and causes the temperature at the current meters to increase. As a consequence of the downwelling, the vertical stratification is reduced and, due to enhanced mixing, the boundary layer grows thicker. The steepening of the isopycnals, as seen in Figure 3.22, causes the cross-slope density gradient to increase and potential energy to accumulate as the pycnocline is depressed. The cross-slope density gradient has its maximum at the slope and decreases as the distance from the slope increases. Now there are two different possibilities for the further development, both of which could lead to bursts of cold water up-slope. Firstly, if the direction of the wind changes so that it is no longer downwelling favourable, or if the wind speed is significantly reduced, there would be a reduction in the down slope flow in the bottom boundary layer. The cross-slope density gradient would no longer be restrained and the accumulated potential energy could possibly be released as a burst of cold water up-slope. Secondly, one could conjecture that if the increase in the cross-slope density gradient continued to a point where it could no longer be restrained, either due to tidal forcing or simply by the high pressure caused by the depression of the pycnocline at the slope, the accumulated potential energy in the depressed pycnocline could release an up-slope burst of cold water. Contrary to what happens during downwelling, the stratification is strengthened and the boundary layer is thinner during traditional upwelling, vertical mixing is minimal, and the flow in the ocean interior can be considered to be decoupled from that in the boundary layer. However, the strong current events that are considered in this paper develop over such a short time that they cannot be explained as traditional upwelling.

Four events are described in the following. The first three can possibly be explained by a change from downwelling- to non-downwelling favourable wind at the surface (i.e. the first mechanism). The fourth event is possibly caused by the second mechanism.

Event 1, 03-Nov-2001, 21:00.

On the HF time-traces from November 3, 2001, at nine o'clock in the evening (day 306.9), maximum values for V_{RMS} were reached for the entire measurement period at all current meters.

Stick-plots of the flow parallel with the sea bed, in the time period between 400 and 900 seconds, for event 1 are shown in Figure 3.23. To begin with, the flow has a down-slope component at all current meters except the one at B1. Here the flow is more in an along-slope direction. This is possibly due to stagnation since B1 is close to the sea bed just up-slope of a small hill (see Figure 3.18 c). After approximately 500 seconds, the water at D1 (5 meters above the sea bed and farthest down-slope of all the current meters) stops its down-slope motion

and starts flowing with an along-slope component for a short while ($\sim$ 1 minute) before it starts flowing up-slope. The turning direction is clockwise, possibly due to topographic effects. The down-slope flow at D2 (15 meters above D1) also stops and turns into an up-slope flow, but the change in flow direction at D2 lags that at D1. Thus, for about 30 seconds, the flow at D2 has a clear down-slope component while the water at D1 is already flowing up-slope. This is evidence of strong velocity shear and possibly unstable conditions and enhanced mixing. The same thing happens at stations A and B. Station A is situated up-slope of station D. The fact that the change in flow direction at A1 lags that at D1 can therefore be interpreted as evidence of a front moving up-slope from the northwest.

What appear to be high-frequency oscillations in the flow direction can be seen at B2 and to some extent at A3 between 500 and 750 seconds, while the major flow direction is clearly down-slope. These oscillations are most likely related to oscillations of the mooring system rather than to some oscillating feature of the flow. A broader discussion of this is provided in section 3.6.8.

Surface wind vectors, mean paralell velocity vectors and temperature variations at B2 during the period in which event 1 took place are shown in Figure 3.24. The surface wind is upwelling favourable during day 303 and most of the first half of day 304, then the wind changes its direction and becomes downwelling favourable until the event occurs. Notice the flow oscillations during the period of upwelling favourable wind conditions. It is difficult to identify the exact period of these oscillations, but we estimate 12-14 hours. The spectrum of mean flow components
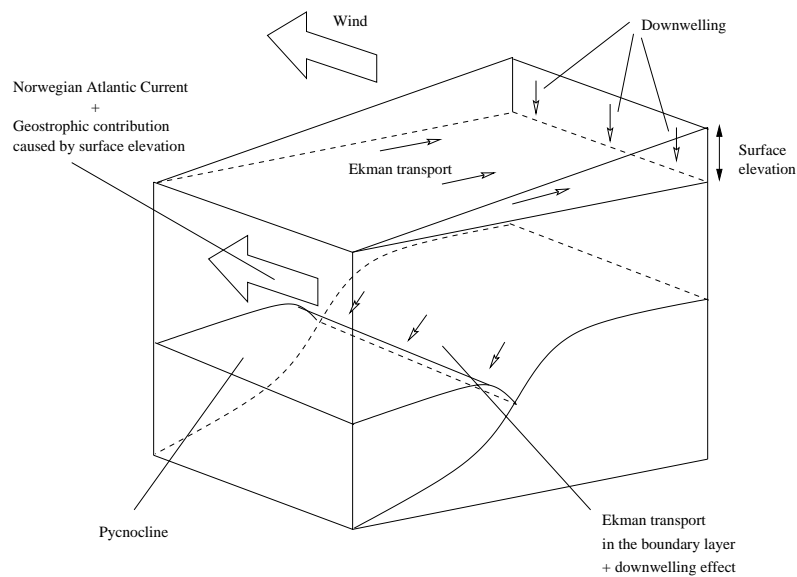

Figure 3.22: *Illustration of the link between surface winds and pycnocline motion.*
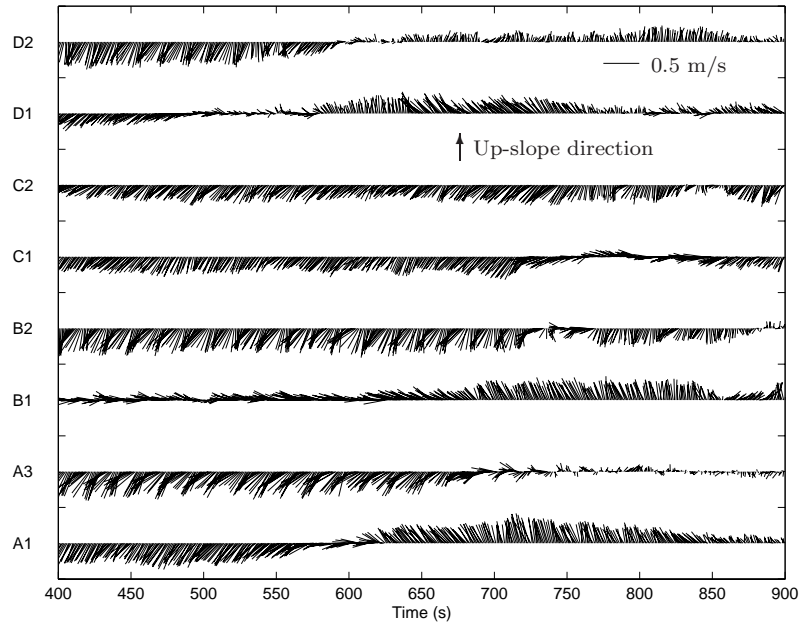
Figure 3.23: *Stick-plot of the flow parallel with the sea bed during event 1. Sticks are drawn relative to the slope-oriented coordinate system.*

(Figure 3.21) has a peak at the M_2-frequency. A close relationship between the pressure at B2, which oscillates at the M_2-frequency, and the oscillations in the flow at B2 from day 303 until day 306 was found, but is not shown here. There was a full moon on day 304. Usually the spring tide occurs a couple of days later, and it is therefore likely that the increasing amplitude of the oscillations, indicated in Figure 3.24, is due to the tidal forcing. Upon studying the temperature record for current meter B2 during the same period, we find that the temperature level is almost constant at 0-2°C during upwelling favourable conditions, indicating that the current meter is below the pycnocline at this time. Some time after the wind has turned to become downwelling favourable, the temperature starts increasing as the pycnocline intersection is pushed down-slope. From day 305 until day 307 we can see the M_2-frequency in the temperature records, first as a slight oscillation between day 305 and 305.5, but then as large oscillations from day 305.5. These oscillations are large because the pycnocline is present at the instruments (brought there by downwelling favourable winds) and the temperature gradient is strong. The mean flow is for the most part down-slope during temperature increase and up-slope when the temperature decreases. The wind ceases to be downwelling favourable sometime during day 306, and soon afterwards event 1 occurs.

Figure 3.24: *Surface wind vectors, water temperature and mean parallel velocity vectors at B2 in the period prior and subsequent to event 1. The time of the event is indicated by a vertical line in each plot. Wind vectors pointing upwards represent wind towards North. Current vectors $\mathbf{V}_{P_{B2}}$ are plotted relative to the slope-oriented coordinate system, and the up-slope direction is indicated in the figure.*

Event 2, 11-Nov-2001, 19:00.

Surface wind vectors, mean parallel velocity vectors and temperature variations at B2 during the period in which event 2 took place are shown in Figure 3.25. The

surface winds are clearly upwelling favourable until mid-day on day 312, when they change to become downwelling favourable. They stay like this for most of day 313, but at the start of day 314 the winds are neither up- nor downwelling favourable and soon afterwards event 2 occurs. The temperature and flow velocity plots in Figure 3.25 show periods of up- and downwelling in correspondence with surface wind direction.

Event 3, 24-Nov-2001, 21:00.

On the HF time-traces from November 24th, at nine o'clock in the evening, the largest cross-slope vertical velocity shear, $\frac{\partial \hat{V}}{\partial z}$, for the entire measurement period was recorded at station A. Cross-slope flow and vertical shear in the cross slope flow at station A during this event are shown in Figure 3.26. The cross-slope flow is up-slope at A1 and down-slope at A3 for the entire HF time-trace, and the shear is consequently very strong.

Surface wind vectors, mean parallel velocity vectors and temperature variations at B2 during the period in which the event took place are shown in Figure 3.27. It is seen that the wind changes from being upwelling favourable for the last part of day 325 and the beginning of day 326, to becoming downwelling favourable approximately one and a half days prior to event 3. During the period of downwelling favourable wind, warm water flows down-slope at all current meters shown. The temperature increases to about 7ºC at A1, B2, C2 and D2, which are all located at about the same depth, before it drops rapidly as colder water washes up-slope. The wind reduces in strength and becomes less downwelling favourable just prior to event 3.

Event 4, 08-Dec-2001, 07:00.

On the HF time-traces from December 8th, at seven o'clock in the morning (day 341.3), the largest velocity for the entire measurement period was recorded at current meters A1, B2, C1, C2 and D2. As can be seen in Figure 3.20, the temperature at current meter B2 has been oscillating quite violently for approximately two weeks prior to the event.

Surface wind vectors, mean parallel velocity vectors and temperature variations at B2 during the period in which event 4 took place are shown in Figure 3.28. An increase in the temperature during the hours preceeding the event is clearly seen. The temperature suddenly drops and shortly thereafter the flow speed increases significantly. The mean direction of the flow during event 4 is towards South-East (i.e. up-slope). During the build-up of the temperature, however, the flow direction is generally down-slope. Flow speeds are largest during the up-slope flow of cold water. Two large temperature fluctuations can be seen in Figure 3.28. They are
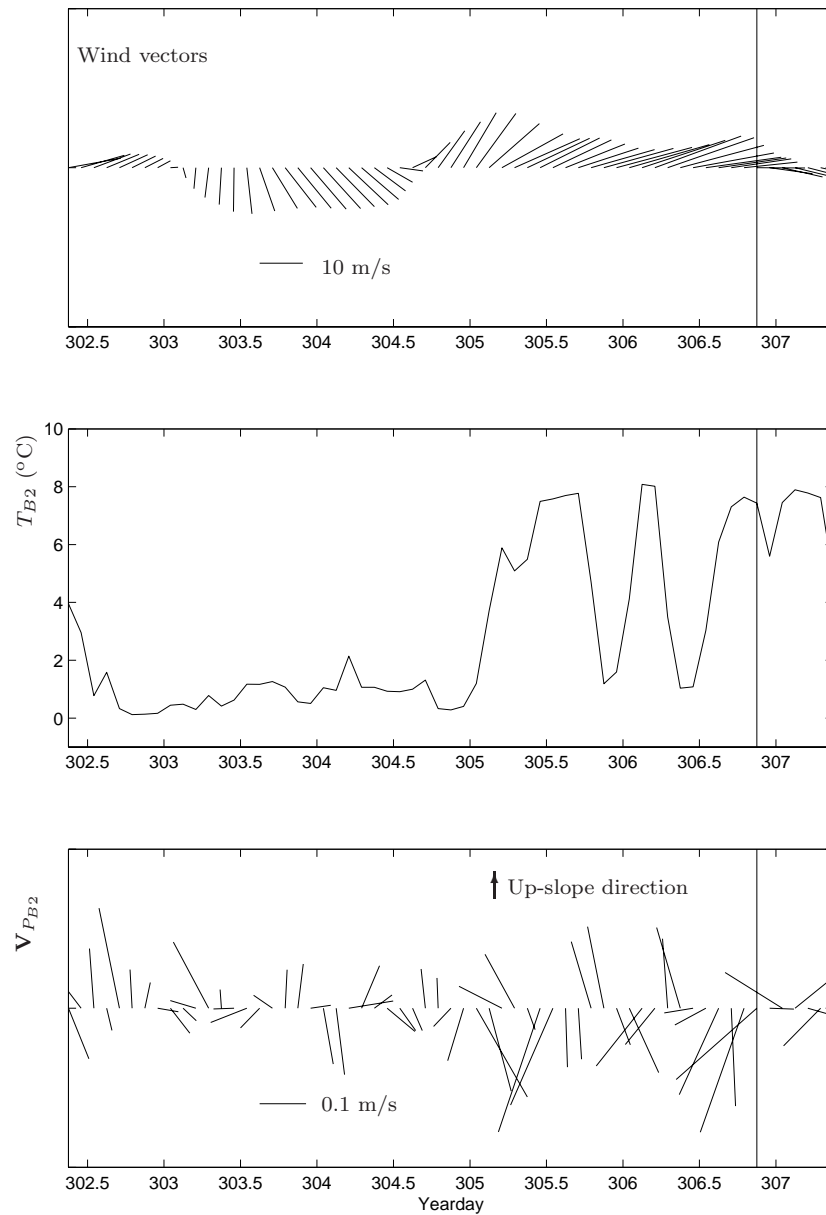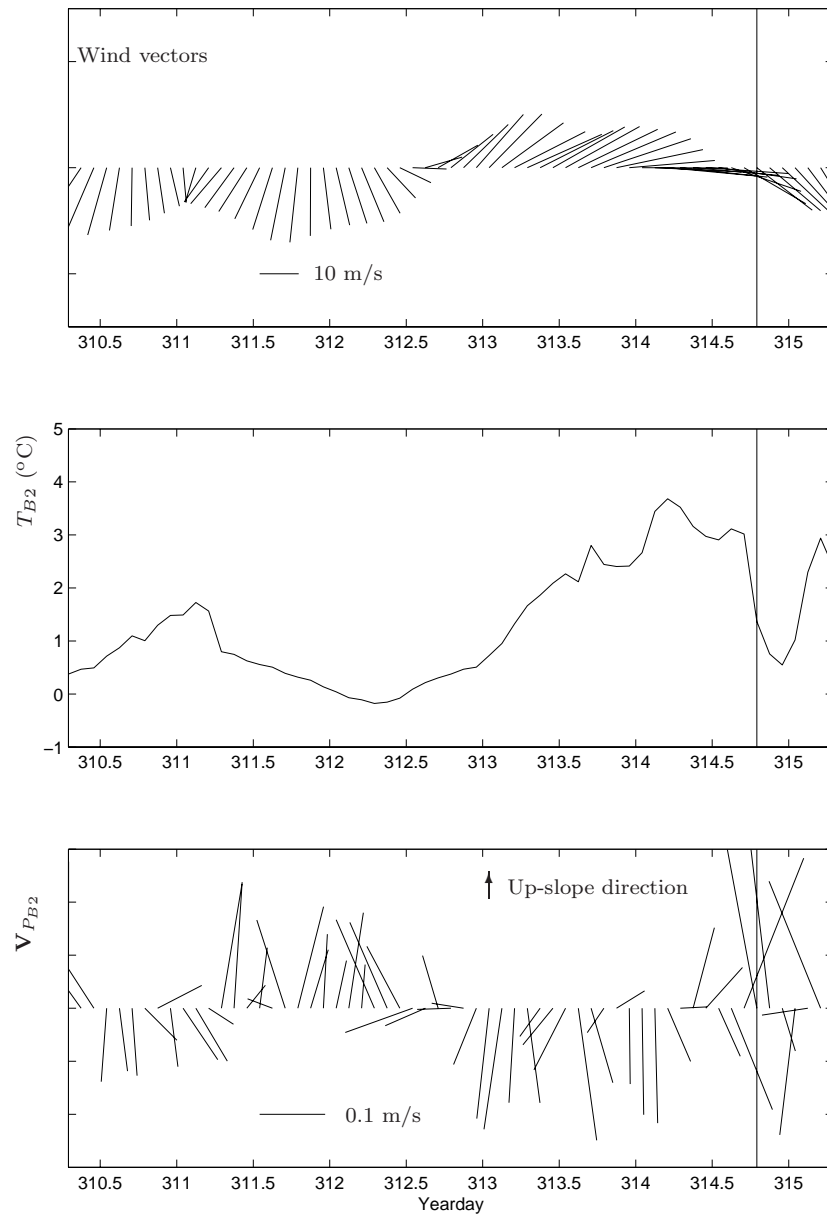
Figure 3.25: *Surface wind vectors, water temperature and mean parallel velocity vectors at B2 in the period prior and subsequent to event 2. The time of the event is indicated by a vertical line in each plot. Wind vectors pointing upwards represent wind towards North. Current vectors $\mathbf{V}_{P_{B2}}$ are plotted relative to the slope-oriented coordinate system, and the up-slope direction is indicated in the figure.*

both characterized by slow temperature build-up as warm water flows down-slope, accompanied by a rapid temperature drop as cold water flows up-slope. The first of these is at the last part of day 337 and the second is at the start of day 341. The
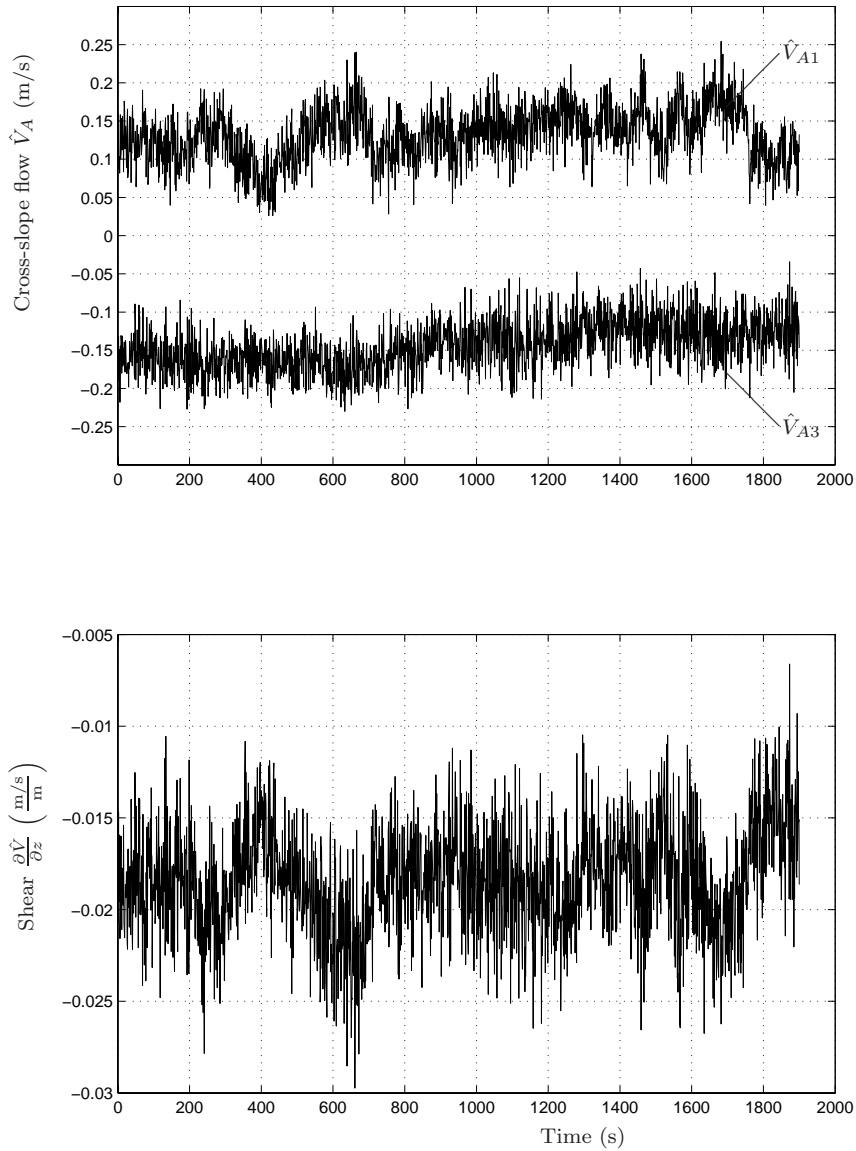
Figure 3.26: *Cross-slope flow, $\hat{V}$, and velocity shear, $\frac{\partial \hat{V}}{\partial z}$, at station A during event 3. Positions A1 and A3 are located 5 and 20 meters above the sea bed, respectively.*

wind is clearly downwelling favourable during the first temperature fluctuation. The wind then decreases significantly for a while before it, approximately one day prior to the start of the second temperature increase, increases in strength and blows in a downwelling favourable direction. From Figure 3.20 it can be seen that the wind is more or less downwelling favourable during the entire time period between events 3 and 4. There is a quite high variability in the flow and temperature during this period, possibly due to repeated strengthening of the
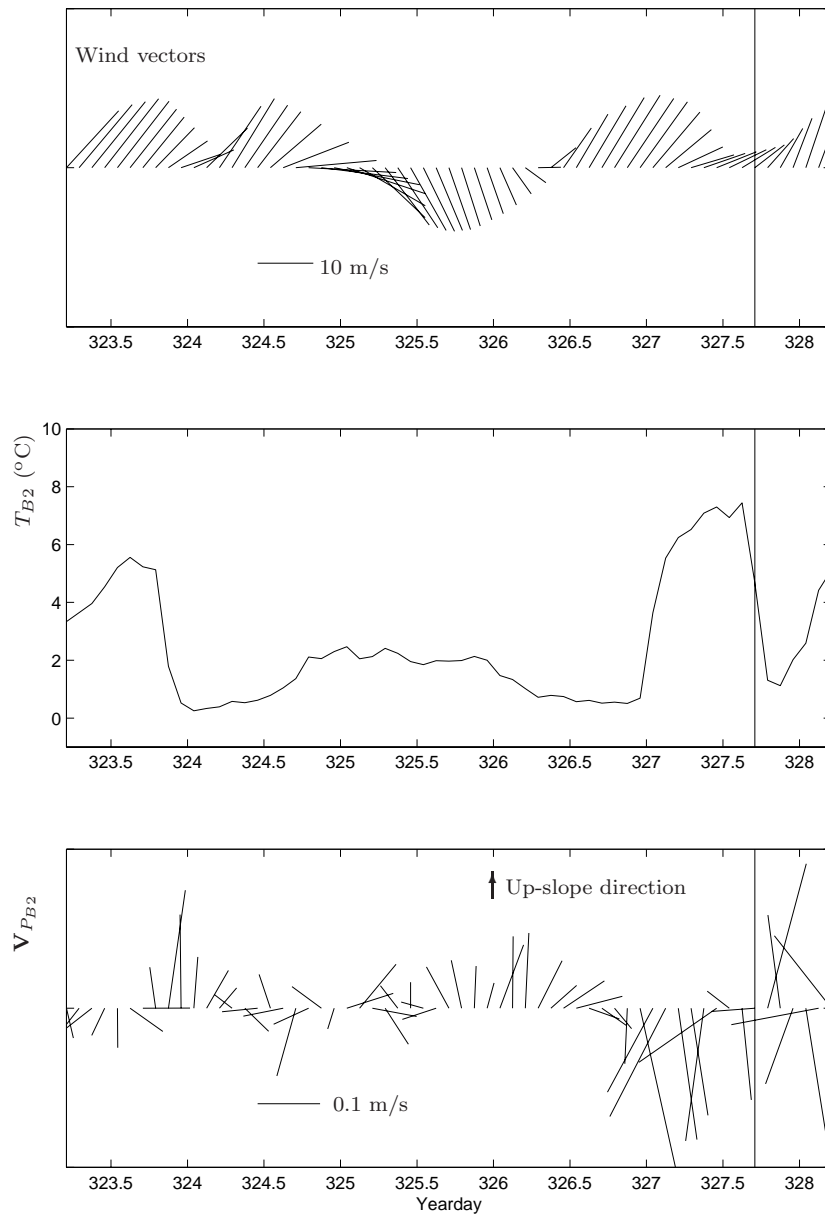
Figure 3.27: *Surface wind vectors, water temperature and mean parallel velocity vectors at B2 in the period prior and subsequent to event 3. The time of the event is indicated by a vertical line in each plot. Wind vectors pointing upwards represent wind towards North. Current vectors $\mathbf{V}_{P_{B2}}$ are plotted relative to the slope-oriented coordinate system, and the up-slope direction is indicated in the figure.*

cross-slope density gradient followed by a release of accumulated potential energy.
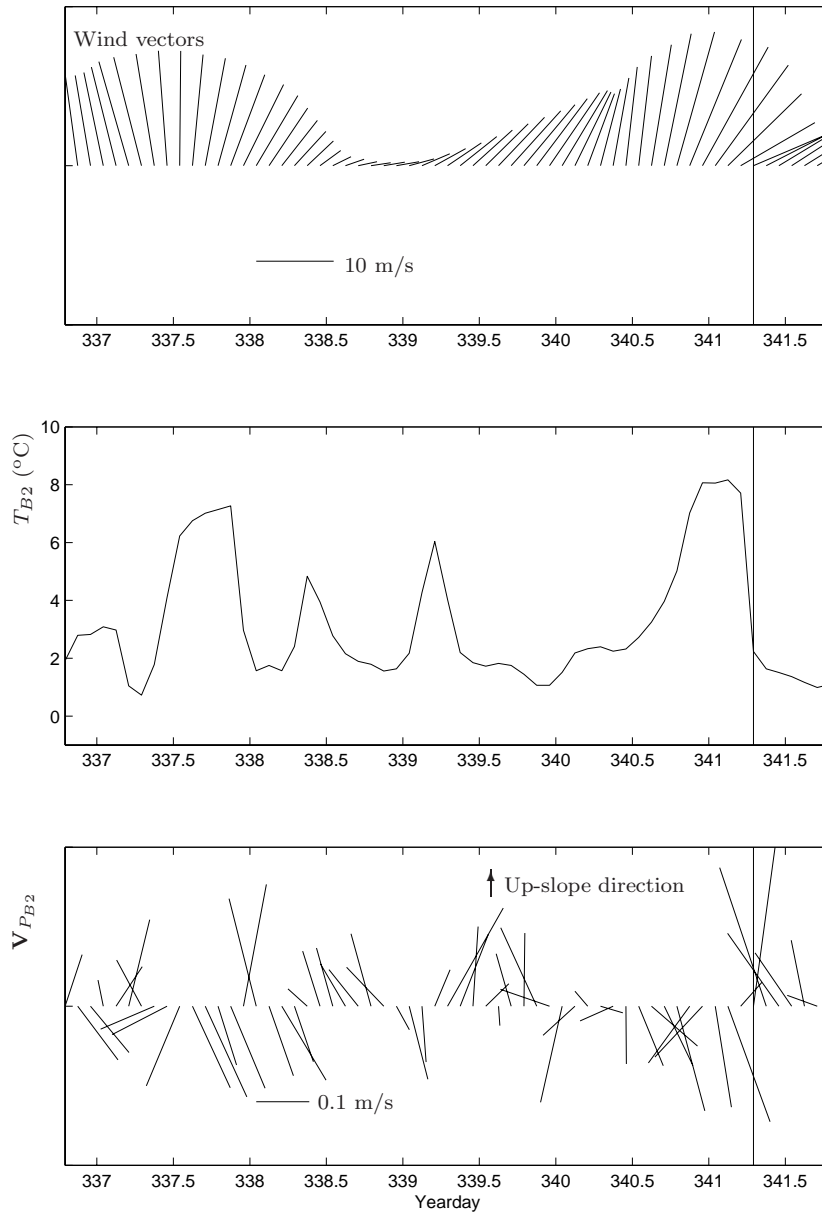
Figure 3.28: *Surface wind vectors, water temperature and mean parallel velocity vectors at B2 in the period prior and subsequent to event 4. The time of the event is indicated by a vertical line in each plot. Wind vectors pointing upwards represent wind towards North. Current vectors $\mathbf{V}_{P_{B2}}$ are plotted relative to the slope-oriented coordinate system, and the up-slope direction is indicated in the figure.*

3.6.7 Summary and conclusion.

Results from measurements of current flow and water temperature in the benthic boundary layer on the continental slope west of Norway, in an area with rough

bottom topography and a deep pycnocline, have been presented and discussed.

The measured data suggest that the fluid flow activity at the measurement site undergoes periods of great variability accompanied by periods of little variability. These periods do not necessarily have the same duration, and there is no evidence that they occur regularly.

Four strong current events are described in the paper. These events are associated with warm water flowing down-slope just prior to a strong up-slope burst of cold water. The physical mechanism, believed to be responsible for some of the events, is well illustrated in Figures 3.24, 3.25 and 3.27. The water temperature at the measurement site increases, the isopycnals steepens and the cross-slope density gradient increases as warm water flows down-slope during a period of downwelling favourable wind at the surface. When the wind becomes less downwelling favourable, an up-slope burst of cold water is released by the strong cross-slope density gradient. Figure 3.28 shows that strong current events may also occur during periods with persistent downwelling favourable winds. Such events may be caused by an increase in the cross-slope density gradient to a point where it can no longer be restrained, resulting in the release of strong up-slope flow of cold water at the slope.

High variability of the flow in the boundary layer on continental slopes has been observed earlier, see e.g. Thorpe (1987a) and White (1994), and many researchers have investigated the dynamics of the flow in such regions. Intermittent spike-like reductions in current speed and direction on the continental slope of the Faeroe-Shetland Channel were observed by Hosegood and van Haren (2003). They attribute their observations to down-slope Ekman transport resulting in unstable stratification and, thus, turbulence, as described by Trowbridge and Lentz (1991) and Lentz and Trowbridge (1991). The interaction between Ekman fluxes and buoyancy forces in the boundary layer on a slope has also been studied by Mac-Cready and Rhines (1991, 1993). In another study, Gemmrich and van Haren (2001) observed rapid temperature falls associated with large variations in the flow speed and direction close to the bottom on the continental slope in the Bay of Biscay. Thorpe (1992b, Thorpe (1997) discuss strong current events which can occur when internal waves, generated elsewhere, encounter the continental slope. Some of these features occur at a semi-diurnal frequency, and are attributed to (although not in the same way) internal gravity waves interacting with a sloping bottom. The strong current events in our data, however, occur at no specific frequency, and give the impression that they result from some non-stationary stochastic process, some of them possibly driven by the local wind field (which is in itself a realisation of a non-stationary stochastic process). This conjecture finds some support in the numerical study by Vikebø, Berntsen, and Furnes (2004) which indicates that trav-

elling weather systems may have a significant effect on the slope currents, even in the bottom boundary layer at significant depths.

3.6.8   Current meter mooring vibrations

Current meter mooring systems are generally compliant structures, and they can therefore be displaced and put into motion by the current. Current-induced oscillations of current meter mooring systems may occur (Loder and Hamilton 1991; Hamilton et al. 1997), and they may then be wrongly identified as turbulent current flow.

In this section, current-induced displacements and vibrations of the mooring system depicted in Figure 3.19 are discussed.

Displacements of the current meter moorings.

Assuming a current speed of 0.5 m/s (which is a typical value of the maximum current), and using the data given in Figure 3.19, the horizontal displacement of the upper buoyancy element is found to be 1.5 meters horizontally. The corresponding downdraught is 0.05 meters. These movements are quite small. Quadratic drag force coefficients of 0.5 and 0.8 for the buoyancy elements and the other components, respectively, were used in calculating this.

Oscillations of the current meter moorings.

Eigenfrequencies and -modes of the mooring system have been calculated using a non-dimensional added mass coefficient for the spherical buoyancy elements of 0.5 (Sarpkaya and Isaacson 1981). The first two eigenmodes are the translational modes of the buoyancy elements. Their eigenfrequencies in undisturbed water are 0.06 Hz and 0.14 Hz, respectively.

Using a Strouhal number, S_t, of 0.2, a mean parallel flow speed, V_P, during event 4 of $\sim$ 0.35 m/s and a diameter, D, of 1.0 meters, we can estimate the vortex shedding frequency, f_v.

$$f_v = \frac{S_t \cdot V_P}{D} = 0.07 s^{-1}$$

This frequency is close to the first theoretical eigenfrequency of the current meter moorings. When a structure in water oscillates, the added mass is affected and the oscillation frequency is therefore a little different from the theoretical eigenfrequency in still water. When the shedding frequency is close to the eigenfrequency, the structure will start oscillating and the vortex shedding may 'lock-in' on the oscillation frequency. Further details on the subject of vortex-induced vibrations

can be found in the book by Blevins (1990).

Frequency power spectra of the velocity components at station D2 for event 4 are shown in Figure 3.29. The spectra at the other events are similar. Two straight lines, indicating the Kolmogorov $-5/3$ power law and the -1 slope, are also shown. It seems that the spectra follow the -1 slope rather than the Kolmogorov power law in the inertial sub-range. Notice the spectral peak at approximately 0.06 Hz in the spectrum of along-slope flow at D2. This peak is especially pronounced in the spectrum of the current velocity at the current meter farthest away from the sea floor. From Table 3.5 we see that the mean flow is in a direction which is close to up-slope flow (81°) at D2 during this event. This means that the spectral peak is caused by oscillations which are perpendicular to the mean flow direction, indicating that they are due to vortex-induced oscillations of the current meters rather than some turbulent feature of the flow.

The fact that it is the first eigenmode that is excited by vortex shedding explains why the peak in the spectra are larger for the current meters farthest away from the sea bed (the mode is a reverse pendulum).

We thus conclude that the current meter moorings sometimes oscillate in a direction perpendicular to the mean flow, and that this oscillation is caused by vortex shedding from the buoyancy elements.

3.6.9 Acknowledgements.

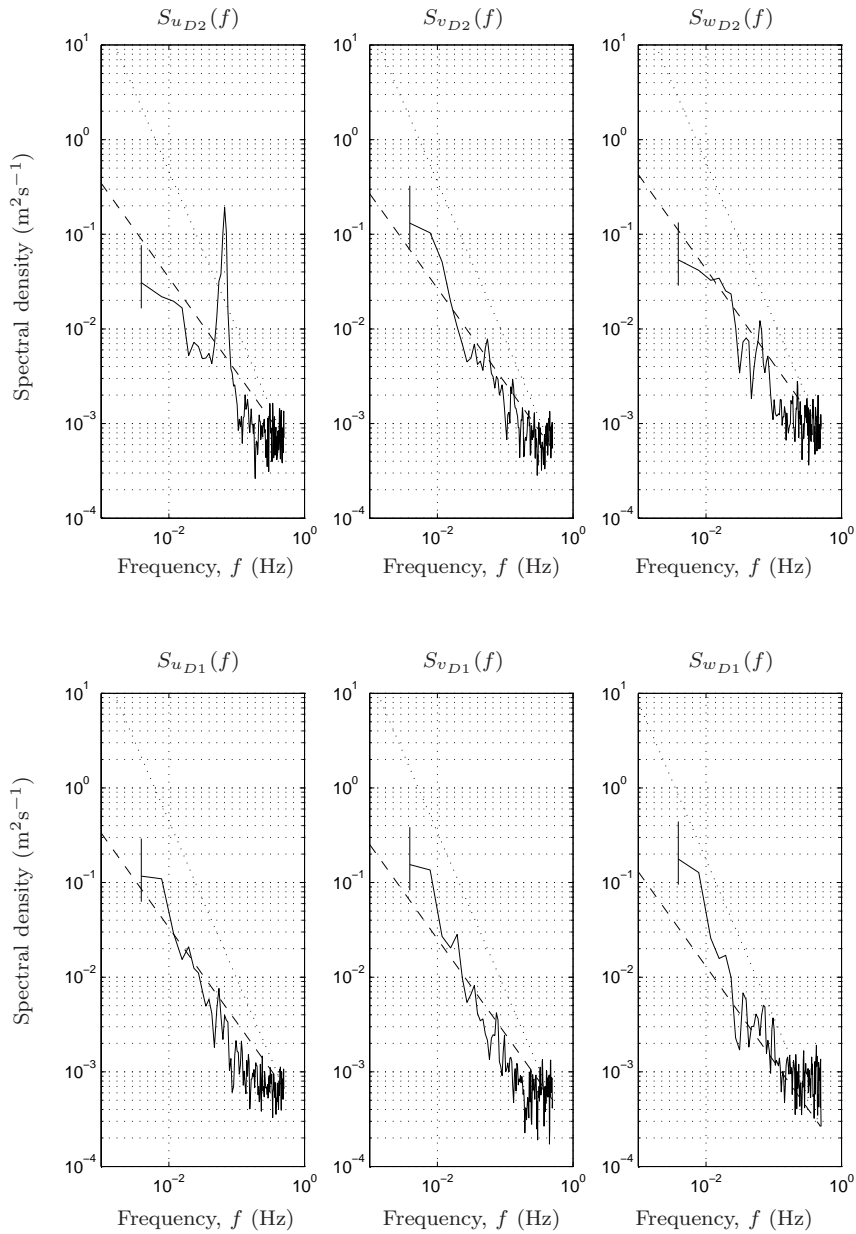**Figure 3.29**: *Frequency spectra for all velocity components at current meters D1 and D2 for event 4. Positions D1 and D2 are located 5 and 20 meters above the sea bed, respectively. The −5/3 slope (dotted) and the −1 slope (dashed) are also drawn. The spectra indicate white noise for frequencies larger than approximately 0.2 Hz.*

Numerical simulations of flow dynamics on the continental slope in a two-layered ocean

4.1   Introduction

This chapter contains a short description of a numerical ocean model and a study on the interaction between a perturbed pycnocline and the continental slope, using this model.

4.2   Numerical ocean modeling

Classical physical oceanography aims at describing the circulation in the oceans and finding physical explanations for observed features and important processes. The oceans are too large for the current to be measured at as many locations as one might want, and, even though observations made from satellites are becoming increasingly important, one has to look for ways of supplementing observational data. The exact solution of the governing equations described in section 2.2.4, together with their exact boundary- and initial conditions, would provide an exact description of the flow. Also, the explanations of observed features and details of certain important processes could be sought by careful analysis of the equations. Unfortunately, it is impossible to obtain an exact mathematical description of the boundary- and initial conditions to the equations, and, even if this difficulty could be overcome, the governing equations, being non-linear partial differential equations, can not be solved analytically without making extensive simplifications. The governing equations must therefore be solved numerically.

The art and science of numerical ocean modelling is fairly young. The first baroclinic global numerical model of the oceans was presented by Bryan (1969), and several books on the subject have been written since then, see e.g. Kowalik and Murty (1993), Heidvogel and Beckman (2000) and Kantha and Clayson (2000). Today, a variety of different models are available, and they are constantly being maintained, refined and extended. Such models can be quite different in the way that they are designed and the method by which the numerical solution is obtained. Numerical ocean models are used for closer studies of particular processes, for testing theories and as tools for monitoring the ocean circulation on different scales. Climate researchers use numerical models in their effort to predict the future climate and understand how the environment on Earth is affected by various changes in the boundary conditions and forcing, either man-made or natural. The development of numerical models with a good ocean-atmosphere interaction is therefore an important part of climate research.

4.3   Background

As was discussed in section 2.4, the shelf edge and the slope into the deep ocean represent a transition zone where a number of physical processes occur as a result

of the adjustment between shelf sea and deep ocean dynamics. The intersection between density surfaces and the relatively steep bathymetry gives rise to special processes and modelling challenges.

Measurements of the currents at the shelf slope in the Storegga region were presented in chapter 3. Some strong current events were characterized by a sudden change in flow direction and a rapid temperature fall at the current meters. It was suggested that some of these events were caused by wind-forcing of the deep pycnocline.

In this chapter, the interaction of a sloping sea bed and an intersecting pycnocline in a 2D section across the shelf edge and slope is studied numerically. The purpose of the study is to get an idea of the flow pattern and the flow speeds that one might expect to find when a perturbed pycnocline interact with a continental slope. A non-hydrostatic numerical model, representing idealised conditions for the area west of Norway, was used for the simulations. Finally, the results from the simulations and from the full-scale measurements are compared with some laboratory results reported by Grue (2002).

4.4   Numerical model

4.4.1   Governing equations

An existing 3D non-hydrostatic σ-coordinate numerical ocean model (Berntsen 2002) was reduced to 2D for the purpose of this study. An idealised 2D cross-section of the continental shelf, continental slope and deep ocean is shown in Figure 4.1. A coordinate system with the x-axis in the cross-slope direction, the y-axis in the along-slope direction and the z-axis vertically upwards is introduced. There can be no variations in flow velocity and density in the along-slope direction since only a 2D-section of the shelf and slope is considered. This means that all terms including $\frac{\partial}{\partial y}$ can be eliminated from the governing equations. Using equation (2.23) for turbulence closure and reinstating the vertical acceleration in equation (2.19), the Reynolds-averaged momentum equations (2.17), (2.18) and (2.19) now become,

$$\frac{\partial U}{\partial t} + U\frac{\partial U}{\partial x} + W\frac{\partial U}{\partial z} - fV = -\frac{1}{\rho_0}\frac{\partial p}{\partial x} + \mathcal{F}_x \tag{4.1}$$

$$\frac{\partial V}{\partial t} + U\frac{\partial V}{\partial x} + W\frac{\partial V}{\partial z} + fU = \mathcal{F}_y \tag{4.2}$$

$$\frac{\partial W}{\partial t} + U\frac{\partial W}{\partial x} + W\frac{\partial W}{\partial z} = -\frac{1}{\rho_0}\frac{\partial p}{\partial z} - \frac{\rho g}{\rho_0} + \mathcal{F}_z \tag{4.3}$$
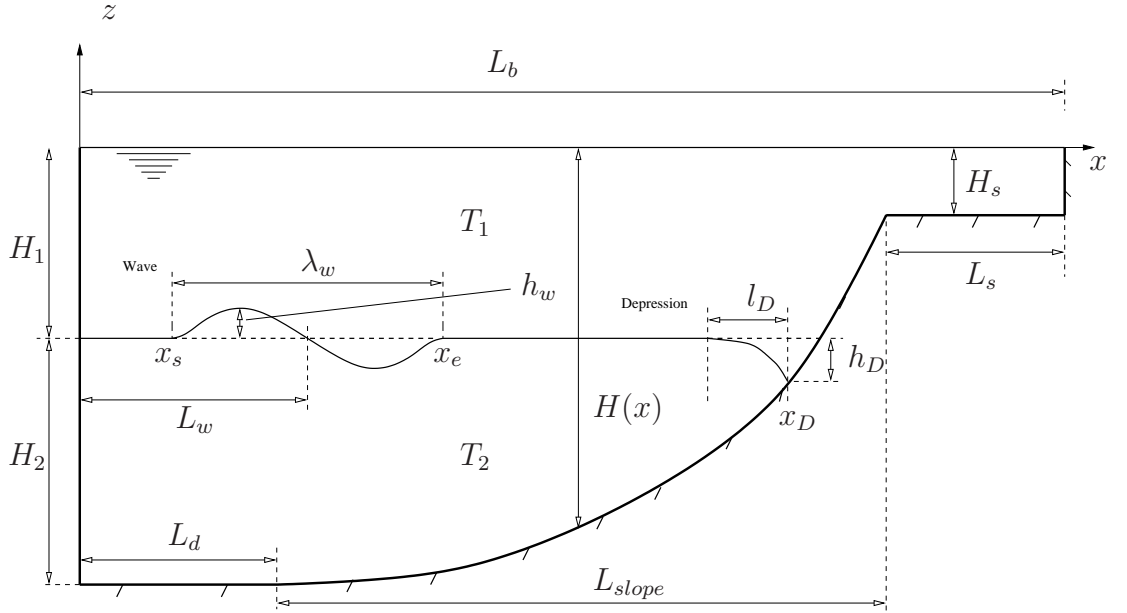
Figure 4.1: *Vertical profile of 2D section; shelf, slope, deep ocean and initial perturbation to the pycnocline (not drawn to scale). The model is initialized either with a wave-shaped perturbation or by a depression. Both perturbation types are shown in the figure though.*

when the friction forces are expressed by,

$$
\begin{aligned}
\mathcal{F}_x &= \frac{\partial}{\partial x}\left(A_M \frac{\partial U}{\partial x}\right) + \frac{\partial}{\partial z}\left(K_M \frac{\partial U}{\partial z}\right)\\[4pt]
\mathcal{F}_y &= \frac{\partial}{\partial x}\left(A_M \frac{\partial V}{\partial x}\right) + \frac{\partial}{\partial z}\left(K_M \frac{\partial V}{\partial z}\right)\\[4pt]
\mathcal{F}_z &= \frac{\partial}{\partial x}\left(A_M \frac{\partial W}{\partial x}\right) + \frac{\partial}{\partial z}\left(K_M \frac{\partial W}{\partial z}\right)
\end{aligned}
$$

and the molecular viscosity terms are negligible in comparison with the eddy viscosity terms. Conservation of mass becomes,

$$
\frac{\partial U}{\partial x} + \frac{\partial W}{\partial z} = 0. \tag{4.4}
$$

Numerical models have to include transport equations for heat (equation 2.14) and salt (equation 2.7) for studies of real ocean dynamics. In the present study, however, the focus is on the dynamics of a moving density surface in the ocean close to a sloping bottom. We therefore introduce a simple equation, linking the water temperature and the density,

$$
\rho(T) = -0.0002 \cdot \rho_0 \cdot T(x, z, t) \tag{4.5}
$$

where $\rho_0 = 1027.8$ kg/m^3 is a reference density. The temperature $T(x, z, t)$ is found by the equation for heat transport,

$$\frac{\partial T}{\partial t} + U\frac{\partial T}{\partial x} + W\frac{\partial T}{\partial z} = \frac{\partial}{\partial x}\left(A_H\frac{\partial T}{\partial x}\right) + \frac{\partial}{\partial z}\left(K_H\frac{\partial T}{\partial z}\right) \qquad (4.6)$$

where A_H is horizontal eddy diffusivity and K_H is vertical eddy diffusivity.

The total pressure consists of a hydrostatic part, p_H, and a non-hydrostatic pressure correction, p', as defined by

$$p(x, z, t) = p_H(x, z, t) + p'(x, z, t). \qquad (4.7)$$

The hydrostatic pressure,

$$p_H(x, z, t) = P_{atm}(x, t) + g\rho_0\eta(x, t) + g\int_z^0 \rho(x, z', t)dz', \qquad (4.8)$$

where $\eta(x, t)$ is the surface elevation, balances the gravity term in the vertical. The non-hydrostatic pressure correction is explained in Appendix A.

The numerical model applies a surface- and bottom following σ-coordinate system (Phillips 1957), and the governing equations are transformed into this new coordinate system before they are solved. Numerical solutions to the transformed equations are found on a staggered Arakawa C-grid (Mesinger and Arakawa 1976) using finite difference methods and the mode splitting technique described by Berntsen et al. (1981). Numerical values for horizontal and vertical eddy viscosities are computed according to the procedure proposed by Smagorinsky (1963),

$$A_{M,H} = C_{M,H}(\Delta x)^2\left[\left(\frac{\partial U}{\partial x}\right)^2 + \frac{1}{2}\left(\frac{\partial V}{\partial x}\right)^2\right]^{\frac{1}{2}} \qquad (4.9)$$

where C_M and C_H are constants. The values for K_H and K_M are calculated using the $2\frac{1}{2}$ level turbulence closure scheme that was proposed by Mellor and Yamada (1982) and modified by Galperin et al. (1988).

A detailed description of coordinate transformations and numerical solution technique, largely based on Berntsen (2002) and Heggelund et al. (2004), is provided in Appendix A.

4.4.2 Geometry, discretization and initialization

A cross section of the continental margin, representing idealised conditions and topography, is described by the parabola

$$H(x) = H_1 + H_2 + (H_S - H_1 - H_2) \cdot \left(\frac{x - L_d}{L_{slope}}\right)^2 \qquad (4.10)$$

for $x \in [L_d, L_d + L_{slope}]$ (see Figure 4.1). This parabolic slope profile is a good approximation of the upper part of the shelf slope off Storegga.

The geometry is discretized using 500 grid cells along the cross section and 114 σ-layers in the vertical. The horizontal grid resolution is 700 m. The distance between the σ-layers is uniform.

A two-layer density field is modelled, and the simulations are initiated with a perturbation of the pycnocline between the layers, either shaped as a wave in the deep ocean or as a depression near the slope, as can be seen in Figure 4.1. The temperature field with a wave-shaped perturbation of the interface between the two layers takes the form

$$T_0(x, z) = \frac{T_1 + T_2}{2} + \frac{T_1 - T_2}{2} \cdot \tanh\left(\frac{z - z_p(x)}{t_{pyc}}\right) \tag{4.11}$$

where $t_{pyc} = 20$ m is the thickness of the pycnocline, T_1 and T_2 are temperature in the upper and lower layers, respectively, and the z-coordinate of the center of the pycnocline is given by

$$z_p(x) = -H_1 + \frac{\lambda_w \cdot S_w(x)}{H_1 + \max\{S_w(x)\}} \cdot \sin\left(2\pi \frac{x - x_s}{\lambda_w}\right) \tag{4.12}$$

$$S_w(x) = h_w \left(1 - e^{-\frac{x - x_s}{0.1 \cdot \lambda_w}}\right) \cdot \left(1 - e^{-\frac{x - x_e}{0.1 \cdot \lambda_w}}\right)$$

The temperature field with a depressed pycnocline at the slope is also expressed by equation (4.11), but the z-coordinate of the center of the pycnocline is now given by

$$z_p(x) = -H_1 - h_D \cdot \left(\frac{x + l_D - x_D}{l_D}\right)^2 \tag{4.13}$$

for $x \in [x_D - l_D, x_D]$ when $H_1 + h_D = H(x_D)$.

Some of the model parameters seen in Figure 4.1 are fixed during the simulations, see Table 4.1. Temperatures T_1 and T_2 are selected such as to model a density difference between the layers similar to that at Storegga (ref. Figure 3.4).

The Coriolis effect was neglected in the simulations ($f = 0$), thus excluding along slope flow. This simplification proved to be necessary in order that the initial wave-shaped perturbation to the pycnocline would start propagating towards the slope. Using a nonzero Coriolis parameter in the simulations starting with a perturbed pycnocline (and no initial flow velocity) and a density difference between the two layers of 0.5 kg/m^3 resulted in no wave propagation, but in a geostrophic balance which held the perturbation in place. In simulations with $\Delta\rho = 2.0$ kg/m^3, however, the wave propagated towards the slope and no geostrophic balance was

Model property	Parameter	Unit	Numerical value
Length of basin	L_b	km	350
Thickness of upper layer	H_1	m	700
Thickness of lower layer	H_2	m	700
Temperature in the upper layer	T_1	^oC	2.5
Temperature in the lower layer	T_2	^oC	0
Length of deep ocean	L_d	km	220
Length of slope	L_{slope}	km	60
Length of shelf	L_S	km	70
Water depth at shelf	H_S	m	250
Position of wave perturbation	L_w	km	122.5
Coefficient of eddy viscosity	C_M	–	0.2
Coefficient of eddy diffusivity	C_H	–	0.0

Table 4.1: *Fixed model properties. See Figure 4.1 for reference.*

established. The available potential energy in a two-layered ocean when the layers are perturbed is larger when $\Delta\rho$ =2.0 kg/m^3 than when it is 0.5 kg/m^3, provided that the perturbation is the same in the two cases. It is possible that the case with $\Delta\rho$ =2.0 kg/m^3 was energetic enough that an internal wave could be maintained, but that the case with $\Delta\rho$ =0.5 kg/m^3 was not. In the real ocean, however, an in-flux of energy is in many cases present, thus allowing internal waves to develop and propagate even if the density difference is small. An attempt was made at forcing an internal wave through the western boundary (left side of Figure 4.1) by specifying oscillating velocities and temperature in a similar manner as Legg and Adcroft (2003). It proved difficult, however, to do this without the pycnocline near the western boundary being smeared out by extensive mixing. Also, the waves that were produced and entered the domain had small amplitudes and died out before they could reach the slope. It should be possible to overcome this problem in some way, but no furter attempts at this has been made here and the simulations are therefore carried out without the Coriolis effect present. The cross-slope velocities that appear in the simulations are not believed to be affected significantly by this, though, because the characteristic time scale of the variations at the slope is significantly shorter than the inertial period. In the case of the simulations with a depression in the pycnocline at the slope, neglecting the Coriolis effect is justified because the up-slope flow that we are interested in take place within the first few hours of the simulations, i.e. before the Coriolis effect has time to evolve.

4.4.3 Boundary conditions

The governing equations must be accompanied by boundary conditions and initial conditions in order to be solved on the computer.

A free-slip condition has been applied in the present simulations, using a bottom drag coefficient of $C_D = 0.0025$. The bottom stress is given by

$$\vec{\tau} = \rho_0 C_D \sqrt{U_b^2 + V_b^2} \cdot \left(U_b \vec{i} + V_b \vec{j} \right) \tag{4.14}$$

where U_b and V_b are the components of the velocity at the bottom (σ = -1). No forcing has been applied on the free surface.

Kinematic boundary conditions at the free surface and on the bottom in a σ-coordinate system are simply that the vertical velocity, ω, be zero, i.e. $\omega(\sigma = 0) = \omega(\sigma = -1) = 0$. There is no flow through the right border. A Flux Relaxation Scheme (FRS) is used to relax the values of the variables inside the domain, computed by the model, toward prescribed values at the borders. This takes place inside an FRS-zone which is `LB=7` grid cells wide. Prognostic variables, ϕ, in the FRS-zone are updated on each time step according to

$$\phi_{i,k} = \alpha_i \phi_{F_{i,k}} + \left(1 - \alpha_i \right) \phi_{M_{i,k}}; \quad i = 1, 2, ..., LB; \quad k = 1, 2, ...KB \tag{4.15}$$

where ϕ_M is the value of the prognostic variable computed by the model. For these simulations we use

$$\phi_{F_{I,k}} = \frac{1}{11} \sum_{i=12}^{22} \phi_{M_{i,k}} \quad I = 1, 2, ..., LB; \quad k = 1, 2, ...KB \tag{4.16}$$

as the specified (forced) solution in the FRS-zone on the left border. At the right border the forced solution is zero (no flow through the border).

No tidal variations are included. We thereby isolate the effect of the interaction between the disturbed pycnocline and the continental slope.

4.5 Results from numerical simulations

A series of numerical simulations have been carried out. The size of the initial perturbations to the pycnocline have been systematically varied. Initial perturbation size and results from the simulations can be found in Table 4.2. The choice of values for initial wave amplitude, h_w, and -length, λ_w, are based on observations of the 0° isotherm in Section Svinøy[1] (Blindheim 2004). Oscillations with wave amplitude of up to 150 meters and wave lengths of around 100 kilometers have been observed along this section. No physical observations or principles have been applied in selecting values for h_D and l_D. These values have been chosen more arbitrarily, seeking only to cover a range for a quick parameter study. Our main interests are the strength of the currents near the seabed and the range of the up- and down-slope motion of the pycnocline.

Simulations initialized with a wave-shaped perturbation of the pycnocline.

Simulation case id.	Wave ampl. h_w (m)	Wave length λ_w (km)	Depth of intersection between pycnocline and slope Maximum (m)	Minimum (m)	Maximum flow speed Down-slope Speed (m/s)	Time (hours)	Up-slope Speed (m/s)	Time (hours)
wave01	150	70	820	590	0.45	80	0.35	68
wave02	150	90	840	550	0.52	57	0.37	67
wave03	200	70	845	560	0.56	80	0.40	68
wave04	200	90	870	510	0.68	58	0.42	67
wave05	250	70	870	530	0.66	58	0.44	65
wave06	250	90	900	470	0.82	58	0.47	67

Simulations initialized with a depressed pycnocline at the slope.

Simulation case id.	Depr. height h_D (m)	Depr. length l_D (km)	Minimum depth of the intersection between pycnocline and slope (m)	Maximum speed Down-slope Speed (m/s)	Time (hours)	Up-slope Speed (m/s)	Time (hours)
depress01	100	15	655	0.11	15	0.24	3.9
depress02	200	15	620	0.24	15	0.41	3.4
depress03	100	25	660	0.09	16	0.20	4.6
depress04	200	25	625	0.19	17	0.36	5.0
depress05	100	35	660	0.08	–	0.17	5.0
depress06	200	35	635	0.17	19	0.32	5.7

Table 4.2: *Input parameters and main results from the numerical simulations. See Figure 4.1 for reference. Down-slope and up-slope flow is nearly parallel with the sea bed (U in the σ-coordinate system).*

4.5.1 Results using a wave-shaped initial perturbation

The strongest flows that occurred in the simulations that were initiated with a wave-shaped perturbation of the pycnocline were down-slope flows (see Table 4.2).

---

[1]Section Svinøy $(66^o22'\text{N}, 05^o12'\text{E} - 64^o40'\text{N}, 00^o00'\text{E/W})$

Envelope plots of maximum up- and down-slope flow speed for the simulations are shown in Figures 4.2 and 4.3, respectively. From these figures we can see that maximum down-slope flow speed occurs higher up on the slope than the maximum up-slope flow speed, but that both up- and down-slope flow is strongest near the slope. The reason for this is believed to be well illustrated in Figure 4.4, which shows the development of U in simulation `wave04` as the wave on the pycnocline encounters the slope. U is positive (red color) under the wave crest and negative (blue color) under the wave trough. After about 46-50 hours the wave crest meets the slope at approximately 500 m depth. This means that heavier water has been lifted about 200 m above its initial equilibrium level. Gravity forces start pulling these water masses down-slope, but this is not the only factor which causes down-slope flow. The wave trough has now arrived at the slope and the flow direction below the trough is away from the slope. This causes a suction effect that furter enhances the down slope flow further up on the slope. The pictures at 54 and 58 hours in Figure 4.4 show how this happens. Slinn and Riley (1996) carried out numerical simulation of turbulent mixing in the benthic boundary layer caused by internal wave reflection from sloping terrain. They also commented upon the suction effect, comparing it to the commonly known backwash on a beach. Next, a new wave crest approaches, and incoming water under this new wave crest meets the down-slope flow at the slope. This causes a breakdown of the flow pattern and this is when the strongest up-slope flow occurs.

As we would expect, increasing either the initial wave amplitude or length (i.e. increasing the available potential energy), causes larger flow speeds and also larger motions of the pycnocline at the slope.

4.5.2   Results using an initial depression of the pycnocline

The strongest flows that occurred in the simulations that were initiated with a depression in the pycnocline at the intersection with the slope were up-slope flows (see Table 4.2). Envelope plots of maximum up- and down-slope flow speed are shown in Figure 4.5 and 4.6, respectively. From Table 4.2, and also from the figures, we find that increasing the height (h_D) of the depression while keeping its length (l_D) fixed causes an increase in the maximum flow speeds (both up-slope and down-slope). If h_D is kept fixed while l_D is increased, however, the maximum flow speeds are reduced. The ratio h_D/l_D is proportional to the cross-slope density gradient and to the available potential energy, and an increase of this ratio gives increased maximum flow speeds.

The envelope plots (figures 4.5 and 4.6) show that the maximum up-slope flow speed always occurs near the slope and that the maximum down-slope flow speed sometimes occurs away from the slope. Also, the maximum up-slope flow speed occurs within just a few hours after the simulation has started, whereas the maximum
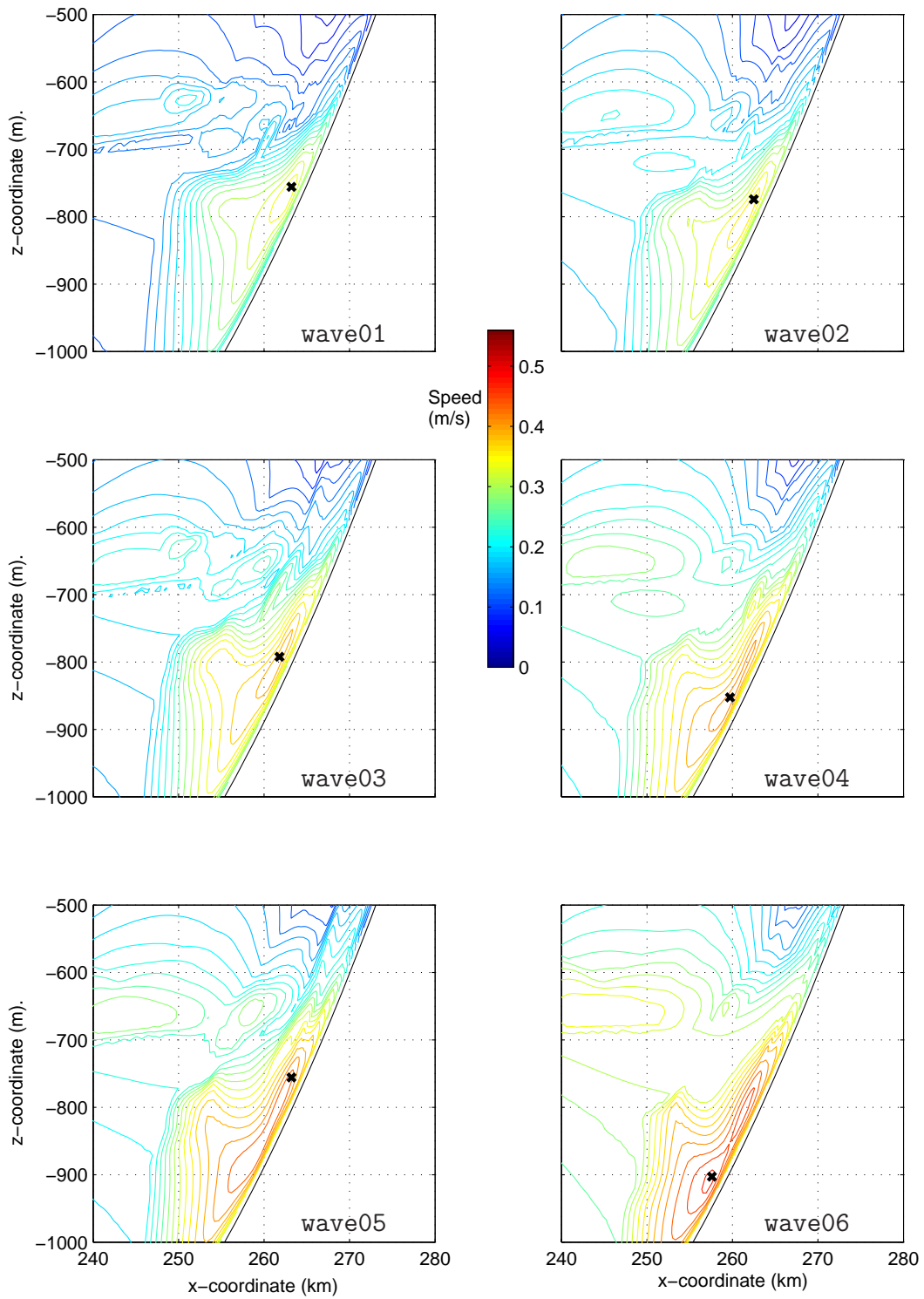
Figure 4.2: *Envelope plots of up-slope flow speed for the cases with a wave-shaped initial perturbation of the pycnocline. The location where the maximum up-slope flow speed appeared is marked with an ×.*
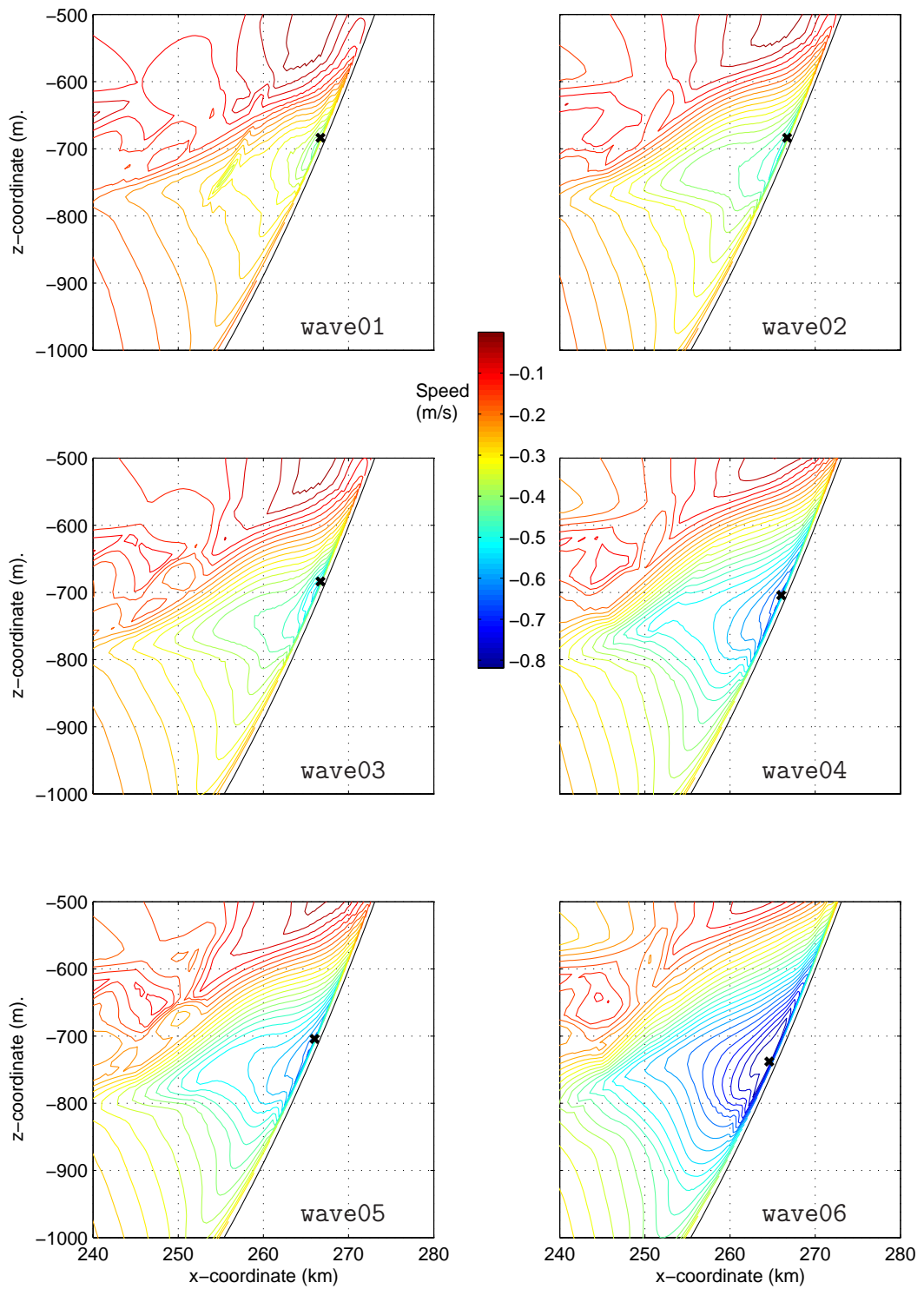
Figure 4.3: *Envelope plots of down-slope flow speed for the cases with a wave-shaped initial perturbation of the pycnocline. The location where the maximum down-slope flow speed appeared is marked with an ×.*
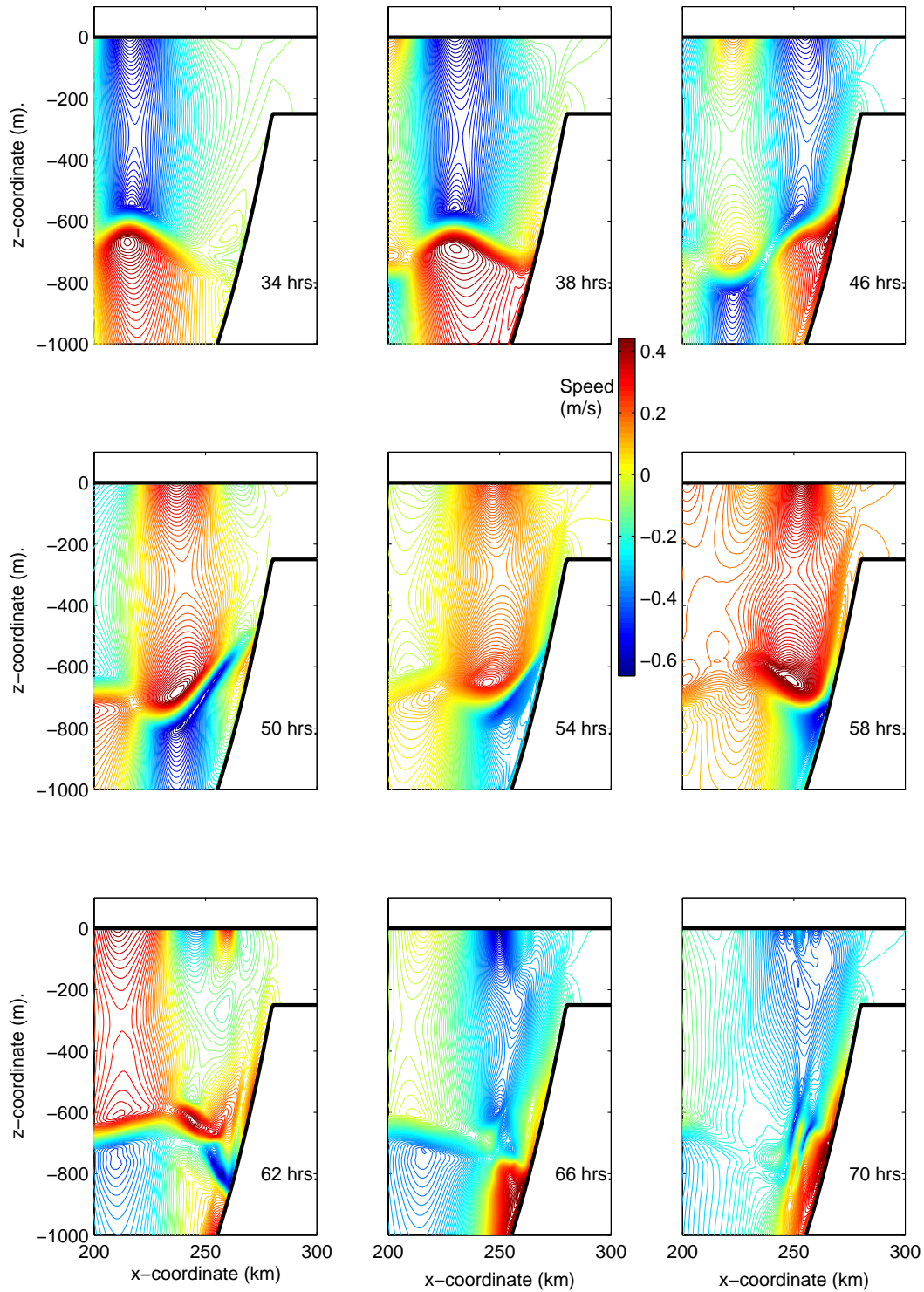
Figure 4.4: *Development of the U-field in simulation* **wave04** *as the wave encounters the slope. Elapsed time since the start of the simulation is given in each picture.*

down-slope flow speed occurs 15-19 hours after simulation start. The development in time of U for simulation `depress04` is shown in Figure 4.7. The figure shows that maximum up-slope flow occurs near the slope approximately 5 hours after start of the simulation, and that the maximum down-slope flow occurs away from the slope after approximately 17 hours as part of an internal wave which propagates away from the slope.

In section 3.6 it was conjectured that downwelling favourable wind over an ocean with a two-layered density structure on a slope would perturb the pycnocline at the slope similarly to what is shown in Figure 4.1, and that the sudden release of the perturbed pycnocline could possibly cause strong current events at the slope. The values of maximum up-slope flow speeds in Table 4.2 are comparable with the observed data discussed in section 3.6, thus providing some support for the above mentioned conjecture.

Figure 4.5: *Envelope plots of up-slope flow speed for the cases with a depression of the pycnocline at the slope. The location where the maximum up-slope flow speed appeared is marked with an ×.*
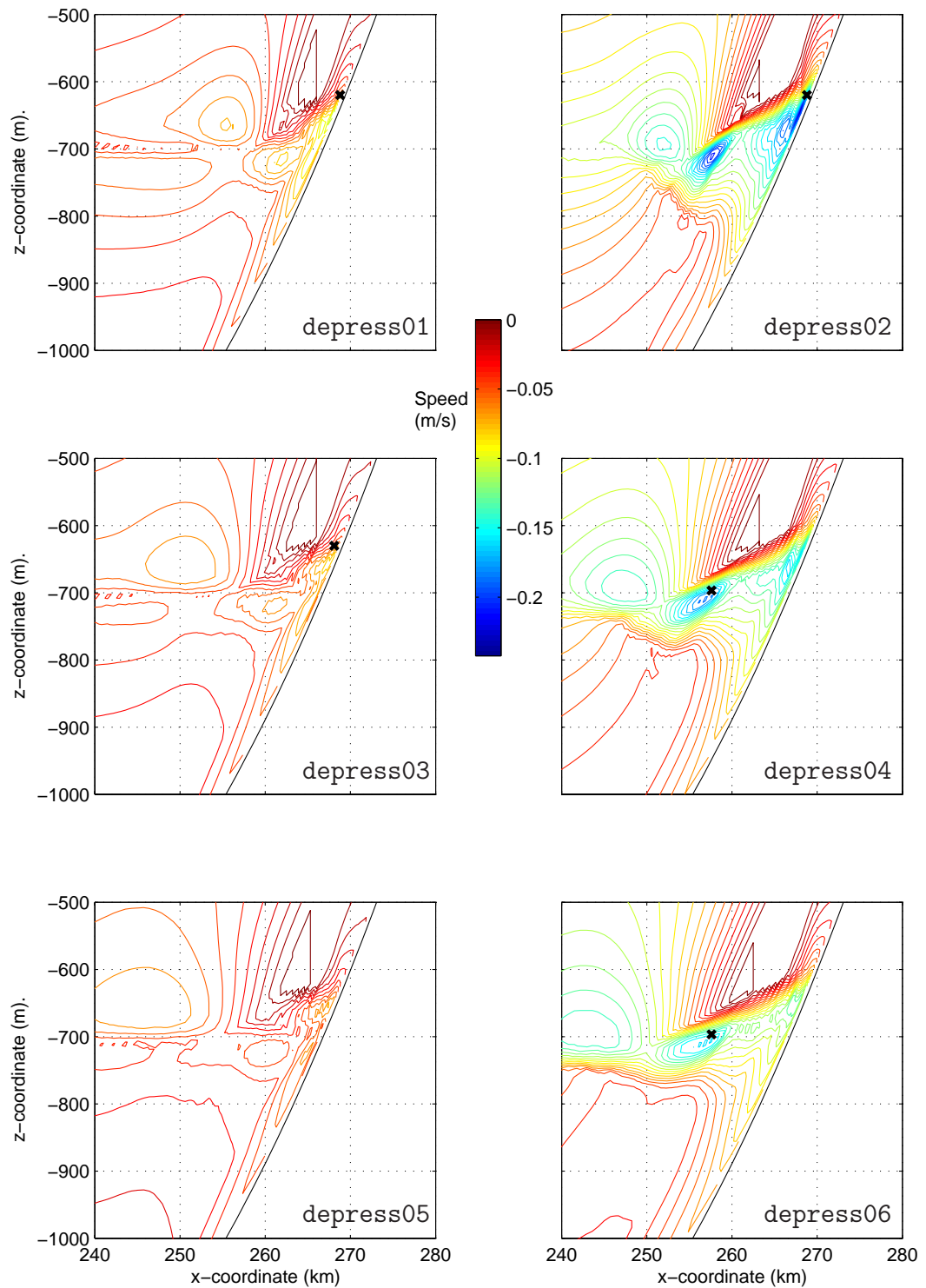
Figure 4.6: *Envelope plots of down-slope flow speed for the cases with a depression of the pycnocline at the slope. The location where the maximum down-slope flow speed appeared is marked with an ×. The maximum down-slope flow speed for case 5 is located outside of the plotted area.*
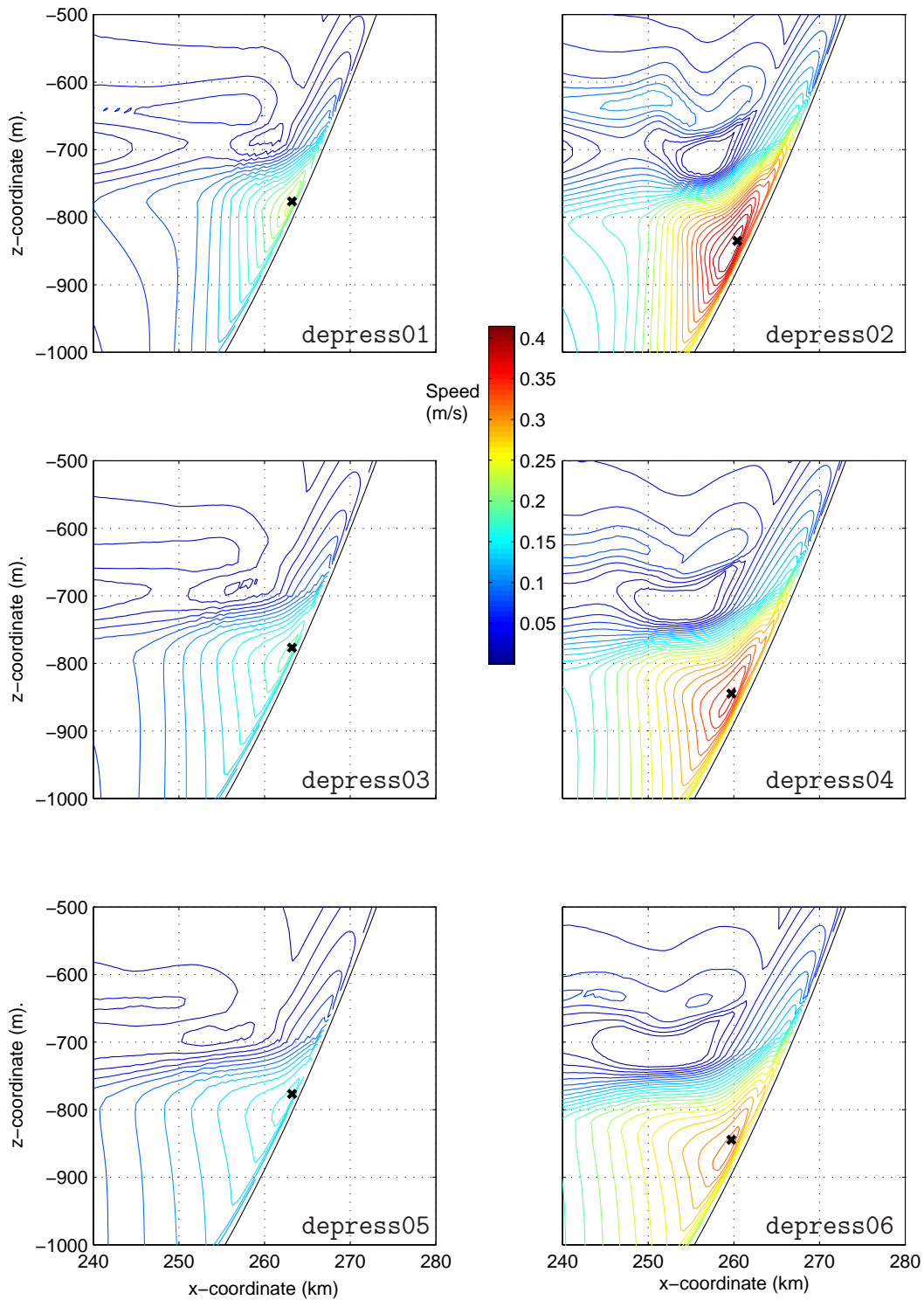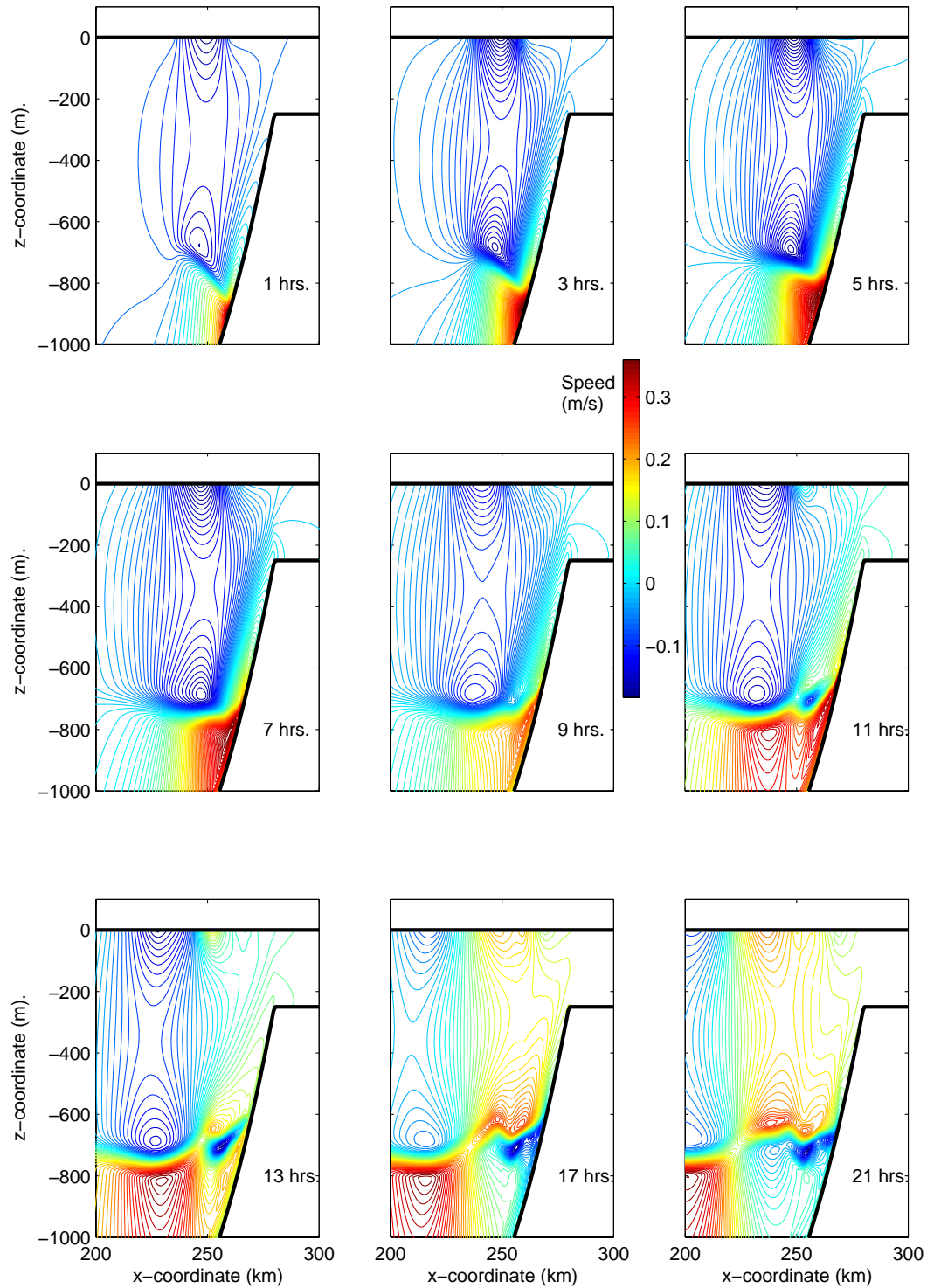
Figure 4.7: *Development of the U-field in simulation `depress04`. Elapsed time since the start of the simulation is given in each picture.*

4.6   Comparison with laboratory experiments

Grue (2002) carried out laboratory experiments of internal waves on a slope in the hydrodynamics laboratory at the University of Oslo in Norway. The experiments were calibrated to represent the conditions at Storegga. A two-layer model was set up with an upper layer thickness of 10 cm and a lower layer thickness of 20 cm. The model test tank was 7 metres long. The tank was fitted with a sloping bottom with a slope factor of 2.5 degrees. The model scale was 1:5000. The pycnocline was displaced at one end of the tank, and when released, an internal wave would travel towards the sloping bottom at the other end of the tank. An illustration of the experiment set-up is shown in Figure 4.8.
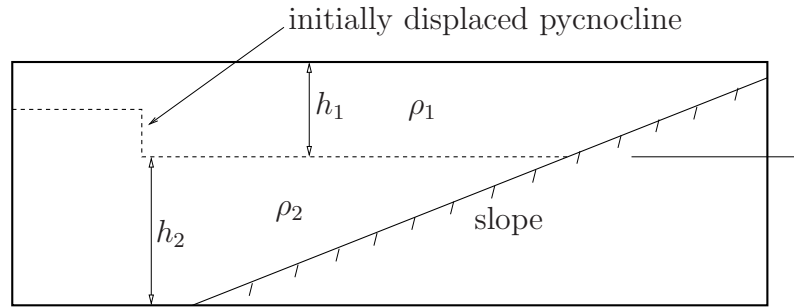
Figure 4.8: *Illustration of the laboratory experiment set-up used by Grue (2002).*

The maximum fluid velocity induced by the internal wave in the experiments was approximately $0.4 \cdot c_0$. The linear internal wave speed of long internal waves in a two-layer fluid is given by

$$c_0 = \left(g \cdot \frac{\rho_2 - \rho_1}{\rho_2} \cdot \frac{h_1 \cdot h_2}{h_1 + h_2} \right)^{\frac{1}{2}} \tag{4.17}$$

where ρ_1, ρ_2, h_1 and h_2 are density and thickness of the upper and lower layers, respectively. At the shelf slope near the Storegga slide area we find $h_1 = h_2 = 600\,\text{m}$, $\rho_1 = 1027.5\,\text{kg/m}^3$ and $\rho_2 = 1028.1\,\text{kg/m}^3$ (from Figure 3.4). This combination of parameters gives us a linear internal wave speed of $c_0 = 1.3\,\text{m/s}$. Maximum flow velocity found in the experiments, therefore, corresponds to a full-scale flow velocity of

$$U_{max,laboratory} = 0.4 \cdot c_0 = 0.5 \text{ m/s} \tag{4.18}$$

Wood (2002) reconstructed the laboratory experiments numerically. She found that her numerical model generated and evolved internal waves similar to those observed in the laboratory, and that the maximum fluid velocity, predicted by the model, was approximately $0.5 \cdot c_0$.

Although initiated differently, the simulations with wave-shaped intitial perturbation reported herein gives maximum up-slope flow speeds of the same order of magnitude as those in Grue's experiments and Wood's numerical simulations.

Ocean current variability applied in offshore engineering

5.1   Introduction

In chapters 1 and 2 it was argued that the loading from current flow on offshore structures becomes increasingly important as the offshore oil and gas industry moves beyond the continental shelf edge and into increasingly deeper waters. As a consequence, well formulated design current conditions will become more important than before.

A stationary current causes static displacements to a structure. Dynamic response as a result of stationary current (or slowly varying current) is known to occur for certain types of slender flexible structures (Blevins 1990). This response is driven by vortex shedding off the surface of the structure. Vortex-induced vibrations (VIV) require that a correlation in the vortex shedding pattern along a slender structure (such as a riser) is allowed to develop. It is believed that such a correlation will not be allowed to develop, or that it will be significantly impaired, if the current changes at a sufficiently high frequency. For structures such as SPAR platforms and risers, the oscillation period due to VIV is only a few minutes, or seconds. VIV of SPAR platforms and risers depend upon the current in the upper $\sim$200 meters (SPAR) or the entire water column (risers), and the temporal variations of the current in this area is too slow to affect vortex shedding. Closer to the sea bed, however, we have seen that the temporal variations can be on a shorter time scale, possibly affecting vortex shedding around free-span pipelines.

A time varying current may cause global dynamic response in a structure exposed to such flow. Provided that the natural frequencies of the structure are well separated from the typical oscillation frequencies of the current, the structural response can be calculated through a quasi-static analysis. If the current fluctuations are sufficiently rapid, however, one must use a full dynamic analysis in order to obtain displacements and stresses in the structure.

Marine operations in deep water will possibly become more complicated and time-consuming than in shallower water. The temporal variability of the current in the entire water column may then become an important factor in the planning of such operations.

A design current profile for an offshore location can be established from measurements of current velocity at a number of current meters arranged along a vertical line at the location in question. There are different methods for converting measured data into design current profiles. The *enveloping current profile* is formed by estimating extreme current speed at each current meter, using probability functions fitted to the observed data. This method has the built-in assumption that extreme current speed occur simultanously at all current meters. As we have seen, this assumption does not generally hold true, but the method is still used because

it is believed to be conservative. However, Adams and Thorogood (1998) showed that the enveloping current profile was unconservative when used for VIV fatigue analysis of a deep water (1300 m) drilling riser. They found that using a *concurrent profile*, established by sorting all observed current profiles according to some criteria, surface current speed for example, and then calculating the mean current profile for each of the current profile sets, much shorter fatigue life was estimated than when the envelope profile was used.

The enveloping current profile takes neither vertical coherence nor flow direction into account. We have seen (sections 3.5.4 and 3.5.5) that the stratification in the deep ocean can be such as to decouple the flow in the various density layers, and the use of an enveloping current profile would not represent the current conditions well in such cases. Therefore, alternative ways of defining design current conditions based on available data should be sought.

Whereas the physical oceanographer is often interested in understanding and predicting the exact large scale flow in an ocean or a sea, the offshore engineer is usually only interested in the current flow conditions at a certain location or in a small area. Contrary to what is the case for the atmosphere, no global system for surveillance of real-time oceanic parameters exist, making it difficult to specify accurate initial- and boundary conditions for numerical ocean models intended for forecasting the current flow conditions at a given time and place (Engedahl and Røed 1999). It would also be extremely expensive with regard to computing resources, if at all possible, to predict the exact current conditions at a given location by solving the governing equations directly. It seems, therefore, that the offshore engineer must settle for a model which is able to generate realistic and consistent design current fields instead of predicting the actual flow at all time.

Based on findings reported in this thesis, and on a general knowledge of oceanic processes and today's practice in the industry, important aspects in establishing new design current conditions are identified and discussed.

5.2 Physically consistent current field

Based on available information, a design current model for an offshore site should produce flow fields that can actually occur (realistic) at the site. Such flow fields must be consistent in the sense that the physical laws that apply (see chapter 2) are obeyed. A consistent and realistic current flow field would cause a consistent and realistic structural response in any marine structure present. However, a structural response, estimated on the basis of a current load condition which can not occur, will yield a structural response which we can not generally expect to occur. Furthermore, as was shown by Adams and Thorogood (1998), we may

not always consider structural response calculated from such unrealistic current conditions to be conservative. Unrealistic design current conditions are therefore of little use to the offshore engineer.

5.3 Statistical description of current field

Realizing that it is not possible to be absolutely sure about everything, statistical methods have been applied in modern design in order to enable the designer to say something useful about the reliability of structures and the availability of systems.

In today's practice for design of marine structures in wave loading, a statistical description of the environmental conditions must be established. Current profiles with various statistical properties can be established from a set of measured or simulated data. In this section, some different ways of doing this are described and discussed.

5.3.1 Existing design philosophy

The probability of occurrence is central in a statistical treatment of environmental conditions. In the well established practice that exist for determining design sea states for surface waves it is assumed that any sea state can be characterized by just a few parameters. The joint distribution of these parameters is then used in order to identify the probability that a given combination of the parameters will occur. All combinations of the parameters which have a return period of R_p constitute the n-dimensional R_p-surface, where n is the number of parameters used in characterizing the wave condition. If there are only two parameters (e.g. significant wave height and peak period) the R_p-surface is reduced to an R_p-contour line. The reason that just a few parameters in most cases are deemed sufficient for characterizing the wave sea state is that it is possible to handle the surface elevation in a certain way (stationary over a limited time, ergodic, gaussian, linear) for most offshore engineering applications. This significantly simplifies the mathematical and statistical treatment of the physical process. When ocean current conditions are concerned, however, there are more parameters (depth, stratification and bottom topography) to consider than for surface waves. As was discussed in chapters 2 and 3, it seems that important features of the current flow field at some locations are related to nonlinearities (unstable boundary layer and turbulence), stratification (decoupling between different layers of water) and surface wind variations. The loading of such surface winds on structures that are floating on the surface are treated statistically as if the wind was stationary (over a certain time). However, on time scales where variations in wind strength and -direction can affect the current flow below the surface ($\sim$12 hours) we can not always say that the wind is stationary. These complications make it impossible to characterize the current

flow using just a few (2-5) parameters.

Forristal and Cooper (1997) showed how the distribution of the principal components of the first two EOF-modes of a set of current measurements can be used for establishing design current profiles with a given return period. In doing this, they combined EOF-analysis of current data and inverse First Order Reliability Method (FORM) as described by Winterstein et al. (1993). Using two EOF-modes produces a contour line for a given return period (probability of occurrence). Vertical coherence was taken into account (via the EOFs), but the directional variability was not (only the along-slope flow was considered). It is possible, however, to also consider the directional variability, but the method then becomes more computationally demanding because more EOF-modes must be included and the dimension of the R_p-surface increases.

As previously noted, the bulk of the variance in a current data set can be contained in the first few EOF-modes. An extreme current condition (in terms of low probability of occurrence) does not necessarily contribute much to the variance of the entire data set. Consequently, we can not generally expect all such extreme conditions to be present in a reconstructed data set which is based on only the first few EOF-modes. Thus, EOF-analysis can not generally be used for establishing extreme current conditions.

Contrary to collapse caused by the ultimate load being exceeded, failure due to accumulated fatigue damage is a result of a large number of load cycles, and, therefore, proportional to the average energy of the current field (i.e. total variance). This indicates that using EOF-analysis for calculating current profile probability of occurrence in relation to fatigue calculations can be expected to give good estimates of fatigue damage, provided, of course, that enough EOF-modes are included such as to account for the bulk of the variance in the flow field over the life time of the structure. This methodology was suggested by Forristal and Cooper (1997). Later, Jeans et al. (2002) provided a broader discussion of the methodology and Meling et al. (2002) applied it in a study of fatigue damage due to VIV in a vertical drilling riser. They found that it was often necessary to include three EOF-modes in the analysis in order to get an acceptable accuracy in the results, but also that sometimes four and five modes were necessary. For low current speeds and fatigue levels, when small changes in the current cause large changes in the estimated fatigue damage, they found that the fatigue damage was overestimated when 3 modes were used, whereas using 2, 4 and 5 modes significantly underestimated the fatigue damage.

Zonal velocity range (m/s)	Location name : Location position : Meridional velocity range (m/s)									Current meter : 12 Depth : 350 m. Period : March 1 2004 - May 1 2004
	-1.0 -0.8	-0.8 -0.6	-0.6 -0.4	-0.4 -0.2	-0.2 0.0	0.0 0.2	0.2 0.4	0.4 0.6	0.6 0.8	0.8 1.0	Sum
-1.0 -0.8	0	0	0	4	2	0	0	0	0	0	6
-0.8 -0.6	0	0	2	4	3	2	1	0	0	0	12
-0.6 -0.4	0	0	2	5	3	2	2	1	0	0	15
-0.4 -0.2	0	1	3	5	4	3	3	2	1	0	22
-0.2 0.0	1	1	2	4	4	4	3	3	2	0	23
0.0 0.2	1	2	2	3	5	5	4	4	2	1	29
0.2 0.4	0	1	2	2	4	4	3	3	1	0	21
0.4 0.6	0	1	1	2	2	2	1	1	0	0	10
0.6 0.8	0	0	0	0	1	2	1	0	0	0	4
0.8 1.0	0	0	0	0	0	0	0	0	0	0	0
Sum :	2	6	14	29	28	24	18	14	6	1	142

Figure 5.1: *Scatter diagram of current measurements (principal form).*

5.3.2   Most probable current condition

Marine operations are sometimes limited by the current at the surface or at the sea bed or both. In such cases it would be useful to have methods for estimating the most probable current profile from a given data set when current speed and direction at one or more levels are pre-defined. Some methods for doing this are described below.

Consider M current meters arranged along a vertical line from the surface to the sea bed, each making recordings of the current velocity at N equally separated time instances. The resulting data set would then contain a time record of current profiles as defined in equations (3.14-3.17). The current velocity at current meter (level) m at time $t_n = \Delta t \cdot n$, where Δt is the sampling period, was defined in equation 3.17 as

$$a_{nm} = U_{nm} + i \cdot V_{nm} \tag{5.1}$$

Here, i is the imaginary unit and U_{nm} and V_{nm} are zonal and meridional flow speeds, respectively.

A scatter-diagram S_m of U and V at level m is easily established. The principal form of such a scatter-diagram is shown in Figure 5.1. The S_m scatter-diagram contains information about the statistics of the flow at level m, independent of all other levels, and is therefore referred to as the independent scatter-diagram. We can also define a conditional scatter-diagram $S_{m|m_{pre}}$ at level m to be the scatter-diagram of U and V at level m when the velocity at level m_{pre} is pre-defined, meaning that only those current profiles in which the velocity at level m_{pre} is within a pre-defined range is used in establishing the conditional scatter-diagram. The conditional scatter-diagram is generally not the same as the independent scatter-

diagram.

The flow at one level is generally not independent of the flow at other levels. In chapter 3 we saw that the correlation between near-by levels was significantly larger than between layers which were located farther away from each other. This knowledge is now used in constructing the most probable current profile when the current velocity at one or more levels is pre-defined. Using the conditional scatter-diagram, the most probable velocity at level m, given the velocity at level $m-1$, is defined by the center of the velocity range with the most occurrences in $S_{m|m-1}$. This velocity is then used as pre-defined when establishing the conditional scatter-diagram for the next $(m+1)$ current level. The procedure can be repeated until the most probable velocity at all levels, given the velocity at the neighbouring level, has been found.

A simple example of how to use the method follows. The task is to find the most probable current profile when the surface current (level $m = 1$) is given. The procedure is then

1. Set $m = 1$

2. Define u_m and v_m (pre-defined velocities)

3. Establish $S_{m+1|m}$ (the conditional scatter-diagram at level $m + 1$ using only the current profiles where u_m and v_m are within the pre-defined range.

4. Use $S_{m+1|m}$ to find the most probable velocity at level $m+1$, u_{m+1} and v_{m+1}.

5. Set $m = m + 1$.

6. Go to 3 if m is equal to or smaller than M.

7. Finished.

If the pre-defined velocity is not given at the first or the last level we can still use the same method, but we have to go up and down from the pre-defined level.

It is also possible to start out with several pre-defined velocities when constructing the most probable current profile. In the case that the velocity is to be pre-defined at several different levels we would use the velocity at the closest pre-defined level as a starting point for finding the most probable velocity at the other levels.

An alternative method, not making use of the assumption that the velocities in neighbouring levels are better correlated than in more distant levels, is to establish conditional scatter-diagrams at all levels using only the current data where the velocity at the pre-defined level(s) is within the pre-defined range.

As an alternative to using the velocity with the highest probability in each conditional scatter-diagram, we could use the mean velocities. This would give us the *expected* (or mean) velocity profile instead of the most probable velocity profile.

5.3.3   Probability of occurrence - counting method

An estimate for the probability of occurrence of current profiles can be made by counting measured profiles. The method is described in the following.

First, a speed range for the velocity components (we use the same range at all levels) is defined as

$$\Delta U = [U_1, U_2] \tag{5.2}$$

$$\Delta V = [V_1, V_2] \tag{5.3}$$

where U_1 and V_1 are observed lower limits of the zonal and meridional velocity components, respectively, and U_2 and V_2 are the corresponding upper observed limits. These speed ranges can be divided into smaller ranges of size,

$$\delta U = \frac{U_2 - U_1}{N_u} \tag{5.4}$$

$$\delta V = \frac{V_2 - V_1}{N_v} \tag{5.5}$$

The measured velocities at a current meter can now be organized in a two-dimensional table (like a scatter-diagram) with $N_u \cdot N_v$ cells. Any observed velocity can then be uniquely identified by its cell number in the table. A current profile at a certain time can thus be described by M cell numbers (if M is the total number of current meters). The complete data set can be written as a matrix of cell numbers,

$$\mathbf{D} = \begin{bmatrix} \mathbf{d}_1^T & \mathbf{d}_2^T & \dots & \mathbf{d}_n^T & \dots & \mathbf{d}_N^T \end{bmatrix} \tag{5.6}$$

$$\mathbf{d_n} = \begin{bmatrix} d_{n1} & d_{n2} & \dots & d_{nm} & \dots & d_{nM} \end{bmatrix} \tag{5.7}$$

where the value of d_{nm} is the number of the cell that the current velocity at current level m at time $t_n = n \cdot \Delta t$ falls into. As before, Δt is the sampling period of the data set and N is the number of observed profiles. Next, we start out with $\mathbf{d}_1$ and compare it with all $N - 1$ remaining $\mathbf{d}$'s. For every $\mathbf{d}$ that is exactly the same as $\mathbf{d}_1$ we increase the value of a counter and remove that $\mathbf{d}$ from the data set. Then we proceed to $\mathbf{d}_2$ and search the remaining data for identical profiles. This process is repeated until all occurring profiles have been identified and counted. The remaining data set now consists of N_e different current profiles ($N_e \leq N$) and a vector $\mathbf{e}$ of dimension N_e with the number of occurrences of each profile. The probability of occurrence for unique profile k can now be written

$$p_k = \frac{e_k}{N_e} \tag{5.8}$$

where $\mathbf{e} = \left[\begin{array}{ccccccc} e_1 & e_2 & \ldots & e_k & \ldots & e_{N_p} \end{array}\right]$.

This profile counting reduces the data set somewhat (depending on the selected values of δU and δV).

5.4   Current condition for ULS design

Structural response due to wave loading is a function of the frequency and the amplitude of the wave. The response can be more severe for some frequencies than for other frequencies, and the relationship between wave frequency and structural response to unit wave amplitude (linear transfer function) is different for different structures. On the other hand, the relationship between structural response magnitude and wave amplitude is such that an increase in the wave amplitude (almost) always causes an increase in the response (provided that the wave frequency is constant). Design wave conditions (sea states) are normally defined by contour lines. Combinations of significant wave height and spectral peak period with equal probability of occurrence define such contour lines. Normally, the contour line representing a return period of the sea state of 100 years is used in ULS design. The response of the structure is calculated for several points on the contour line and compared with the capacity. The reason for checking several points is that the point on the contour line that gives the most severe response depends on the structure itself. This means that a sea state with a return period of 100 years does not necessarily produce a response with the same return period. This is also the case for response to current load.

Current forces occur over the entire water column. Now, as an example, it is possible that a current profile with a strong current near the sea bed has a shorter return period than a current profile with a strong current near the surface. In an analysis of a vertical drilling riser it would clearly be wrong to use the profile with a strong surface current for calculating the angle at the sea bed and, at the same time, state that the calculated angle would not be exceeded in any other current condition with a shorter return period. Several similar examples could be imagined. Thus, in order to determine the probability of exceedance of a structural response which is caused by current loading, it is not sufficient to use information about the probability of occurrence of the current profiles. The probability of exceeding a response level in a given current flow environment depends very much upon which type of response we are looking at.

In ULS design of marine structures in wave loading it is customary to use the 100-year wave condition in combination with a current condition with a lower return period, assuming that the current condition causes a static response with that same return period. In view of the conjecture above, this assumption may not
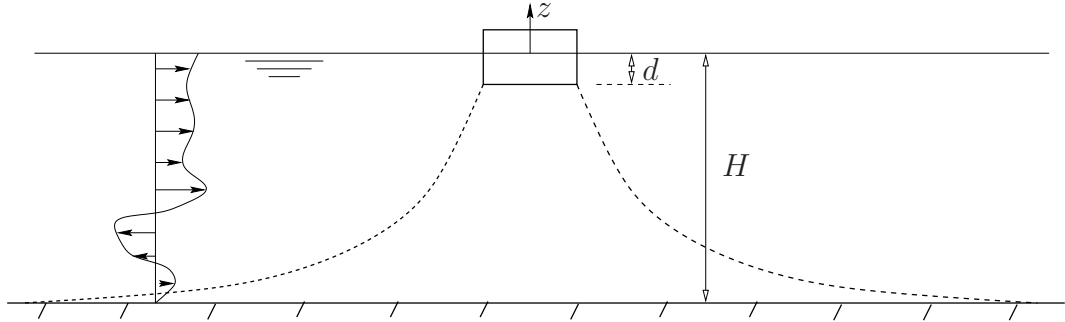
Figure 5.2: *Typical passively moored floating structure.*

always be taken to be correct in deep waters. Of course, the same applies in ULS design when current loading is the only environmental condition to be considered.

A few different response types to current load which must be considered in ULS design are discussed in the following, and suggestions are made as to how current conditions could be classified.

5.4.1   Offset of surface vessel

Current forces on passively moored floating structures cause such structures to be offset from their neutral position. The total force from the current comprise one part which arise from the drag on the floating structure itself and one part which is the integrated 'offsetting effect' of drag on mooring lines, risers, umbilicals and other structures that might be attached to the floater. When the water depth increses, the drag on mooring lines etc. may become increasingly important.

The surface current is defined as the mean current in the slice from the free surface to a depth equal to the draught of the floater, see Figure 5.2. Current profiles with strong surface currents must therefore be selected when searching for design current when offset of the surface vessel is important. The property

$$\mathbf{D}_F = \int_{z=-d}^{0} A(z) \cdot |\mathbf{V}(z)| \cdot \mathbf{V}(z) dz \qquad (5.9)$$

where $A(z)$ is a drag area and $\mathbf{V}(z)$ is the horizontal current vector at z can be used to classify the 'offsetting effect' of the drag on the floater itself.

Next, consider the integrated property,

$$\mathbf{D}_S = \int_{z=-H}^{-d} \frac{\frac{z}{H}+1}{T_{VH}(z)} \rho(z) \cdot C_D(z) \cdot D(z) \cdot |\mathbf{V}(z)| \cdot \mathbf{V}(z) dz, \qquad (5.10)$$

where $C_D(z)$ is the drag coefficient of the suspended structure, $D(z)$ is an equivalent diameter, $\rho(z)$ is water density and $T_{VH}(z)$ is a measure of the vertical variation in the horizontal stiffness. Assuming that the total structure (floater and attached structure) can be viewed to rotate around a hinge at the seabed, this property expresses the integrated moment of the current force on a vertical cylinder about that hinge, and is believed to be useful for evaluating which current profiles will be more important for the offset of the floater (when the effect of current force on suspended structure only is considered). The term $\frac{z}{H} + 1$ accounts for the effect that a current force close to the hinge contributes less to the total offset than a current force farther away from the hinge, whereas the division by $T_{VH}(z)$ accounts for the vertical variation in the horizontal stiffness. For a vertical riser, a suitable expression for $T(z)_{VH}$ would be

$$T_{VH}(z) = T_{VH,top} + W_w \cdot z \qquad (5.11)$$

where W_w is weigth in water per unit length of the riser. An expression for $T_{VH}(z)$ for a complete mooring and riser system would be different. Whereas the vertical riser is stiffer near the surface, a complete mooring system would be stiffer near the seabed, and a suitable expression for $T_{VH}(z)$ could be

$$T_{VH}(z) = T_{VH,1} - T_{VH,2} \cdot z \qquad (5.12)$$

where $T_{VH,1}$ and $T_{VH,2}$ would have to be determined in each case.

Thus, available current data can be organised according to integrated properties $\mathbf{D}_F$ and $\mathbf{D}_S$ which can be used to select profiles which should be used as 1-year, 10-year, 100-year etc. design current conditions when offset of a passively moored surface vessel is a design criterion.

5.4.2 Riser angle at top/bottom

A critical parameter in designing risers and umbilicals which are to be attached to floating or fixed structures is the angle that may occur between the riser axis and a reference axis at the attachment points, see Figure 5.3. Usually these attachement points are at the top and/or at the seabed.

When flexible structures like risers and mooring lines, which have little bending stiffness, are loaded laterally by a current force they tend to absorb the load by deflecting such as to take the load as axial tension. Thus, the angles at the top and bottom occur as a result of the total drag force, and it seems appropriate to introduce the parameter

$$\mathbf{F}_{ct} = \int_{z=-H}^{0} \rho(z) \cdot D(z) \cdot |\mathbf{V}(z)| \cdot \mathbf{V}(z) dz, \qquad (5.13)$$
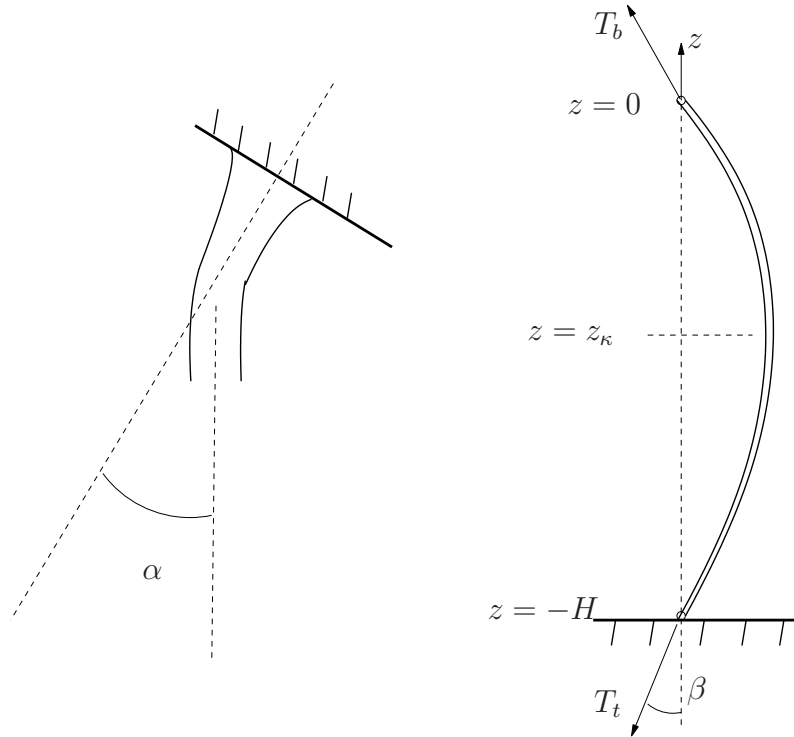
Figure 5.3: *Riser angle.*

in order to determine which current profiles will result in the largest angles.

This method can be improved by introducing two new parameters,

$$\mathbf{F}_b = \frac{1}{T_b} \int_{z=-H}^{z_\kappa} \rho(z) \cdot D(z) \cdot |\mathbf{V}(z)| \cdot \mathbf{V}(z) dz, \tag{5.14}$$

$$\mathbf{F}_t = \frac{1}{T_t} \int_{z=z_\kappa}^{z=0} \rho(z) \cdot D(z) \cdot |\mathbf{V}(z)| \cdot \mathbf{V}(z) dz, \tag{5.15}$$

where the various properties are defined in Figure 5.3. It is necessary to carry out a static analysis for every current profile in order to find z_κ for that current profile, thus making the improved method a bit more expensive.

5.5 Current conditions for FLS design

5.5.1 Fatigue due to waves

In FLS design of marine structures subject to wave loading it is customary to use a scatter diagram of wave amplitude and period for the dynamic loading. The

static offset, however, over which the dynamic motions are superimposed, is due to wind, wave drift and, as was discussed in section 5.4.1, current. For some types of structures, the dynamic responses that occur due to waves depend in some cases upon the original static offset. A good example of such a structure is a steel catenary riser (SCR) that is attached to a floater on the surface. The touch-down point (TDP) on the seabed of such an SCR will be different for different static offsets of the floater to which it is attached. Now, the TDP of an SCR is generally where the stress ranges in the riser are largest during dynamic loading, and it is therefore important to use the correct static offset of the floater with the various wave cases when we estimate the fatigue life of an SCR. The wave drift is directly proportional to the wave case, and therefore has the correct probability of occurrence. The appropriate current load for a given wave case, however, is not easily determined. In cases where the static response to current load of a structure or system is important for the estimated fatigue damage due to wave loading one should ideally have information about the joint probability between wave height, wave period and current profile. A possible procedure would then be, for each combination of wave height, wave period and corresponding current profile possible, to use the current profiles which are the most unfavourable with respect to fatigue damage. Such profiles should be selected based on knowledge about the response type, as exemplified in sections 5.4.1 and 5.4.2.

5.5.2 Fatigue due to current load (VIV)

VIV of a structure in a current flow is caused by vortices being shed from the structure (see e.g. Blevins 1990). Results of VIV are increased drag (Vandiver 1983; Blevins 1990), leading to larger offsets and increased static displacements, and an oscillating stress at several locations in the structure, leading to accumulated fatigue damage and, possibly, failure.

In calculating the fatigue damage which is inflicted on a structure over several years it is important to represent the statistics of the loading correctly. The probability of occurrence of a current profile decides the annual damage to the structure, caused by that profile. The profile counting method, outlined in section 5.3.3, is an accurate method for determining probability of occurrence, but the computational costs may be quite large. EOF-analysis is another way of estimating probability of occurrence. As mentioned in section 5.3.1, it is believed that EOF-analysis has the potential of producing good estimates of fatigue damage due to VIV. The method is not expected to be as computationally intensive as the counting method, but the accuracy will generally be lower. An assessment of the uncertainties that must be expected when using the EOF-method would possibly be useful. An example of how such an assessment could be carried out is outlined in the following.

Using n EOF-modes, establish a set of current profiles with a target probability

of occurrence, p_t, by considering the joint distribution of the n principal components. Then determine the true probability of occurrence for these profiles by using the counting method. This procedure can be repeated for a number of different values of n and p_t, and the suitability of EOF-analysis in determining the probability of occurrence for different current profiles would then be indicated as the deviation between results from the counting method and from the EOF-method. However, the uncertainty in the estimated fatigue damage, using counting method and EOF-method, respectively, is not necessarily the same as the uncertainty in the statistics of the current load. By also doing a fatigue analysis for each current profile found by the counting method and by the EOF-method, for different n and p_t, this uncertainty could be determined.

In qualifying the EOF-method for fatigue analysis in risers which are prone to VIV, assessments such as the one described above should be made for different riser topologies, depths and current conditions in order to document the robustness of the EOF-method and make recommendations as to how a fatigue calculation of a riser using the EOF-method should be carried out when measurements of the current exist.

5.6   Current conditions during marine operations

Different current conditions must sometimes be considered when planning and training for marine operations.

Critical phases of marine operations are usually related to activity at or near the surface or at or near the seabed. Positioning and installing objects correctly on the seabed is often the aim of a marine operation. Any external disturbance that can affect the operator's ability to achieve that aim must be considered. External environmental forces on an object which is suspended on a cable from a surface vessel in the deep ocean occur from waves (some part of the vessel motions are transferred through the cable) and current flow. Wave-induced forces are handled by using heave-compensators and/or by simply not commencing with the operation until the wave conditions are acceptable. The forcing from the current flow can be more difficult to handle. As we have seen in chapter 3, the current near the seabed can change significantly on time scales relevant for marine operations (minutes-hours). Such changes may occur during a marine operation and the operator should be prepared for that and able to handle it. Strong currents in themselves are not that important if they are constant in time, it is the temporal variation that can be difficult to handle.

Tidal variability is regular, the frequencies that appear are well known and the energy contents can be found by relatively short measurements ($\sim$months). The

variability that is caused by internal waves, stratification, topography, boundary layer turbulence, atmospheric forcing and possibly other non-stationary stochastic processes is more difficult to model. Unlike the physics of the tidal variation, the interaction and relative significance of the different physical processes responsible for other types of variations is not fully understood yet. It is believed that a better understanding of these physical processes would better enable us to treat the resulting variability to the current flow statistically, and lead to improved safety and reliability of marine operations. This can only be achieved through extensive research involving measurements in the oceans and theoretical development.

Meanwhile, the offshore engineer must make the best of what is available. Realizing that abrupt temporal variations are probably the most critical feature of the flow, the data (if available) should be searched for large values of $\frac{\partial}{\partial t}(\frac{\partial V}{\partial z})$, $\frac{\partial}{\partial t}(\frac{\partial V}{\partial x})$, $\frac{\partial}{\partial t}(\frac{\partial V}{\partial y})$ and $\frac{\partial V}{\partial t}$. A time period (e.g. ∼4-8 hours) containing one or more time instances when one or more of these parameters are anomalous can be defined as events which must be accounted for in planning and training for the marine operation in question. Such events should also be handled statistically in order to be able to say something about the reliability of the operation (see section 5.7).

If no data are available at the site, data from similar sites could be used. The fewer data available, the larger the uncertainty. If the consequences of a marine operation going wrong are severe, then a low probability of failure is wanted in line with the philosophy behind risk management.

5.7 Extreme events

Recordings of strong current events at the continental slope west of Norway have been described in section 3.6 of this thesis. Although the record length is a bit short for making firm conclusions, it seems that the events do not occur regularly and that they appear to be the realisation of some nonstationary stochastic process.

Another example of strong current events, this time in the upper part of the water column, is the vortices at Troll, briefly described in section 2.3.2.

It would be convenient for the offshore engineer to be able to predict such strong events, and also to be able to estimate the extreme flow speeds that are likely to occur during the events.

A good understanding of the physical process(es) involved is a prerequisite for predicting strong current events with any significant degree of certainty. In the case of the vortices at Troll, it seems that the wind conditions in the North Sea and the water level in the Skagerak and the Baltic Sea are important parameters, whereas

the strong flow at the continental slope west of Norway in some cases seems to be related to the wind conditions on the surface in the area. After identifying the most important physical processes and properties that are involved in producing extreme events, a model for predicting such strong events could possibly be devised. Such a model could be based on physical principles and laws, making use of the governing equations, or it could be established based entirely on measured data. Now, if the physical properties that are important in creating strong current events (wind conditions, water level, etc.) are easily observed or predicted (weather forecasts), then it would also be possible to predict the strong current events.

Estimating extreme values of flow speed related to strong current events require a large set of measurements and statistical methods that can handle such nonstationary processes. Also, the strong spatial variability that occurs is an important reason why a large set of measurements is required.

5.8   Design current conditions based on measurements

When designing offshore structures with respect to wave loading it is customary to use measurements of wave height and period in order to establish a relationship between the wave energy on different frequencies (wave spectrum). A wave spectrum is usually defined by just a few parameters such as e.g. significant wave height H_s and peak period T_p. A random realisations of the wave elevation η in a sea state, assuming that the process is Gaussian, can be constructed by $\eta(t) = \sum_{n=1}^{N}(a_n \cos \omega_n t + b_n \sin \omega_n t)$, where the amplitudes a_n and b_n are independent random variables chosen from a Gaussian distribution with common variance given by $S(\omega_n)\Delta\omega$. Here, $S(\omega)$ is the wave spectrum, ω_n is the wave frequency and $\Delta\omega$ is the frequency discretization that is used (Larsen 1992; Tucker et al. 1984). It is thus possible to generate several different physically consistent sea states with certain statistical properties for use in design.

A similar approach could possibly be used for generating different physically consistent current conditions based on a set of measured data. Two important issues that must be studied and resolved in establishing such a process are

1. Methods for statistical analysis and reconstruction of current conditions must be developed.

2. Characteristic parameters of a current condition must be identified and implemented in the above mentioned methods.

A considerable research effort is believed to be necessary in order to resolve these two tasks, and the following only serves as introductory comments on the subject.

5.8.1 Statistical analysis and reconstruction of current conditions

We require a method which can be used for establishing a random realistic and physically consistent realisation of a current condition based on available measured data. Such realisations should possess certain pre-defined statistical properties.

Three different methodologies for reconstructing current conditions on the basis of measured data are briefly discussed in the following.

EOF analysis

In chapter 3 it was shown how EOF-analysis can be used to transform a measured set of current conditions into orthogonal modes and principal components, and vice versa. However, the current conditions that are reconstructed in the EOF-analysis are exactly identical to the original data set that was used in establishing the modes and principal components themselves. The reconstructed current conditions are therefore not random, and not particularly useful in a true stochastic analysis.

Frequency spectra

Frequency power spectra are often used in design against wave loading. The principle of 'local stationarity', i.e. that the sea state is stationary for a certain period of time (e.g. 3 hours), is applied in doing this. The same principle is applied in wind modelling. Davenport (1977) formulated wind spectra using surface drag, mean wind speed 10 meters above ground and a scale length as characteristic parameters.

On this background, it is tempting to try to apply frequency spectra in current modelling also. However, whereas wind spectra are developed for the atmospheric boundary layer and wave spectra only for the ocean surface, current modelling must span the entire ocean space from surface to bottom in the area of interest. The spectrum of the current velocity components at one location is more or less related to the flow at other locations (ref. chapter 3). Phase relationships between velocity components at different locations can be taken care of by introducing cross-spectra in addition to the (auto)spectra that are used in wind- and wave modelling. Based on auto- and cross-spectra of measured current velocity in an area one could possibly generate random realisations of the current field in the area in a similar way as random realisations of the surface elevation are generated for design against wave load. The principle of local stationarity must still be applied

and an estimate of the length of the time period during which the current condition
can be considered to be stationary is needed.

Wavelet transform

In using Fourier transform for creating frequency spectra of measured time se-
ries, we inherently assume that the process is stationary. If this method is used
on a nonstationary process, however, and a realisation of the process is recon-
structed from the frequency spectrum, the nonstationarity would be lost because
the Fourier transform would smear out the detailed information of the changing
process (Emery and Thompson 2001). Whereas Fourier transforms decompose the
original time trace into frequency-space, the wavelet analysis decomposes a time
trace into time-frequency space, thus retaining information about dominant modes
of variability and how these modes vary in time (Torrence and Compo 1998).

Since being introduced as a tool for processing seismic data (Goupillaud et al.
1984), wavelet analysis is now being used in a variety of fields, also in geophysical
fluid dynamics.

The seemingly nonstationary dynamic behaviour of the flow that was reported in
section 3.6 could possibly be reconstructed by a model based on wavelet analysis.

5.8.2   Characteristic parameters of current conditions

It would be convenient to be able to describe a current condition by a model (see
previous section) and a few characteristic parameters. A few candidates for such
parameters are described in the following.

Mean flow speed

The turbulence in the ocean takes its energy from the mean flow, and it is therefore
likely that the mean flow speed will be a useful parameter in characterizing the
current condition.

Peak periods

There are several principal tidal constituents. The energy content on the respective
frequencies will vary, and on some frequencies it will be significant. Also, the
inertial period $\frac{2\pi}{f}$ (f is the Coriolis parameter) could be important in characterizing
the current condition.

Energy dissipation rate per unit mass, ϵ

Turbulent flows are dissipative and ϵ is therefore an important parameter in the spectrum of turbulence, see e.g. Tennekes and Lumley (1972). The unit of ϵ is $\mathrm{m}^2\mathrm{s}^{-3}$.

Frequency and wavenumber

The turbulent field can be described by energy distribution over frequency f_t or over wavenumber κ. When transforming from wavenumber-space to frequency-space it is necessary to apply the assumption that the mean flow speed is so much larger than the turbulent flow speeds that the turbulence field does not change in the time it takes for it to pass an observer fixed in space. This is often referred to as *Taylor's hypothesis* or the *frozen-turbulence approximation*.

Stratification and distance from sea bed

The vertical density distribution (stratification) is an important parameter in ocean circulation and could possibly be useful as a characteristic parameter in a model. Also, the distance from the sea bed (and the surface) is important in how the flow is restricted or affected by these boundaries, and it should be considered as a characteristic parameter.

5.9 Design current conditions - a simple model

5.9.1 Motivation

Direct measurements or simulations of the current flow conditions are not always available to the offshore engineer during the early phases of planning and development of an offshore field. Some tasks, such as e.g. feasibility studies of various concepts and early availability analyses, can generally not be carried out without taking the current flow conditions into account. A simple current flow model, making use of whatever scarce information may be available, and a general knowledge of ocean dynamics and the particular area, would therefore be useful. The details for such a model are not worked out here, but a procedure for how to establish it is outlined.

5.9.2 Relevant information

The amount of relevant information that is available in the early design phase will vary. Some sites will be close to other sites where the conditions are well known and may be assumed to resemble those at the site in question. Other sites may be located where less is known about the conditions. Relevant information, and different means of obtaining it, are listed in Table 5.1.
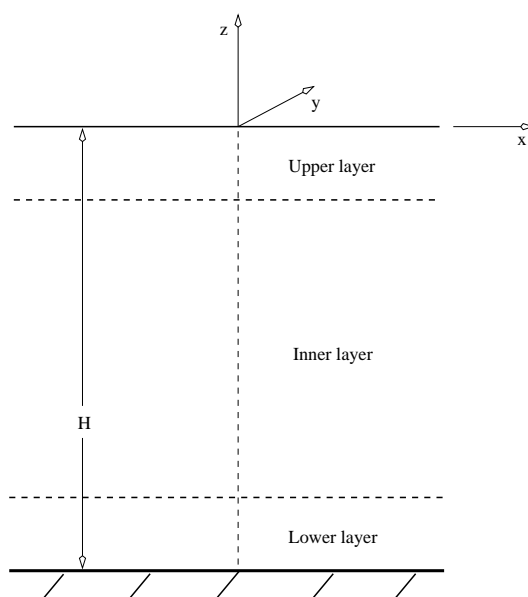
Figure 5.4: *Main horizontal layers.*

5.9.3 Considerations and assumptions

To begin with, the water column at the site is divided into three main layers, see Figure 5.4. Assumptions about the dominating effects in the respective layers are then made, boundary- and initial conditions are specified, continuity is required at the intersection between the layers and a linear set of equations can be established. Solving this set of equations gives us a consistent current condition. The linearity

Information type	Source of information
Stratification, temperature and salinity	CTD-casts
	Climatology
	Oceanographic publications
Wind speed and direction	Meteorological observations
	Vessel limitations
Roughness, slope, topography and depth of the seabed	Echo soundings
	Bottom topography maps
	Bottom samples
	Oceanographic publications
Large scale background flow speed and direction	Climatology
	Oceanographic publications

Table 5.1: *Relevant information for a simple model of current conditons.*

of the model allows for superpositioning of contributions from various sources.

Inner layer

First, the properties of the inner layer are defined. This layer is normally the thickest. Information about the stratification in the inner layer must be established, either from CTD-casts[1], climatology or other published material. One component of the flow in the inner layer is assumed to be geostrophic (background flow) and is either specified by climatology (see e.g. Engedahl et al. 1998 and Levitus 1982), by using available knowledge about horizontal density gradients or by information found in various oceanographic publications. A comprehensive literature study should always be carried out.

At its upper and lower border the inner layer provide boundary conditions for the upper and lower layers, respectively.

Time varying flow components such as tidal variations, internal waves, travelling vortices etc. can be added if relevant as long as the model is linear.

Upper layer

This is the mixed layer and it is assumed that the stratification is zero in this layer (constant density). Wind, friction and the Coriolis effect are assumed to be the dominating effects, together with a background flow such as e.g. the Atlantic inflow to the Norwegian Sea. The effect of the windstress is superimposed on the background flow in the upper layer. Governing equations for the wind-frequency-coriolis balance can be established from classical Ekman theory and empiric relations for windspeed and windstress on the sea surface. The background flow must be known so that it can be prescribed in the model.

At the interface with the inner layer, the flow must be continous.

Lower layer

This layer contains the benthic boundary layer (BBL). Friction and the Coriolis effect is assumed to govern the mean flow in this layer, following classical Ekman theory. Turbulence is provided by specifying turbulence spectra according to traditional theory (Tennekes and Lumley 1972). Continuity is required at the border with the inner layer. The effect of friction and rotation on the mean flow is added to the background flow.

---

[1]A CTD is an instrument which can measure conductivity, temperature and pressure of seawater. Salinity and density are then derived from the measured data. A CTD-cast is done by lowering this instrument through the water column and thereby logging a profile of temperature, salinity and density (i.e. stratification) for that particular location.

5.10 Design current conditions - direct simulations.

One way of aquiring information about the current conditions at a location is by direct numerical simulations with an ocean model. Local flow conditions depend upon large scale features as well as small scale features, and variations in the large scale flow will affect the flow locally. Numerical models, used for estimating the flow conditions at a specific location, must therefore have the capability of estimating large scale variations and features of the flow. This means that the domain of the model must be large. As previously mentioned, providing detailed initial- and boundary conditions for numerical ocean models is generally difficult. Boundary conditions for large scale models are often taken from climatology data such as those provided by e.g. Engedahl et al. (1998) and Levitus (1982). Provided that the location that we are interested in is far away from the boundaries of the domain, the possible inaccuracies in the boundary conditions will to some extent be rectified by the numerical model inside the domain, taking large- and small-scale features into account. Furthermore, the need to account also for small-scale features (e.g. local topography, turbulence) calls for a high resolution model. Now, a large domain with a high resolution will be computationally expensive. Today it is not practical to run a 3D model using a mesh with a grid size (Δx and Δy) of ~ 10 meters of an entire ocean basin like, for instance, the Norwegian Sea. A way of circumventing this difficulty is to use a fine grid in the area near the location we are interested in, and an increasingly coarser grid as the distance to that site increases. This can be achieved by either using a single model with varying horizontal grid size (expandable grid) or by using several models in parallel (nesting), each with a different grid size. See Figure 5.5 for an illustration of the two methodologies.

A majority of today's numerical ocean models use finite difference techniques in solving the governing equations. This does not allow for local refinement of the mesh within one model, and nesting is therefore the most common way of obtaining this. Spectral element models, such as e.g. SEOM (Patera 1984), however, allow for an expandable grid.

In the nested model the solution on a coarser grid is used as boundary conditions on a finer grid. This can be done an arbitrary number of times until the desired resolution at the location is achieved. There are two types of nested models. In *passive nested models* the solution on the coarser grid is applied on the boundary of the finer grid, but there is no feedback the other way, i.e. flow features generated inside the finer grid do not propagate outward into the coarser grid. *Interactive nested models*, on the other hand, have this coupling in place, and are therefore more complicated to implement and more costly with regard to computer time.
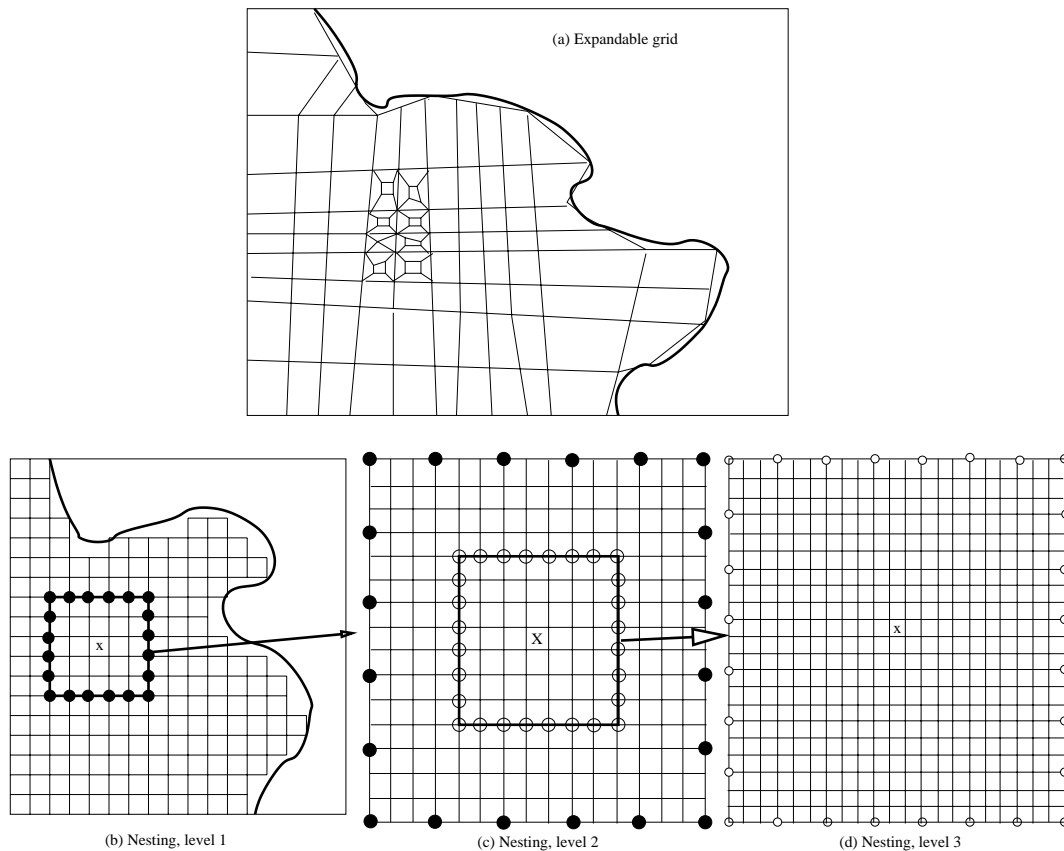
Figure 5.5: *Illustration of expandable grid models (a) and nested models (b-d). The results computed by the level 1 model in the black gridpoints are used as boundary conditions for the level 2 model in the black gridpoints. Boundary conditions on the gridpoints in between are found by interpolation. Correspondingly, the results at the white gridpoints in the level 2 model are used as boundary conditions for the level 3 model in the white gridpoints.*

Numerical models in which the governing equations of the ocean and the atmosphere are coupled are now useful tools in climate research. Such a model, either nested or with expandable grid, could possibly be useful to the offshore engineering community also. However, a significant effort would have to be made in formulating, coding and operating such a model. A first step, requiring less effort than establishing a complete coupled model, would be to create an ocean model, without direct coupling to the atmosphere, but with the possibility of achieving the required grid refinements.

Some effects of current flow variations on marine structures and operations

6.1 Introduction

In section 1.4, the question: 'How is the structure/operation affected by the current?' was posed. It is not possible to provide a general answer to this question for all types of structures and operations imaginable. Every case must be analyzed by itself.

This chapter contains an analysis of a free-span pipeline in a slowly varying current (no transient motion), and an analysis of typical marine operations in a variable current flow environment. The results from these analyses provide examples of how typical marine structures/operations in relatively deep waters (700-1000 meters) may be affected by a variable flow environment.

6.2 VIV of free span pipeline

6.2.1 Introduction

When leaving the relativeley flat continental shelf, and moving into deeper water, a more irregular bottom topography is often encountered. On-bottom pipelines from off-shelf fields, required to climb onto the continental shelf, may have to be installed so that parts of the pipeline are suspended freely between two supports. Freely suspended parts of the pipeline are usually referred to as *free spans*. This type of structure may also be found closer to the coast when crossing rough topography such as one may find in the vicinity of fjord sills, see Bjerke et al. (1995). The hydrodynamic loading on free span pipelines below the shelf edge is mostly due to current flow. Wind generated surface waves does not significantly influence the flow patterns close to the sea bed at these depths. It is well known that current flow may cause vortex induced vibrations (VIV) in free span pipelines. This phenomenon has been investigated in a series of research programs, see Marchesani et al. (1995), Bryndum et al. (1997) and references therein for an overview. The motivation for such a considerable research effort was to gain insight and understanding of the process, and to manifest this insight in a set of design guidelines for free-spanning pipelines. Parameters such as turbulence in the flow, proximity of the sea bed, pipe sagging, flow inclination angle relative to the longitudinal axis of the pipe, pipe-soil interaction and the dynamic coupling between adjacent free spans all influence the VIV of the pipe.

The quality of a fatigue life estimate of a given free span at a given location depends upon the quality of the input to the analysis and, of course, upon the 'goodness' of the analysis tool itself. Several tools are available. Det Norske Veritas have issued a set of guidelines (Veritas 2001a). These guidelines are developed on the basis of the aforementioned free span VIV research programs. There are also several

computer programs available that aim at predicting the VIV-response of conventional riser systems correctly, see e.g. Vandiver and Li (1995), Larsen et al. (2000), Triantafyllou (2000) and Furnes and Berntsen (2003). Not all of these computer programs, however, are able to calculate VIV of free-span pipelines.

Strong current perpendicular to the pipe will cause large VIV-amplitudes and, consequently, large fatigue damage in a free span. The pipeline can be accepted only if it is documented that the fatigue life of all spans is above an acceptable limit. Since the direction of the current relative to the pipeline axis is important when it comes to VIV response, it is necessary to include current directionality in the statistical description of the current.

Bjerke et al. (1995) reported results from current measurements in rough topography close to a fjord sill in Norway. The purpose of the study was to provide a design basis for a pipeline for transportation of oil from a field in the North Sea to the west coast of Norway. This study concluded that the near seabed currents close to the fjord sill were dominated by sporadic sill overflows of heavy Atlantic water intruding the deeper parts of the Norwegian Trench. Mathiesen (1996) presented analyses of near bottom current measurements over irregular seabeds for four locations outside the coast of Norway, and Mathiesen et al. (1997) discussed various aspects of the flow over irregular topography using measurements and numerical models.

In this section, the distribution of current speed and direction obtained from the measurements described in section 3.6 are applied in a VIV-analysis of a typical free span pipeline. The measurements are from a location where the bottom topography is very rough (see Figure 3.3). First, only the statistical distribution of the current speed is used, thereby neglecting the directional variability of the current, and the VIV of the free span is calculated as if the pipe was always exposed to flow perpendicular to its longitudinal axis. Next, the information that is available about the current direction is applied by decomposing the current velocity vector into a perpendicular component and an axial component. The perpendicular component is then used in the VIV calculations. The calculations are carried out for a set of different free span lengths, and for different global orientations of the free span. The effect on VIV of the longitudinal axis of the pipe being inclined to the current direction is also discussed, and some model test results, illustrating how the VIV is reduced in such cases, are presented.

The main contents of this section has been published earlier (Yttervik et al. 2003).

6.2.2 Current data

We use the data logged 20 meters above the top of the peak (current meter A3) for the purpose of this study (see section 3.6). We calculate three values of the 10 minute mean horizontal speed, $V_{H_{10}}$, on each HF time-trace and the corresponding horizontal flow directions, $\theta_{H_{10}}$, defined in the same way as θ_H in Figure 3.10. The 2D probability density function for $V_{H_{10}}$ and $\theta_{H_{10}}$ is defined by

$$p(v,\theta)\,dv\,d\theta = P[(v \le V_{H_{10}} \le v + dv) \cap (\theta \le \theta_{H_{10}} \le \theta + d\theta)] \qquad (6.1)$$

$$\int_0^{2\pi} \int_0^\infty p(v,\theta)\,dv\,d\theta = 1 \qquad (6.2)$$

where v is some horizontal speed and θ is some direction. Probability density functions for one of the variables are obtained by integration over the other variable.

$$p(v) = \int_0^{2\pi} p(v,\theta)\,d\theta \qquad (6.3)$$

$$p(\theta) = \int_0^\infty p(v,\theta)\,dv \qquad (6.4)$$

Plots of $p(v)$ and $p(\theta)$ for the current meter which was positioned 20 meters above the top of the peak (current meter A3) can be seen in Figure 6.1.

6.2.3 VIV-analysis procedure

The existing computer program system, VIVANA, described by Larsen et al. (2001), was used for the VIV-analyses. VIVANA in its original form predicts the vortex-induced vibrations perpendicular to the flow direction, i.e. the cross flow response. It is, however, also possible for the vortex shedding to excite the pipe in line with the current flow direction. This type of response is referred to as *in-line VIV*. The third type of VIV response occurs when the cross flow motion of the pipe induces oscillations in the in-line direction, see e.g. Furnes and Berntsen (2003). This type of VIV response is referred to as *cross-flow induced in-line VIV*. Only cross-flow VIV and in-line VIV are considered in the following analysis.

Cross-flow VIV in VIVANA

A thorough description of the theoretical background for the analysis method implemented in VIVANA for predicting cross flow VIV is given by Larsen et al. (2001). A brief outline will be given in the following.

VIVANA applies nonlinear 3D finite element technique for system modeling and static analysis. The specific VIV-analysis starts with finding a static solution for the forces and displacements of the structure to be analysed for a given current
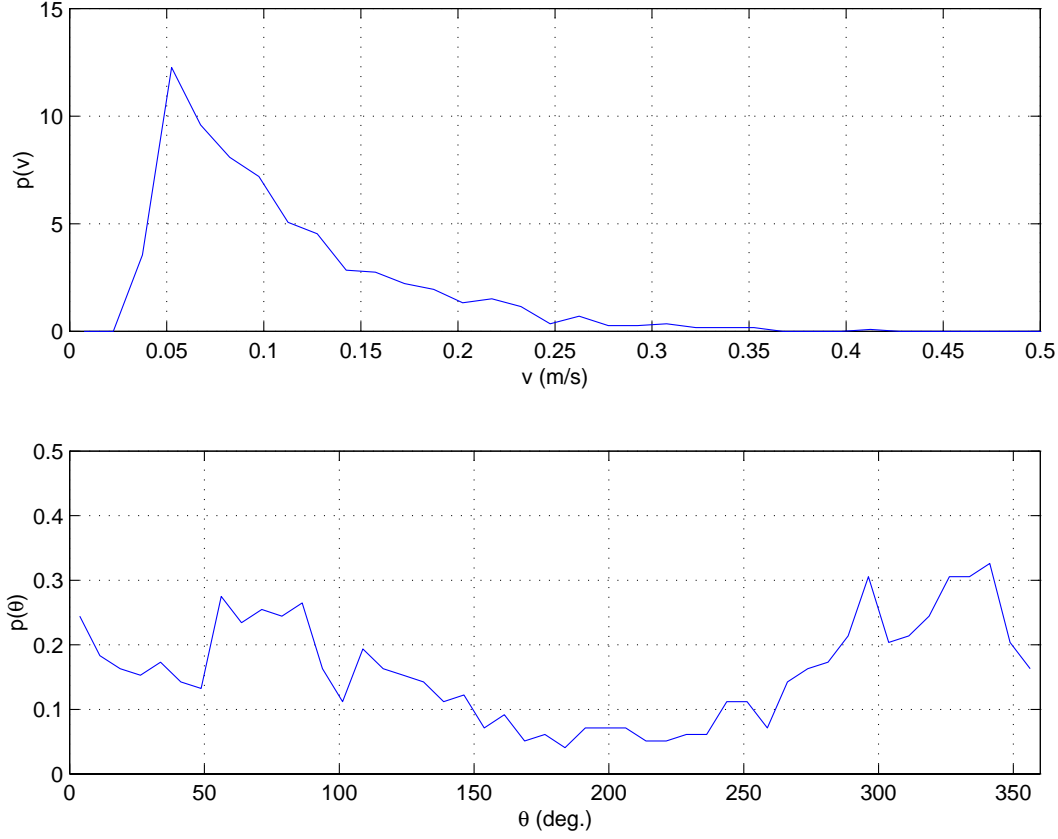
Figure 6.1: *Probability density functions.*

condition. The next issue is to find the response frequency. The basic assumption is that the response frequency is an eigenfrequency, and that this eigenfrequency is close to a corresponding eigenfrequency, calculated for still-water (non-oscillating structure). The eigenfrequency in still-water is different than the response frequency because added mass varies. The added mass along the cylinder is given as a function of a non-dimensional frequency, $\hat{f}_{CF}$, defined by

$$\hat{f}_{CF} = \frac{f_{osc,CF} \cdot D}{U} \tag{6.5}$$

where $f_{osc,CF}$ is the cross-flow oscillation frequency of the structure, D is the diameter of the cylinder and U is the cross flow speed. Several eigenvalue analyses are necessary in order to, through an iteration, find response frequencies which are consistent with the distribution of added mass along the pipe. The still-water frequencies that take part in the iteration are selected by considering the distribution of a non-dimensional frequency along the pipe, defined by

$$\hat{f}_{sw} = \frac{f_{sw} \cdot D}{U} \tag{6.6}$$

where f_{sw} is still-water eigenfrequency. The distribution of $\hat{f}_{sw}$ is compared to the maximum Strouhal frequency along the pipe. The Strouhal frequency is defined by

$$f_v = \frac{S_t(Re) \cdot U}{D} \tag{6.7}$$

where $S_t(Re)$ is the Strouhal number as a function of the Reynolds number, $Re = \frac{U \cdot D}{\nu}$. The kinematic viscosity of seawater, ν, is generally temperature dependant. All still-water eigenfrequencies which produce a non-dimensional frequency, $\hat{f}_{sw}$, anywhere along the pipe which is smaller than $max(f_v)$, are included in the iterations to find the possible response frequencies.

Once the candidates for the response frequencies have been established, excitation and damping zones along the cylinder are defined based on empirical data. Preliminary excitation zones along the pipe, for each of the possible response frequencies, are defined by the distribution of $\hat{f}_{CF}$. All areas of the pipe where $\hat{f}_{CF}$ is in the range from 0.12 to 0.2, using only the main excitation zone defined by Gopalkrishnan (1993), are considered to be a preliminary excitation zone. Once all possible response frequencies have been assigned their preliminary excitation zones, an excitation parameter, $E_{x,f_{osc}}$, is calculated for all possible response frequencies as

$$E_{x,f_{osc}} = \int_{L_{ex}} D^2(l) \cdot U^3(l) dl \tag{6.8}$$

where the integration is over the preliminary excitation zones belonging to the respective response frequenies. The possible response frequencies are then ranked according to the magnitude of $E_{x,f_{osc}}$, and the preliminary excitation zones are adjusted such that the preliminary excitation zone of the highest ranking frequency is left unchanged. The second highest response frequency retains its preliminary excitation zone, minus the length already occupied by the highest ranking frequency. The third ranked response frequency is assigned its preliminary excitation zone, minus the length already occupied by the two higher ranking frequencies, and so on.

Energy is put into the system in the excitation zones and removed through the damping zones. If there are no damping zones, which will be the case for most free spans where the cross flow speed is uniform along the pipe, damping is introduced by a self limiting mechanism. The lift coefficient becomes negative, and will contribute positively to hydrodynamic damping, when the amplitude exceeds a certain limit. This feature is illustrated in Figure 6.2.

VIVANA applies a set of lift coefficient curves where each curve is a second order polynomial defined by three points as can be seen in Figure 6.2. The points depend upon $\hat{f}_{CF}$ as are shown in the upper window of Figure 6.3. The curves are established based on empirical data from Gopalkrishnan (1993) and Vikestad
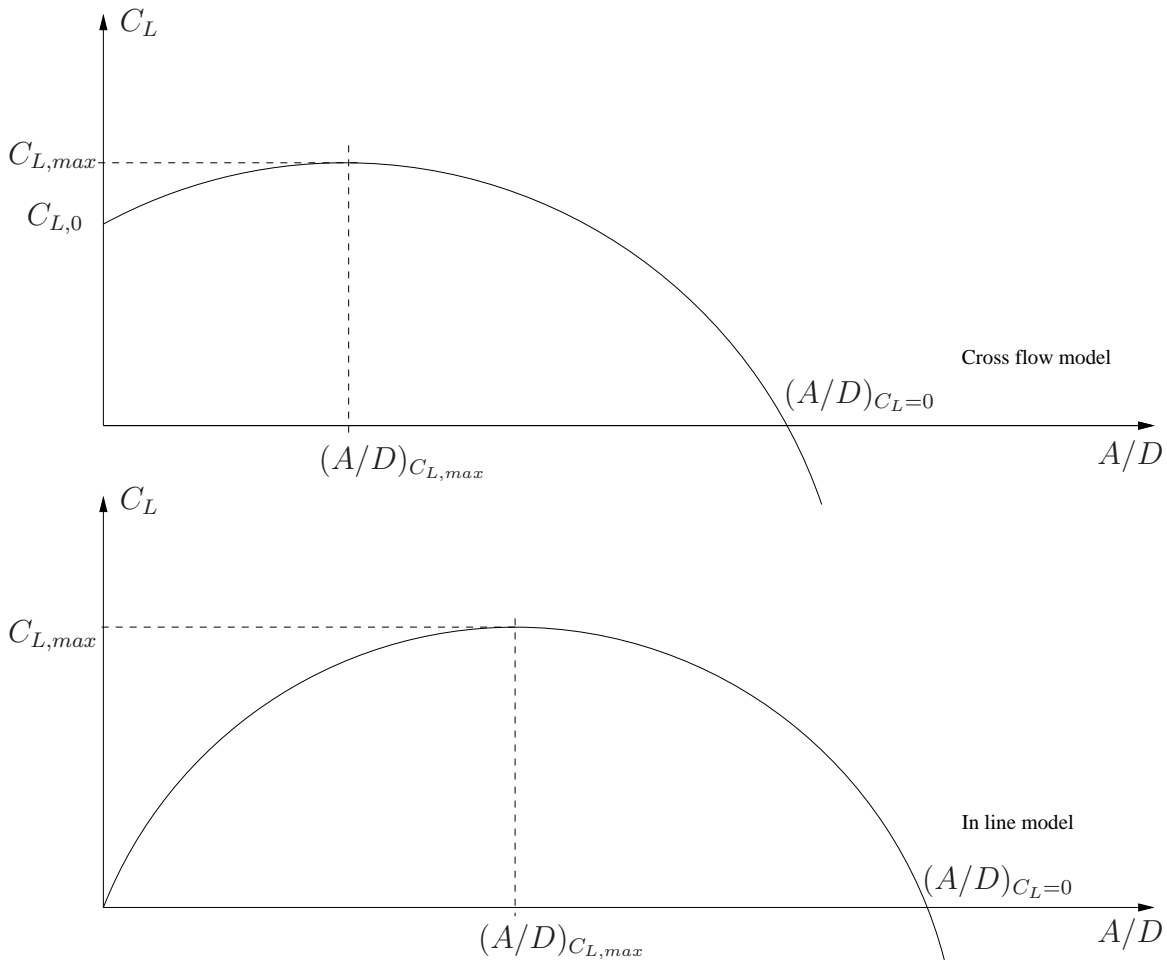
Figure 6.2: *Lift coefficient models in VIVANA.*

(1998).

In-line VIV in VIVANA

The VIVANA program has been extended to take in-line VIV into account. A simple model, based on the in-line response model recommended by DNV (Veritas 2001b), is used.

An important difference between the well-established cross-flow VIV model in VI-VANA and the new in-line VIV model, is in the method by which the response frequencies are found. Whereas the cross-flow response frequencies are consistent with a frequency dependent added mass, it is not possible to achieve this for the in-line response frequencies at present. The reason is that the relationship between frequency and added mass is not known for in-line oscillations. Therefore,

Figure 6.3: *Lift coefficient parameters for VIVANA.*

in the simple in-line VIV model proposed here, the assumption that the response frequencies are identical to the natural frequencies in still water, $f_{sw,IL}$, for the in-line modes is made. A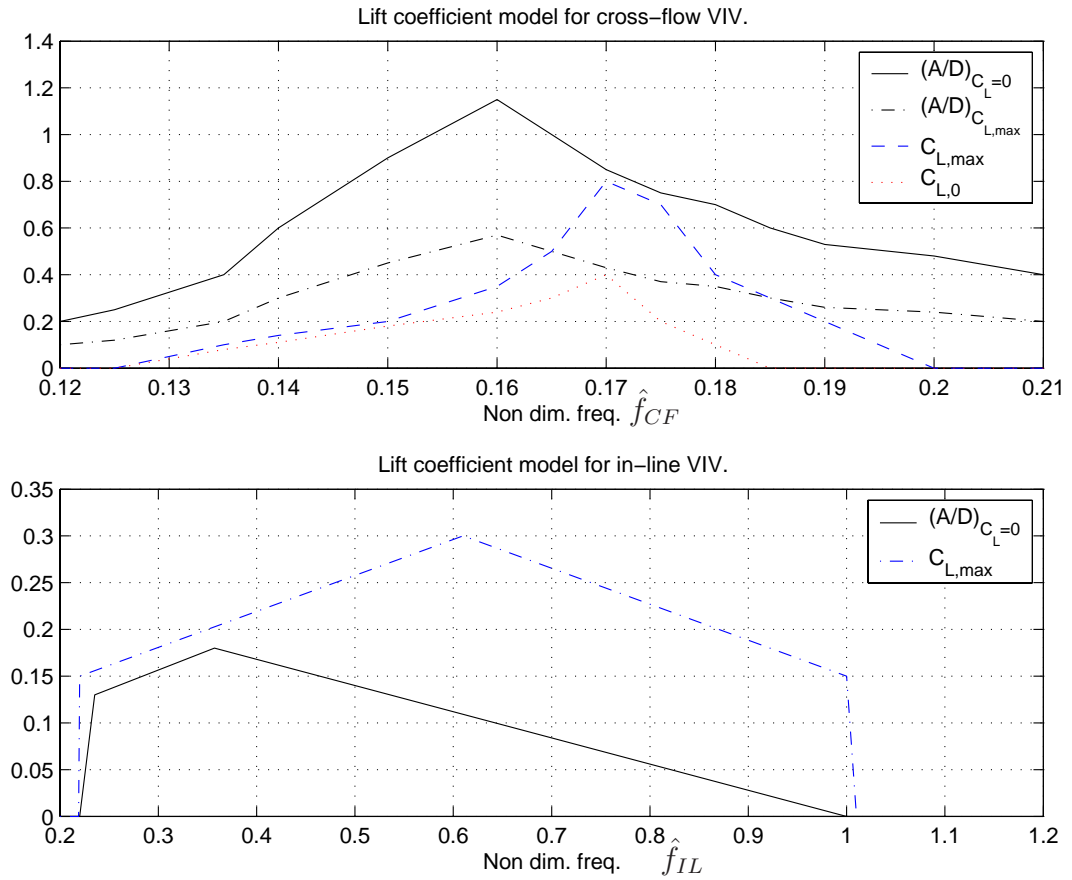ny in-line frequency giving a non-dimensional frequency, $\hat{f}_{IL} = \frac{f_{sw,IL} \cdot D}{U}$, between 0.25 and 1.0 anywhere along the pipe is considered to be a possible in-line VIV response frequency. Excitation zones and damping zones along the pipe are defined in the same way as for cross-flow VIV, using the non-dimensional frequency range 0.25-1.0. The same self-limiting mechanism, which comes into effect when the response amplitude exceeds a certain limit, as is used in the cross-flow VIV model is also at work in the new in-line VIV model.

A set of curves defining the relationship between reduced velocity, U_R, maximum in-line response, $(A/D)_{max}$, and a stability parameter, K_{SD}, is given in DNV's Recommended Practice for free spanning pipelines, (Veritas 2001b). The reduced velocity is defined by

$$U_R = \frac{U}{f_{sw,IL} \cdot D} \qquad (6.9)$$

The stability parameter represents the damping for a given modal shape. The curve corresponding to $K_{SD} = 0$ (zero damping) is used in the new model for in-line VIV. Structural- and hydrodynamical damping for in-line VIV is included in VIVANA in the same way as in the traditional cross-flow VIV model. Transforming the curve for $K_{SD} = 0$ so that it is given as a function of $\hat{f}_{IL} = \frac{f_{sw,IL} \cdot D}{U}$, which is the form used by VIVANA, we obtain the curve drawn with a solid line in the lower window of Figure 6.3. This curve has the same significance for prediction of in-line VIV as the solid-line curve in the upper window of Figure 6.3 has for prediction of cross-flow VIV. The lift coefficient model for in-line VIV is similar to that for cross-flow VIV. A set of lift coefficient curves where each curve is defined by two points as can be seen in Figure 6.2 is applied. The points depend upon $\hat{f}_{IL}$ as can be seen in the lower window of Figure 6.3. The curve for $C_{L,max}$ in the lower window of Figure 6.3 is tentatively drawn due to the lack of relevant empirical data. The lift coefficient corresponding to $A/D = 0$, C_{L_0}, is set to zero in the in-line VIV model, and

$$(A/D)_{C_{L,max}} = 0.5 \cdot (A/D)_{C_L=0}$$

is used for all values of $\hat{f}_{IL}$.

Response calculation

The VIV-response is calculated by the frequency response method. However, an iteration is necessary, and the reason for this is that the load depends upon the response (see Figure 6.2), and so does the hydrodynamic damping. The iteration, if successful, yields response amplitudes at the element nodes consistent with the loading. The frequency response method is not able to take into account all the nonlinearities that occur in connection with free spans, see Larsen et al. (2002). The focus here, however, is on the effect of directional distribution of the current speed and reduced lift from inclined flow. A linear response model is deemed sufficient for investigating these properties.

The assumption that several cross-flow induced in-line oscillation frequencies can coexist is made in computing the VIV-response. Recent model tests (Øritsland 2004) provide some support for this assumption. Assuming that this holds true for in-line VIV also, all possible in-line VIV response frequencies are considered to be active simultanously, irrespective of the presence of any cross flow response. The fatigue damage is thus calculated by adding the contributions from all possible in-line frequencies and from any cross flow frequency that is also present. Alternatively, in-line VIV could be treated in the same way as cross-flow VIV, i.e. by defining dominating frequencies. However, whereas a more refined procedure for selecting in-line VIV frequencies would no doubt lead to more accurate estimates of in-line VIV fatigue damage, the effect of current flow variability would still be the same.

6.2.4   Effect of inclined flow on VIV

Most of the lift coefficient data shown in Figures 6.2 and 6.3 are obtained from experiment. The exception is the curve for $C_{L,max}$ as a function of $\hat{f}_{IL}$ for in-line VIV, this curve is tentatively drawn due to lack of relevant empirical data. Most experimental data of VIV response is valid only when the current flow is perpendicular to the longitudinal axis of the pipe.

An extensive series of model tests of free span pipelines have been carried out at the Ocan Basin Laboratory facilities in Norway, Huse (2002). Some of the tests were performed with an inclined flow onto the pipeline, as is illustrated in Figure 6.4. The length of the span during the inclined flow tests was 11.413 meters
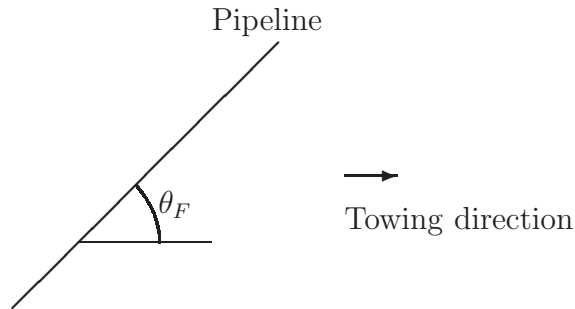

Figure 6.4: *Model tests with inclined flow.*

in model scale. This corresponds to 194.6 meters in full scale (the linear model scale during the tests was 1:17.05). Three flow directions were tested, $\theta_F = 90$, 60 and 30 degrees. The bending stiffness of the pipe was $300 \cdot 10^6\ Nm^2$ (full scale) and the diameter was 0.556 meters (full scale). The pretension was set to 344.5 kN (full scale) for the tests with $\theta_F = 90$ degrees, and 346.5 kN for the tests with $\theta_F = 60$ and 30 degrees. Time traces of the measured pipe curvature was logged at 10 locations along the length of the pipe for a number of different towing speeds. Mo and Solaas (2002) processed these data to obtain estimates of the pipe displacement by the method of modal decomposition. The relationship between a non-dimensional frequency and the maximum cross-flow displacement of the pipe can be seen in Figure 6.5. The two windows in Figure 6.5 contain exactly the same information, the only difference is the way that the non-dimensional frequency is calculated. The data, which are sparse, indicate that the maximum response as a function of $\hat{f}$ is the same for all θ_F if the flow direction is included in the calculation of $\hat{f}$. This indicates that inclined flow is sufficiently accounted for by using the component of the flow that is perpendicular to the pipe in the analysis of VIV.
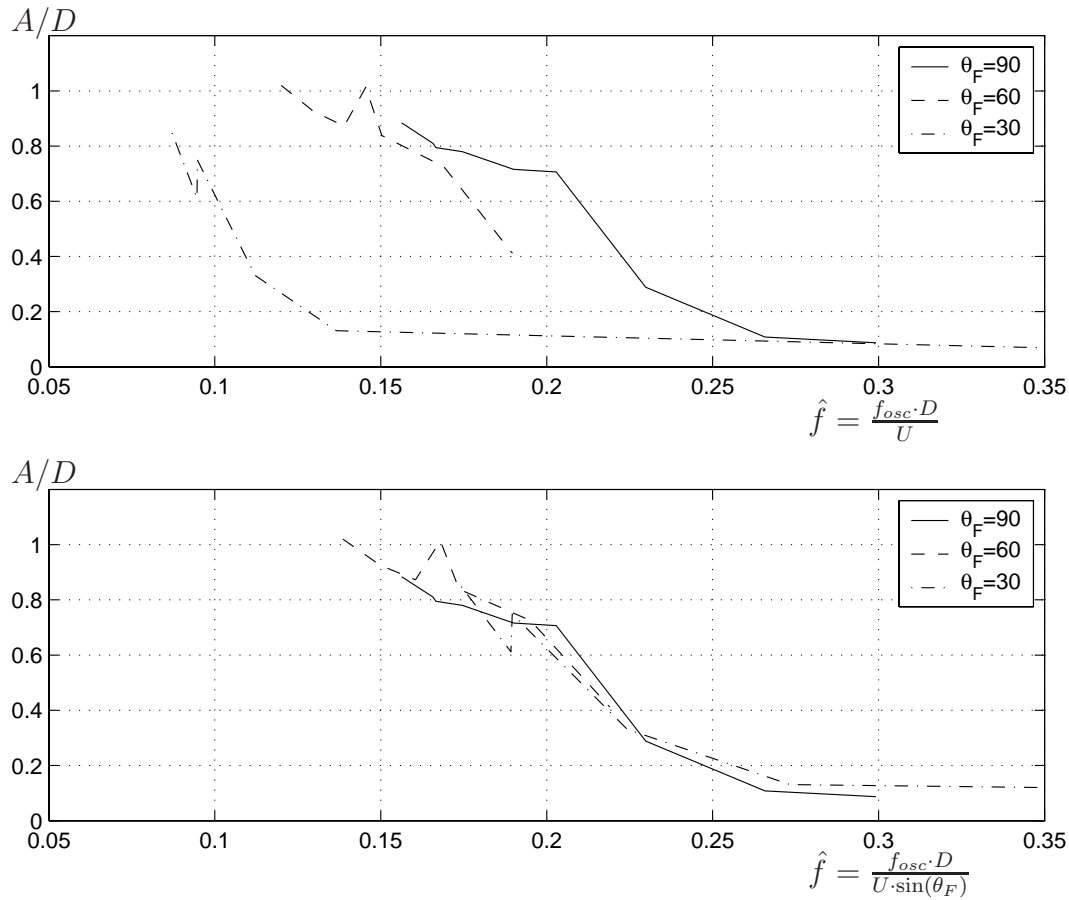
Figure 6.5: *Maximum displacement as a function of $\hat{f}$.*

One can read more on this feature in the book by Mutlu Sumer and Fredsøe (1997).

This means that a larger flow speed is required for the oscillation amplitude to reach a certain level, for a given response frequency, when the flow is increasingly inclined to the longitudinal axis of the pipe. The method by which the inclined flow is accounted for is therefore simply to use the component of the flow velocity vector that is perpendicular to the pipe in the analysis, otherwise the VIV analysis is unchanged. Even though only cross-flow response has been considered in reaching this conclusion, the same method is used for in-line VIV as for cross-flow VIV when calculating lift coefficients due to inclined flow. By this method the flow is always applied normal to the pipe. The static solution and the natural frequencies will therefore not be exactly the same as they would if the true current direction was used. A more refined method would be to use the static solution for the true current direction, and thereafter to include θ_F in the calculations of $\hat{f}$ throughout the remaining part of the analysis. Here, however, the 'perpendicular

flow component'-method is used. The error in making this simplification (neglecting axial drag on the pipe) is small.

6.2.5 Case studies

Near-bed current flow data, and the findings from model tests of VIV in inclined flow, are applied in an analysis of the fatigue life of a typical free span pipeline. Annual fatigue damage is estimated by two different methods as outlined in the following. Total fatigue life is the inverse of total annual fatigue damage.

Method 1 - Not accounting for the directional distribution of the current flow or the pipeline orientation.

Using this method, the directional distribution of the current is disregarded and only the statistical distribution for the flow speed is used when the fatigue damage is calculated. The orientation of the pipeline in the global coordinate system is irrelevant for this method because all flow is considered to be directed perpendicular to the longitudinal axis of the pipe. The total annual fatigue damage is found from

$$D_1 = \int_0^{0.5} D(v) \cdot p(v) \, dv \qquad (6.10)$$

where $D(v)$ is the resulting annual fatigue damage from a VIV-analysis using a flow speed of magnitude v directed perpendicular to the longitudinal axis of the pipe. The probability density function for the current speed, $p(v)$, is defined in equation (6.3). Calculations are carried out for different free span lengths.

Method 2 - Accounting for the directional distribution of the current flow and the pipeline orientation.

With this method, the available statistical distribution of the current speed and direction is taken into account when the fatigue damage is calculated. The following variables are used (see Figure 6.6),

- θ_{CG} - positive clockwise.

  - Current direction in the global coordinate system. The directional distribution, $p(\theta)$, refers to this parameter.

- θ_R - positive clockwise.

  - The orientation of the free span in the global coordinate system.

- θ_{CR} - positive counter-clockwise.

– Current flow direction relative to a local coordinate system (X_V, Y_V, Z_V) used by the computer program VIVANA.

From Figure 6.6, the following expression for θ_{CR} can be established (note that angles are defined differently in the global and the local coordinate system),

$$\theta_{CR} = 360 + \theta_R - \theta_{CG}$$

The total annual fatigue damage for a given span direction (θ_R) is found from

$$D_{\theta_R,2} = \int_0^{0.5} \int_0^{360} D_2(v, \theta_{CG}) \cdot p(v, \theta_{CG}) \, d\theta_{CG} \, dv \tag{6.11}$$

where $D_2(v, \theta_{CG})$ is the resulting annual fatigue damage from a VIV-analysis using a flow speed of magnitude $V_{CF} = v \cdot \sin \theta_{CR}$ directed perpendicular to the longitudinal axis of the pipe. The 2D probability density function for current speed and direction, $p(v, \theta)$, is defined in equation (6.1).
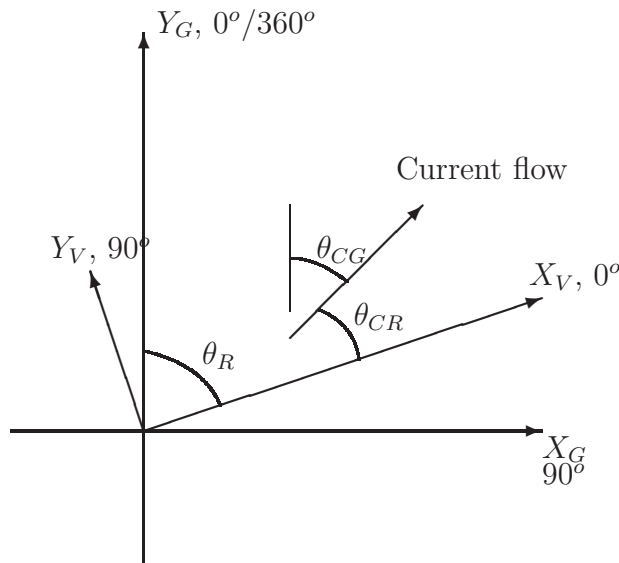
Figure 6.6: *Definition of θ_{CG}, θ_R, and θ_{CR}.*

The effect of the directional distribution of the current on the estimated fatigue damage due to VIV is thus studied by running the fatigue analyses for different global orientations of the free span. Calculations are carried out for different free span lengths.

Structural model of the free span

An idealized model of a free span was used for the case studies, see Figure 6.7. In
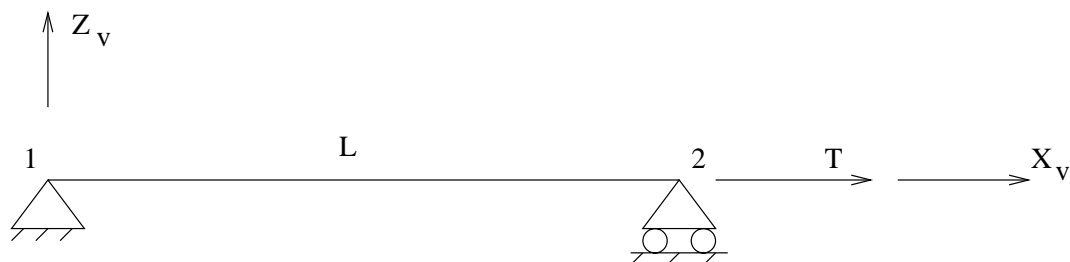

Figure 6.7: *Idealized model of a free-span pipeline.*

this model, the pipe is pinned at both ends. Translational degrees of freedom are all fixed at end 1. At end 2 the vertical degree of freedom and the horizontal degree of freedom normal to the longitudinal axis of the pipe is fixed, but the horizontal degree of freedom along the longitudinal axis of the pipe is free. A pretension, T, is applied in this degree of freedom. A total of 150 3D beam elements were used for modelling the free span. Mechanical and geometrical properties for the structural model of the pipeline can be found in Table 6.1. Natural frequencies in still water for all span lengths considered are listed in Table 6.2.

Property	Symbol	Unit	Numerical value
Outer diameter	D	m	0.55
Inner diameter	D_i	m	0.50
Wall thickness	t	m	0.025
Modulus of elasticity	E	kN/m^2	$2.07 \cdot 10^8$
Mass per unit length	M	kg/m	324
Submerged weight	W	kN/m	0.786
Steel area	A_{st}	m^2	0.041
Section modulus	W_{st}	m^3	0.0518
Pretension	T	kN	200

Table 6.1: *Mechanical and geometrical properties of the structural model.*

6.2.6   Results, discussion and conclusions

Results from the analyses are compiled in Tables 6.3 and 6.4. Plots are enclosed in Appendix B. Estimated fatigue damage along the pipe, calculated by method 1, is shown in Figures B.1 and B.2. The maximum estimated fatigue damage due to cross-flow VIV and in-line VIV is shown in Figures B.3 and B.4, respectively.

Span length	Mode1	Mode2	Mode3
(m)	(Hz)	(Hz)	(Hz)
50	0.49	1.85	4.17
80	0.21	0.75	1.63
100	0.15	0.49	1.05
125	0.10	0.33	0.69
150	0.08	0.24	0.49
180	0.06	0.17	0.35

Table 6.2: *Natural frequencies in still water.*

Estimated fatigue damage along the pipe, calculated by method 2, is shown in Figures B.5-B.10.

Length of	Cross flow		In line	
free span	Min. fatigue life	Location	Min. fatigue life	Location
(m)	(years)	(m)	(years)	(m)
50	$2.4 \cdot 10^8$	24.8	8664	24.8
80	1324	39.7	15858	21.6
100	2606	49.7	7104	23.7
125	2203	62.1	3984	24.6
150	618	111.5	2916	23.5
180	863	133.8	1775	23.4

Table 6.3: *Results from the calculations by method 1. Minimum estimated fatigue life (years) and location of worst damage (m from end 1).*

When the length of the free span is decreased, the damage from cross flow VIV, calculated by method 1, first increases, then it decreases until L=100m, and then it increases again (L=80m), see Figure B.3. The large damage at L=180m and L=150m is caused by the presence of the second mode in the response (see Figure B.1). Only first mode response is observed for the shorter span lengths. The accumulated damage is governed by the stresses that are caused by the VIV and by how often they appear. If the span length is reduced, the flow speed that is required to create VIV increases, and the number of occurrences of VIV (for a given distribution of the flow speed) decreases. At the same time, the stresses that occur, if VIV is created, increase. In conlusion, a reduction of the span length affects the parameters that govern the fatigue damage differently. It is therefore difficult to say something beforehand on whether the fatigue damage will go up or down if the span length is changed. Detailed analyses, using a model of the actual pipe, are necessary. This feature is not seen as clearly for in-line VIV or when

Length of free span (m)	θ_R (deg.)	Cross flow		In line	
		Min. fatigue life (years)	Location (m)	Min. fatigue life (years)	Location (m)
50	0.0	$2.38 \cdot 10^{18}$	24.8	41309	24.8
	45.0	$1.30 \cdot 10^{18}$	24.8	21025	24.8
	90.0	$1.10 \cdot 10^{19}$	24.8	$1.37 \cdot 10^{5}$	24.8
	135.0	-	-	-	-
80	0.0	$4.50 \cdot 10^{15}$	39.7	53758	39.7
	45.0	$2.26 \cdot 10^{15}$	39.7	41704	39.7
	90.0	$6.62 \cdot 10^{15}$	39.7	58988	39.7
	135.0	$1.68 \cdot 10^{18}$	39.7	$5.78 \cdot 10^{5}$	39.7
100	0.0	4048	49.7	37721	25.7
	45.0	4170	49.7	19744	27.1
	90.0	20020	49.7	$1.06 \cdot 10^{5}$	29.6
	135.0	$7.23 \cdot 10^{16}$	49.7	$4.91 \cdot 10^{5}$	62.1
125	0.0	10177	62.1	19895	26.3
	45.0	3940	62.1	11165	27.1
	90.0	21417	62.1	42002	29.6
	135.0	$2.37 \cdot 10^{16}$	62.1	$1.25 \cdot 10^{6}$	62.1
150	0.0	8725	73.5	13207	27.5
	45.0	7625	73.5	6785	27.5
	90.0	9735	73.5	27276	30.5
	135.0	$5.96 \cdot 10^{16}$	75.5	$6.81 \cdot 10^{5}$	30.5
180	0.0	6890	132.6	9070	27.0
	45.0	3573	133.8	5007	27.0
	90.0	23729	87.0	17210	30.6
	135.0	64486	87.0	$3.92 \cdot 10^{5}$	46.2

Table 6.4: *Results from the calculations by method 2. Minimum estimated fatigue life (years) and location of worst damage (m from end 1).*

method 2 is applied. This does not mean, however, that it is not present for these cases. It is entirely possible that a different current distribution would bring it out.

It is clearly seen that the orientation of the free span, relative to the prevailing flow directions, is an important parameter when estimating the fatigue life of free span pipelines. As one would expect, the accumulated fatigue damage is significantly reduced when the directional distribution of the current flow is taken into account.

The damage from in-line VIV is generally lower than the damage from cross flow VIV for all but the shortest span lengths, the exception is the damage calculated

for $\theta_R = 45$ degrees for the span length of 150 meters. In this case the cross flow damage and the in-line damage are comparable.

From Figures B.1 - B.10 it can be seen that the in-line response often contains higher modes than the cross flow response. The reason for this is that the excitation zone for in-line VIV extends over the non-dimensional frequency range 0.2 to 1.0, whereas the excitation zone for cross flow VIV is in the range from 0.125 to 0.2.

6.3 Marine operations in deep water in a variable current flow environment

6.3.1 Introduction

Floating offshore structures installed in deep water areas require longer mooring lines than those installed in shallower areas. The floating structure needed to carry the load of such mooring systems, and the accompanying riser systems, must be larger than for shallower water depths. Mooring systems and the floating structure for deep water fields will thus be more expensive than for shallower water fields. It is therefore believed that the increasing number of deep water fields for oil- and gas production will be developed using sub-sea solutions to a greater extent than what has been common practice at more moderate water depths, thus prompting an increased need of marine operations for maintenance and installation. Combinations of surface vessels, slender structures (spool pieces, risers, cables), lifted/lowered objects and underwater robotic tools may have to be called upon to interact simultanously during marine operations. The large distance from the sea bed to the surface, together with the complexity of such operations, will cause the duration of typical operations to increase as the water depth increases.

Over time scales typical of complex marine operations ($>$ 6 hours) it is not always correct to view the current conditions in the ocean as being constant at a given location. Variations on a time scale of $O(1\,\mathrm{h})$ in direction and speed of the flow can be observed for the entire water column. Variations on a time scale of $O(1\,\mathrm{min})$, due to the interaction between the sea bed and a rotating stratified fluid, have been observed in the bottom boundary layer of the ocean, see e.g. Gemmrich and van Haren (2001). This interaction can be especially energetic on a continental slope and when the topography is rough, as has already been discussed in section 2.4.

If marine operations become more time consuming (due to increased complexity and increased water depth), and the current forces become more important than the wave forces (due to increased water depth), it is possible that variations of the current in time and space sometimes will be of importance and may cause unforeseen, and possibly unwanted, forces and motions.

The work reported in this section was carried out in order to study the influence of a variable current environment on simple marine operations in relatively deep waters (700-1100 meters).

Results from computer simulations of an operation, involving the lowering of three different objects from the surface to the sea bed, are presented. Measurements of the current flow in the entire water column, at two locations on the continental slope outside Mid-Norway (OL-I and OL-II, see Figure 3.2), described in section 3.5, were used as input to the simulations. The current data were sampled using sampling periods of 10 and 30 minutes, and the small scale variability of the current is therefore not well resolved. Typical time scales for marine operations, however, are well resolved by this sampling interval.

Results from computer simulations of the behaviour of objects near the seabed, suspended from a surface vessel in a variable current environment, are also presented. The current flow data used for these simulations were sampled five meters above the seabed in the same area.

The main contents of this section has been published earlier (Yttervik et al. 2003).

6.3.2   Current flow input

Measured current profiles

From the measured current profiles described in section 3.5, a number of data sets, each with a duration of 12 hours, have been selected and used as input to the computer simulations. Data sets containing large flow speed and/or abrupt changes in flow speed and direction were selected. See Table 6.5 for a list of the selected data sets. Time traces of the flow speed components for current flow case LFP1 are plotted in Figure 6.8.

Measured current close to the sea bed

Some time traces from the HF-measurements of current flow near the sea bed, described in section 3.6, have been selected and used as input to the simulations of motion of suspended objects. As noted in section 3.6, it seems evident that the measurements are sometimes influenced by vortex-induced vibrations of the buoyancy elements used in the current meter mooring system, see Figure 3.19.

The time traces used as input to the simulations were band-pass filtered prior to further use. Filter frequencies were 0.057 and 0.064 Hz.

Profile id.	Location	Water depth (m)	Start time of current time trace (date and time)	Start winch	Stop winch
LFP1	OL-II	775	25-Nov-1999 17:10	3.9	5.9
LFP2	OL-II	775	04-Nov-1999 04:50	6.1	8.1
LFP3	OL-II	775	28-Nov-1999 13:00	5.7	7.7
LFP4	OL-II	775	20-Apr-2000 21:50	6.1	8.1
LFP5	OL-II	775	23-Apr-2000 03:30	6.9	8.9
LFP6	OL-II	775	13-Jul-2000 16:00	5.9	7.9
LFP7	OL-II	775	20-Jul-2000 11:50	1.9	3.9
LFP8	OL-II	775	21-Nov-2000 08:40	3.9	5.9
LFP9	OL-II	775	28-Nov-2000 01:40	4.0	6.0
LFP10	OL-I	1088	22-Nov-1999 22:30	4.6	7.4
LFP11	OL-I	1088	02-Dec-1999 01:30	3.7	6.5
LFP12	OL-I	1088	16-Dec-1999 13:10	1.4	4.2
LFP13	OL-I	1088	06-Mar-2000 23:50	3.1	5.9
LFP14	OL-I	1088	21-Mar-2000 08:10	4.6	7.4
LFP15	OL-I	1088	17-Jul-2000 22:20	4.6	7.4
LFP16	OL-I	1088	02-Jul-2000 10:30	4.8	7.4

Table 6.5: *Selected current flow cases (profiles). The start and stop times of the winch are in hours after the start time of the current time trace.*

Trace ID.	Time of occurrence	V_H (m/s)	θ_H (deg)	V_{MAX} (m/s)
HF-1	03-Nov-2001 21:00	0.22	21	0.47
HF-2	08-Dec-2001 07:00	0.37	135	0.54
HF-3	08-Dec-2001 09:00	0.31	113	0.48
HF-4	15-Nov-2001 09:00	0.20	351	0.33
HF-5	15-Nov-2001 13:00	0.22	143	0.38
HF-6	04-Dec-2001 23:00	0.29	138	0.50

Table 6.6: *Selected time-traces from the HF-measurements (near the sea bed).*

As can be seen from Figure 3.20 there were periods of much current activity and periods of less current activity during the entire period of HF-current measurements. The largest flow velocities ocurred during periods of much current flow activity. Some time traces, containing large flow velocities and abrupt changes to the flow, have been selected to be used as input to the simulations of suspended objects.

The time when the selected time traces were recorded, and some characteristic parameters, such as mean horizontal flow speed, V_H, mean horizontal flow direction, θ_H, and maximum recorded flow speed, V_{MAX}, are listed in Table 6.6. All selected time traces are plotted in Figure 6.9.
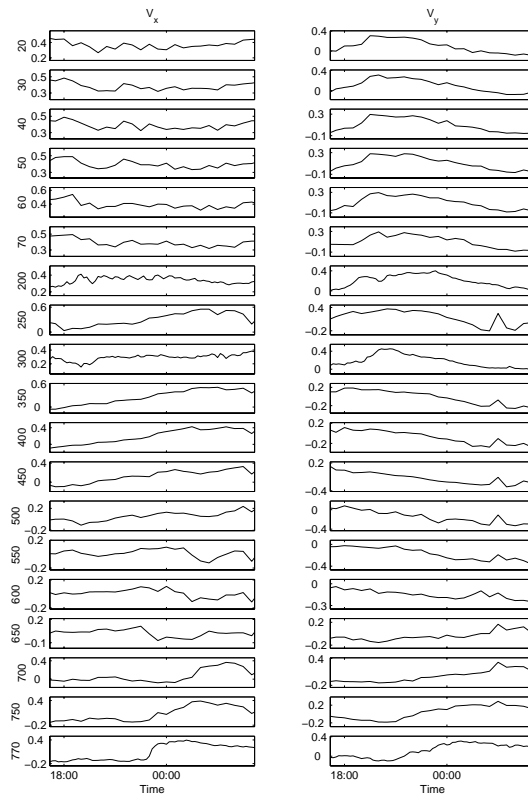
Figure 6.8: *Time traces of measured flow velocity components for each respective depth for the current flow at OL-II on November 25th. Flow speed unit is m/s.*

6.3.3   Simulation of marine operations

General

Marine installation/intervention operations often involve vertical transport of objects from a surface vessel to the sea bed. Such objects can be Remote Operated Vehicles (ROVs) with cable drums and Tether Management System (TMS) of various sizes, or they can be larger structures such as Universal Tie-In System tools (UTIS) used for tie-in of pipes to subsea templates. A variety of other objects will generally also be of interest, but the present work is concentrated on objects similar to the ROV (with TMS) and the UTIS.

Physical properties and hydrodynamic coefficients for the objects used in the simulations are presented in Table 6.7. Hydrodynamic drag in the x-direction on an object is calculated from

$$F_x = \frac{1}{2}\rho B_x C_{db} v_{rx} |v_{rx}|$$

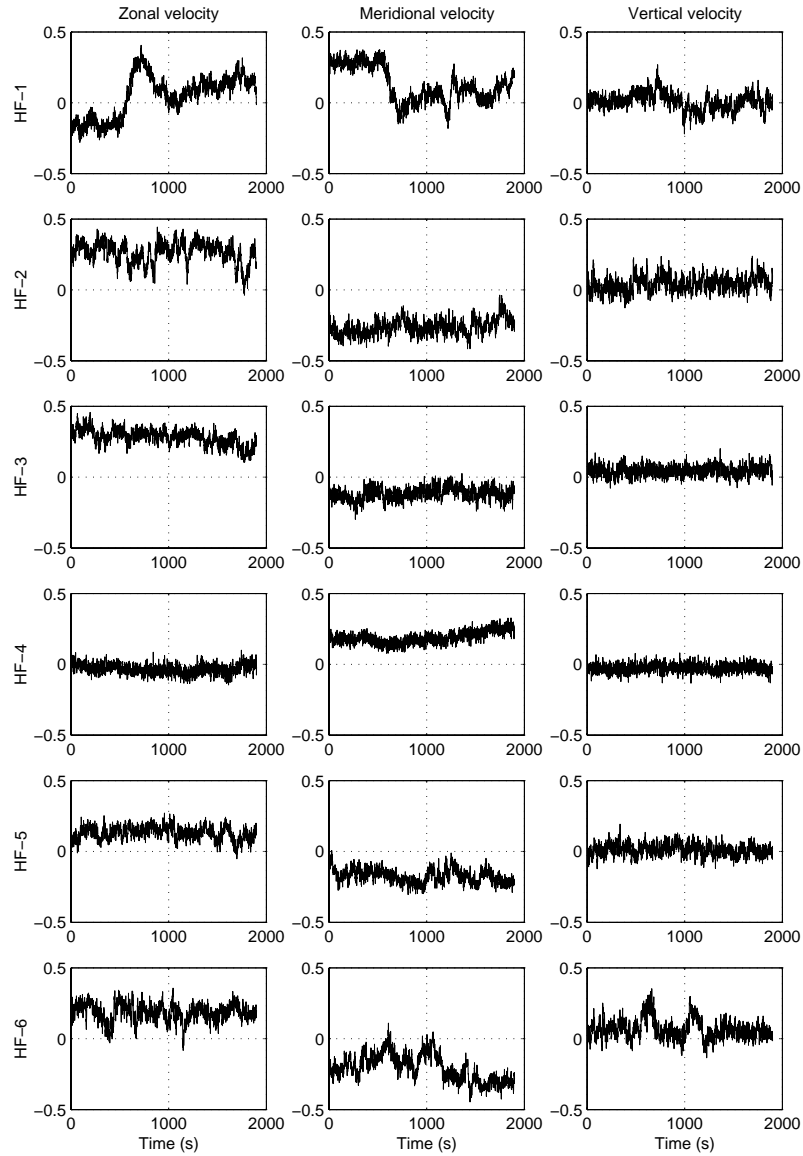Expressions for the drag in the other directions follow suit. The vertical stratifi-

Figure 6.9: *Selected time traces of measured flow speed (in m/s) near the sea bed.*

cation, described in section 3.4 and depicted in Figure 3.4, is not considered to be so strong as to require the use of variable water density when calculating the drag forces on the lowered objects. We therefore use a constant value of 1025 kg/m³ for the density of the seawater, ρ, when calculating forces on an object. Further, v_{rx} is relative velocity in the x-direction between the water and the object , and B_x is explained in Table 6.7. Added mass is not important for the simulations of the lowering of an object from the surface to the sea bed. The response of the object is considered to be quasi-static during this operation, and an added mass equal to

Object				ROV1	ROV2	UTIS
	Property	Symbol	Unit	Numerical value		
Body						
	Mass	M	ton	3.9	6.1	16.0
	Buoyancy	B	ton	2.5	5.13	2.05
	x-dir. drag area	B_x	m^2	7.75	12.0	10.0
	y-dir. drag area	B_y	m^2	7.75	12.0	7.2
	Vert. drag area	B_z	m^2	4.0	6.0	5.0
	x-dir. added mass	A_{M_x}	ton	6.0	12.0	7.2
	y-dir. added mass	A_{M_y}	ton	6.0	12.0	5.2
	Vert. added mass	A_{M_z}	ton	3.1	6.0	3.6
	Drag coefficient	C_{db}		1.0	1.0	1.0
Cable						
	Diameter	D_c	mm	32	32	40
	Mass	m_c	kg/m	2.83	2.83	5.5
	Buoyancy	b_c	kg/m	0.79	0.79	1.29
	Axial stiffness	EA	kN	26e3	26e3	72.6e3
	Drag coefficient	C_{dc}		1.5	1.5	1.5

Table 6.7: *Physical properties and hydrodynamic coefficients for the objects used in the simulations.*

the structural mass is used as input to the dynamic analysis. In the simulations using the HF-current measurements, however, the added mass values listed in Table 6.7 were used.

The parameter

$$\gamma = \frac{(M - B) \cdot g}{\rho B_x U^2} \qquad (6.12)$$

gives the ratio between weight in water and drag force, and is used in order to explain the differences in response of the various objects.

Simulation of winch operation

The motions of the objects described in Table 6.7, prior to-, during- and after being lowered from just below the water surface to approximately five meters above the sea bed in a variable current environment, described by the measured current profiles described in section 6.3.2, have been calculated. The objects were connected to a fixed point on the surface by a lift-wire, modelled by 3D finite elements. Pay-out of lift-wire was simulated by increasing the stressfree length of the finite elements (while keeping the number of elements constant) during the non-linear time domain analysis option offered by the RIFLEX computer program (Fylling and Sødahl 1995). RIFLEX is a non-linear finite element program for time domain simulation of motion and forces of slender flexible structures such as lift-wires, mooring lines, umbilicals, pipelines and risers. Static and dynamic

forces due to the motion of the line, attached objects and the current are included.
A pay-out speed of v_w was obtained by elongating the elements in the line by

$$\Delta l_e = \frac{v_w \cdot \Delta t}{N_e} \tag{6.13}$$

within each time step, Δt. N_e is the number of elements used for modelling the
lift-wire. The node at the lower end will have the correct vertical velocity, but all
other nodes will have a lower vertical velocity when this method is used. For a
bare lift-wire, however, axial drag can generally be neglected, and the discrepancy
in the axial velocity of the line, therefore, has no significant effect on the calculated
response.

An initial lift-wire length of 50 m was used for the simulation cases LFP1 - LFP9,
whereas a length of 75 m was used for the the cases LFP10 - LFP16. A pay-out
speed of $v_w = 0.1$ m/s was used for all cases. Total time required for lowering the
object to a height of five m above the sea bed is, thus, 2 hours at 775 m water
depth and 2.8 hours at 1088 m water depth. Pay-out of lift wire was started at
different times for the various cases as can be seen in Table 6.5. The entire length
of the current flow data set (12 hours) was used in each respective simulation, and
the motions of the objects were calculated over the whole of that period.

Simulation of objects near the sea bed

The motions of the objects described in Table 6.7, using the current flow events
listed in Table 6.6 and plotted in Figure 6.9, as external forcing, have been calcu-
lated. This was done in order to study the response of the objects under the influ-
ence of rapid current variations near the sea bed. Generally, ROVs are equipped
with thrusters for active manoevring and positioning. For the purpose of this
study, however, all objects were kept passive during the simulations in order to
illustrate the effect of the fluctuating current flow on objects of different size and
shape. A full model of a typical offshore supply vessel, with the submerged ob-
jects attached to a lift-wire suspended from a crane, was used in the simulations.
Simulations were carried out in calm water, i.e. with the upper end of the lift-wire
fixed, and also in irregular waves with a direction of 30 degrees to the bow of the
vessel. Waves with a significant wave height of 1 meter and a peak period of 7 sec-
onds were used. The water depth in the simulations was 680 meters. The vessel
was kept on location by a dynamic positioning (DP) system. The SIMO computer
program (Reinholdtsen and Falkenberg 2001) was used for the simulations. SIMO
is a time domain simulation program for multibody systems, allowing non-linear
effects to be included in the wave-frequency range. A catenary element model was
used for modelling the lift-wire. Static current drag forces on the elements are
included in the model, but relative velocity between the cable and the current flow
is not accounted for at present. Further information of the element formulation

and application may be found in Leonard (1988), Peyrot and Goulois (1979) and Sødahl (1991).

Whereas the forces on the suspended objects were computed from the current flow time series described in section 6.3.2, a uniform static current profile with a flow speed of 0.2 m/s and a flow direction of 270 degrees (due west) was used for applying current force to the lift-wire. This was done because no current flow data are available for the water masses above the boundary layer. The uniform static current profile is obviously not consistent with the time varying current. However, the effect of using a different static current profile would only be to change the static offset of the lift-wire and the suspended object. The stiffness characteristics of the system (wire and suspended load) will change as a result of a change in static offset. When the angle of attack of the lift wire increases due to increased current load the horizontal stiffness of the system also increases. It is believed, however, that a significantly larger change in the angle of attack of the lift wire, than what would occur with realistic current profiles, is required for the motions of the suspended objects, due to the fluctuating current, to be significantly changed.

A total of 1900 seconds were simulated for each event, corresponding to the total length of the measured current flow time series.

6.3.4   Results and discussions

Winch operation

Simulations of the lowering operations were carried out using combinations of the current cases in Table 6.5 and the objects listed in Table 6.7.

In addition to calculating the position of the object at all time before and during the lowering process, and also after arriving at the desired depth, a target position on the sea bed was estimated. This was done by performing a static analysis of the full length lift-wire with the suspended object at the end, using the measured current profile at the time when the lowering operation was started. If the entire current profile could have been measured from the supply vessel, this target position would be the best guess possible of where the lowered object would land at the sea bed, assuming that the current did not change in the meantime. Horizontal distance between estimated target position and actual position of the object when arriving at the desired water depth, for all cases simulated, are listed in Table 6.8.

Results from the simulations of the lowering operation can be found in Figures C.1-C.8 in Appendix C. Traces of the horizontal (x-y) position of the objects are shown with dots for every 15 minutes. The starting position is near the origin. The crosses in each figure mark the estimated target positions, whereas the circles mark the

OL-II. Depth : 775 m				OL-I. Depth : 1088 m			
Current profile case	ROV2	ROV1	UTIS	Current profile case	ROV2	ROV1	UTIS
	(m)	(m)	(m)		(m)	(m)	(m)
LFP1	9.0	5.8	1.1	LFP10	11.9	3.2	0.7
LFP2	20.1	11.9	2.0	LFP11	12.5	9.6	1.3
LFP3	57.4	28.9	5.4	LFP12	16.4	13.4	2.9
LFP4	7.1	4.3	0.6	LFP13	9.9	5.3	0.9
LFP5	9.8	6.4	1.0	LFP14	5.4	3.9	1.1
LFP6	3.7	2.3	0.4	LFP15	12.9	9.8	2.0
LFP7	7.9	6.7	1.3	LFP16	5.9	4.4	0.8
LFP8	6.2	3.6	0.6				
LFP9	8.2	5.2	1.2				

Table 6.8: *Horizontal distance between the estimated target position of the object and the actual position when arriving at the sea bed.*

actual positions of the object when arriving at the desired depth. The upper row in each particular figure contain the results for ROV2, which is the object with the lowest ratio between weight in water and drag force, γ, for the current cases selected. Results for ROV1 are displayed in the middle row, and results for the object with the largest weight in water, the UTIS, are shown in the third row.

ROV2 is slightly lighter in water than ROV1, but it has a significantly larger drag area. From Figures C.1-C.8 it is clearly seen that ROV1 has the smallest motions of the two ROVs in a time-varying current. It is also evident that the difference between the estimated target position and the actual position of the object when arriving at the desired depth is reduced when γ is increased, as can also be seen in Table 6.8. This is according to what one would expect (incresed tension results in increased stiffness). The magnitude of the difference between predicted and actual position for any object is, of course, totally dependent upon the current variability, and is seen to vary considerably for the cases shown in Figures C.1-C.8.

The pay-out speed used on the winch when lowering objects from the surface during marine operations depends upon the type of object being lowered. Light objects are generally lowered faster than heavier objects. It could be argued that using v_w = 0.1 m/s for ROV1 and ROV2 is not necessary realistic, and that the difference between the estimated target position and the actual position when arriving at the desired depth is therefore overestimated in this study. Although this is true, most marine operations will last longer than just the time required for lowering an object from the surface to the sea bed. The motions that occur after the desired depth is reached are therefore also of interest. These motions are considerable for the cases shown (Figures C.1-C.8).

Suspended objects near the sea bed

Simulations of the objects described in Table 6.7, suspended near the sea bed have been carried out. The HF-measurements of current speed, listed in Table 6.6, were used for external current forcing. A uniform static current profile was used for applying current force to the lift-wire, and the simulations were carried out with- and without vessel motions present at the upper end of the lift-wire.

Some selected results from the simulations are presented in Figures C.9-C.13 in Appendix C. Traces of the horizontal (x-y) position of the objects are shown with dots for every two minutes. Horizontal speed of the objects, due to the forcing from measured time trace HF-1, have been calculated, and are shown in Figure C.9. Horizontal speeds of as much as 0.3 m/s were found for ROV2 (low γ), whereas the UTIS (large γ) moved more slowly.

The influence of the wave frequency motions and the minor low-frequency motions (controlled by dynamic positioning) of the surface vessel on the motions of the suspended object is taken into account in the simulation model. Figures C.10 and C.11 contain results from simulations with- and without a dynamically positioned vessel at the upper end of the lift-wire, and ROV2 and UTIS, respectively, at the lower end of the lift-wire. Results using current cases HF-1, HF-2 and HF-3 of Table 6.6 for forcing on the objects are shown. RMS-values, mean values and maximum values of the horizontal distance between the objects and the origo, with- and without the presence of a supply vessel at the upper end of the lift wire, are presented in Table 6.9. Even though the effect of vessel motions is noticeable, the horizontal motions of the suspended objects are the same order of magnitude, irrespective of whether the upper end is kept fixed or attached to a moving vessel. In the vertical direction, however, there was some transferral of motion, as can be seen in Figure 6.10. These vertical motions can in many cases be handled by a heave-compensator. It is known that for some combinations of (large) water depths, periods of wave excitation and lift-wire characteristics, a significant vertical motion may occur due to resonance in the lift-wire. Resonant vertical motions of the suspended objects are normally not easily compensated.

Results from simulations of all three objects, using all the selected HF-traces for forcing on the objects, uniform current profile applied to the lift-wire and a fixed upper end, can be seen in Figures C.12 and C.13. The simulated motions are considerable. As expected, the motions are sensitive to the lift-wire tension, i.e. the weight in water of the objects. These motions would have been somewhat different if the relative velocity between the lift-wire and the surrounding water had been accounted for in the simulation model (see section 6.3.3).

Traditionally, horizontal positioning of suspended objects have been obtained by

	RMS_{dist}					
Current	ROV 1		ROV 2		UTIS	
profile	No vessel	Vessel	No vessel	Vessel	No vessel	Vessel
case						
HF-1	7.3	7.4	10.8	13.8	1.2	1.2
HF-2	4.2	4.2	7.3	8.4	0.8	0.8
HF-3	2.5	2.5	5.7	5.3	0.6	0.5
HF-4	1.2	1.1	1.5	2.6	0.2	0.2
HF-5	1.4	0.6	2.0	1.4	0.3	0.1
HF-6	4.3	1.2	5.1	2.7	0.7	0.4
	$Mean_{dist}$					
Current	ROV 1		ROV 2		UTIS	
profile	No vessel	Vessel	No vessel	Vessel	No vessel	Vessel
case						
HF-1	12.3	12.3	15.1	18.1	2.1	2.6
HF-2	15.7	15.4	21.8	33.1	2.2	1.5
HF-3	6.6	6.4	14.0	16.9	1.1	0.8
HF-4	13.1	13.1	16.3	18.8	2.3	2.7
HF-5	9.1	11.2	8.2	15.3	1.5	2.5
HF-6	10.5	8.7	10.8	12.5	1.6	1.4
	Max_{dist}					
Current	ROV 1		ROV 2		UTIS	
profile	No vessel	Vessel	No vessel	Vessel	No vessel	Vessel
case						
HF-1	28.9	28.9	36.0	43.3	6.0	6.7
HF-2	24.9	24.1	35.0	45.6	4.6	3.9
HF-3	14.0	13.7	29.4	29.3	3.5	3.2
HF-4	16.4	16.2	21.0	25.6	2.7	3.4
HF-5	12.7	12.5	13.3	18.0	2.3	2.8
HF-6	19.7	11.9	21.2	19.8	4.1	2.4

Table 6.9: *RMS-values, mean values and maximum values of horizontal distance
between the origo and the objects, with- and without the presence of a supply vessel
at the upper end of the lift wire.*

use of guide-wires that are mounted prior to the operation. At large water depths,
this might not be a practical solution. A possible solution may then be to hori-
zontally move the surface vessel for gross manoevring, while thrusters mounted on
the objects are used for final positioning.

6.3.5 Conclusions

Results from simulations of a simple marine operation in a variable current flow
environment, and of the behaviour of three different suspended objects near the sea
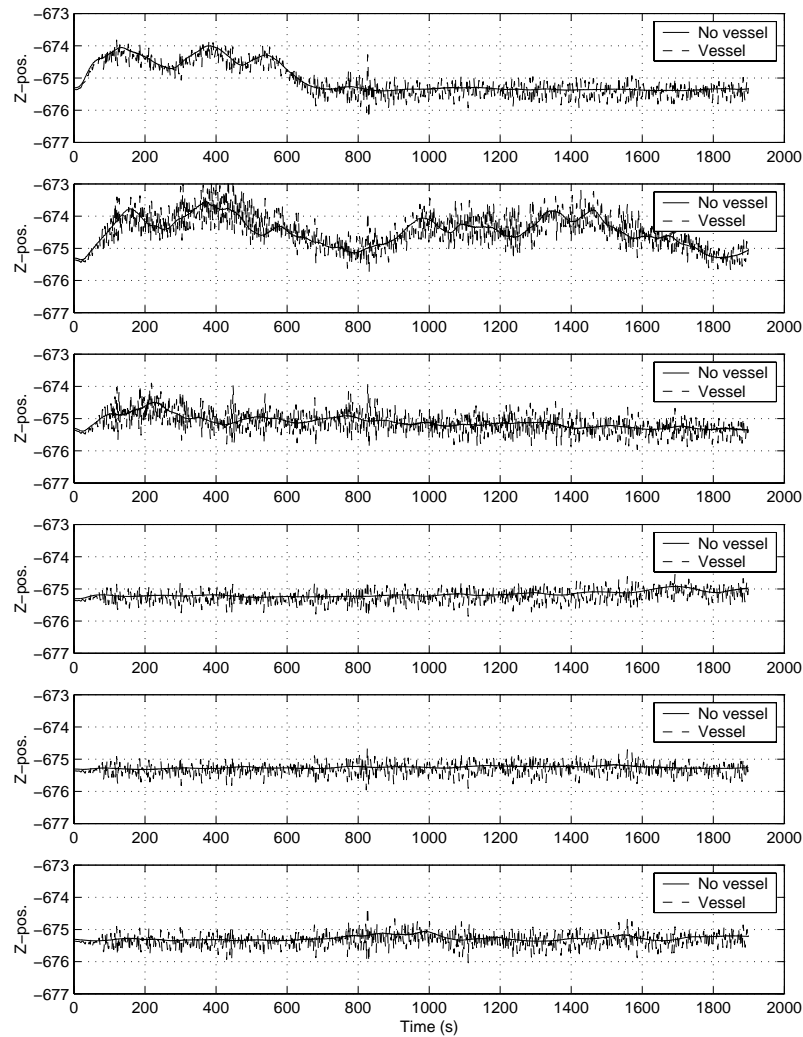bed, exposed to rapidly varying current flow, have been presented and discussed.

Figure 6.10: *Vertical motions of ROV 2 with- and without vessel at upper end.*

The position of an object, being lowered from the surface to the sea bed in a variable current flow environment, may deviate considerably from the position predicted by static analysis using the current profile at the start of the lowering process. For ROVs, which are equipped with thrusters for manoevring, the offsets presented here do not represent any difficulty. For passive objects of the same size and shape, however, large offsets must be compensated by other means, thus increasing the complexity of the operation. It can therefore be concluded that current variability is of interest for, and should be included in, planning and execution of marine operations in deep waters.

Figures C.9, C.12 and C.13 illustrate the fact that the displacements and velocities

of objects suspended near the sea bed in a variable current environment can be considerable. The current fluctuations, like those described in section 6.3.2, that may occur close to the seabed in some regions can therefore not generally be disregarded when planning or training for final positioning of objects on the sea bed.

CHAPTER 7

Conclusions and recommendations for further work

7.1   Conclusions

This thesis deals with the temporal and spatial variability in ocean currents near the continental slope, and how this variability relates to offshore engineering activities. The work is motivated by the fact that more and more offshore oil- and gas industry developments take place beyond the continental shelf and in increasingly deeper waters, thus rendering the forces from the current increasingly important in design of marine structures and planning of marine operations. As a consequence of this, well formulated design current conditions, including a quantification of the current variability, will become more important than before. A good knowledge about the physical processes in the ocean is necessary in order to establish such conditions.

The main focus in the thesis is on the current variability (chapters 2, 3 and 4), whereas the question of how to relate this variability to offshore engineering activities is adressed by merely formulating some necessary requirements to design current conditions, discussing today's practice and loosely suggesting a few ways of treating current data in relation to offshore engineering (chapter 5). A few examples which illustrate the effect of a variable current environment on some typical offshore marine structures/operations are also included (chapter 6).

7.1.1   Current variability

Current variability in the oceans of the world take place on a wide range of spatial- and temporal scales. The current conditions at one specific location is a result of global current conditions and local conditions such as e.g. bottom topography, stratification (vertical density distribution) and surface winds. Global circulation and some of the features that affect the current locally are briefly described, whereas processes taking place on the continental slope are discussed in more detail.

Measurements of current profiles west of Norway have been presented and discussed. The water column in this area has a two-layer structure with warm water from the North Atlantic over colder (and heavier) water from the Arctic. This stratification, possibly aided by the bottom topography, was seen to decouple the flow in the two-layers.

Also, some measurements of water temperature and current flow in the benthic boundary layer on the continental slope west of Norway were made available for analysis. These measurements were carried out in the same area as the current profile measurements, close to where the deep pycnocline ($\sim$680 m depth) intersects the continental slope. The measured data suggest that the fluid flow activity at the measurement site undergoes periods of strong variability accompanied by

periods of less variability. These periods do not necessarily have the same duration, and there is no evidence that they occur regularly. It is argued that variation in surface wind, causing steepening and release of the isopycnals at the slope, is a possible driving mechanism for strong current events at the slope. Hindcast data of wind velocity on the sea surface in the area of the measurements provide some support for this theory.

Results from numerical simulations using a two-layer model and an idealised continental slope were found to be of the same magnitude as those measured.

7.1.2 Offshore engineering in a variable current environment

Some important aspects in establishing new design current conditions have been identified and discussed. It is deemed important that the current conditions that are used in design are physically consistent and realistic. Ways of treating current data statistically, obtaining most probable current condition and probability of occurrence of current conditions, have been described, but not followed up by case studies.

The severity of structural response caused by current forces is not generally linked with the probability of occurrence of the current condition. Different structures and response types react differently to current load. This means that we must consider which type of structure, response and/or operation that is to be studied when determining which current conditions to use in ULS-design, rendering the probability of occurrence of the current conditions less important. For fatigue analyses, however, the probability of occurrence of various current conditions is very important.

Analyses of fatigue damage due to VIV of an idealised free-span pipeline, taking the directional variability of the current into account, have been carried out. As one would expect, the calculated accumulated fatigue damage to the pipe is significantly reduced when this variability is accounted for. Simulations of a simple marine operation in an variable current environment have also been carried out. The simulations show that the current variability can be an important factor when planning and executing marine operations in deep waters.

7.2 Recommendations for further work

I recommend that further work in this area is centered around two main fields.

Firstly, a considerable amount of work on establishing well formulated and relevant design current conditions for various structures/operations in a variable current environment, based on measured data, simulated results and qualitative descriptions, needs to be carried out. The following activities are imortant parts of such an undertaking:

- ocean current measurements

- studies of critical current conditions for various types of structures

- techniques for establishing joint probability distributions of waves, wind and current conditions

Secondly, methods for predicting certain current events, or estimating the probability that such events occur, should be sought. The research effort that is required in order to establish such a methodology is considerable, requiring extensive work within the following fields:

- synoptic observations of geophysical parameters (waves, wind, current, atmospheric pressure, etc.)

- understanding of the physical processes that govern the flow in the oceans, both globally and locally

- further development and improvement of numerical tools and methods (algorithms and computer technology) for direct calculations/predictions

Finally, one should also consider exploring alternative methods of predicting current conditions based on observed data. Neural networks is an example of such a technique, presently applied in climate research (see e.g. Tangang et al. 1997), and it might be worthwhile to explore its possibilities in forecasting ocean current conditions.

References

Adams, A. J. and J. L. Thorogood (1998). On The Choice of Current Profiles for Deep-Water Riser Design. In *SPE Annual Technical Conference and Exhibition*, New Orleans, USA.

Adams, J. K. and V. T. Buchwald (1969). The generation of continental shelf waves. *Journal of Fluid Mechanics 35*, 815–826.

Baines, P. G. (1971). The reflection of internal/inertial waves from bumpy surfaces. *Journal of Fluid Mechanics 46*, 273–291.

Baines, P. G. (1973). The reflection of internal/inertial waves from bumpy surfaces. part 2. split reflection and diffraction. *Journal of Fluid Mechanics 49*, 113–131.

Berntsen, H., S. Kowalik, S. Sælid, and K. Sørli (1981). Efficient numerical simulation of ocean hydrodynamics by a splitting procedure. In *Modelling, Identification and Control*, pp. 181–199.

Berntsen, J. (2002, September). User's guide for a modesplit σ-coordinate numerical ocean model. version 3.0. Technical report, Department of Mathematics, University of Bergen, Johs. Brunsgt. 12, N-5008 Bergen, Norway. available at `http://www.mi.uib.no/BOM/`.

Berntsen, J. and G. K. Furnes (2002). Small scale topographic effects on the near-seabed flow at Ormen Lange. Technical Report (in press), Department of Mathematics, University of Bergen, Johs. Brunsgt. 12, N-5008 Bergen, Norway.

Bjerke, P. E., H. Moshagen, L. P. Røed, G. Eidnes, and T. Mc-Climans (1995). Troll Oil Pipeline: Current measurements and modelling. Data basis for pipeline free span design. In *Proceedings of the 14th International Conference on Offshore Mechanics and Arctic Engineering*, Volume V of *Pipeline Technology*, pp. 29–36. ASME.

Blevins, R. D. (1990). *Flow-induced vibration* (2 ed. ed.). New York, USA: Van Nostrand Reinhold.

BLINDHEIM, J. (2004). Private communication.

BOWDEN, K. F. (1962). Measurements of turbulence near the sea-bed in a tidal current. *Journal of Geophysical Research 67*, 3181–3186.

BRADSHAW, P. (1975). *An Introduction to Turbulence and its Measurement.* Pergamon Press. Reprinted with corrections.

BRYAN, K. (1969). A numerical model for the study of the circulation of the world oceans. *Journal of Computational Physics 4*, 347–359.

BRYNDUM, M., A. TØRUM, L. VITALI, AND R. VERLEY (1997). Multispan project, laboratory tests on in-line viv of pipes subjected to current loads. In *Proceedings of the 16th International Conference on Offshore Mechanics and Arctic Engineering*, Volume V of *Pipeline Technology*, Yokohama, Japan, pp. 7–15. ASME.

CACCHIONE, D. AND C. WUNCH (1974). Experimental study of internal waves over a slope. *Journal of Fluid Mechanics 66, part 2*, 223–239.

CACCHIONE, D. A. AND L. F. PRATSON (2004). Internal Tides and the Continental Slope. *American Scientist 92*(2), 130–137.

CSANADY, G. T. (1973). Wind-Induced Baroclinic Motions at the Edge of the Continental Shelf. *Journal of Physical Oceanography 3*, 274–279.

CSANADY, G. T., J. H. CHURCHILL, AND B. BUTMAN (1988). Near-bottom currents over the continental slope at the Mid-Atlantic Bight. *Continental Shelf Research 8*(5-7), 653–671.

CUSHMAN-ROISIN, B. (1994). *Introduction to Geophysical Fluid Dynamics.* Englewood Cliffs, New Jersey: Prentice Hall.

DAVENPORT, A. G. (1977). *Safety of Structures under Dynamic Loading*, Volume 1, Chapter Wind Structure and Wind Climate, pp. 209–237. Norwegian Institute of Technology, Trondheim, Norway.

DAVIES, A. M. AND G. K. FURNES (1980). Observed and Computed M_2 Tidal Currents in the North Sea. *Journal of Physical Oceanography 10*.

DE SILVA, I. P. D. I., J. IMBERGER, AND G. N. IVEY (1997). Localised mixing due to a breaking internal wave ray at a sloping boundary. *Journal of Fluid Mechanics 350*, 1–27.

DEWEY, R. K., P. H. LEBLOND, AND W. R. CRAWFORD (1988). The turbulent bottom boundary layer and its influence on local dynamics over the continental shelf. *Dyn. Atmos. Oceans 12*, 143–172.

DHANAK, M. R., E. AN, AND K. HOLAPPA (2001). An AUV Survey in the Littoral Zone: Small-scale Subsurface Variability Accompanying Synoptic Observations of Surface Currents. *IEEE Journal of Oceanic Engineering 26*, 752–768.

ELLIOTT, B. A. (1982). Anticyclonic Rings in the Gulf of Mexico. *Journal of Physical Oceanography 12*, 1292–1309.

EMERY, W. J. AND J. MEINCKE (1986). Global water masses: summary and review. *Oceanologia Acta 9*, 383–391.

EMERY, W. J. AND R. E. THOMPSON (2001). *Data Analysis Methods in Physical Oceanography* (Second and Revised ed.). Amsterdam, The Netherlands: Elsevier Science B.V.

ENGEDAHL, H., B. ÅDLANDSVIK, AND E. A. MARTINSEN (1998). Production of monthly mean climatological archives for the Nordic Seas. *Journal of Marine Research 14*, 1–26.

ENGEDAHL, H. AND L. P. RØED (1999). Forecasting Ocean Currents in Deep Water Areas: The Ormen Lange Case (1997). Research report no. 80, issn 0332-9879, Norwegian Meteorological Institute., Oslo, Norway.

ERIKSEN, C. C. (1985). Implications of Ocean Bottom Reflection for Internal Wave Spectra and Mixing. *Journal of Physical Oceanography 15*, 1145–1156.

FORRISTAL, G. Z. AND C. K. COOPER (1997). Design current profiles using Empirical Orthogonal Functions (EOF) and inverse FORM methods. In *Proceedings of the 29th Annual Offshore Technology Conference*, OTC 8267, Houston, USA. Offshore Technology Conference.

FURNES, G., H. ENGEDAHL, D. HAREIDE, AND J. AURE (2001). Strømvirvler langs kysten av Sør-Norge. Et tilbakeblikk på hendelsen ved Trollfeltet 18. november 2000. Technical Report NH-00039406, Norsk Hydro U& P Norge, Bygdøy allé 2, N-0240 Oslo, Norway.

FURNES, G. K. AND J. BERNTSEN (2003). On the response of a free span pipeline subjected to ocean currents. *Ocean Engineering 30*(12), 1553–1577.

FYLLING, I. AND N. SØDAHL (1995). Riflex - General Description. Technical Report STF70 A95217, Norwegian Marine Technology Research Institute, MARINTEK, P.O.Box 4125 Valentinlyst, Trondheim, Norway.

GALPERIN, B., L. H. KANTHA, S. HASSID, AND A. ROSATI (1988). A Quasi-equilibrium Turbulent Energy Model for Geophysical Flows. *Journal of the Atmospheric Sciences 45*(1), 55–62.

GARFIELD, N. (1990). *The Brazil Current at subtropical latitudes.* Ph. D. thesis, University of Rhode Island.

GARRETT, C. (1979). Mixing in the ocean interior. *Dyn. Atmos. Oceans 3*, 239–265.

GARZOLI, S. L. AND Z. GARRAFFO (1989). Transports, frontal motions and eddies at the Brazil-Malvinas Currents Confluence. *Deep-Sea Research 36*(5), 681–703.

GEMMRICH, J. R. AND H. VAN HAREN (2001). Thermal Fronts Generated by Internal Waves Propagating Obliquely along the Continental Slope. *Journal of Physical Oceanography 31*, 649–655.

GILL, A. E. (1982). *Atmosphere-Ocean Dynamics.* New York : Academic Press, Inc. International geophysics series - volume 30.

GJEVIK, B. (1991). Simulation of shelf sea response due to travelling storms. *Continental Shelf Research 11*(2), 139–166.

GLENN, S. M. AND C. C. EBBESMEYER (1993). Drifting Buoy Observations of a Loop Current Anticyclonic Eddy. *Journal of Geophysical Research 98*(C11), 20105–20119.

GOPALKRISHNAN, R. (1993). *Vortex-Induced Forces on Oscillating Bluff Cylinders.* Ph. D. thesis, Department of Ocean Engineering, MIT, and Department of Applied Ocean Phys. and Eng., WHOI, USA.

GORDON, A. L. AND C. L. GREENGROVE (1986). Geostrophic circulation of the Brazil-Falkland Confluence. *Deep-Sea Research 33*, 573–585.

GOUPILLAUD, P., A. GROSSMANN, AND J. MORLET (1984). Cycle-octave and related transforms in seismic signal analysis. *Geoexploration 23*, 85–105.

GRANT, C. K., R. C. DYER, AND I. M. LEGGETT (1995). Development of a New Metocean Design Basis for the NW Shelf of Europe. In *Proceedings of the 27th Annual Offshore Technology Conference*, OTC 7685, Houston, USA. Offshore Technology Conference.

GROSE, C. (2002). Inconsistencies in the hydroplate theory - liquefaction. http://www.promisoft.100megsdns.com/OYSI/Articles/Chris Grose/liquefaction.htm.

GRUE, J. (2002). Strong current events at a slope. Report to Norsk Hydro. Technical report, University of Oslo, Department of Mathematics, Mechanics Division., Oslo, Norway.

HAMILTON, J. M., G. A. FOWLER, AND D. J. BELLIVEAU (1997). Mooring Vibration as a Source of Current Meter Error and Its Correction. *Journal of Atmospheric and Oceanic Technology 14*(3), 646–655.

HAMILTON, P. (1990). Deep Currents in the Gulf of Mexico. *Journal of Physical Oceanography 20*, 1087–1104.

HAMILTON, P., G. S. FARGION, AND D. C. BIGGS (1999). Loop Current Eddy Paths in the Western Gulf of Mexico. *Journal of Physical Oceanography 29*, 1180–1206.

HAMILTON, P. AND A. LUGO-FERNANDEZ (2001). Observations of high speed deep currents in the northern Gulf of Mexico. *Geophysical Research Letters 28*(14), 2867–2870.

HANSEN, B. AND S. ØSTERHUS (2000). North Atlantic - Nordic Seas exchanges. *Progress in Oceanography 45*, 109–208.

HEATHERSHAW, A. D. (1974). Bursting phenomena in the sea. *Nature 248*, 394–395.

HEATHERSHAW, A. D. (1979). The turbulent structure of the bottom boundary layer in a tidal current. *Geophys. J. R. astr. Soc. 58*, 395–430.

HEATHERSHAW, A. D. AND P. D. THORNE (1985). Sea-bed noise reveal role of turbulent bursting phenomenon in sediment transport by tidal currents. *Nature 316*, 339–342.

HEGGELUND, Y., F. VIKEBØ, J. BERNTSEN, AND G. FURNES (2004). Hydrostatic- and non-hydrostatic studies of gravitational adjustment over a slope. *Continental Shelf Research (accepted)*.

HEIDVOGEL, D. B. AND A. BECKMAN (2000). *Numerical ocean circulation modeling*. London, UK: Imperial College Press.

HOREL, J. D. (1984). Complex Principal Component Analysis: Theory and Examples. *Journal of Climate and Applied Meteorology 23*, 1660–1673.

HOSEGOOD, P. AND H. VAN HAREN (2003). Ekman-induced turbulence over the continental slope in the Faeroe-Shetland Channel as inferred from spikes in current meter observations. *Deep-Sea Research 50*, 657–680.

HOWARD, L. N. (1961). Note on a paper of John W. Miles. *Journal of Fluid Mechanics 13*, 158–160.

HUSE, E. (2002). Ormen Lange 3D Phase II Model Tests. Main Report. Technical report, Norwegian Marine Technology Research Institute, MARINTEK, P.O.Box 4125 Valentinlyst, Trondheim, Norway.

HUTHNANCE, J. M. (1995). Circulation, exchange and water masses at the ocean margin: the role of physical processes at the shelf edge. *Progress in Oceanography 35*, 353–431.

IVEY, G. N. AND R. I. NOKES (1989). Vertical mixing due to breaking of critical waves on sloping boundaries. *Journal of Fluid Mechanics 204*, 479–500.

JAVAM, A., J. IMBERGER, AND S. W. ARMFIELD (1999). Numerical study of internal wave reflection from sloping boundaries. *Journal of Fluid Mechanics 396*, 183–201.

JEANS, D. R. G. AND G. FELD (2001). A method for deriving extreme current profiles to support design of deep water drilling risers. In *Proceedings of the 20th International Conference on Offshore Mechanics and Arctic Engineering*, Rio de Janeiro, Brazil. ASME.

JEANS, D. R. G., C. GRANT, AND G. FELD (2002). Improved current profile criteria for deepwater riser design. In *Proceedings of the 21st International Conference on Offshore Mechanics and Arctic Engineering*, Oslo, Norway. ASME.

KANTHA, L. H. AND C. A. CLAYSON (2000). *Numerical Models of Oceans and Oceanic Processes*. San Diego, California, USA: Academic Press.

KLEIVEN, G. (2002). Identifying VIV modes by use of the Empirical Orthogonal Functions technique. In *Proceedings of the 21st International Conference on Offshore Mechanics and Arctic Engineering*, Oslo, Norway. ASME.

KOWALIK, Z. AND T. S. MURTY (1993). *Numerical ocean circulation modeling*. Farrer Road, Singapore: World Scientific Publishing Co. Pte. Ltd.

KUNDU, P. K. (1976). Ekman veering observed near the ocean bottom. *Journal of Physical Oceanography 6*, 238–242.

KUNDU, P. K. (1990). *Fluid Mechanics*. San Diego, California 92101, USA: Academic Press Inc.

KUNDU, P. K. AND J. S. ALLEN (1976). Some Three-Dimensional Characteristics of Low-Frequency Current Fluctuations near the Oregon Coast. *Journal of Physical Oceanography 6*, 181–199.

LARSEN, C., K. VIKESTAD, R. YTTERVIK, AND E. PASSANO (2000). Vivana theory manual. Technical report, Norwegian Marine Technology Research Institute, MARINTEK, P.O.Box 4125 Valentinlyst, Trondheim, Norway.

LARSEN, C. M. (1992). Use of Stochastic Dynamic Analysis in Marine Riser Design. Keynote paper presented at NSF Workshop on Riser Mechanics, University of Michigan, Ann Arbor.

LARSEN, C. M., K. KOUSHAN, AND E. PASSANO (2002). Frequency and time domain analysis of vortex induced vibrations for free span pipelines. In *Proceedings of the 21st International Conference on Offshore Mechanics and Arctic Engineering*, Oslo, Norway. ASME.

LARSEN, C. M., K. VIKESTAD, R. YTTERVIK, AND E. PASSANO (2001). Empirical model for analysis of vortex-induced vibrations - theoretical background and case studies. In *Proceedings of the 20th International Conference on Offshore Mechanics and Arctic Engineering*, Rio de Janeiro, Brazil. ASME.

LEGG, S. AND A. ADCROFT (2003). Internal Wave Breaking at Concave and Convex Continental Slopes. *Journal of Physical Oceanography 33*, 2224–2246.

LENTZ, S. J. AND J. H. TROWBRIDGE (1991). The bottom boundary layer over the North California Shelf. *Journal of Physical Oceanography 21*, 1186–1201.

LEONARD, J. W. (1988). *Tension Structures*. McGraw-Hill.

LEVATHES, L. (1997). *When China Ruled the Seas*. Oxf.U.P. NY.

LEVITUS, S. (1982). Climatological Atlas of the World Ocean. NOAA Professional Paper 13, U.S. Government Printing Office, Washington D.C. 173pp.

LODER, J. W. AND J. M. HAMILTON (1991). Degradation of Some Mechanical Current Meter Measurements by High-Frequency Mooring or Wave Motion. *IEEE Journal of Oceanic Engineering 16*(4), 343–349.

LOHRMANN, A. (2003). NORTEK. Private communication.

LØNSETH, L., G. EIDNES, AND J.-P. MATHISEN (2001). Current Measurements at Ormen Lange - Final report. Technical Report OCN R-21022, OCEANOR., Trondheim, Norway.

LORENZ, E. (1956). Empirical orthogonal functions and statistical weather prediction. Scientific report no. 1, Air Force Cambridge Research Center, Air Research and Development Command., Cambridge Mass.

LUCHNIK, T. S. AND W. G. TIEDERMAN (1987). Timescale of ejections and bursts in turbulent channel flows. *Journal of Fluid Mechanics 174*, 529–552.

LUDVIGSEN, M., I. H. ELLINGSEN, Ø. T. ØDEGAARD, AND B. SORTLAND (2003). Model supported auv freshwater distribution surveys in the upper layers of deep fjords. OCEANS MTS/IEEE Conference and Exhibition.

MacCREADY, P. AND G. PAWLAK (2001). Stratified Flow along a Corrugated Slope: Separation Drag and Wave Drag. *Journal of Physical Oceanography 31*, 2824–2839.

MacCREADY, P. AND P. B. RHINES (1991). Buoyant inhibition of Ekman transport on a slope and its effect on stratified spin-up. *Journal of Fluid Mechanics 223*, 631–661.

MacCREADY, P. AND P. B. RHINES (1993). Slippery boundary layers on a slope. *Journal of Physical Oceanography 23*, 5–22.

MARCHESANI, F., F. GIANFELICI, R. BRUSCHI, AND M. BRYNDUM (1995). Response of very long and multi-span pipelines in turbulent flows - experimental results. In *Proceedings of the 14th International Conference on Offshore Mechanics and Arctic Engineering*, Volume V of *Pipeline Technology*, pp. 487–498. ASME.

MATHIESEN, M. (1996). Current data for the design of multispanning pipelines. In *Proceedings of the 15th International Conference on Offshore Mechanics and Arctic Engineering*, Florence, Italy. ASME.

MATHIESEN, M., E. A. HANSEN, O. J. ANDERSEN, AND R. BRUSCHI (1997). The multispan project, near seabed flow in macro-roughness areas. In *Proceedings of the 16th International Conference on Offshore Mechanics and Arctic Engineering*, Yokohama, Japan. ASME.

MELING, T. S., K. J. EIK, AND E. NYGAARD (2002). An assessment of EOF current scatter diagrams with respect to riser VIV fatigue damage. In *Proceedings of the 21st International Conference on Offshore Mechanics and Arctic Engineering*, Oslo, Norway. ASME.

MELLOR, G. L. AND A. F. BLUMBERG (1985). Modeling Vertical and Horizontal Diffusivities with the Sigma Coordinate System. *Monthly Weather Review 113*, 1379–1383.

MELLOR, G. L. AND T. YAMADA (1974). A Hierarchy of Turbulence Closure Models for Planetary Boundary Layers. *Journal of the Atmospheric Sciences 31*, 1791–1806.

MELLOR, G. L. AND T. YAMADA (1982). Development of a Turbulence Closure Model for Geophysical Fluid Problems. *Rewiev of Geophysics and Space Physics 20*(4), 851–875.

MESINGER, F. AND A. ARAKAWA (1976). Numerical models used in atmospheric models. Volume I of *No. 17*. Garp Publication. WMO/ICSU Joint Organizing Committee.

MILES, J. W. (1961). On the stability of heterogenous shear flows. *Journal of Fluid Mechanics 10*, 496–508.

MO, K. AND F. SOLAAS (2002). Ormen lange 3d phase ii modal analysis. Technical Report 512352.00.02, Norwegian Marine Technology Research Institute, MARINTEK, P.O.Box 4125 Valentinlyst, Trondheim, Norway.

MOROSHKIN, K. V., V. A. BUNOV, AND R. P. BULATOV (1970). Water circulation in the eastern South Atlantic Ocean. *Oceanology 10*, 27–34.

MÜLLER, P. AND N. XU (1992). Scattering of oceanic internal gravity waves off random bottom topography. *Journal of Physical Oceanography 22*, 474–488.

MUTLU SUMER, B. AND J. FREDSØE (1997). *Hydrodynamics around Cylindrical Structures*, Volume 12 of *Advanced Series on Ocean Engineering*. World Scientific, Singapore.

NEWLAND, D. E. (1993). *Random Vibrations, Spectral & Wavelet Analysis* (Third ed.). Essex, England: Longman Scientific & Technical.

NYLUND, S. (2003). NORTEK. Private communication.

ØRITSLAND, O. (2004). Private communication.

ORVIK, K. A. AND P. NIILER (2002). Major pathways of Atlantic water in the northern North Atlantic and Nordic Seas toward Arctic. *Geophysical Research Letters 29*(19). 1896, doi:10.1029/2002GL015002.

PATERA, A. T. (1984). A spectral element method for fluid dynamics: Laminar flow in a channel expansion. *Journal of Computational Physics 54*, 468–488.

PETERSON, R. G. AND L. STRAMMA (1990). Upper-level circulation in the South Atlantic Ocean. *Progress in Oceanography 26*, 1–73.

PEYROT, A. H. AND A. M. GOULOIS (1979). Analysis of cable structures. *Computer and Structures 10*, 805–813.

PHILANDER, S. G. (1990). *El Niño, La Niña, and the southern oscillation.* Academic Press. International geophysics series - volume 46.

PHILLIPS, N. A. (1957). A coordinate system having some special advantages for numerical forecasting. *Journal of Meteorology 14*, 184–185.

PHILLIPS, O. M. (1977). *The Dynamics of the Upper Ocean* (2nd ed.). Cambridge University Press.

PICKARD, G. L. AND W. J. EMERY (1990). *Descriptive Physical Oceanography* (5th ed.). Linacre House, Jordan Hill, Oxford OX2 8DP: Butterworth-Heinemann.

POND, S. AND G. L. PICKARD (1983). *Introductory Dynamical Oceanography* (2nd ed.). Linacre House, Jordan Hill, Oxford OX2 8DP: Butterworth-Heinemann.

REDDY, M. P. M. (2001). *Descriptive Physical Oceanography.* Linacre House, Jordan Hill, Oxford OX2 8DP: A.A. Balkema.

REINHOLDTSEN, S.-A. AND E. FALKENBERG (2001). Simo - General Description. Technical Report MT51 F93-0184, Norwegian Marine Technology Research Institute, MARINTEK, P.O.Box 4125 Valentinlyst, Trondheim, Norway.

RICHARDSON, P. L. AND G. REVERDIN (1987). Seasonal cycle of velocity in the Atlantic North Equatorial Countercurrent as measured by surface drifters, current meters and ship drifts. *Journal of Geophysical Research 92*, 3681–3708.

RØED, L. P. AND I. FOSSUM (2004). Mean and eddy motion in the Skagerrak/Northern North Sea: insight from a numerical model. *Ocean Dynamics 54*(2), 197–220.

SARPKAYA, T. AND M. ISAACSON (1981). *Mechanics of wave forces on offshore structures.* Van Nostrand Reinhold Company.

SCHLICHTING, H., K. GERSTEN, AND K. MEYES (2000). *Boundary-layer theory* (8th rev. and enl. ed. ed.). Berlin, Germany: Springer.

SCHMID, C., H. SCHÄFER, G. PODESTÁ, AND W. ZENK (1995). The Vitória Eddy and Its Relation to the Brazil Current. *Journal of Physical Oceanography 25*, 2532–2546.

SCHMIDT, H., J. G. BELLINGHAM, M. JOHNSON, D. HEROLD, D. M. FARMER, AND R. PAWLOWICZ (1996). Real-Time Frontal Mapping with

AUVs in a Coastal Environment. In *Oceans 96 MTS/IEEE*, Ft. Lauderdale, Florida,USA.

SIMPSON, J. E. (1997). *Gravity Currents in the Environment and the Laboratory* (2 ed. ed.). Cambridge University Press.

SLINN, D. N. AND J. J. RILEY (1996). Turbulent mixing in the oceanic boundary layer caused by internal wave reflection from sloping terrain. *Dyn. Atmos. Oceans 24*, 51–62.

SLINN, D. N. AND J. J. RILEY (1998). Turbulent dynamics of a critically reflecting internal gravity wave. *Theor. Comput. Fluid Mech. 11*, 281–304.

SMAGORINSKY, J. (1963). General circulation experiments with the primitive equations. *Monthly Weather Review 91*(3), 99–164.

SØDAHL, N. (1991). *Methods for Design and Analysis of Flexible Risers.* Ph. D. thesis, Norwegian University of Science and Technology, Trondheim, Norway.

SOULSBY, R. L. (1977). Similarity Scaling of Turbulence Spectra in Marine and Atmospheric Boundary Layers. *Journal of Physical Oceanography 7*, 934–937.

STANSFIELD, K., D. A. SMEED, G. P. GASPARINI, S. D. MCPHAIL, N. MILLARD, P. STEVENSON, A. WEBB, V. A., AND B. RABE (2001). Deep-sea, high-resolution, hydrography and current measurements using an autonomous underwater vehicle: The overflow from the Strait of Sicily. *Geophysical Research Letters 28*(13), 2645–2648.

STOMMEL, H. M. (1948). The westward intensification of wind-driven currents. *Transactions, American Geophysical Union 29*, 202–206.

STOMMEL, H. M. (1958). The abyssal circulation. *Deep-Sea Research 5*, 80–82.

STURGES, W., J. C. EVANS, S. WELSH, AND W. HOLLAND (1993). Separation of Warm-Core Rings in the Gulf of Mexico. *Journal of Physical Oceanography 23*, 250–268.

SVERDRUP, H. U. (1947). Wind-driven currents in a baroclinic ocean, with application to the equatorial currents of the eastern pacific. In *Proc. Natl. Acad. Sci.*, Volume 33, USA, pp. 318–326.

SVERDRUP, H. U., M. W. JOHNSON, AND R. H-FLEMING (1942). *The Oceans: their Physics, Chemistry and general Biology.* Englewood Cliffs, N.J.: Prentice Hall.

TANGANG, F. T., W. W. HSIEH, AND B. TANG (1997). Forecasting the regional sea surface temperatures for the tropical Pacific by neural network models, with wind stress and sea level pressure as predictors. *Journal of Geophysical Research 103*, 7511–7522.

TAYLOR, J. R. (1993). Turbulence and mixing in the boundary layer generated by shoaling internal waves. *Dyn. Atmos. Oceans 19*, 233–258.

TENNEKES, H. AND J. L. LUMLEY (1972). *A First Course in Turbulence*. Massachusetts Institute of Technology, Cambridge, Massachusetts 02142: The MIT Press. Eighteenth printing, 2001.

THORPE, S. A. (1987a). Currents and temperature variability on the continental slope. *Philos. Trans. Roy. Soc. London 323A*, 471–517.

THORPE, S. A. (1987b). On the reflection of a train of finite-amplitude internal waves from a uniform slope. *Journal of Fluid Mechanics 178*, 279–302.

THORPE, S. A. (1992a). The generation of internal waves by flow over the rough topography of a continental slope. *Proc. Roy. Soc. London A 439*, 115–130.

THORPE, S. A. (1992b). Thermal Fronts Caused by Internal Gravity Waves Reflecting from a Slope. *Journal of Physical Oceanography 22*, 105–108.

THORPE, S. A. (1997). On the Interactions of Internal Waves Reflecting from Slopes. *Journal of Physical Oceanography 27*, 2072–2078.

THORPE, S. A. (2001). Internal wave reflection and scatter from sloping rough topography. *Journal of Physical Oceanography 31*, 537–553.

THORPE, S. A. AND A. P. HAINES (1987). A note on observations of wave reflection on a 20° slope. Appendix to a paper by S. A. Thorpe : On the reflection of a train of finite-amplitude internal waves from a uniform slope. *Journal of Fluid Mechanics 178*, 299–301.

TORRENCE, C. AND G. P. COMPO (1998). A Practical Guide to Wavelet Analysis. *Bulletin of the American Meteorological Society 79*(1), 61–78.

TRIANTAFYLLOU, M. (2000, April). Vortex-Induced Vibration Analysis Marine Riser Software. User's Manual. DOS Version 3.2. Technical report, David Tein Consulting Engineers, Ltd., Houston, TX, USA.

TROWBRIDGE, J. H. AND S. J. LENTZ (1991). Asymmetric behaviour of an oceanic boundary layer above a sloping bottom. *Journal of Physical Oceanography 21*, 1171–1185.

TUCKER, M. J., P. G. CHALLENOR, AND J. T. CARTER (1984). Numerical Simulation of a Random Sea: A Common Error and its Effect upon Wave Group Statistics. *Applied Ocean Research 6*(2).

VANDIVER, J. K. (1983). Drag coefficients of long flexible cylinders. In *Proceedings of the 1983 Offshore Technology Conference*, OTC 4490, Houston, USA. Offshore Technology Conference.

VANDIVER, J. K. AND L. LI (1995). Shear7 program theoretical manual. Technical report, Massachusetts Institute of Technology (MIT).

Veritas, D. N. (2001a). Free spanning pipelines. Technical report, Det Norske Veritas, Høvik, Norway.

Veritas, D. N. (2001b). Free spanning pipelines - Recommended practice. Technical Report DNV-RP-F105, Det Norske Veritas, Høvik, Norway.

Veronis, G. (1973). Model of World Ocean Circulation. *Journal of Marine Research 31*, 228–288.

Vianna, M. L. and V. V. de Menezes (2004). Shelf edge circulation off the campos basin from altimetry and current meter moorings. Private communication.

Vikebø, F., J. Berntsen, and G. K. Furnes (2004). Numerical studies of the current response at Ormen Lange to a travelling storm. *Journal of Marine Systems 45*(3-4), 205–220.

Vikestad, K. (1998). *Multi-frequency response of a cylinder subjected to vortex shedding and support motions.* Ph. D. thesis, Norwegian University of Science and Technology, Trondheim, Norway.

Vukovich, F. M. (1986). Aspects of the Behaviour of Cold Perturbations in the Eastern Gulf of Mexico: A case study. *Journal of Physical Oceanography 16*, 175–188.

Vukovich, F. M. (1988). Loop Current Boundary Variations. *Journal of Geophysical Research 93*(C12), 15585–15591.

White, M. (1994). Tidal and subtidal variability in the sloping benthic boundary layer. *Journal of Geophysical Research 99*(C4), 7851–7864.

Wimbush, M. and W. Munk (1970). The benthic boundary layer. In A. E. Maxwell (Ed.), *The Sea*, Volume 4, pp. 731–758. New York: Interscience.

Winterstein, S. R., T. C. Ude, C. A. Cornell, P. Bjerager, and S. Haver (1993, August). Environmental parameters for extreme response: Inverse form with omission factors. In *ICOSSAR-93, Paper no. 509/11/3*, Innsbruck, Austria.

Wood, D. J. (2002). Modelling of an internal wave gravity current using Euler's equations. In *Proceedings of the 21st International Conference on Offshore Mechanics and Arctic Engineering*, Oslo, Norway. ASME.

Yoshida, K. (1955). Coastal upwelling off the California coast. *Records of Oceanographic Works in Japan 2*(2), 8–20.

Yttervik, R. and G. K. Furnes (2005). Current measurements on the continental slope west of Norway in an area with a pronounced two-layer density profile. *Deep-Sea Research Part I 52*(1), 161–178.

Yttervik, R., C. M. Larsen, and G. K. Furnes (2003). Fatigue from vortex-induced vibrations of free span pipelines using statistics of current

speed and direction. In *Proceedings of the 22nd International Conference on Offshore Mechanics and Arctic Engineering*, Cancun, Mexico. ASME.

YTTERVIK, R., S.-A. REINHOLDTSEN, C. M. LARSEN, AND G. K. FURNES (2003). Marine operations in deep water and a variable current flow environment. In R. EATOCK-TAYLOR (Ed.), *Proceedings of the third International Conference on Hydroelasticity in Marine Technology*, Oxford, UK, pp. 63–73. The University of Oxford.

Equations and solution techniques for a 2D σ-coordinate numerical ocean model.

This appendix contains the governing equations and solution methods of a 2D σ-coordinate numerical ocean model. The model, and the description given herein, is largely based on a full 3D model (Berntsen 2002) and the non-hydrostatic technique described by Heggelund et al. (2004).

A.1 Introduction.

The Bergen Ocean Model (BOM, Berntsen 2002) is a numerical tool for solving the non-linear partial differential equations governing the circulation of water in the ocean. These equations can be expressed in a variety of earth-fixed coordinate systems. BOM uses a bottom- and surface following σ-coordinate system. This appendix gives a description of this coordinate system, a description of how the governing equations are transformed from the Cartesian coordinate system to the σ-coordinate system and a description of how the equations are solved on the computer.

A.2   Coordinate systems.

A.2.1   Cartesian coordinate system.

The 2D Cartesian coordinate system, $O(x, z)$, consists of two orthogonal axes which intersect at the origin. The z-axis is pointing upwards and the origin is at the undisturbed free surface.

A.2.2   σ-coordinate system.

The σ-coordinate system (Phillips 1957) is a coordinate system with a topography- and surface following vertical coordinate σ. The transformation of the independent variables of the cartesian coordinate system (x^c, z, t^c) to those of the σ-coordinate system $(x^\sigma, \sigma, t^\sigma)$ is given by

$$x^c = x^\sigma = x \qquad \sigma = \frac{z - \eta}{H + \eta} = \frac{z - \eta}{D} \qquad t^c = t^\sigma = t$$

where $\eta(x, t)$ is the surface elevation, $H(x)$ is the static depth (distance from the undisturbed free surface to the sea bed). The dynamic depth, D, is defined by,

$$D(x, t) = H(x) + \eta(x, t).$$

A property, ϕ, of the fluid flow at some location must be the same in the σ-coordinate system as in the Cartesian coordinate system,

$$\phi(x, z, t) = \phi(x, \sigma(x, z, t), t).$$

A.2.3   Some rules for differentiation.

The derivative of the property ϕ with respect to the free variable x is written as

$$\left.\frac{\partial \phi}{\partial x}\right|_c = \frac{\partial \phi}{\partial x} + \left.\frac{\partial \phi}{\partial \sigma}\frac{\partial \sigma}{\partial x}\right|_c$$

where $\left.\frac{\partial}{\partial \xi}(\cdot)\right|_c$ is the derivative of $(\cdot)$ with respect to ξ in the Cartesian coordinate system, and $\frac{\partial}{\partial \xi}(\cdot)$ is the derivative of $(\cdot)$ with respect to ξ in the σ-coordinate system. We now have,

$$\left.\frac{\partial \phi}{\partial x}\right|_c = \frac{\partial \phi}{\partial x} + \left.\frac{\partial \phi}{\partial \sigma}\frac{\partial \sigma}{\partial x}\right|_c \tag{A.1}$$

$$\left.\frac{\partial \phi}{\partial z}\right|_c = \left.\frac{\partial \phi}{\partial \sigma}\frac{\partial \sigma}{\partial z}\right|_c \tag{A.2}$$

$$\left.\frac{\partial \phi}{\partial t}\right|_c = \frac{\partial \phi}{\partial t} + \left.\frac{\partial \phi}{\partial \sigma}\frac{\partial \sigma}{\partial t}\right|_c \tag{A.3}$$

Finally, we have the derivative of the vertical coordinate with respect to x, z and t as

$$\left.\frac{\partial \sigma}{\partial x}\right|_c = \frac{\partial \sigma}{\partial x} = -\frac{1}{D}\left(\frac{\partial \eta}{\partial x} + \sigma \frac{\partial D}{\partial x}\right) \tag{A.4}$$

$$\left.\frac{\partial \sigma}{\partial z}\right|_c = \frac{\partial \sigma}{\partial z} = \frac{1}{D} \tag{A.5}$$

$$\left.\frac{\partial \sigma}{\partial t}\right|_c = \frac{\partial \sigma}{\partial t} = -\frac{1}{D}\left(\frac{\partial \eta}{\partial t} + \sigma \frac{\partial D}{\partial t}\right) \tag{A.6}$$

A.2.4 Total derivative in the σ-coordinate system.

The total (material) derivative of the property, ϕ, in the σ-coordinate system can be derived by considering the ratio between a small change in ϕ and a small change in time.

$$\frac{\Delta \phi}{\Delta t} = \frac{\phi(x + \Delta x, \sigma + \Delta \sigma, t + \Delta t) - \phi(x, \sigma, t)}{\Delta t}$$

By performing a Taylor expansion around (x, σ, t) and neglecting higher order terms in Δx, $\Delta \sigma$, Δt, we can write

$$\frac{\Delta \phi}{\Delta t} = \frac{\partial \phi}{\partial x}\frac{\Delta x}{\Delta t} + \frac{\partial \phi}{\partial \sigma}\frac{\Delta \sigma}{\Delta t} + \frac{\partial \phi}{\partial t}\frac{\Delta t}{\Delta t} \tag{A.7}$$

An expression for $\Delta \sigma$ can be found by Taylor expansion of σ around (x, z, t). Again, we neglect higher order terms and obtain

$$\Delta \sigma = \left.\frac{\partial \sigma}{\partial x}\right|_c \Delta x + \left.\frac{\partial \sigma}{\partial z}\right|_c \Delta z + \left.\frac{\partial \sigma}{\partial t}\right|_c \Delta t \tag{A.8}$$

Introducing this into equation (A.7), and letting $\Delta t \to 0$, we obtain an expression for the total derivative of ϕ in the σ-coordinate system,

$$\frac{d\phi}{dt} = U\frac{\partial \phi}{\partial x} + \widetilde{W}\frac{\partial \phi}{\partial \sigma} + \frac{\partial \phi}{\partial t} \tag{A.9}$$

U and W are flow velocity in x-direction and z-direction, respectively. The new variable

$$\widetilde{W} = U\left.\frac{\partial \sigma}{\partial x}\right|_c + W\left.\frac{\partial \sigma}{\partial z}\right|_c + \left.\frac{\partial \sigma}{\partial t}\right|_c$$

can be interpreted as the total derivative of σ in a Cartesian coordinate system.

A.2.5 Vertical velocity in the σ-coordinate system.

An expression for the vertical fluid flow velocity in the σ-coordinate system can be found by replacing ϕ in equation (A.9) with z. This gives us

$$
\begin{aligned}
\omega = \frac{dz}{dt} &= U\frac{\partial z}{\partial x} + \widetilde{W}\frac{\partial z}{\partial \sigma} + \frac{\partial z}{\partial t} \\
&= \sigma\left(\frac{\partial D}{\partial t} + U\frac{\partial D}{\partial x}\right) + D\left(\frac{\partial \sigma}{\partial t} + U\frac{\partial \sigma}{\partial x} + \widetilde{W}\right) + \frac{\partial \eta}{\partial t} + U\frac{\partial \eta}{\partial x}
\end{aligned}
\tag{A.10}
$$

Inserting (A.4) and (A.6) into (A.10), we get

$$
\omega = -U\left(\frac{\partial \eta}{\partial x} + \sigma\frac{\partial D}{\partial x}\right) + W + D\frac{\partial \sigma}{\partial t}
\tag{A.11}
$$

The last term in equation (A.11) can be written as,

$$
D\frac{\partial \sigma}{\partial t} = -\frac{\partial \eta}{\partial t} - \sigma\frac{\partial D}{\partial t} = -(1+\sigma)\frac{\partial \eta}{\partial t}
$$

We can now write the relationship between the vertical velocity in the Cartesian coordinate system, W, and the σ-velocity in the σ-coordinate system, ω, as

$$
W = \omega + U\left(\frac{\partial \eta}{\partial x} + \sigma\frac{\partial D}{\partial x}\right) + (1+\sigma)\frac{\partial \eta}{\partial t}
\tag{A.12}
$$

A.3 Governing equations.

A.3.1 The equations in the cartesian coordinate system.

Conservation of mass - Cartesian coordinates.

Conservation of mass requires that

$$
\left.\frac{\partial \rho}{\partial t}\right|_c + \left.\frac{\partial}{\partial x}(\rho U)\right|_c + \left.\frac{\partial}{\partial z}(\rho W)\right|_c = 0
$$

which for an incrompressible fluid like seawater can be simplified to

$$
\left.\frac{\partial U}{\partial x}\right|_c + \left.\frac{\partial W}{\partial z}\right|_c = 0
\tag{A.13}
$$

Here, we have introduced the density, ρ, of seawater. It is customary to define a reference density, ρ_0, and a perturbation, $\rho'(x,z,t)$, such that

$$
\rho(x,z,t) = \rho_0 + \rho'(x,z,t)
$$

Momentum equations - Cartesian coordinates.

We assume that $\rho_0 \ll \rho'$ (the Boussinesq approximation) and define the total pressure according to

$$p(x, z, t) = p_H + p' = P_{atm}(x, t) + g\rho_0\eta(x, t) + g\int_z^0 \rho(x, z', t)dz' + p' \quad (A.14)$$

where the first three terms constitute the hydrostatic pressure, balancing the surface elevation and the gravity term in the vertical, and the last term is a non-hydrostatic pressure correction.

The following set of equations express conservation of momentum,

$$\left.\frac{\partial U}{\partial t}\right|_c + U\left.\frac{\partial U}{\partial x}\right|_c + W\left.\frac{\partial U}{\partial z}\right|_c - fV = -\frac{1}{\rho_0}\left.\frac{\partial p_H}{\partial x}\right|_c + \left.\frac{\partial}{\partial z}\left(K_M\frac{\partial U}{\partial z}\right)\right|_c + F_x \quad (A.15)$$

$$\left.\frac{\partial V}{\partial t}\right|_c + U\left.\frac{\partial V}{\partial x}\right|_c + W\left.\frac{\partial V}{\partial z}\right|_c + fU = \left.\frac{\partial}{\partial z}\left(K_M\frac{\partial V}{\partial z}\right)\right|_c + F_y \quad (A.16)$$

$$\left.\frac{\partial U_c}{\partial t}\right|_c + U_c\left.\frac{\partial U_c}{\partial x}\right|_c + W\left.\frac{\partial U_c}{\partial z}\right|_c = -\frac{1}{\rho_0}\left.\frac{\partial p'}{\partial x}\right|_c \quad (A.17)$$

$$\left.\frac{\partial V_c}{\partial t}\right|_c + U_c\left.\frac{\partial V_c}{\partial x}\right|_c + W\left.\frac{\partial V_c}{\partial z}\right|_c = 0 \quad (A.18)$$

$$\left.\frac{\partial W}{\partial t}\right|_c + U\left.\frac{\partial W}{\partial x}\right|_c + W\left.\frac{\partial W}{\partial z}\right|_c = -\frac{1}{\rho_0}\left.\frac{\partial p'}{\partial z}\right|_c + \left.\frac{\partial}{\partial z}\left(K_M\frac{\partial W}{\partial z}\right)\right|_c + F_z \quad (A.19)$$

The Coriolis parameter is given by

$$f = 2\Omega sin\varphi \quad (A.20)$$

where $\Omega = \frac{2\pi}{T_e}$, and φ is the latitude. T_e (=23 h 56 min 4 s) is the time required for the earth to rotate once about its axis. K_M is vertical eddy viscosity. The new variables U_c and V_c are non-hydrostatic corrections to the horizontal velocities. The friction terms are given by

$$F_x = \left.\frac{\partial}{\partial x}\left(A_M\frac{\partial U}{\partial x}\right)\right|_c \quad (A.21)$$

$$F_y = \left.\frac{\partial}{\partial x}\left(A_M\frac{\partial V}{\partial x}\right)\right|_c \quad (A.22)$$

$$F_z = \left.\frac{\partial}{\partial x}\left(A_M\frac{\partial W}{\partial x}\right)\right|_c \quad (A.23)$$

where A_M is horizontal eddy viscosity according to Smagorinsky (1963).

Heat transport - Cartesian coordinates.

Heat transport is given by,

$$\frac{\partial T}{\partial t}\bigg|_c + U\frac{\partial T}{\partial x}\bigg|_c + W\frac{\partial T}{\partial z}\bigg|_c = \frac{\partial}{\partial z}\left(K_H\frac{\partial T}{\partial z}\right)\bigg|_c + F_T \tag{A.24}$$

where

$$F_T = \frac{\partial}{\partial x}\left(A_H\frac{\partial T}{\partial x}\right)\bigg|_c \tag{A.25}$$

and K_H and A_H is vertical and horizontal diffusivity, respectively.

A.3.2   σ-coordinate equations.

We want to express the governing equations in the σ-coordinate system. This section gives a description of how the equations of section A.3.1 are transformed to the σ-coordinate system.

Conservation of mass - σ-coordinates.

Starting with equation (A.13), and applying the rules we have from equations (A.1) and (A.2) in section A.2.3, we can express conservation of mass as

$$\frac{\partial U}{\partial x} + \frac{\partial U}{\partial \sigma}\frac{\partial \sigma}{\partial x} + \frac{\partial W}{\partial \sigma}\frac{\partial \sigma}{\partial z} = 0 \tag{A.26}$$

Next, the expression for the vertical velocity (A.12) is inserted into (A.26). This gives us

$$\frac{\partial U}{\partial x} + \frac{\partial U}{\partial \sigma}\left(-\frac{\partial \eta}{\partial x} - \sigma\frac{\partial D}{\partial x}\right) + \frac{\partial}{\partial \sigma}\left(\omega + U\left(\sigma\frac{\partial D}{\partial x} + \frac{\partial \eta}{\partial x}\right) + (1+\sigma)\frac{\partial \eta}{\partial t}\right)\frac{1}{D} = 0 \tag{A.27}$$

By multiplying equation (A.27) by D and carrying out the differentiations, a compact equation for the conservation of mass in the σ-coordinate system on flux form can be written,

$$\frac{\partial}{\partial x}\left(UD\right) + \frac{\partial w}{\partial \sigma} + \frac{\partial \eta}{\partial t} = 0 \tag{A.28}$$

In reaching this result, the chain-rule relationship

$$\frac{\partial}{\partial \sigma}\left(U\sigma\frac{\partial D}{\partial x}\right) = U\frac{\partial D}{\partial x} + \sigma\frac{\partial U}{\partial \sigma}\frac{\partial D}{\partial x} \tag{A.29}$$

was applied (note that $\frac{\partial D}{\partial \sigma} = 0$).

Momentum equations - σ-coordinates.

In the following, each of the terms in equation A.15 will be transformed to the σ-coordinate system. We start out with the local term of the acceleration of a water parcel in the x-direction,

$$\left.\frac{\partial U}{\partial t}\right|_c = \frac{\partial U}{\partial t} + \frac{\partial U}{\partial \sigma}\frac{\partial \sigma}{\partial t} = \frac{\partial U}{\partial t} - \frac{1}{D}\frac{\partial U}{\partial \sigma}\frac{\partial D}{\partial t} - \frac{\sigma}{D}\frac{\partial U}{\partial \sigma}\frac{\partial D}{\partial t} \qquad (A.30)$$

Next, the advective terms become

$$U\frac{\partial U}{\partial x} = U\left[\frac{\partial U}{\partial x} + \frac{\partial U}{\partial \sigma}\frac{\partial \sigma}{\partial x}\right] = U\frac{\partial U}{\partial x} - \frac{U}{D}\frac{\partial U}{\partial \sigma}\frac{\partial \eta}{\partial x} - \frac{U\sigma}{D}\frac{\partial U}{\partial \sigma}\frac{\partial D}{\partial x} \qquad (A.31)$$

$$W\left.\frac{\partial U}{\partial z}\right|_c = W\frac{1}{D}\frac{\partial U}{\partial \sigma} = \frac{1}{D}\frac{\partial U}{\partial \sigma}\left(w + U\frac{\partial \eta}{\partial x} + U\sigma\frac{\partial D}{\partial x} + \frac{\partial \eta}{\partial t} + \sigma\frac{\partial \eta}{\partial t}\right) \qquad (A.32)$$

The Coriolis term stays the same, but the terms on the r.h.s. of equation (A.15) must be transformed. The pressure term becomes

$$-\frac{1}{\rho_0}\left.\frac{\partial p_H}{\partial x}\right|_c = -\frac{1}{\rho_0}\frac{\partial P_{atm}}{\partial x} - g\frac{\partial \eta}{\partial x} - \frac{g}{\rho_0}\frac{\partial}{\partial x}\left(\int_z^0 \rho dz\right)\Big|_c \qquad (A.33)$$

and the vertical diffusivity term is transformed to

$$\frac{\partial}{\partial z}\left(K_M\frac{\partial U}{\partial z}\right)\Big|_c = \frac{\partial}{\partial \sigma}\left(K_M\frac{\partial U}{\partial z}\Big|_c\right)\frac{\partial \sigma}{\partial z} = \frac{1}{D}\frac{\partial}{\partial \sigma}\left(\frac{K_M}{D}\frac{\partial U}{\partial \sigma}\right) \qquad (A.34)$$

When it comes to the horizontal diffusivity terms, however, all the terms that occur upon transforming to the σ-coordinate system are not retained. Instead, the simplified formulation of horizontal viscosity and diffusivity in σ-coordinate models, suggested by Mellor and Blumberg (1985), are used. In this formulation, the transformed friction terms becomes, when multiplied by D,

$$DF_x = \frac{\partial}{\partial x}\left(A_M\frac{\partial UD}{\partial x}\right) \qquad (A.35)$$

$$DF_y = \frac{\partial}{\partial x}\left(A_M\frac{\partial VD}{\partial x}\right) \qquad (A.36)$$

$$DF_z = \frac{\partial}{\partial x}\left(A_M\frac{\partial WD}{\partial x}\right) \qquad (A.37)$$

Now, all terms in equation (A.30) have been transformed. The next step is to multiply (A.30), (A.31), (A.32), (A.33) and (A.34) by D and add them together with (A.35). This gives us

$$\begin{aligned} D\frac{\partial U}{\partial t} + DU\frac{\partial U}{\partial x} + w\frac{\partial U}{\partial \sigma} + \frac{D}{\rho_0}\frac{\partial P_{atm}}{\partial x} + gD\frac{\partial \eta}{\partial x} \\ = \frac{\partial}{\partial \sigma}\left(\frac{K_M}{D}\frac{\partial U}{\partial \sigma}\right) - \frac{gD}{\rho 0}\frac{\partial}{\partial x}\left(\int_z^0 \rho dz\right) + DF_x \end{aligned} \qquad (A.38)$$

when we use the fact that $\frac{\partial \eta}{\partial t} = \frac{\partial D}{\partial t}$.

In order to be able to write the equation on flux form, the equation for conservation of mass (A.28) is multiplied by U and added to the left side of equation (A.38). This gives us the transformed hydrostatic momentum equation in the x-direction on flux form,

$$
\frac{\partial UD}{\partial t} + \frac{\partial U^2 D}{\partial x} + \frac{\partial U\omega}{\partial \sigma} - fVD + \frac{D}{\rho_0}\frac{\partial P_{atm}}{\partial x} + gD\frac{\partial \eta}{\partial x} =
$$
$$
\frac{\partial}{\partial \sigma}\left(\frac{K_M}{D}\frac{\partial U}{\partial \sigma}\right) - \frac{gD^2}{\rho_0}\int_\sigma^0 \left(\frac{\partial \rho}{\partial x} - \frac{\sigma}{D}\frac{\partial D}{\partial x}\frac{\partial \rho}{\partial \sigma}\right)d\sigma + DF_x \tag{A.39}
$$

Following the same procedure, we can now transform equations (A.16), (A.17), (A.18) and (A.19).

Heat transport - σ-coordinates.

The equation for heat transport transforms into

$$
\frac{\partial TUD}{\partial t} + \frac{\partial TD}{\partial x} + \frac{\partial T\omega}{\partial \sigma} = \frac{\partial}{\partial \sigma}\left(\frac{K_H}{D}\frac{\partial T}{\partial \sigma}\right) + \frac{\partial}{\partial x}\left(DA_H\frac{\partial T}{\partial x}\right) \tag{A.40}
$$

Complete set of transformed equations - σ-coordinates.

The complete set of transformed equations become, for hydrostatic horizontal momentum

$$
\frac{\partial UD}{\partial t} + \frac{\partial U^2 D}{\partial x} + \frac{\partial U\omega}{\partial \sigma} - fVD + \frac{D}{\rho_0}\frac{\partial P_{atm}}{\partial x} + gD\frac{\partial \eta}{\partial x} =
$$
$$
\frac{\partial}{\partial \sigma}\left(\frac{K_M}{D}\frac{\partial U}{\partial \sigma}\right) - \frac{gD^2}{\rho_0}\int_\sigma^0 \left(\frac{\partial \rho}{\partial x} - \frac{\sigma}{D}\frac{\partial D}{\partial x}\frac{\partial \rho}{\partial \sigma}\right)d\sigma + DF_x \tag{A.41}
$$

$$
\frac{\partial VD}{\partial t} + \frac{\partial UVD}{\partial x} + \frac{\partial V\omega}{\partial \sigma} + fUD = \frac{\partial}{\partial \sigma}\left(\frac{K_M}{D}\frac{\partial V}{\partial \sigma}\right) + DF_y \tag{A.42}
$$

and for the non-hydrostatic corrections

$$
\frac{\partial U_c D}{\partial t} + \frac{\partial U_c^2 D}{\partial x} + \frac{\partial U_c\omega}{\partial \sigma} = -\frac{D}{\rho_0}\frac{\partial p'}{\partial x} + \frac{1}{\rho_0}\frac{\partial p'}{\partial \sigma}\left(\frac{\partial \eta}{\partial x} + \sigma\frac{\partial D}{\partial x}\right) \tag{A.43}
$$

$$
\frac{\partial V_c D}{\partial t} + \frac{\partial U_c V_c D}{\partial x} + \frac{\partial V_c\omega}{\partial \sigma} = 0 \tag{A.44}
$$

$$
\frac{\partial WD}{\partial t} + \frac{\partial U_c WD}{\partial x} + \frac{\partial W\omega}{\partial \sigma} = -\frac{1}{\rho_0}\frac{\partial p'}{\partial \sigma} \tag{A.45}
$$

Conservation of mass and heat transport can still be expressed by,

$$
\frac{\partial}{\partial x}(UD) + \frac{\partial w}{\partial \sigma} + \frac{\partial \eta}{\partial t} = 0 \tag{A.46}
$$

and

$$\frac{\partial TUD}{\partial t} + \frac{\partial TD}{\partial x} + \frac{\partial T\omega}{\partial \sigma} = \frac{\partial}{\partial \sigma}\left(\frac{K_H}{D}\frac{\partial T}{\partial \sigma}\right) + \frac{\partial}{\partial x}\left(DA_H\frac{\partial T}{\partial x}\right). \qquad (A.47)$$

The temperature is coupled with the density through a simple equation of state,

$$\rho(T) = -0.0002 \cdot \rho_0 \cdot T \qquad (A.48)$$

where ρ_0 is a reference density.

A.4 Solution technique

A.4.1 Numerical grid

Numerical solutions to the governing equations are found using finite difference methods on a staggered Arakawa C-grid (Mesinger and Arakawa 1976), see Figure A.1.
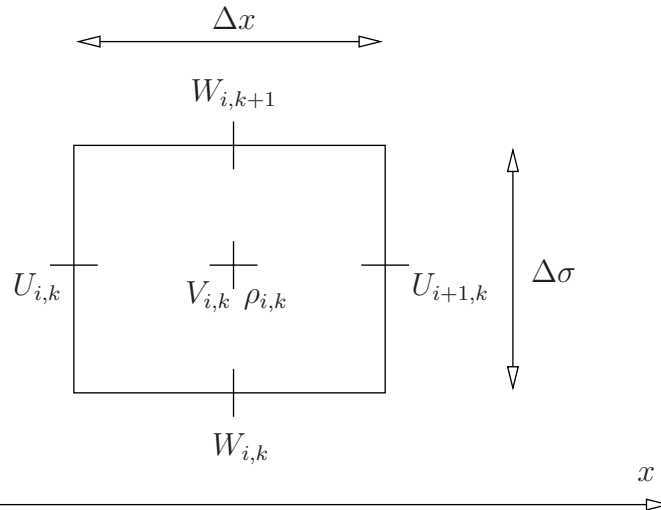
Figure A.1: *Arakawa C-grid in 2D. The illustration shows grid cell (i,k). Indices i and k refer to horizontal and vertical position of the grid cell, respectively.*

A.4.2 Mode splitting

Different numerical schemes are used for the different terms in the equations, but explicit schemes are preferred in order to keep the computation time as low as

possible. However, numerical instability will occur for explicit schemes when the Courant number is too large. The Courant number is defined by,

$$C_n(x) = \frac{\Delta t}{\Delta x} \sqrt{2 \ g \ \max(H)}. \tag{A.49}$$

Thus, it is the largest possible speed of surface gravity waves that dictates the largest possible stable time-step for explicit finite difference schemes on a given grid. The time-step required to resolve fast surface gravity waves is much smaller than the time-step required to propagate the two-dimensional fields. In order to save time on the computer, the two-dimensional velocity field is split into a one-dimensional barotropic (external) mode and a two-dimensional baroclinic (internal) mode. This is expressed by

$$U(x, \sigma, t) = U_E(x, t) + U_I(x, \sigma, t) \tag{A.50}$$

$$U_E(x, t) = \int_{-1}^{0} U(x, \sigma, t) d\sigma \tag{A.51}$$

where U_E and U_I are barotropic (external) and baroclinic (internal) velocity components, respectively. Integrating the horizontal momentum equations (A.41) and (A.42), and the continuity equation (A.46), vertically from the seabed to the surface, using the boundary conditions that $\omega(0)=\omega(-1)=0$, we obtain the governing equations for the barotropic mode. For the depth-integrated continuity equation we have,

$$\frac{\partial U_E D}{\partial x} + \frac{\partial \eta}{\partial t} = 0 \tag{A.52}$$

Then we have for the depth-integrated momentum equations

$$\frac{\partial U_E D}{\partial t} - fV_E D + gD\frac{\partial \eta}{\partial x} = \frac{\partial}{\partial x} \left(A_{M2D}\frac{\partial U_E D}{\partial x} \right) + \frac{1}{\rho_0} \left(\tau_{0x} - \tau_{bx} \right) + A_x \tag{A.53}$$

and

$$\frac{\partial V_E D}{\partial t} + fU_E D = \frac{\partial}{\partial x} \left(A_{M2D}\frac{\partial V_E D}{\partial x} \right) + \frac{1}{\rho_0} \left(\tau_{0y} - \tau_{by} \right) + A_y \tag{A.54}$$

where

$$\frac{1}{\rho_0} \left(\tau_{0x}, \tau_{0y} \right) = \frac{K_M}{D} \left(\frac{\partial U}{\partial \sigma}, \frac{\partial V}{\partial \sigma} \right) \tag{A.55}$$

and

$$\frac{1}{\rho_0} \left(\tau_{bx}, \tau_{by} \right) = \frac{K_M}{D} \left(\frac{\partial U}{\partial \sigma}, \frac{\partial V}{\partial \sigma} \right) \tag{A.56}$$

are boundary conditions at the surface and at the bottom, respectively. Bottom stress is specified by,

$$(\tau_{bx}, \tau_{by}) = \rho_0 \cdot C_D \cdot |U_b, V_b| \cdot (U_b, V_b) \tag{A.57}$$

where U_b and V_b are flow velocity components at the bottom. Surface stress in the present model is set to zero (no wind stress), i.e.

$$(\tau_{0x}, \tau_{0y}) = 0. \tag{A.58}$$

The 2D horizontal viscosity is calculated according to Smagorinsky (1963),

$$A_{M2D} = C_M (\Delta x)^2 \left[\left(\frac{\partial U_E}{\partial x} \right)^2 + \frac{1}{2} \left(\frac{\partial V_E}{\partial x} \right)^2 \right]^{\frac{1}{2}} \tag{A.59}$$

The terms A_x and A_y are given by

$$(A_x, A_y) = \left(\int_{-1}^{0} \Delta U \, d\sigma, \int_{-1}^{0} \Delta V \, d\sigma \right) \tag{A.60}$$

where

$$\Delta U = -\frac{gD^2}{\rho_0} \int_{\sigma}^{0} \left(\frac{\partial \rho}{\partial x} - \frac{\sigma}{D} \frac{\partial D}{\partial x} \frac{\partial \rho}{\partial \sigma} \right) - \frac{\partial U^2 D}{\partial x} + \frac{\partial U \omega}{\partial \sigma} \tag{A.61}$$

$$\Delta V = -\frac{\partial UVD}{\partial x} + \frac{\partial V \omega}{\partial \sigma} \tag{A.62}$$

Governing equations for the baroclinic mode are obtained by subtracting the depth-integrated equations from the full two-dimensional equations, thus obtaining

$$\frac{\partial U_I D}{\partial t} - f V_I D + \frac{1}{\rho_0} (\tau_{0x} - \tau_{bx}) + A_x = \\ \frac{\partial}{\partial x} \left(A_M \frac{\partial U_I D}{\partial x} \right) + \frac{\partial}{\partial \sigma} \left(\frac{K_M}{D} \frac{\partial U_I}{\partial \sigma} \right) + \Delta U \tag{A.63}$$

and

$$\frac{\partial V_I D}{\partial t} + f U_I D + \frac{1}{\rho_0} (\tau_{0y} - \tau_{by}) + A_y = \\ \frac{\partial}{\partial x} \left(A_M \frac{\partial V_I D}{\partial x} \right) + \frac{\partial}{\partial \sigma} \left(\frac{K_M}{D} \frac{\partial V_I}{\partial \sigma} \right) + \Delta V \tag{A.64}$$

Equations (A.52), (A.53) and (A.54) can be solved independently from equations (A.63) and (A.63), using different time-steps. A time step of $\Delta t_I = \Delta t_E \cdot \text{NSI}$ is used for propagating the baroclinic field, Δt_E is the time step used for propagating the 2D fields and NSI is 32. This technique is known as mode splitting (Berntsen et al. 1981).

A.4.3 Time integration

Procedure

Starting with a solution at time $t_n = n\Delta t_I$, where n is the current time step, for all variables $(U^n, V^n, \omega^n, T^n, \eta^n)$, the solution at the next time step $n+1$ at time $t_{n+1} = (n+1)\Delta t_I$ is estimated according to the following procedure.

The final solution is estimated using a θ-method in which a predictor step and a corrector step is taken. At first ΔU and ΔV are calculated, using U^n, V^n, ω^n and T^n. Then, the depth-integrated equations (A.52), (A.53) and (A.54) are solved and predictors for the surface elevation η^* and the barotropic velocity components U_E^* and V_E^* are found. Now, two velocity components defined as

$$U_{AH}^* = U_E^* + U_I^n \tag{A.65}$$

$$V_{AH}^* = V_E^* + V_I^n \tag{A.66}$$

are introduced. These variables can be viewed as hydrostatic horizontal advection velocities.

The next step is to introduce the non-hydrostatic pressure correction, p', and the corresponding corrections to the horizontal velocities, U_c^* and V_c^*. The pressure correction occurs because U_{AH}^*, V_{AH}^*, ω^n, η^n and η^* do not conserve volume locally. It is this lack of volume conservation that is used to establish equations (A.43) and (A.44). Solving this set of equations produces U_c^* and V_c^*. A detailed description of the procedure is provided by Heggelund et al. (2004).

Once U_c^* and V_c^* have been determined, new horizontal advection velocities are defined as

$$U_A^* = U_{AH}^* + U_c^* \tag{A.67}$$

$$V_A^* = V_{AH}^* + V_c^*. \tag{A.68}$$

Also, the baroclinic velocity components are corrected

$$\widetilde{U}_I = U_I^n + U_c^* \tag{A.69}$$

$$\widetilde{V}_I = V_I^n + V_c^* \tag{A.70}$$

Then equations (A.63) and (A.64) are propagated in time, using $\widetilde{U}_I$ and $\widetilde{V}_I$ instead of U_I and V_I, respectively, and we obtain the predictors U_I^* and V_I^*. We can now write the predictors for U and V,

$$U^* = U_E^* + U_I^* \tag{A.71}$$

$$V^* = V_E^* + V_I^* \tag{A.72}$$

A predictor for the temperature, T^*, is then found by propagating equation (A.47).

The corrector step is performed by using the predictors U_A^*, V_A^*, T^* and ω^* for computing new values of ΔU and ΔV. Then, the same procedure as was used for obtaining predictors is used in order to obtain the correctors U^{**}, V^{**}, ω^{**}, T^{**} and η^{**}.

Now, the solution at time t_{n+1} is estimated as

$$\phi^{n+1} = \phi^n + \theta \left(\phi^{**} - \phi^n\right) + \left(1 - \theta\right)\left(\phi^* - \phi^n\right) \tag{A.73}$$

where ϕ can be replaced by U, V, ω, η and T.
These velocity components are used for calculating advective terms and the σ-coordinate velocity, ω^*, from equation (A.12).

Appendix B

VIV analyses of free span pipelines

This appendix contains plots of results from a VIV-analysis of a free span pipeline in a variable current flow environment. Two methods were used for computing the fatigue damage. In the first method it is assumed that the current flow is always directed perpendicular to the pipe, and in the second method the directional distribution of the current is accounted for. Calculations are carried out for a range of free-span lengths, L, and for a variety of pipe orientations, θ_R, in a global coordinate system in which North is $0/360^o$ and East is 90°.
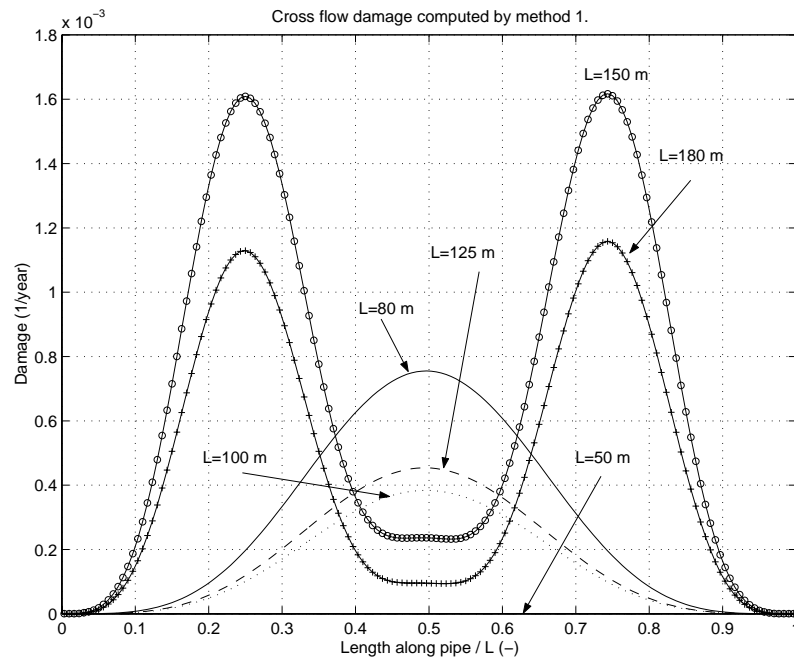
Figure B.1: *Distribution of fatigue damage due to cross flow VIV calculated by method 1. The denomination on the x-axis is non-dimensional length along the longitudinal axis of the pipe.*
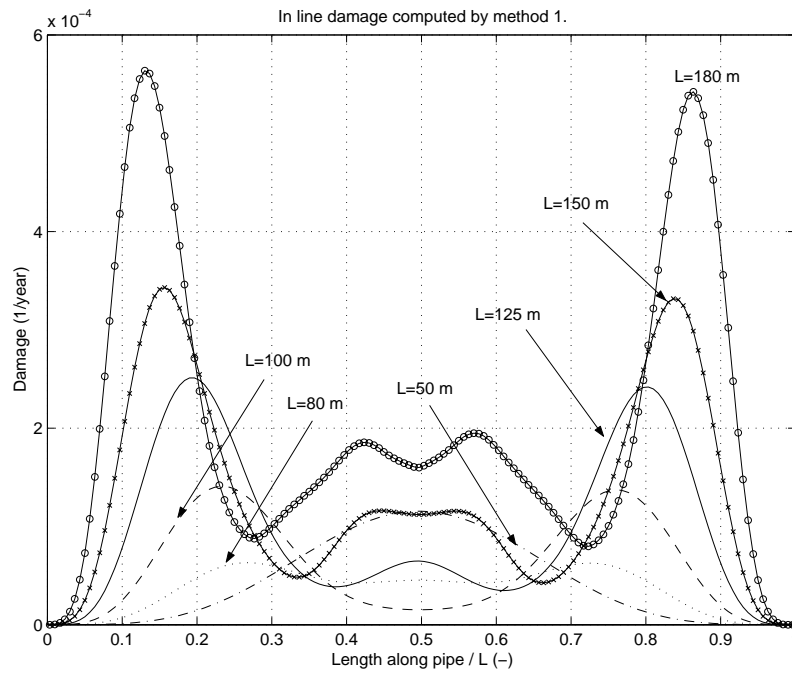
Figure B.2: *Distribution of fatigue damage due to in line VIV calculated by method 1. The denomination on the x-axis is non-dimensional length along the longitudinal axis of the pipe.*
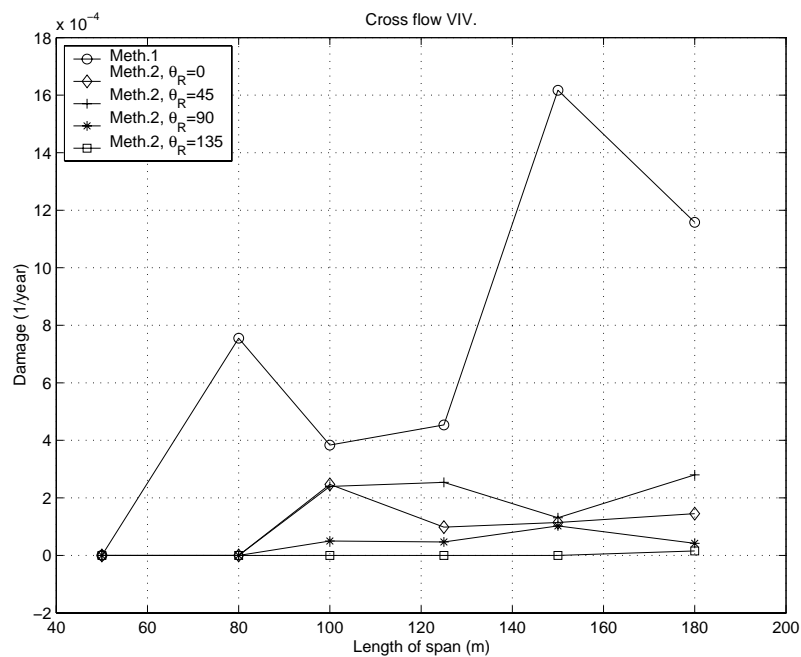
Figure B.3: *Maximum estimated damage due to cross flow VIV.*
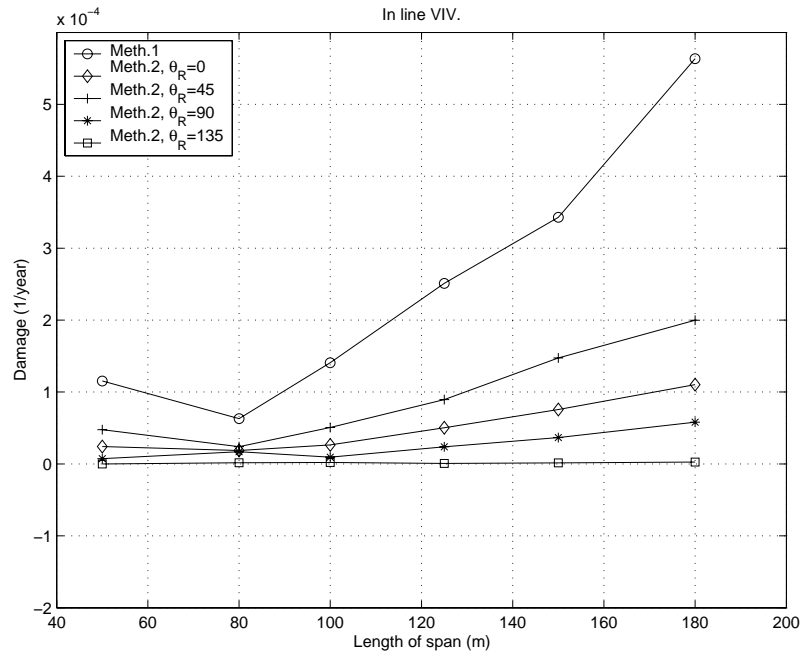
Figure B.4: *Maximum estimated damage due to in-line VIV.*
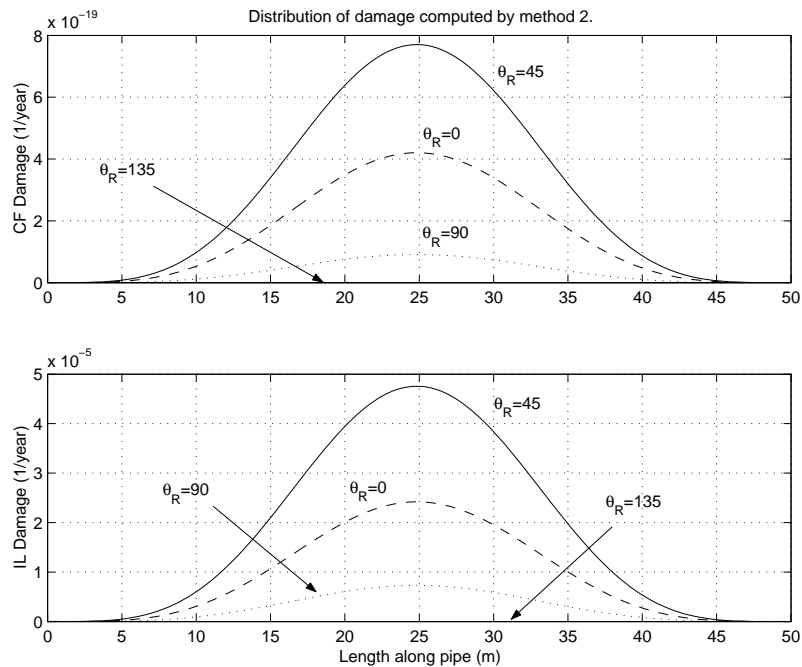
Figure B.5: *Distribution of estimated fatigue damage. Calculated by method 2. Span length is 50 meters. Cross flow (top) and in-line (bottom) damage is shown.*
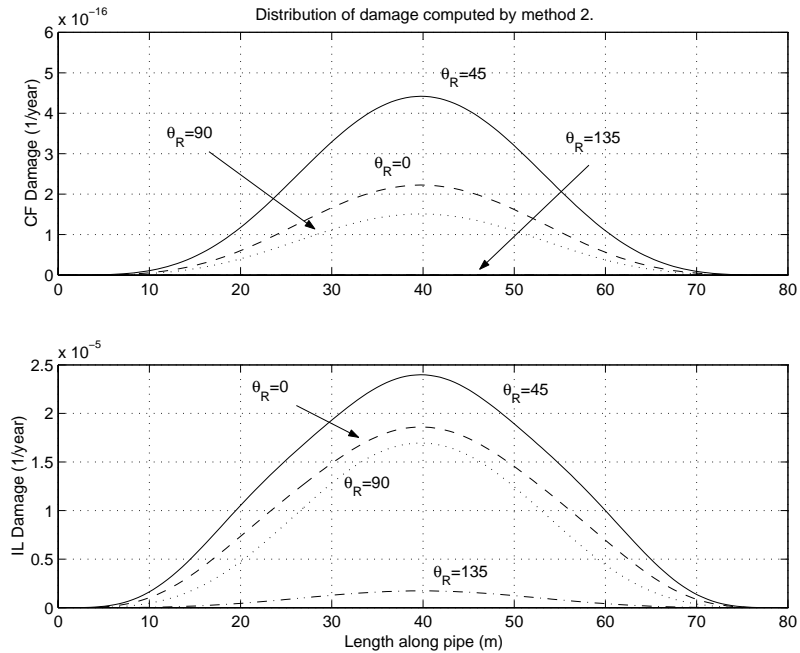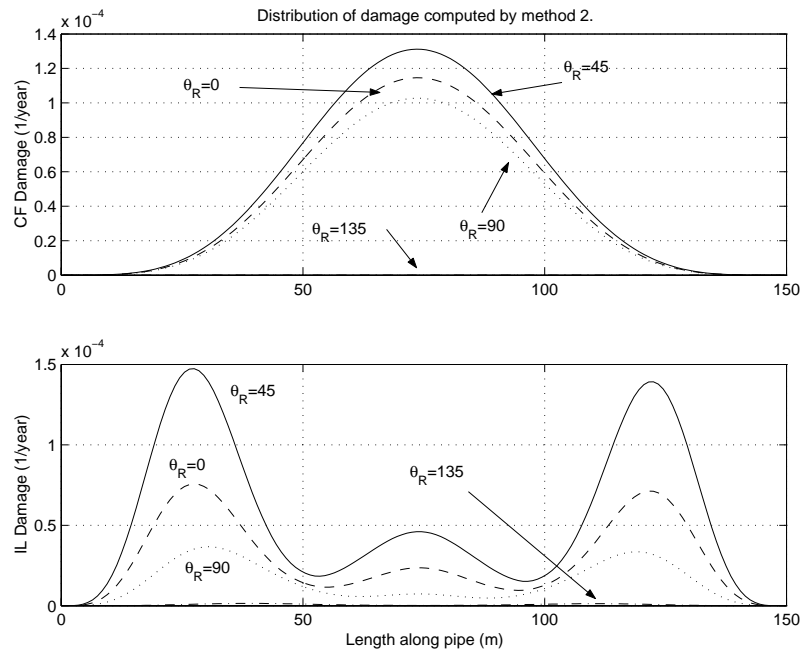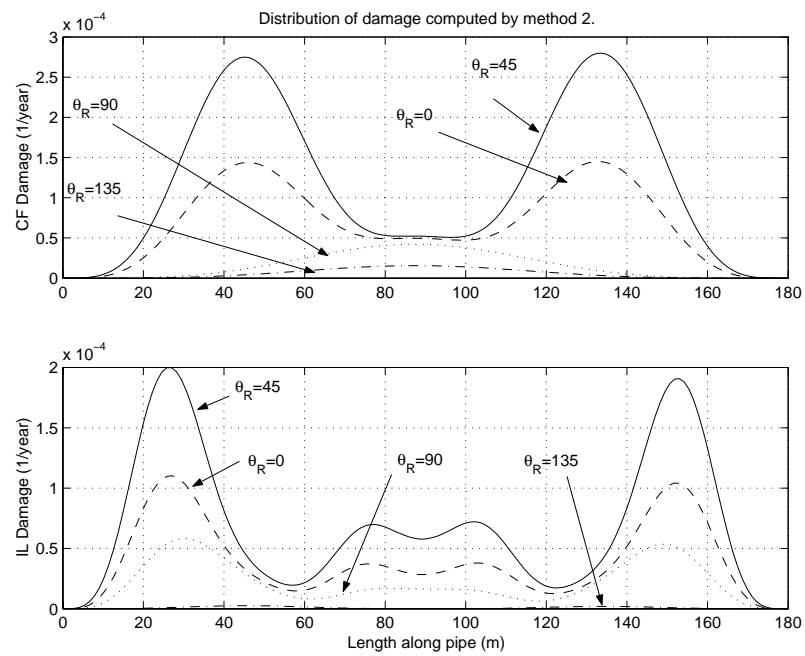
Figure B.6: *Distribution of estimated fatigue damage. Calculated by method 2. Span length is 80 meters. Cross flow (top) and in-line (bottom) damage is shown.*
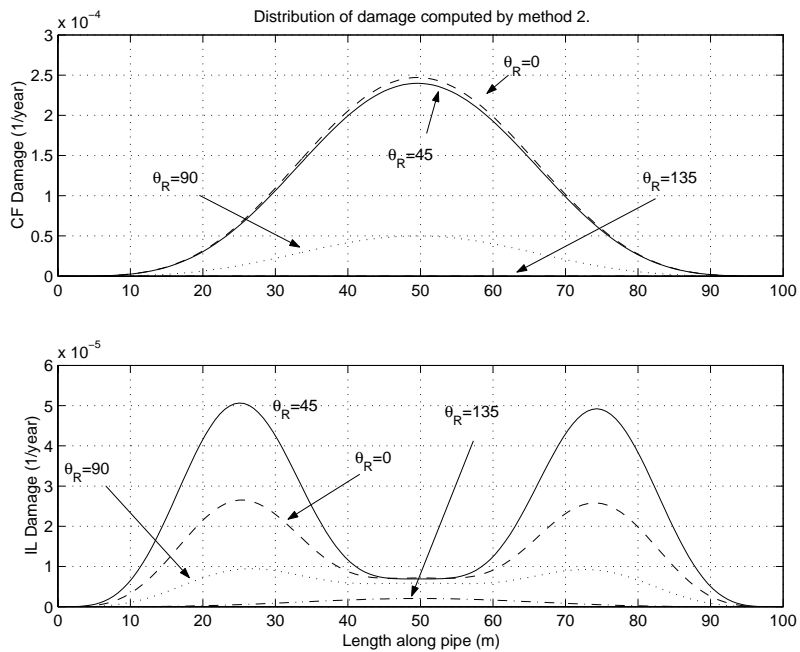
Figure B.7: *Distribution of estimated fatigue damage. Calculated by method 2. Span length is 100 meters. Cross flow (top) and in-line (bottom) damage is shown.*
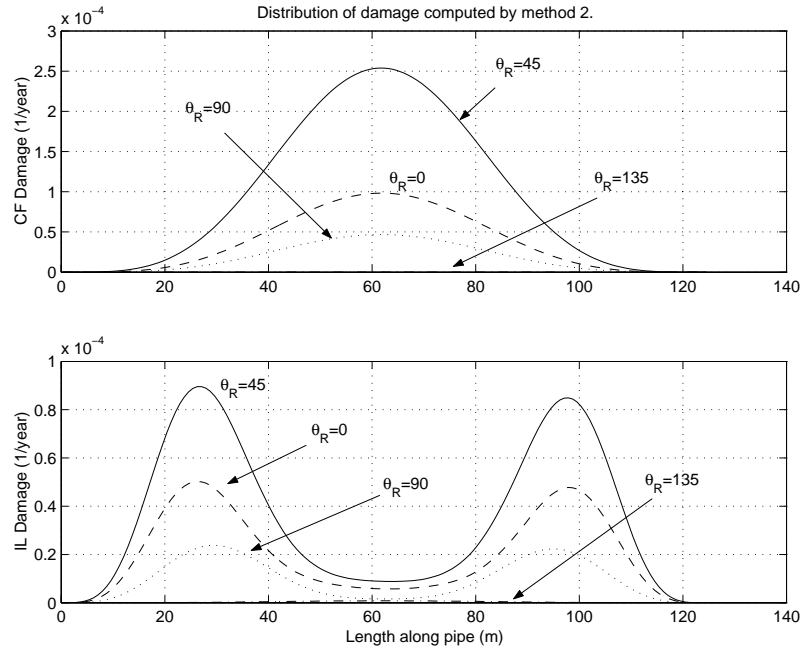
Figure B.8: *Distribution of estimated fatigue damage. Calculated by method 2. Span length is 125 meters. Cross flow (top) and in-line (bottom) damage is shown.*

Figure B.9: *Distribution of estimated fatigue damage. Calculated by method 2. Span length is 150 meters. Cross flow (top) and in-line (bottom) damage is shown.*

Figure B.10: *Distribution of estimated fatigue damage. Calculated by method 2. Span length is 180 meters. Cross flow (top) and in-line (bottom) damage is shown.*

Appendix C

Results from simulations of marine operations

This appendix contains plots of results from simulations of marine simulations.

Figures C.1-C.8 show results from simulations of lowering an object from the surface to the sea bed. Estimated position of the object when arriving at the desired depth, based on static current profile measured at the start of the lowering process, is marked with a cross, simulated position in a time-varying current is marked with a circle. Dots are separated by 15 minutes.

Figures C.9-C.13 show results from simulations of the motions of an object suspended just above sea bed in an area where the current sometimes changes abruptly. Dots are separated by two minutes.
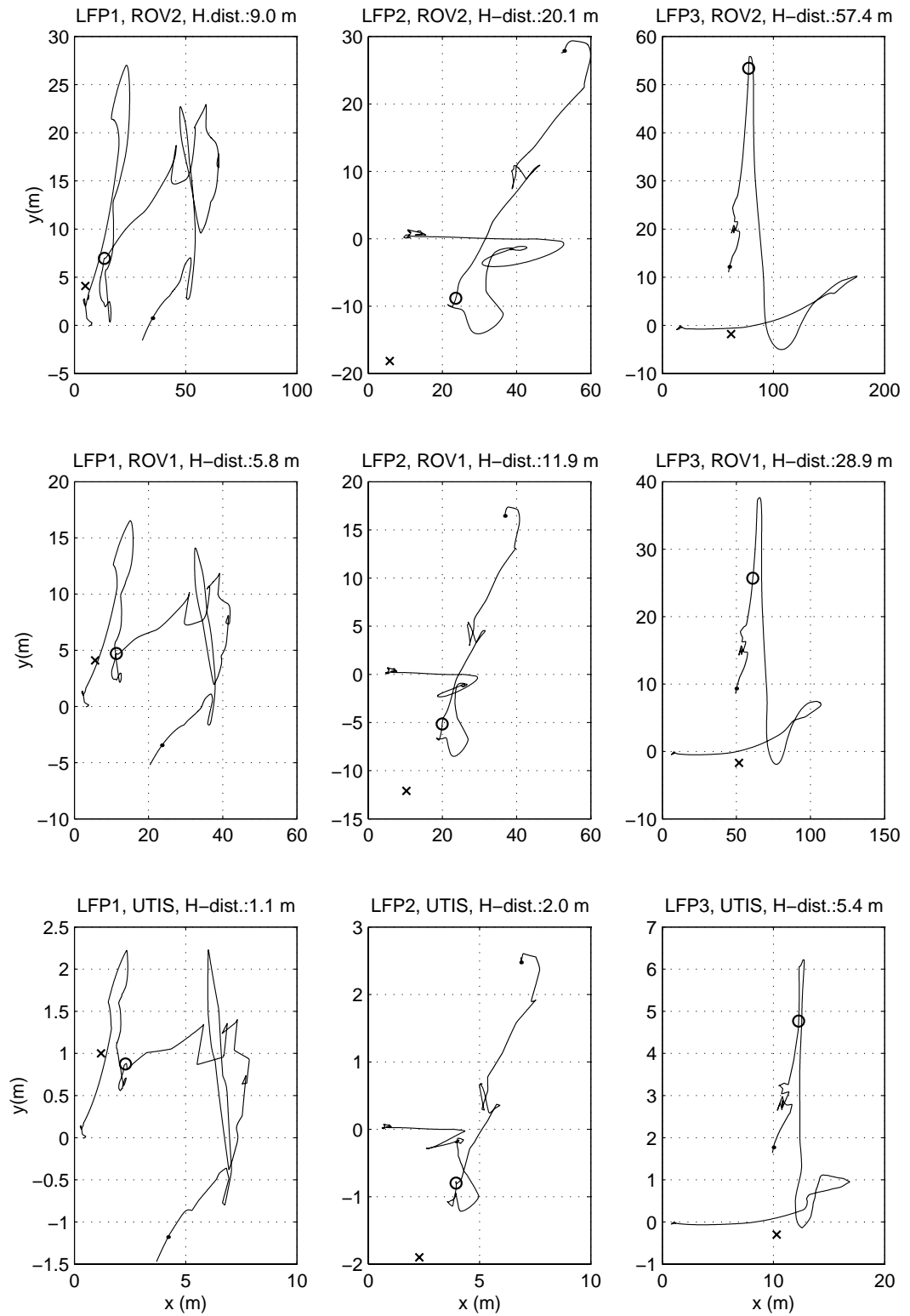
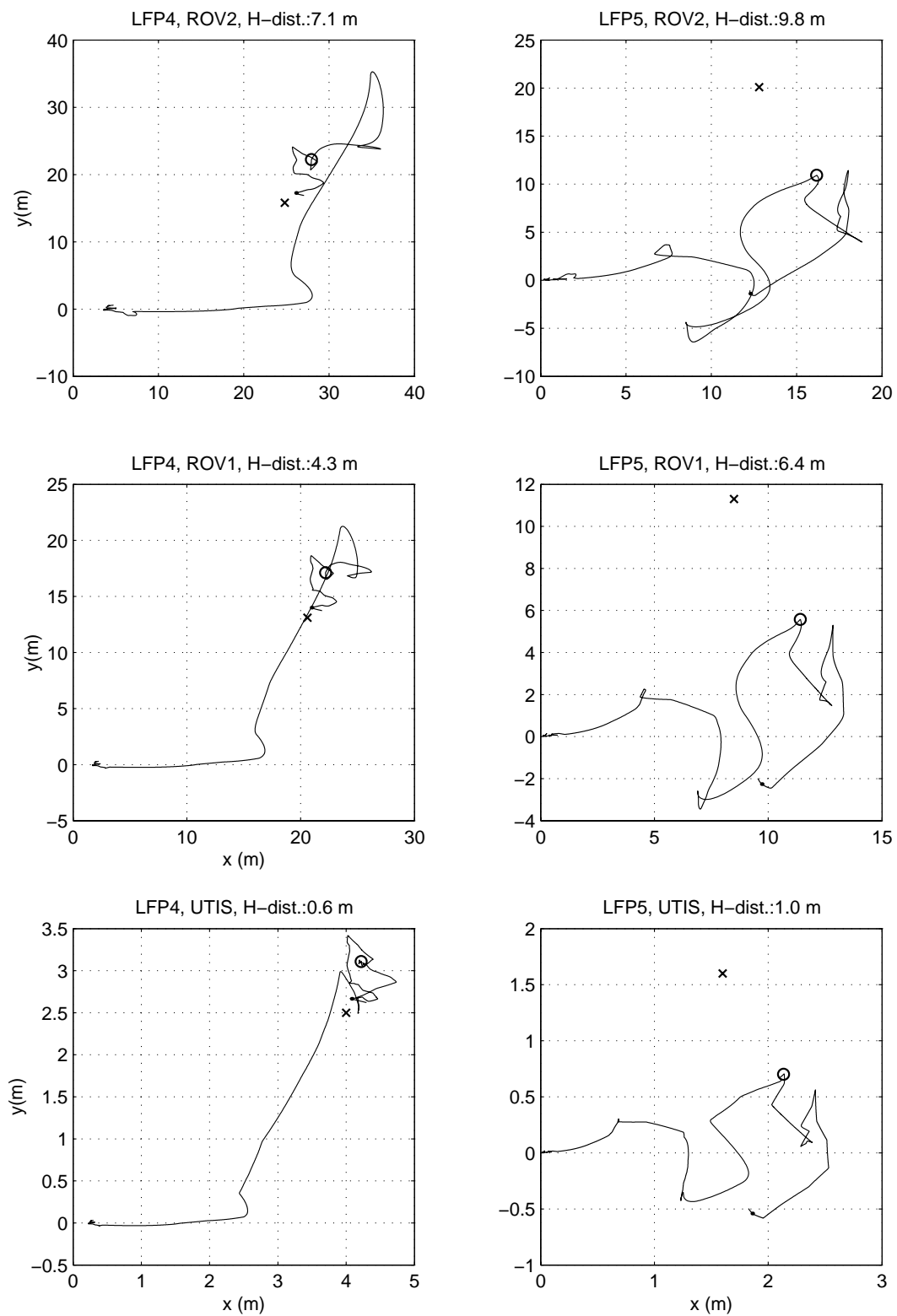**Figure C.1**: *November 1999, 775 m water depth, OL-II.*
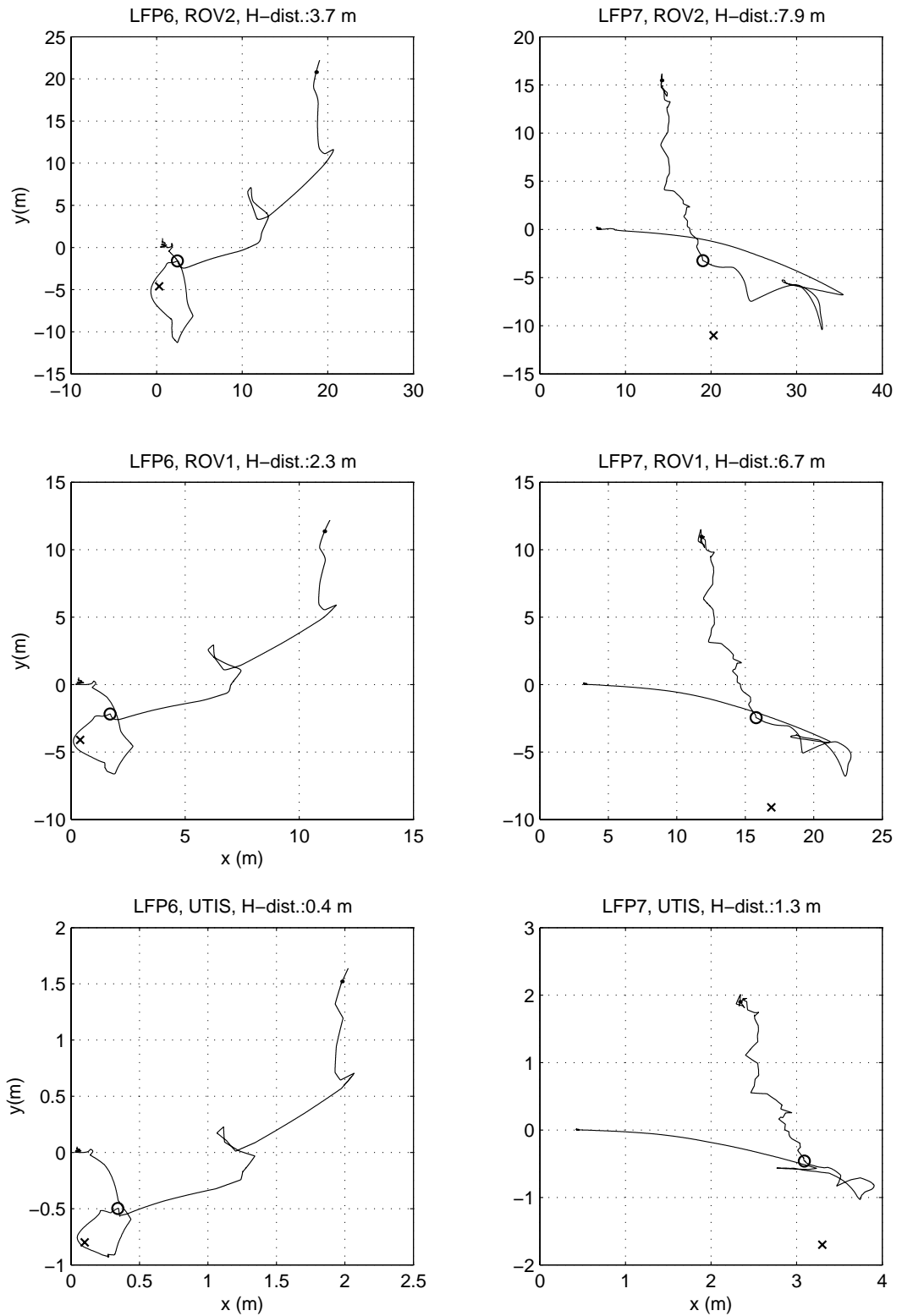
Figure C.2: *April 2000, 775 m water depth, OL-II.*

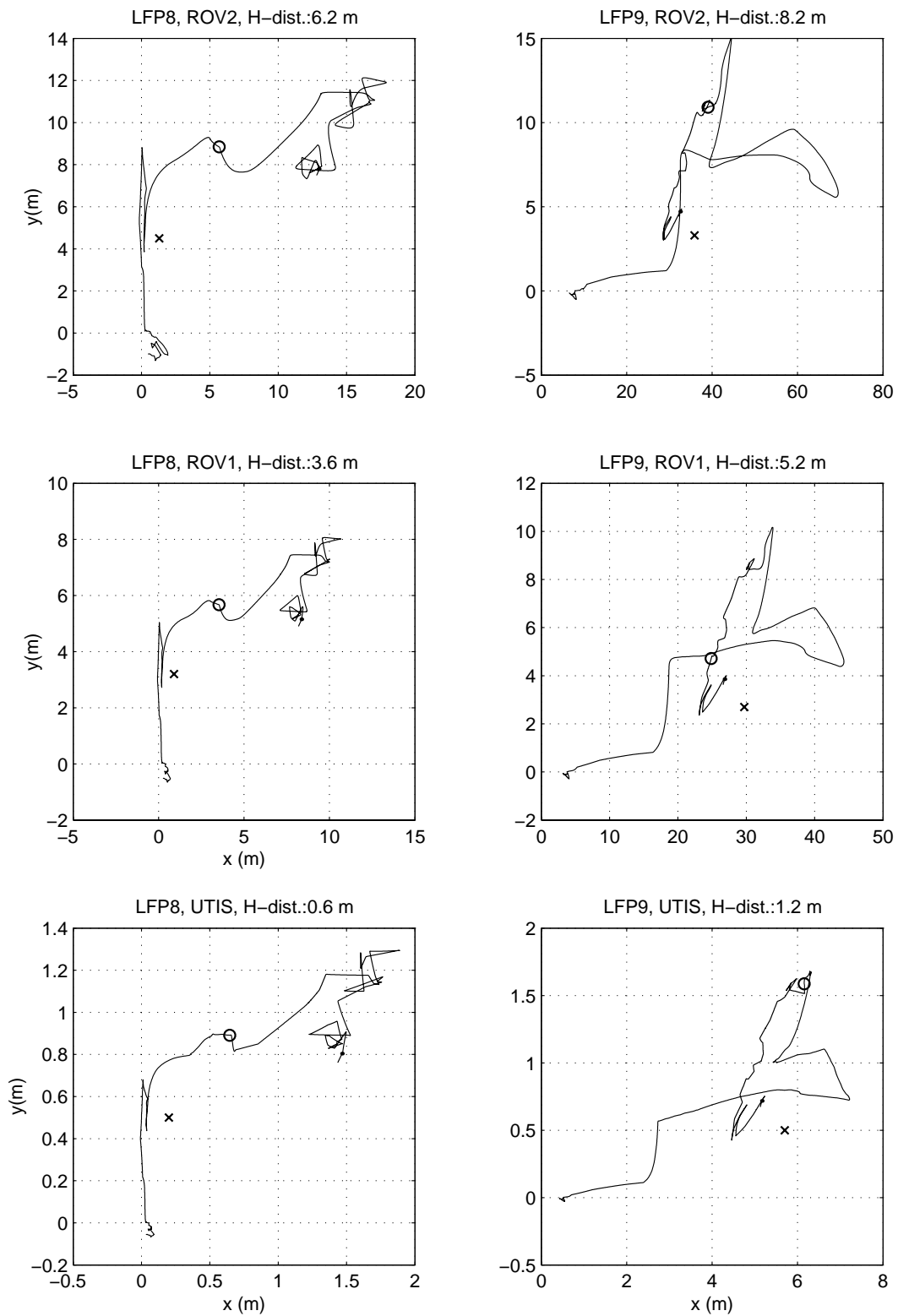**Figure C.3**: *July 2000, 775 m water depth, OL-II.*

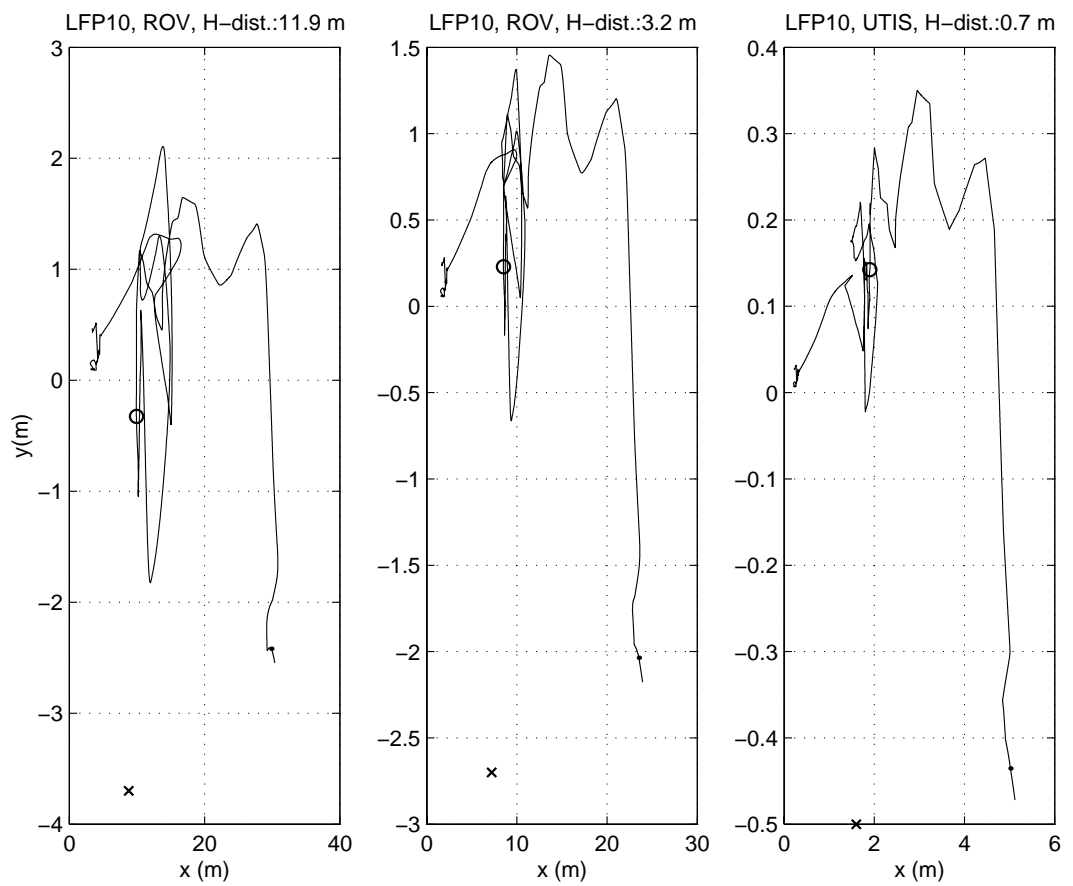**Figure C.4**: *November 2000, 775 m water depth, OL-II.*

Figure C.5: *November 1999, 1088 m water depth, OL-I.*
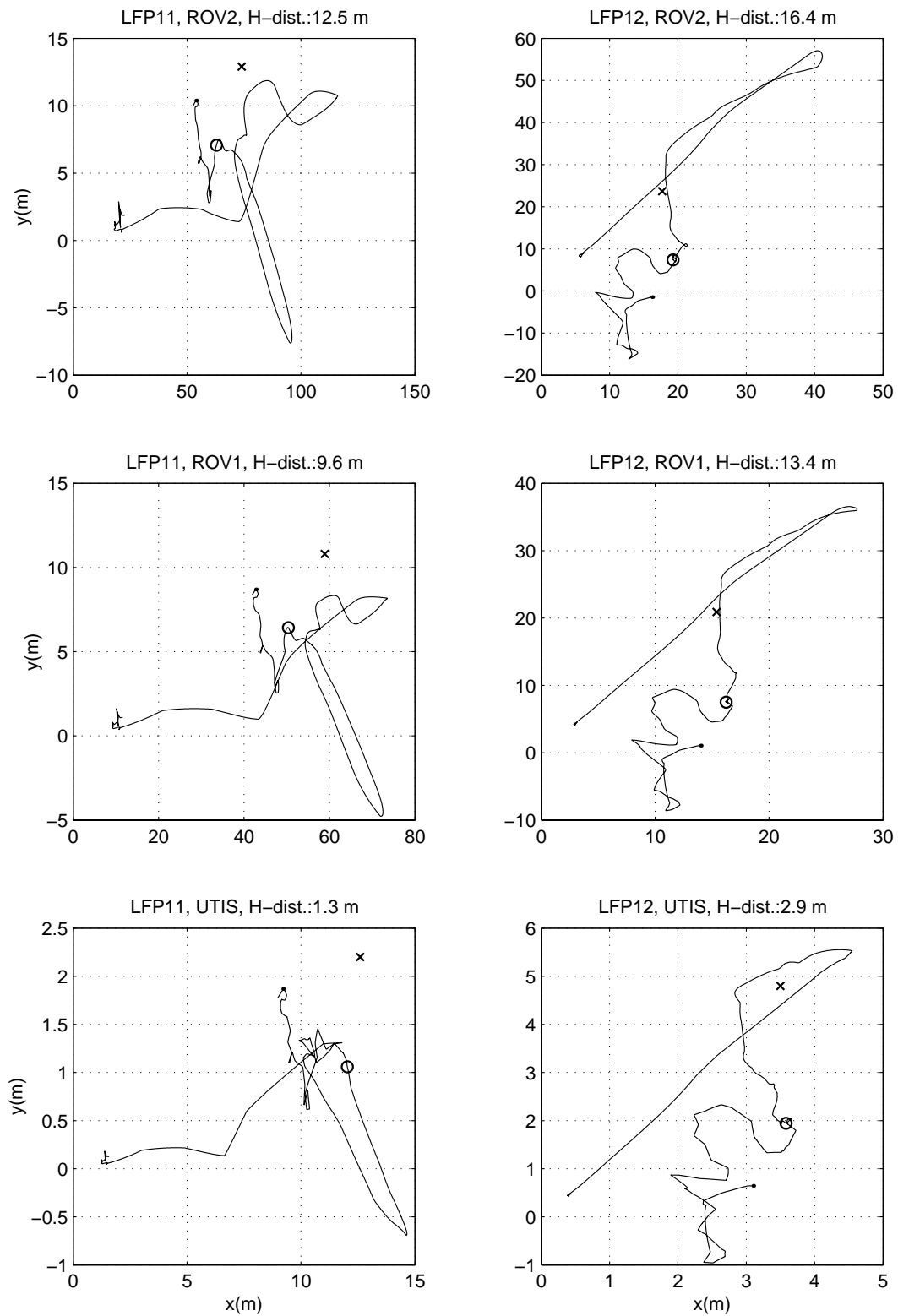
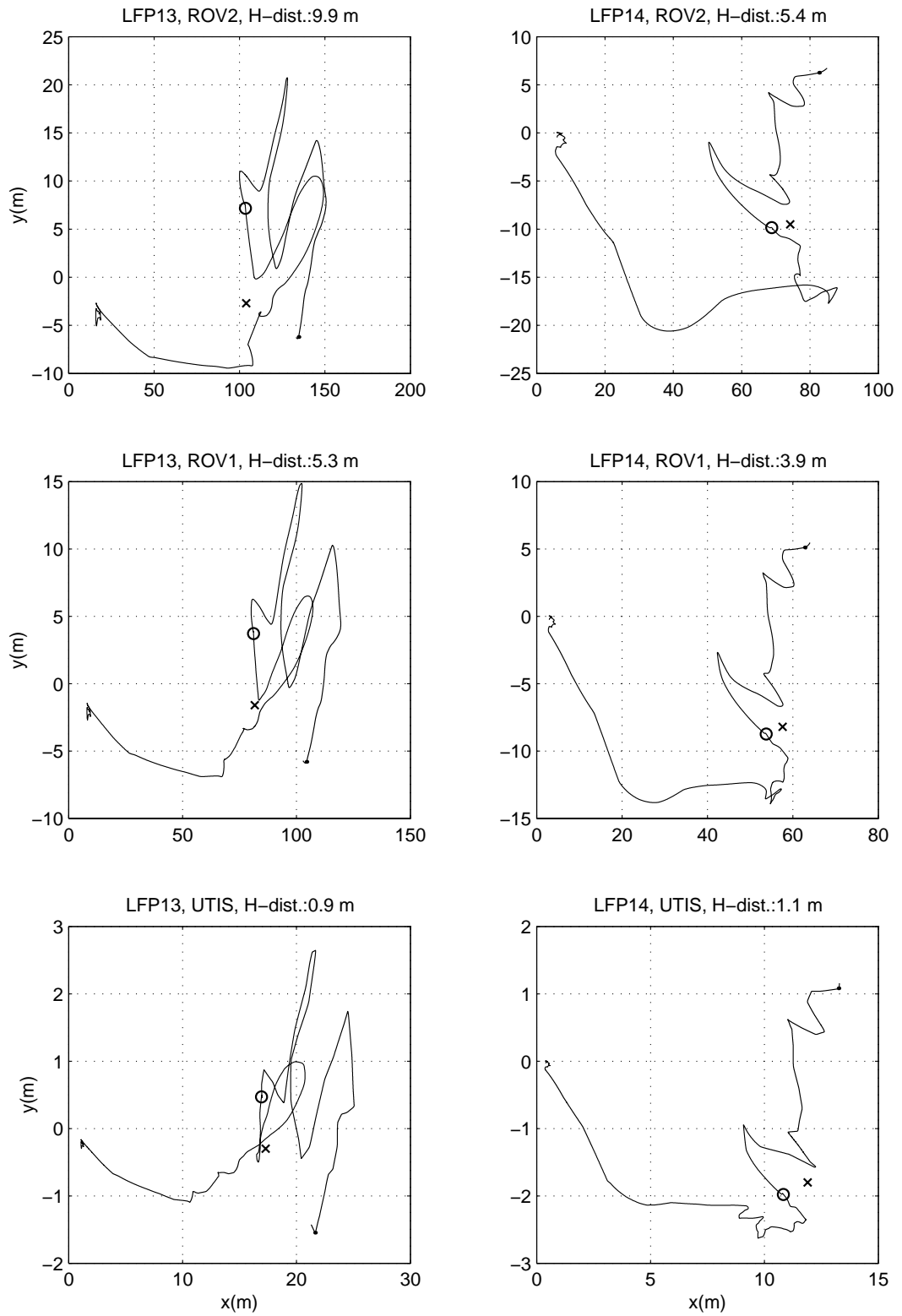**Figure C.6**: *December 1999, 1088 m water depth, OL-I.*

Figure C.7: *March 2000, 1088 m water depth, OL-I.*
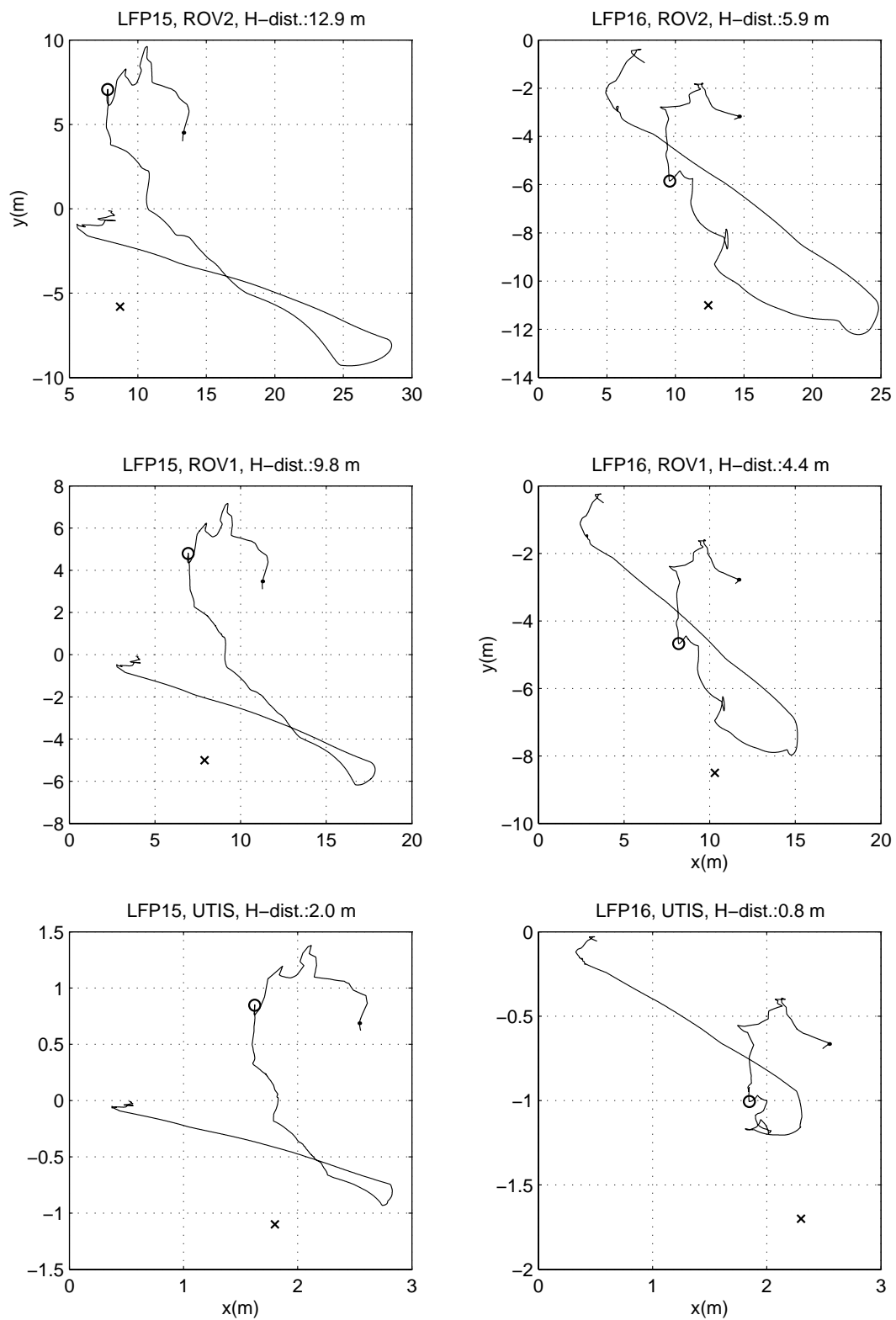
Figure C.8: *July 2000, 1088 m water depth, OL-I.*
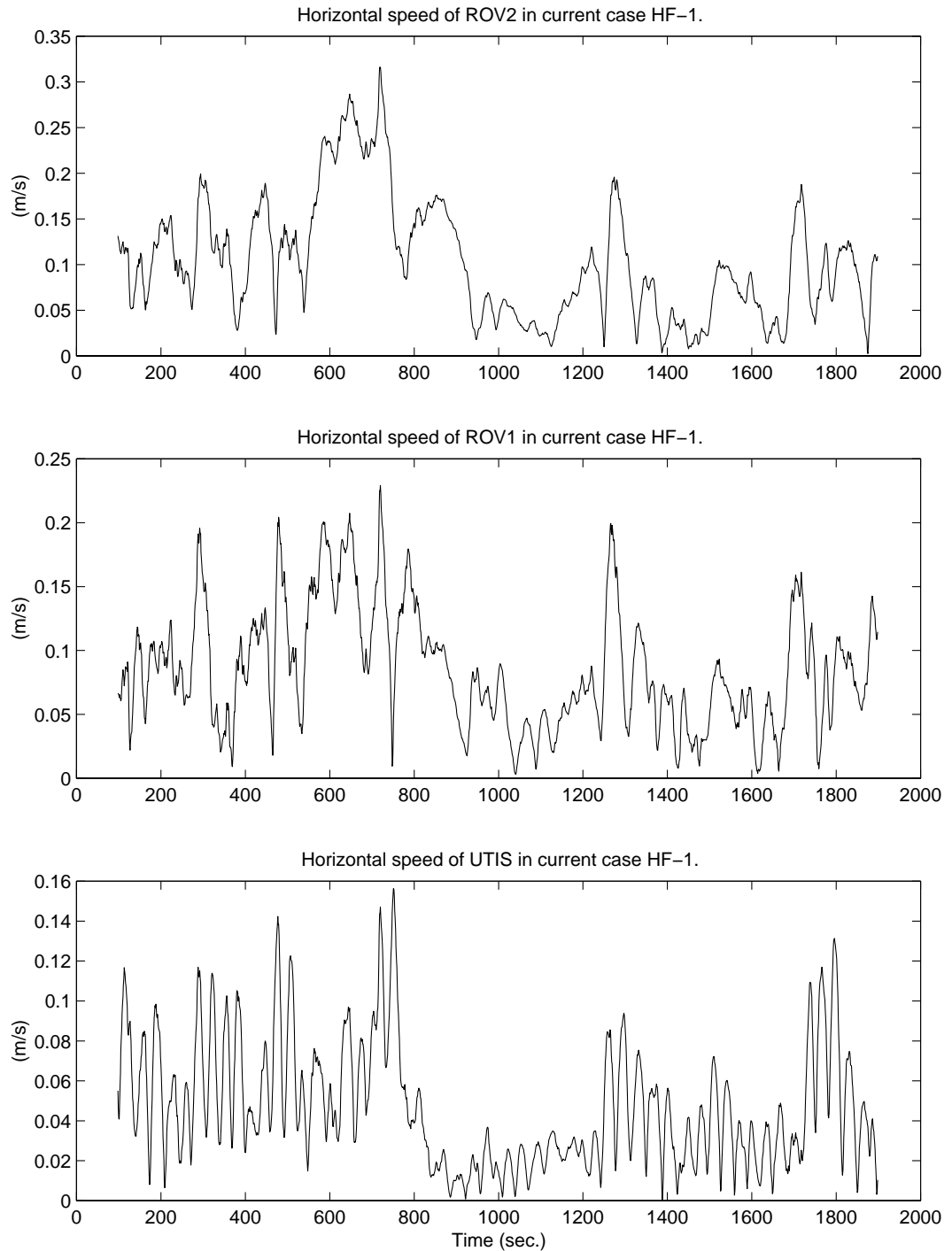
Figure C.9: *Horizontal speed of the objects due to current flow measured during event 1.*
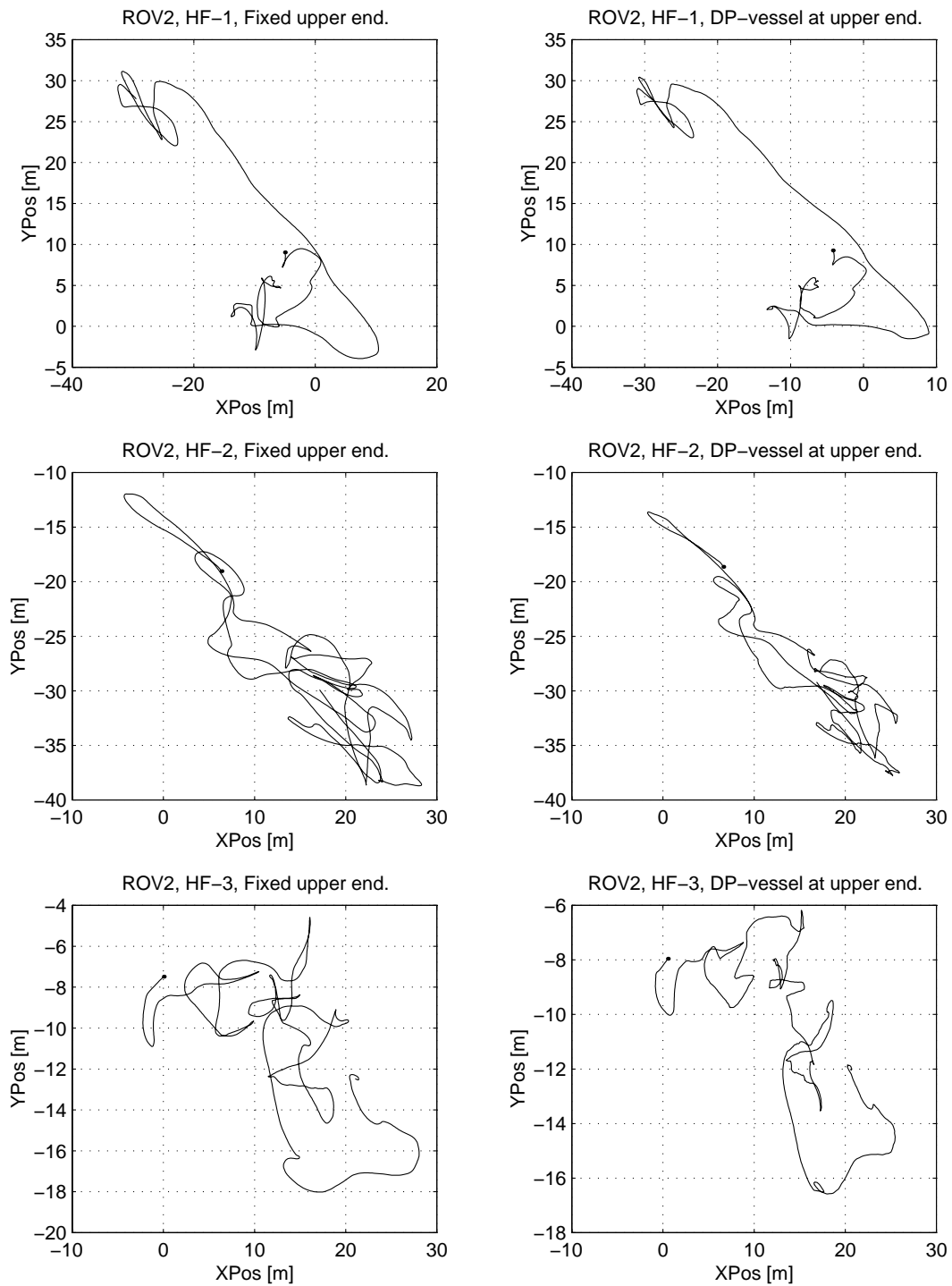
Figure C.10: *Effect of vessel motions. ROV2. Forcing is by the current flow recorded in traces HF-1, HF-2 and HF-3.*

Figure C.11: *Effect of vessel motions. UTIS. Forcing is by the current flow recorded in traces HF-1, HF-2 and HF-3.*

Figure C.12: *Response of all objects when forced by the current flow recorded in traces HF-1, HF-2 and HF-3.*

Figure C.13: *Response of all objects when forced by the current flow recorded in traces HF-4, HF-5 and HF-6.*

Previous reports published at the Institute of Marine Technology (previously : Faculty of Marine Technology) at the Norwegian University of Science and Technology.
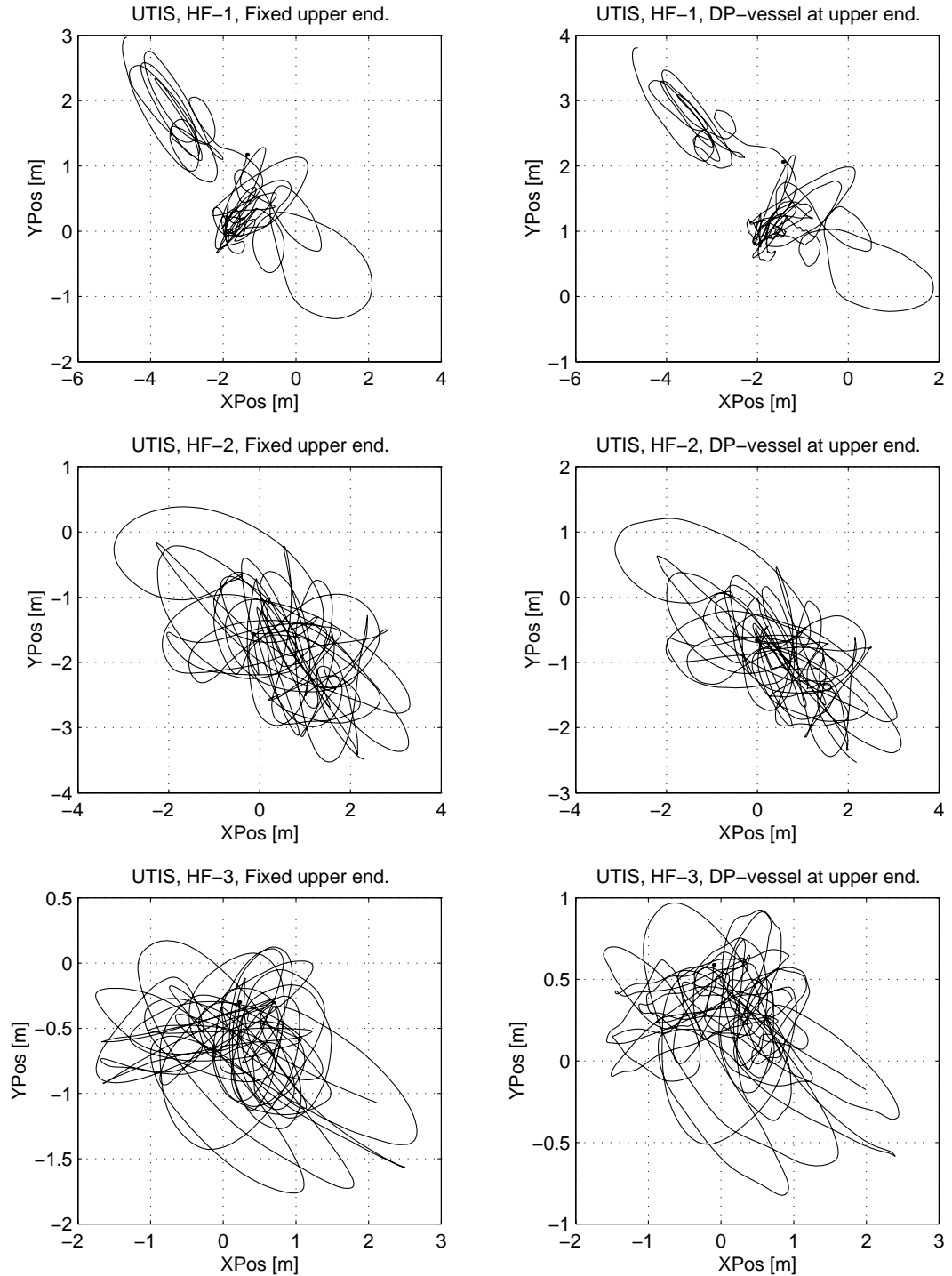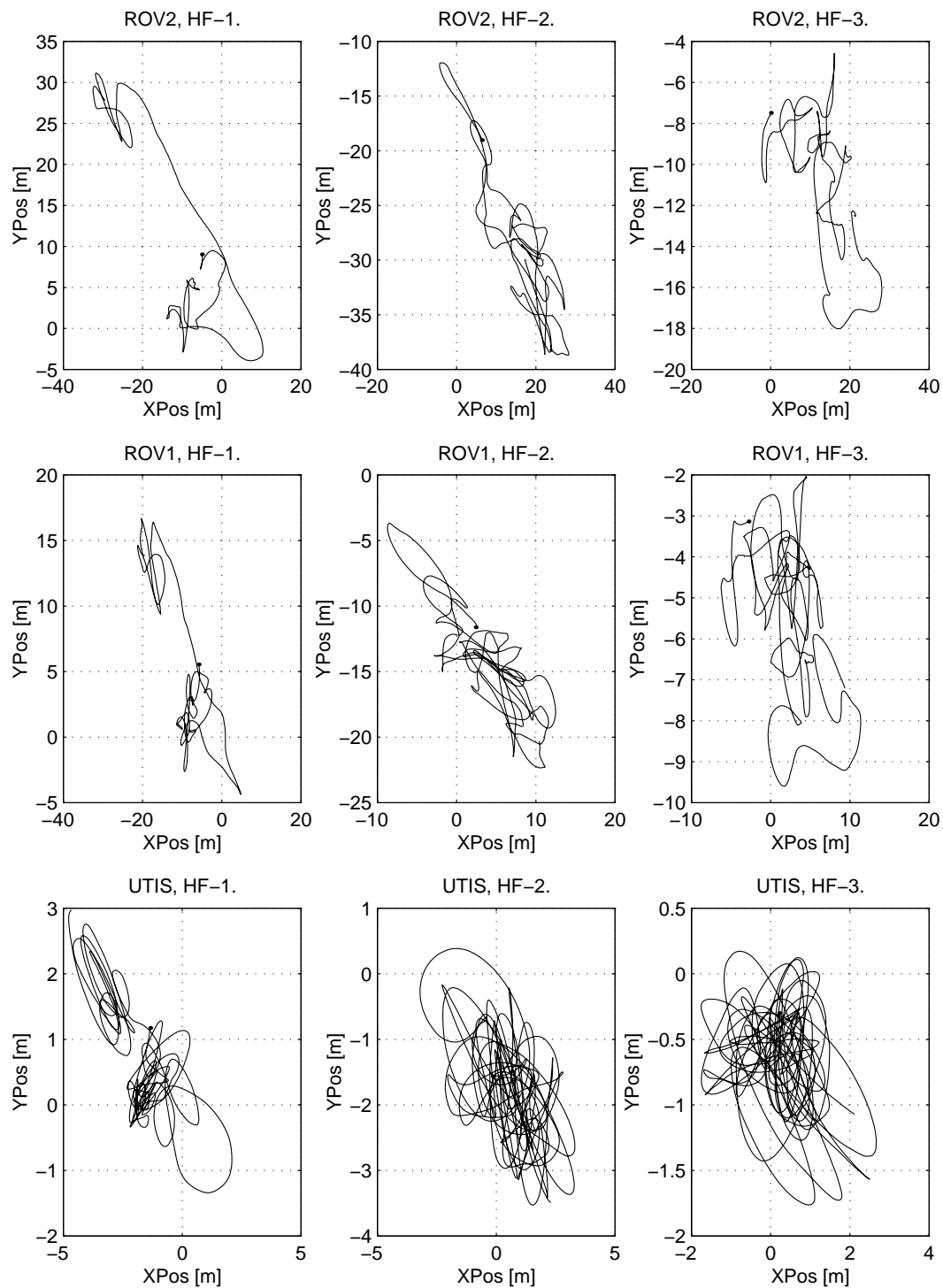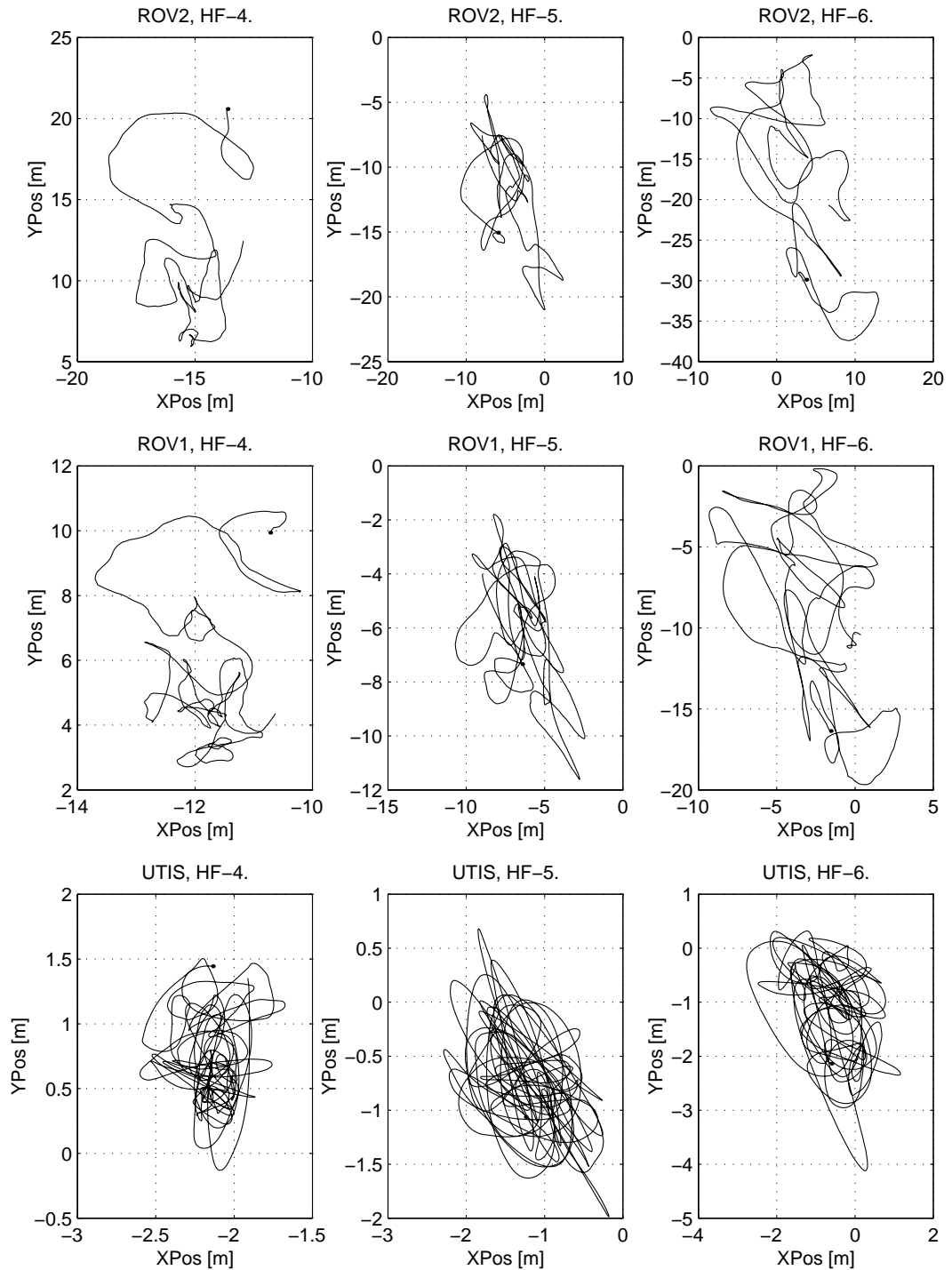
UR-79-01 Brigt Hatlestad, MK: The finite element method used in a fatigue evaluation of fixed offshore platforms. (Dr.Ing.Thesis).

UR-79-02 Erik Pettersen, MK: Analysis and design of celluar structures. (Dr.Ing.Thesis).

UR-79-03 Sverre Valsgård, MK: Finite difference and finite element methods applied to nonlinear analysis of plated structures. (Dr.Ing.Thesis).

UR-79-04 Nils T. Nordsve, MK: Finite element collapse analysis of structural members considering imperfections and stresses due to fabrication. (Dr.Ing.Thesis).

UR-79-05 Ivar J. Fylling, MK: Analysis of towline forces in ocean towing systems. (Dr.Ing.Thesis).

UR-80-06 Nils Sandsmark, MM: Analysis of Stationary and Transient Heat Conduction by the Use of the Finite Element Method. (Dr.Ing.Thesis).

UR-80-09 Sverre Haver, MK: Analysis of uncertainties related to the stochastic modeling of ocean waves. 1980.

UR-85-45 Nere Skomedal, MH   Three-Dimensional Flow Past Lifting Surfaces and Blunt Bodies. (Dr.Ing.Thesis). 1985.

UR-85-46 Alf G. Engseth, MK: Finite element collapse analysis of turbular steel offshore structures. (Dr.Ing.Thesis).

UR-86-47 Dengody Sheshappa, MP: A Computer Design Model for Optimizing Fishing Vessel Designs Based on Techno-Economic Analysis. (Dr.Ing.Thesis).

UR-86-48 Vidar Aanesland, MH: A Theoretical and Numerical Study of Ship Wave Resistance. (Dr.Ing.Thesis).

UR-86-49 Heinz-Joachim Wessel, MK: Fracture Mechanics Analysis of Crack Growth in Plate Girders. (Dr.Ing.Thesis).

UR-86-50 Jon Taby, MK: Ultimate and Post-ultimate Strength of Dented Tubular Members. (Dr.Ing.Thesis).

UR-86-51 Walter Lian, MH: A Numerical Study of Two-Dimensional Separated Flow Past Bluff Bodies at Moderate KC-Numbers. (Dr.Ing.Thesis).

UR-86-52 Bjørn Sortland, MH: Force Measurements in Oscillating Flow on Ship Sections and Circular Cylinders in a U-Tube Water Tank. (Dr.Ing.Thesis).

UR-86-53 Kurt Strand, MM: A System Dynamic Approach to One-dimensional Fluid Flow. (Dr.Ing.Thesis).

UR-86-54 Arne Edvin Løken, MH: Three Dimensional Second Order Hydrodynamic Effects on Ocean Structures in Waves. (Dr.Ing.Thesis).

UR-86-55 Sigurd Falch, MH: A Numerical Study of Slamming of Two-Dimensional Bodies. (Dr.Ing.Thesis).

UR-87-56 Arne Braathen, MH: Application of a Vortex Tracking Method to the Prediction of Roll Damping of a Two-Dimension Floating Body. (Dr.Ing.Thesis).

UR-87-57 Bernt Leira, MR: Caussian Vector Processes for Reliability Analysis involving Wave-Induced Load Effects. (Dr.Ing.Thesis).

UR-87-58 Magnus Småvik, MM: Thermal Load and Process Characteristics in a Two-Stroke Diesel Engine with Thermal Barriers (in Norwegian) (Dr.Ing.Thesis).

MTA-88-59 Bernt Arild Bremdal, MP: An Investigation of Marin Installation Processes - A Knowledge- Based Planning Approach. (Dr.Ing.Thesis).

MTA-88-60 Xu Jun, MK: Non-linear Dynamic Analysis of Space-framed Offshore Structures. (Dr.Ing.Thesis).

MTA-89-61 Gang Miao, MH: Hydrodynamic Forces and Dynamic Responses of Circular Cylinders in Wave Zones. (Dr.Ing.Thesis).

MTA-89-62 Martin Greenhow, MH:	Linear and Non-Linear
Studies of Waves and Floating Bodies.
Part I and Part 11. (Dr.Techn.Thesis).

MTA-89-63 Chang Li, MH:	Force Coefficients of Spheres and Cubes
in Oscillatory Flow with and without
Current.(Dr.Ing.Thesis).

MTA-89-64 Hu Ying, MP:	A Study of Marketing and Design in
Development of Marine Transport
Systems. (Dr.Ing.Thesis).

MTA-89-65 Arild Jæger, MH:	Seakeeping, Dynamic Stability and
Performance of a Wedge Shaped Planing
Hull. (Dr.Ing.Thesis).

MTA-89-66 Chan Siu Hung, MM:	The dynamic characteristics of
tilting-pad bearings.

MTA-89-67 Kim Wikstrøm, MP:	Analysis av projekteringen fʻr ett offshore
projekt. (Licenciat-avhandl.)

MTA-89-68 Jiao Guoyang, MR:	Reliability Analysis of Crack Growth
under Random Loading, considering Model
Updating. (Dr.Ing.Thesis).

MTA-89-69 Arnt Olufsen, MK:	Uncertainty and Reliability Analysis
of Fixed Offshore
Structures. (Dr.Ing.Thesis).

MTA-89-70 Wu Yu-Lin, MR:	System Reliability Analyses of
Offshore Structures using improved
Truss and Beam
Models. (Dr.Ing.Thesis).

MTA-90-71 Jan Roger Hoff, MH:	Three-dimensional Green function of a
vessel with forward speed in
waves. (Dr.Ing.Thesis).

MTA-90-72 Rong Zhao, MH:	Slow-Drift Motions of a Moored
Two-Dimensional Body in Irregular
Waves. (Dr.Ing.Thesis).

MTA-90-73 Atle Minsaas, MP:	Economical Risk Analysis. (Dr.Ing. Thesis).

MTA-90-74 Knut-Aril Farnes, MK:	Long-term Statistics of Response in
Non-linear Marine Structures. (Dr.Ing. Thesis).

MTA-90-75 Torbjrrn Sotberg, MK: Application of Reliability Methods for Safety Assessment of Submarine Pipelines. (Dr.Ing. Thesis).

MTA-90-76 Zeuthen, Steffen, MP: SEAMAID. A computional model of the design process in a constraint-based logic programming environment. An example from the offshore domain. (Dr.Ing. Thesis).

MTA-91-77 Haagensen, Sven, MM: Fuel Dependant Cyclic Variability in a Spark Ignition Engine - An Optical Approach. (Dr.Ing. Thesis).

MTA-91-78 Løland, Geir, MH: Current forces on and flow through fish farms. (Dr.Ing. Thesis).

MTA-91-79 Hoen, Christopher, MK: System Identification of Structures Excited by Stochastic Load Processes. (Dr.Ing. Thesis).

MTA-91-80 Haugen, Stein, MK: Probabilistic Evaluation of Frequency of Collision between Ships and Offshore Platforms. (Dr.Ing. Thesis).

MTA-91-81 Sødahl, Nils, MK: Methods for Design and Analysis of Flexible Risers. (Dr.Ing. Thesis).

MTA-91-82 Ormberg, Harald, MK: Non-linear Response Analysis of Floating Fish Farm Systems. (Dr.Ing. Thesis).

MTA-91-83 Marley, Mark J., MK: Time Variant Reliability Under Fatigue Degradation. (Dr.Ing. Thesis).

MTA-91-84 Krokstad, Jørgen R., MH: Second-order Loads in Multidirectional Seas. (Dr.Ing. Thesis).

MTA-91-85 Molteberg, Gunnar A., MM: The application of system identification techniques to Performance Monitoring of four stroke turbocharged Diesel Engines. (Dr.Ing. Thesis).

MTA-92-86 Mørch, Hans Jørgen Bjelke, MH: Aspects of Hydrofoil Design; with Emphasis on Hydrofoil Interaction in Calm Water. (Dr.Ing. Thesis).

MTA-92-87 Chan Siu Hung, MM: Nonlinear Analysis of Rotordynamic Instabilities in High-speed Turbomachinery. (Dr.Ing. Thesis).

MTA-92-88 Bessason, Bjarni, MK: Assessment of Earthquake Loading and Response of Seismically Isolated Bridges. (Dr.Ing. Thesis).

MTA-92-89 Langli, Geir, MP: Improving Operational Safety through Exploitation of Design Knowledge - an investigation of offfshore platform safety. (Dr.Ing. Thesis).

MTA-92-90 Sævik, Svein, MK: On Stresses and Fatigue in Flexible Pipes. (Dr.Ing. Thesis).

MTA-92-91 Ask, Tor Ø., MM: Ignition and Flame Growth in Lean Gas-Air Mixtures. An Experimental Study with a Schlieren System. (Dr.Ing. Thesis).

MTA-86-92 Hessen, Gunnar, MK: Fracture Mechanics Analysis of Stiffened Tubular Members. (Dr.Ing. Thesis).

MTA-93-93 Steinebach, Christian, MM: Knowledge Based Systems for Diagnosis of Rotating Machinery. (Dr.Ing. Thesis).

MTA-93-94 Dalane, Jan Inge, MK: System Reliability in Design and Maintenance of Fixed Offshore Structures. (Dr.Ing. Thesis).

MTA-93-95 Steen, Sverre, MH: Cobblestone Effect on SES. (Dr.Ing. Thesis).

MTA-93-96 Karunakaran, Daniel, MK: Nonlinear Dynamic Response and Reliability Analysis of Drag-dominated Offshore Platforms. (Dr.Ing. Thesis).

MTA-93-97 Hagen, Arnulf, MP: The Framework of a Design Process Language. (Dr.Ing. Thesis)

MTA-93-98 Nordrik, Rune, MM: Investigation of Spark Ignition and Autoignition in Methane and Air Using Computational Fluid Dynamics and Chemical Reaction Kinetics. A Numerical Study of Ignition Processes in Internal Combustion Engines. (Dr.Ing.Thesis).

MTA-94-99 Passano, Elizabeth, MK: Efficient Analysis of Nonlinear Slender Marine Structures. (Dr.Ing.Thesis).

MTA-94-100 Kvålsvold, Jan, MH: Hydroelastic Modelling of Wetdeck Slamming on Multihull Vessels. (Dr.Ing.Thesis).

MTA-94-101 (Dr.Ing.Thesis) Ikke godkjent.

MTA-94-102 Bech, Sidsel M., MK: Experimental and Numerical Determination of Stiffness and Strength of GRP/PVC Sandwich Structures. (Dr.Ing.Thesis).

MTA-95-103 Paulsen, Hallvard, MM: A Study of Transient Jet and Spray using a Schlieren Method and Digital Image Processing. (Dr.Ing.Thesis).

MTA-95-104 Hovde, Geir Olav, MK: Fatigue and Overload Reliability of Offshore Structural Systems, Considering the Effect of Inspection and Repair. (Dr.Ing.Thesis).

MTA-95-105 Wang, Xiaozhi, MK: Reliability Analysis of Production Ships with Emphasis on Load Combination and Ultimate Strength. (Dr.Ing.Thesis).

MTA-95-106 Ulstein, Tore, MH: Nonlinear Effects of a Flexible Stern Seal Bag on Cobblestone Oscillations of an SES. (Dr.Ing.Thesis).

MTA-95-107 Solaas, Frøydis, MH: Analytical and Numerical Studies of Sloshing in Tanks. (Dr.Ing.Thesis).

MTA-95-108 Hellan, Øyvind, MK: Nonlinear Pushover and Cyclic Analyses in Ultimate Limit State Design and Reassessment of Tubular Steel Offshore Structures. (Dr.Ing.Thesis).

MTA-95-109 Hermundstad, Ole A., MK: Theoretical and Experimental Hydroelastic Analysis of High Speed Vessels. (Dr.Ing.Thesis).

MTA-96-110 Bratland, Anne K., MH: Wave-Current Interaction Effects on Large-Volume Bodies in Water of Finite Depth. (Dr.Ing.Thesis).

MTA-96-111 Herfjord, Kjell, MH: A Study of Two-dimensional Separated Flow by a Combination of the Finite Element Method and Navier-Stokes Equations. (Dr.Ing.Thesis).

MTA-96-112 Æsøy, Vilmar, MM: Hot Surface Assisted Compression Ignition in a Direct Injection Natural Gas Engine. (Dr.Ing.Thesis).

MTA-96-113 Eknes, Monika L., MK: Escalation Scenarios Initiated by Gas Explosions on Offshore Installations. (Dr.Ing.Thesis).

MTA-96-114 Erikstad, Stein O.,MP: A Decision Support Model for Preliminary Ship Design. (Dr.Ing.Thesis).

MTA-96-115 Pedersen, Egil, MH: A Nautical Study of Towed Marine Seismic Streamer Cable Configurations. (Dr.Ing.Thesis).

MTA-97-116 Moksnes, Paul O., MM: Modeling Two-Phase Thermo-Fluid Systems Using Bond Graphs. (Dr.Ing. Thesis).

MTA-97-117 Halse, Karl H., MK: On Vortex Shedding and Prediction of Vortex-Induced Vibrations of Circular Cylinders. (Dr.Ing. Thesis).

MTA-97-118 Igland, Ragnar T., MK: A Thesis Submitted in Partial Fulfilment of the Requirements for the Degree of "Doktor Ingeniør". (Dr.Ing. Thesis).

MTA-97-119 Pedersen, Hans-P., MP: Levendefiskteknologi for fiskefartøy. (Dr.Ing. Thesis).

MTA-98-120 Vikestad, Kyrre, MK: Multi-Frequency Response of a Cylinder Subjected to Vortex Shedding and Support Motions. (Dr.Ing. Thesis).

MTA-98-121 Azadi, Mohammad R.E., MK: Analysis of Static and Dynamic
Pile-Soil-Jacket Behaviour.
(Dr.Ing. Thesis).

MTA-98-122 Ulltang, Terje, MP: A Communication Model for Product
Information. (Dr.Ing. Thesis).

MTA-98-123 Torbergsen, Erik, MM: Impeller/Diffuser Interaction
Forces in Centrifugal
Pumps. (Dr.Ing. Thesis).

MTA-98-124 Hansen, Edmond, MH: A Descrete Element Model to Study
Marginal Ice Zone Dynamics and the
Behaviour of Vessels Moored in Broken
Ice. (Dr.Ing. Thesis).

MTA-98-125 Videiro, Paulo M., MK: Reliability Based Design of Marine
Structures. (Dr.Ing. Thesis).

MTA-99-126 Mainon, Philippe, MK: Fatigue Reliability of Long Welds
Application to Titanium
Risers. (Dr.Ing. Thesis).

MTA-99-127 Haugen, Elin M., MH: Hydroelastic Analysis of Slamming
on Stiffened Plates with Application to
Catamaran Wetdecks. (Dr.Ing. Thesis).

MTA-99-128 Langhelle, Nina K., MK: Experimental Validation and
Calibration of Nonlinear Finite Element
Models for Use in Design of Aluminium
Structures Exposed to Fire.
(Dr.Ing. Thesis).

MTA-99-129 Berstad, Are J., MK: Calculation of Fatigue Damage in
Ship Structures. (Dr.Ing. Thesis).

MTA-99-130 Andersen, Trond M., MM: Short Term Maintenance
Planning. (Dr.Ing.Thesis).

MTA-99-131 Tveiten, Bård Wathne, MK: Fatigue Assessment of Welded
Aluminum Ship Details. (Dr.Ing.Thesis).

MTA-99-132 Søreide, Fredrik, MP: Applications of underwater
technology in deep water archaeology.
Principles and practice. (Dr.Ing.Thesis).

MTA-99-133 Tønnessen, Rune, MH: A Finite Element Method Applied to Unsteady Viscous Flow Around 2D Blunt Bodies With Sharp Corners. (Dr.Ing.Thesis).

MTA-99-134 Elvekrok, Dag R., MP: Engineering Integration in Field Development Projects in the Norwegian Oil and Gas Industry. The Supplier Management of Norne. (Dr.Ing.Thesis).

MTA-99-135 Fagerholt, Kjetil, MP: Optimeringsbaserte Metoder for Ruteplanlegging innen skipsfart. (Dr.Ing.Thesis).

MTA-99-136 Bysveen, Marie, MM: Visualisation in Two Directions on a Dynamic Combustion Rig for Studies of Fuel Quality. (Dr.Ing.Thesis).

MTA-2000-137 Storteig, Eskild, MM: Dynamic characteristics and leakage performance of liquid annular seals in centrifugal pumps. (Dr.Ing.Thesis).

MTA-2000-138 Sagli, Gro, MK: Model uncertainty and simplified estimates of long term extremes of hull girder loads in ships. (Dr.Ing.Thesis).

MTA-2000-139 Tronstad, Harald, MK: Nonlinear analysis and design of cable net structures like fishing gear based on the finite element method. (Dr.Ing.Thesis).

MTA-2000-140 Kroneberg, Andr, MP: Innovation in shipping by using scenarios. (Dr.Ing.Thesis).

MTA-2000-141 Haslum, Herbjørn Alf, MH: Simplified methods applied to nonlinear motion of spar platforms. (Dr.Ing.Thesis).

MTA-2001-142 Samdal, Ole Johan, MM: Modelling of Degradation Mechanisms and Stressor Interaction on Static Mechanical Equipment Residual Lifetime. (Dr.Ing.Thesis).

MTA-2001-143 Baarholm, Rolf Jarle, MH: Theoretical and experimental studies of wave impact underneath decks of offshore platforms. (Dr.Ing. Thesis).

MTA-2001-144 Wang, Lihua, MK: Probabilistic Analysis of Nonlinear
                                       Wave-induced Loads on Ships.
                                       (Dr.Ing. Thesis).

MTA-2001-145 Kristensen, Odd H. Holt, MK: Ultimate Capacity of
                                       Aluminium Plates under Multiple Loads,
                                       Considering HAZ
                                       Properties. (Dr.Ing. Thesis).

MTA-2001-146 Greco, Marilena, MH: A Two-Dimensional Study of
                                       Green-Water Loading. (Dr.Ing. Thesis).

MTA-2001-147 Heggelund, Svein E., MK: Calculation of Global Design
                                       Loads and Load Effects in Large High
                                       Speed Catamarans. (Dr.Ing. Thesis).

MTA-2001-148 Babalola, Olusegun T., MK: Fatigue Strength of Titanium
                                       Risers - Defect Sensitivity.
                                       (Dr.Ing. Thesis).

MTA-2001-149 Mohammed, Abuu K., MK: Nonlinear Shell Finite Elements
                                       for Ultimate Strength and Collapse
                                       Analysis of Ship Structures.
                                       (Dr.Ing. Thesis).

MTA-2002-150 Holmedal, Lars E., MH: Wave-current interactions in the
                                       vicinity of the sea bed.
                                       (Dr.Ing. Thesis).

MTA20-02-151 Rognebakke, Olav F., MH: Sloshing in rectangular tanks
                                       and interaction with ship motions

MTA-2002-152 Lader, Pål Furset, MH: Geometry and Kinematics of
                                       Breaking Waves. (Dr.Ing. Thesis).

MTA-2002-153 Yang, Qinzheng, MH: Wash and wave resistance of ships
                                       in finite water depth.
                                       (Dr.Ing. Thesis).

MTA-2002-154 Melhus, Øyvin, MM: Utilization of VOC in Diesel
                                       Engines. Ignition and combustion of
                                       VOC released by crude oil tankers.
                                       (Dr.Ing. Thesis).

MTA-2002-155 Ronæss, Marit, MH: Wave Induced Motions of Two Ships
                                       Advancing on Parallel Course.
                                       (Dr.Ing. Thesis).

MTA-2002-156 Økland, Ole D., MK: Numerical and experimental investigation of whipping in twin hull vessels exposed to severe wet deck slamming. (Dr.Ing. Thesis).

MTA-2002-157 Ge, Chunhua, MK: Global Hydroelastic Response of Catamarans due to Wet Deck Slamming. (Dr.Ing. Thesis).

MTA-2002-158 Byklum, Eirik, MK: Nonlinear Shell Finite Elements for Ultimate Strength and Collapse Analysis of Ship Structures. (Dr.Ing. Thesis).

IMT-2003-1 Chen, Haibo, MK: Probabilistic Evaluation of FPSO-Tanker Collision in Tandem Offloading Operation. (Dr.Ing.Thesis).

IMT-2003-2 Skaugset, Kjetil Bjørn, MK: On the Suppression of Vortex Induced Vibrations of Circular Cylinders by Radial Water Jets. (Dr.ing.Thesis).

IMT-2003-3 Chezhian, Muthu Three-Dimensional Analysis of Slamming (Dr.ing. Thesis).

IMT-2003-4 Buhaug, Øyvind Deposit Formation on cylinder Liner Surfaces in Medium Speed Engines

IMT-2003-5 Tregde, Vidar Aspects of Ship Design; Optimization of Aft Hull with Inverse Geometry Design

IMT-2003-6 Wist, Hanne Therese Statistical Properties of Successive Ocean Wave Parameters

IMT-2004-7 Ransau, Samuel Numerical Methods for Flows with Evolving Interfaces

IMT-2004-8 Soma, Torkel Blue-Chip or Sub-Standard- A data interrogation approach of identify safety characteristics of shipping organizations.

IMT-2004-8 Ersdal, Svein An Experimental Study of Hydrodynamic Forces on Cylinders and Cables in Near Axial Flow